PH.D. THESIS IN CHEMICAL ENGINEERING

XXV Cycle

Characterization of advected-surfaces. The sinews of a "MultiSECtioning" approach for non-premixed combustion

Scientific Committee

Prof. Antonio Cavaliere
Eng. Raffaele Ragucci
Eng. Pasquale Di Martino

Candidate

Eng.Giancarlo Sorrentino

To my family and mentors

Characterization of advected-surfaces. The sinews of a “MultiSECtioning” approach for non-premixed combustion

Table of Contents

Introduction

The field of turbulent combustion has undergone significant progress since the first original paradigms for modeling turbulent combustion flows emerged more than 60 years ago. In the seventies, the emergence of computational fluid dynamics (CFD) and access to more advanced non-intrusive laser-based techniques for combustion measurements have enabled further development in the field. More recently, rapid progress in the modeling and simulation of turbulent flows has occurred.

This progress may be attributed to different factors. First, we have access to more advanced computational and experimental resources. Advanced computational resources enable the computations of more realistic combustion flows with better description of the flow and chemical reactions. The higher access to computational resources also enabled the emergence of new paradigms in turbulent combustion simulation that address direct computations of unresolved physics. Turbulent combustion has long been considered a paradigm for multiscale problems and has long been identified as one of the important problems to solve, hence the increasing interest from the computational and applied mathematics communities.

In this sense, combustion science needs a very high level of interdisciplinarity to be analyzed.

Turbulent combustion has a particular relevance since in common devices involved flows are inevitably turbulent, because of their large flow rates and the request of intense heat and mass exchanges.

Moreover the subject of turbulent combustion spans a broad range of applications. For power generation, the burning of fossil fuel and an increasing range of alternative fuels form a significant component of both stationary power and transportation systems. Any

further advancement in the understanding of turbulent combustion processes is also an important step toward the prevention of accidental fires and explosions. The modeling paradigms of turbulent combustion are also relevant to an even broader range of physical phenomena, which exhibit multiscale and multiphysics natures.

Therefore, accounting for the multiscale nature of turbulent combustion is unavoidable in turbulent combustion model elaboration.

Combustion is both a complicated and complex process.

As matter of facts, it has to be noted that, without a correct strategy, the problem is commonly faced with the specification of a long list of submodels, whose selection is often motivated only for some appealing peculiarity.

On the opposite the definition of specific subsets of submodels can favour the accumulation of information on their effectiveness that, in time, can lead to the achievement of a critical and recognized assessment of their overall performance that eventually would allow for the establishment of standard methodologies.

A second consideration is that submodels choice can be guided by the specific interlinking between them. This link has to be identified for each single strategy and it can guide at least the choices related to the model core.

These observations, many of which have only recently become possible through advances in simulation, suggest that the level to which such interactions can be observed are in fact degrees of resolution, or scale.

A possible strategy should at least have the common feature to be realistic and quantifiable in their realism. This is not a trivial requirement since the validation of a high level model is rarely done without suitable adjustment of parameters or even adjustment of some of its components.

This means that validation has to be performed in a knowledgeable way by selecting representative samples of cases to be used for a thorough evaluation of carefully selected sub-models sets on the basis of their features and of their potential interaction with the model core.

Of course, this is true only for sequential processes and in the case each single subprocess can be successfully described.

On the ground of these considerations a strategy allowing for the analysis of the influence of single subprocesses has been conceived.

Such strategy could be named “MultiSECtioning” Process Evaluation Strategy since it refers to a Multidimensional, Multiscale, Multicomponent and Multiphysics process.

The acronym evokes that the procedure consists in sectioning the whole process in parts, by means of both geometrical sectioning of the control volumes and/or selection of a subset of physical effects, which can be modelled and validated when added ones at the time to the process.

This approach has been followed in a rigorous way only in some passages from one level of complexity to a higher one or in empirical way in the whole process analysis. It deserves, thus, a systematic review work of both the possible steps for its application and the sparse information that can be inserted in such framework. Furthermore a more explicit and proper classification of all the effects to be evaluated for such strategy is needed because this can affect in turn subsequent choices along the complexity enlargement process.

The thesis concerns the study of this strategy and its applicability at different non-premixed combustion processes.

The main parts of this approach are reported in this thesis with emphasis on the literature surveys on each piece of this methodology.

In particular, the advected-surfaces are considered the building-block of each non-premixed combustion process and therefore their characterization lays the foundation for a sequentially-structured approach.

Turbulent combustion can be viewed as a three-stage process of stirring, diffusion and ignition spanning the full spectrum of space-time scales of the flow.

An exact description of stirring phenomena is given by the location of the interface that in this thesis work is seen as the basic structure which binds together stirring, mixing and ignition processes (i.e. the “sinews” of a MultiSECtioning strategy).

The thesis shows that the viability of a sequential approach is related to the measurability or modeling of some "critical" amounts. The thesis work is focused on these quantities and on the critical points of the proposed strategy. These issues (related in some way to the Lagrangian nature of the process) can be exploited by a body of knowledge that has now consolidated in a structured manner on individual subprocesses well characterized in parametric conditions. In fact the latter require a unifying procedure in order to submit their information content in the description of complex processes.

In relation to these quantities, an original image processing procedure closely correlated with measures of Particle Image Velocimetry has been developed to overcome the critical steps of the proposed methodology for the analysis of combustion processes.

The evaluated quantities represent the strength and give remarkable flexibility to the presented approach in relation to the different ignition-processes that may occur in a combustion system.

The critical points concerning the ignition step have been deeply analyzed in the PhD thesis.

In fact, even in this case the thesis clarifies that this survey could not be conducted along the lines of works of literature, but required a specific analysis.

In this context it is noteworthy the application of the MultiSECtioning procedure to the MILD combustion processes.

In particular, novel contributions concerning the diffusive reactive structures in non-conventional combustion conditions are reported in the first part of the PhD thesis and they are discussed in relation to the different chemical/diffusion time scales.

Chapter I
Paradigms in turbulent combustion: strategies and experimental/computational challenges

I.1 The multiscale and multiphysics nature of turbulent combustion flows

Combustion is one of the most important processes in nature and in the man generated habitat. Chemistry, fluid-dynamics, electro-magnetism disciplines are all required in describing different aspects of combustion processes. In addition, all the matter state: solid, liquid, gas and plasma are involved (Kuo KK 2005, Williams FA 1985).

The topic is both relevant and persistent.

Its relevance is obvious, given the continuing dominance of the combustion of hydrocarbon fuels to meet the world's energy demands. Turbulent combustion has a particular relevance since in common devices involved flows are inevitably turbulent, because of their large flow rates and the request of intense heat and mass exchanges.

The persistence of research on turbulent combustion over many decades reflects the formidable challenges of the subject, which yield slowly to our increasing understanding and technological capabilities in terms of computer power and instrumentation.

The modeling paradigms of turbulent combustion are also relevant to an even broader range of physical phenomena, which exhibit multiscale and multiphysics natures (Law CK 2006).

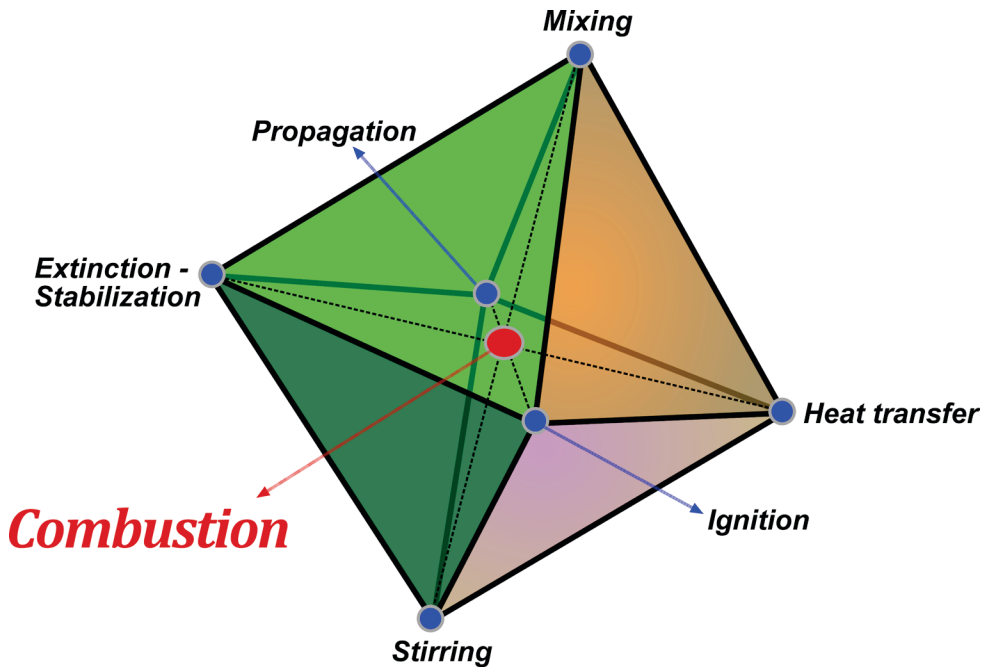

Figure I.1 *Combustion as a complex multi-physics phenomena*

As schematized in Fig. I.1, combustion processes are complex multi-physics phenomena with simultaneous presence of multiphase flow, turbulence, heat and mass transport, and chemical kinetics, which non-linearly interact with each other.

Semantically, a multiphysics system consists of more than one component governed by its own principle(s) for evolution or equilibrium, typically conservation or constitutive laws. A major classification in such systems is whether the coupling occurs in the bulk or over an idealized interface that is lower dimensional or a narrow buffer zone.

All scales and physics are relevant and coupled must be resolved or modeled

Perhaps the main challenge in predicting turbulent combustion flows arises from their multiscale nature (Peters N 2009). Turbulent combustion flows exhibit a broad range of length and time scales. The most elementary processes, which lead to the breaking of chemical bonds, may occur at time scales as short as 10^{-15} s. These scales may need to be taken into account in order to formulate constitutive relations for the rate constant of elementary reactions. These relations enable the integration of chemistry within the

continuum models for combustion flows and are characterized by longer times than their underlying atomistic processes. However, the gap in time scales between some elementary chemical reactions and relevant flow or device scales may still remain wide.

Characteristic time scales of most of the chemical reactions occurring in a combustion process are in the order of 10^{-10} s; while other, much slower, reactions such as the ones involved in the thermal formation of NO, can be of the order of milliseconds. Important processes evolve in time scales comparable with chemical ones. They include molecular transport, which together with chemistry form the basic ingredients of flame structures. They also include soot processes from the formation of soot precursors to primary particles, and their associated roles in radiation transport from flames. Finally, molecular processes are coupled with turbulent transport and, in many problems, there is considerable overlap between their corresponding time scales.

The range of length scales is equally broad. On the atomic scale, forces (attractive or repulsive) between molecules act within a distance as short as the molecular scales, while collisions between molecules, which are responsible for chemical reactions, depend on the molecular mean free path. Fortunately, most of what occurs on the atomic scales can be represented through constitutive relations (e.g. the Arrhenius form of reaction kinetics). Within continuum scales, reaction zone thicknesses in hydrocarbon flames associated with intermediate species are in the order of 10^{-5} m, and are approximately one order of magnitude smaller than the thermal thicknesses of these flames. Device scales of the order of 10 cm or higher represent the upper range of length scales. Therefore, accounting for the multiscale nature of turbulent combustion is unavoidable in turbulent combustion model elaboration.

At this point, it is important to make a distinction between different types of coupling among physical processes.

The type of coupling determines the type of multiscale strategy adopted (Echekki T 2009). Here, we consider two important classification categories: (i) whether these processes have weak or strong physical coupling (i.e. strong coupling translates into a strong change in a process due to a change in another process) and (ii) whether the scales of these processes are coupled (i.e. there is overlap between scales represented by two processes). Further subdivision within the different types of physical coupling may be explored as well; in particular, whether the dependence of two processes acts both ways or whether only one process is dependent upon the other has very important consequences. The two major classifications result in four different types (types A–D) of interactions as summarized in table 1 and illustrated in figure I.2.

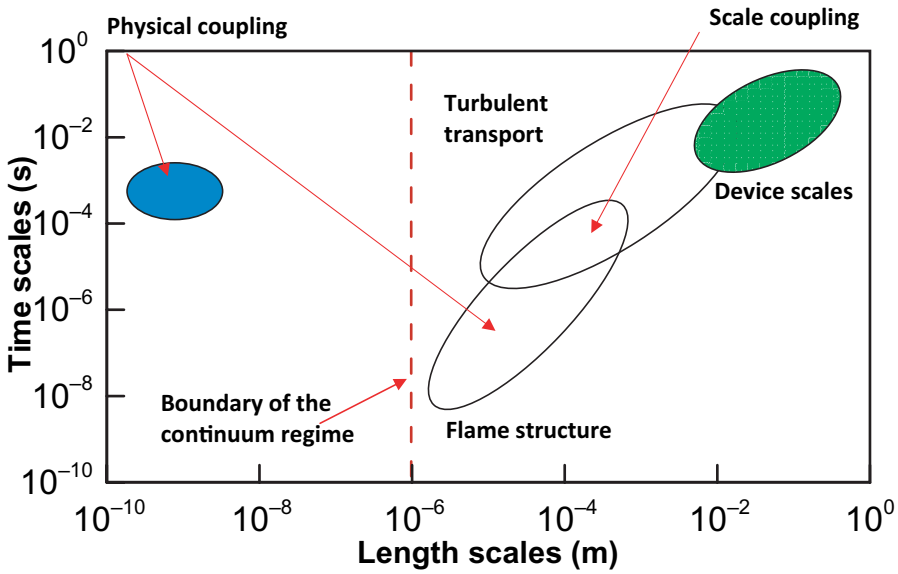

Figure I.2. Length and time scales in turbulent combustion.

Type A coupling includes processes that have strong physical coupling and when the scales over which these processes operate overlap. An example of such a process is diffusion and reaction within a laminar premixed or diffusion flame. Type B coupling includes processes that have weak physical or one-way coupling and the scales over which these processes

operate overlap. An example of such a process is thermal NO formation in flames. As a matter of fact, in combustion simulations, it is common to evaluate NO formation as a post-processing step once the major species are computed and steady-state relations are assumed for intermediates. Type C coupling involves strong physical coupling between processes, while the scales are not coupled. An example of such a process is thermo-acoustic coupling in a combustion chamber. A second, very relevant case, of strong physical coupling and of no scale coupling, is the well-know flamelet approximation. In this model the flames in turbulent flow are assumed to be so thin that they behave locally as laminar flamelets. Another example is soot formation and soot radiation in turbulent flames. Type D coupling involves weak coupling and no overlap of scales between processes.

Table 1. Types of coupling between physical processes.

Type A. Strong physical coupling and scale coupling	Type B. Weak physical coupling and scale coupling
Type C. Strong physical coupling and no scale coupling	Type D. Weak physical coupling and no scale coupling

		Physical Coupling	
		strong	**weak**
Scale coupling	**strong**	A	
	weak		B
	NO	C	D

Table 1 *Types of coupling between physical processes, adapted from Echekki, T. (2009). Computational Science & Discovery, 2(1), 013001.*

There is a large variety of possible conditions where one of the interaction condition occurs. It is not simple to establish “a priori” which is the most appropriate modelization

and, moreover, many concurrent processes can be characterized by different coupling conditions. A synthetic and fascinating way of expressing these concepts is by stating that combustion is both a complicated and complex process.

It is complicated because it is composed of many interrelated parts and has to be dealt with the contemporaneous use of many relationships. This in turn entails that the construction of the model can be subjected to unpredictable errors. For instance, it would not be easy to verify if a sub-model will be used in a working condition outside its validation range. Furthermore, the transfer of the construction of the model is itself a difficulty and several uncontrollable errors are possible.

It is also complex because the interaction either of the different effects in the direct numerical approach or of the different submodels is highly non-linear according to the equation nature. This has been documented in centennial experiences accumulated on turbulent flows and in a more recent recognition of the mathematical formulation of the complexity (Ashby WR 1962, Prigogine I 1984, Strogatz S 2003, Strogatz S 1994, Amaral LA and Ottino JM 2004).

The difference between complexity and complication has to be underlined. Complexity is now a well defined concept related to open dissipative systems with particular repetitive feedback. Complication refers only to the number of pieces of information to be dealt with or to be communicated.

For both reasons it is very difficult to assess the predictability of a model. Even its validation in a specific domain cannot be straightforwardly extended to a wider domain. This is indeed true when equation parameters and/or coefficients are empirically adjusted to fit the predictions with available experimental data.

It is straightforward that complicated and complex problems need rational, effective and well-established strategies to be faced with.

As a matter of fact, it has to be noted that, without a correct strategy, the problem is commonly dealt with the specification of a long list of submodels, whose selection is often motivated only for some appealing peculiarity. For instance, it is fashionable to exploit the most recent submodels for some specific sub-processes (say LES for turbulence submodel) without any change of other submodels (say mixing, radiation etc.) and without a deep analysis of possible non-linear interaction between them. On the opposite, the definition of specific subsets of submodels can favour the accumulation of information on their effectiveness that, in time, can lead to the achievement of a critical and recognized assessment of their overall performance that eventually would allow for the establishment of standard methodologies. Each single strategy can be named with a short name or an acronym, so that skilled users can recognize it. In some way this has been implicitly done by commercial codes, which uses fixed submodels. They have a name, they collect an ensemble of submodels and they are assembled and optimized for specific conditions.

A second consideration is that submodels choice can be guided by the specific interlinking between them. This link has to be identified for each single strategy and it can guide at least the choices related to the model core. This is needed not only for formal self-consistency of the model, but also because complicated problems need simplifications also in the communication and in the expert use of the single pieces. On the opposite, "undeclared" strategies make the list of the choice arbitrary and the historical memory of the model formulation is lost. Possible ad hoc assumptions made in the original elaboration of the model are buried in a myriad of details, which does not have any internal diagnostic tool able to point out potential errors in the model formulation and use.

A complex system is one in which numerous independent elements continuously interact and spontaneously organize and reorganize themselves into more and more elaborate structures over time. As with chaos, the behavior of self-organizing complex systems

cannot be predicted, and they do not observe the principle of additivity, i.e., their components cannot be divided up and studied in isolation. Complex systems can naturally evolve to a state of self-organized criticality, in which behavior lies at the border between order and disorder.

With increased computational capability, and with the increasing desire to create autonomous or near-autonomous systems that can exhibit complex life-like behaviors, challenges arise in applying existing system formalisms to describe the behaviour of complex and complicated systems and of their emerging properties. Complexity related to the physics of combustion rapidly converging upon a common observation: robustness, richness, and diversity observed in a combustion process is more than the simple sum of the components. Interaction amongst constituent components at local-level, affects (both directly and indirectly) to varying degrees, the behavior of the system of which they are a part, and this global-level behavior in turn indirectly affects the interactions of the components. These observations, many of which have only recently become possible through advances in simulation, suggest that the level to which such interactions can be observed are in fact degrees of resolution, or scale. Depending on the perspective of the observer there is some level of emergent behavior, global at that scale, at which interesting and useful behaviors are observed (Holland TO 2007)

I.2 The need for strategies in combustion processes

Now, we turn our attention to general strategies for modeling the different types of multiscale processes, and, in particular, for combustion. When there is little physical coupling, the solutions involved for different processes may be implemented independently of each other if they are governed by different governing equations. The order in which

these solutions are implemented is, in principle, inconsequential to the solution. Strong physical coupling with coupled time and length scales involves two important strategies:

- a sequential solution strategy if the physical coupling is important only in one direction (from one process to another one)
- a concurrent solution if the physical coupling is important in both directions (i.e. two processes are strongly dependent on each other).

A sequential solution involves the solution of the controlling process and subsequently of the dependent process. A concurrent solution involves the mathematical coupling of the two solutions for both processes. However, it is possible to implement the solution as a sequential solution with a correction step. A common example of such a simplified analysis is the implementation of operator-split schemes for reaction and transport in laminar and turbulent flame solutions. A correction for splitting errors may be needed for accurate solutions.

Figure I.2 shows a schematic of selected processes in turbulent combustion, which may be relevant to a broad range of applications, including combustion in internal combustion engines. The figure illustrates the types of coupling discussed above. The figure shows that a broad range of scales are represented within the combustion problem spanning more than 10 decades in time and length scales. In the figure, flame structure encompasses all processes involved in defining the different layers within the flame. This includes layers in the reaction zone that define the profiles of the radicals formed during the consumption of hydrocarbon fuels (e.g. CH or CH3 profiles). A temporal resolution of the fastest reactions may be necessary to capture these layers. In practical combustion devices, turbulence intensities may be high enough to yield Kolmogorov scales that are of similar magnitudes to the preheat layers in flames and the broader profiles in the reaction zone. Therefore, some overlap between turbulence and flame scales may be present. On the larger scales,

combustor geometry or the motion of its moving parts (e.g. pistons and valves) may also result in large-scale motions, such as tumble or swirl, or recirculation zones for flame stabilization that determine the range of device scales in the figure. Other processes that may be scale decoupled, yet physically coupled, include soot formation events within the reaction zone and the impact on radiation transport from the flames. Given the different types of coupling present, different strategies for modeling them may be formulated according to the extent of scale and physical coupling.

In this framework, traditional approaches to turbulent combustion modeling have sought to exploit the natural separation of scales under different regimes of combustion (Bilger RW et al. 2005). For example, the classic eddy-breakup (EBU) model (Spalding DB 1971) and the eddy dissipation concept (EDC) (Magnussen BF and Hjertager BH 1977) assume fast chemistry, and therefore, a rate of reaction that is limited by, and proportional to, the rate of mixing. The later flamelet models (Peters N 1983) used similar concepts to separate the flame scales from those of turbulence; with this separation, the intricate coupling between molecular transport and chemistry is incorporated. The separation of scales also introduced concepts of reduced parameter spaces that characterize the flame response. For example, in non-premixed flames, the flame response is parameterized in terms of the mixture fraction and the scalar dissipation rate. An important consequence of such a parameterization is that transport equations in physical space are solved for moments of these parameters; In a second stage the remaining reactive scalar statistics are evaluated from the reduced parameter space. Moment-based methods offer some very practical advantages in turbulent combustion modeling. Therefore, they will remain an attractive choice, even if alternative strategies will become more feasible. The reasons for this are as follow. Firstly, a large body of experiences has developed since the early implementations of combustion computational fluid dynamics (CFD) (Westbrook C et al. 2005) that provided strategies for

fine-tuning moment-based models. Secondly, these approaches remain computationally affordable and are commonly available in commercial CFD software. Moreover, in many applications these approaches predict the desired statistics associated with the flow or the reactive scalars reasonably well. However, it has to be noted that they are frequently used beyond the bounds of their original assumptions. In terms of implementation, the discretization of the governing equations for the scalars follows closely that of the moments associated with momentum, enabling an easy extension of the number of moments if needed.

While moment-based models have been successful in predicting problems in combustion applications, they remain limited by their underlying assumptions. These assumptions are related to combustion mode (e.g. premixed versus non-premixed), combustion regime (e.g. flamelet versus distributed reaction) and dominant chemistry. These assumptions determine the choice of transported moments, the implementation of closure in the moment equation and the reconstruction of the spatial statistical distributions for these moments.

These assumptions are increasingly challenged by evolving needs in combustion technologies that are pushing for higher efficiencies and lower emissions. These challenges impose themselves not only in the volume of statistics that needs to be predicted but also in the types of operational regimes that are being explored. As an example, lean and ultra-lean burning in gas-turbine combustors may result in strong non- equilibrium effects, such as extinction–reignition events, which represent an important departure from steady operation (Keller JO 1990). Similar constraints have evolved from the burning of non-conventional alternative fuels with lower heating values. Strategies to burn in unconventional regimes to reduce emissions are already under development or testing (e.g. supercritical combustion, MILD and flameless combustion) (Cavaliere A and de Joannon M 2004, Galletti C et al. 2007, Mancini M et al. 2007, Christo FC and Dally BB 2005).

The scenarios above depicted and the emerging new trends in combustion technologies, including the growing trend to make large use of computational tools in the design of combustion system, either for economical and time constrains, bring to the conclusion that considerable effort has to be paid to the individuation of more reliable numerical models. An increasing reliance on CFD in the design of practical combustion applications requires models with less empiricism to model combustion scenarios that may not be anticipated a priori and potentially involving different regimes or modes of combustion.

Recent advances in computational sciences and multiscale mathematics have enabled the development of a parallel track to the 'art' of combustion modeling (those based on conceptual models build on intuition and observation) to the broader community of computational and mathematical modelers (Chen JH et al. 2009, Krause E and Jäger W 2002).

Although a number of advanced turbulent combustion models may not strictly adhere to all the criteria above, they may be easily extended to yield multiscale models. An example of such a model is the transported probability density function (PDF) approach (Pope S B 1985) and its extension to large-eddy simulation (LES), the transported filtered density function (FDF) approach (Colucci PJ et al. 1998, Gao F and O'Brien EE 1993). Both models construct the joint momentum- scalar or scalar PDF/FDF.

Mesh adaptivity is an alternative strategy for addressing the multiscale nature of turbulent combustion. Mesh adaptivity is achieved by grid refinement in the physical domain or decomposition into multi-resolution basis functions. The representative method for the first strategy is AMR (Berger M and Oliger J 1984), while the second is best represented using wavelet methods. Both methods are ideally suited for applications where physics is localized in the computational domain (e.g. premixed or non-premixed flames).

These strategies should at least have the common feature to be realistic and quantifiable in their realism. This is not a trivial requirement since the validation of a high level model is rarely done without suitable adjustment of parameters or even adjustment of some of its components. As a matter of fact, sometimes an unsatisfactory agreement between experimental and numerical results entails the recursive change of entire portion of its submodels until the agreement becomes "reasonable" (Parente A et al. 2011, Oberkampf WL et al. 2002). This procedure cannot in general be considered a validation of the model since the resulting agreement with experimental evidences is not based on a clear physical underpinning and it can be even due to an error compensation effect. Furthermore, the comparison with experimental results is unavoidably restricted to a limited number of cases, possibly on a narrow domain of the parameters and variables values, making the extrapolation of the validation to "extended" conditions and domains quite objectionable. In this case the model would be better considered a sort of expert system, which can be effectively used inside the domain in which validation/experience has been done and that contains a very high number of information in compact way. This means that validation has to be performed in a knowledgeable way by selecting representative samples of cases to be used for a thorough evaluation of carefully selected sub-models sets on the basis of their features and of their potential interaction with the model core. The role of interlinking among different subprocesses has to be carefully evaluated since it can prevent the isolation of functional dependences on controlling parameters that has to be studied by introducing unpredictable feedback mechanisms acting in different ways in physical and numerical models respectively. Very few papers have been devoted to this subject (Barlow RS et al. 1999, Davis RW et al. 1990) whereas this is a fundamental hypothesis in the development of nearly every model. In fact, the usual procedure consists in sectioning the whole process in parts, by means of geometrical sectioning of the control volumes or

selection of a subset of one or more physical effects, which can be separately modelled and are, hence, separately validated.

Examples of a very successful application of such procedures are the processes formed by sequential subprocess. Unfortunately, these cases are very rare and only partial sectioning is sometime possible. For instance combustion in gasoline engine or LPP gas-turbine can be considered as divided in two sequential blocks of subprocess. The atomization, vaporization and mixing evolve contemporaneously, i.e. in parallel way, but they are separated in more (in spark engine) or less (in LPP gas turbine) straight way from the oxidation stage. In line of principle only for these sequential processes it is possible to check the accuracy of the numerical predictions through the comparison with the experimental data "side by side" for the two stages in which the whole combustion process has been sectioned. In other words, the validation, made separately for the two parts, is sufficient to ensure a reasonable prediction also for the whole process. Furthermore also the sensitivity analysis in respect to the initial and intermediate parameters is easy to be performed and the experimental and numerical results can support each other in the complete description of the system.

An analogous analysis is possible also for solid fuels combustion.

Of course, this is true only for sequential processes and in the case each single subprocess can be successfully described. It is well documented the difficulty in achieving such target for each single piece of the process (Baydar E and Ozmen Y 2005; Rachner M et al. 2002) but it is straight to understand that also their partial description may be an useful intermediate step in the understanding of the process. On the opposite, it is difficult to determine intermediate levels of understanding for strongly entangled processes.

For gases this analysis is much more complicated and there is the need to identify peculiar surfaces on which is possible to apply such a strategy.

I.3 General characteristics of MultiSECtioning strategy

The synthesis of the previous section is that complicated and complex reactive flow systems need proper strategies for their modeling.

Because of high interconnectivity between the different subprocesses, it can often be difficult to associate effect with cause in a combustion process. These rich and pervasive dependencies place fundamental limitations on the ability to develop and validate appropriate models for complex systems.

On the ground of these considerations a strategy allowing for the analysis of the influence of single subprocesses has been conceived. It is only outlined in this section in order to give an overlook of the following sections, in which some steps of the strategy are analyzed in detail. It can be thought as divided in different parts, which corresponds to a "Separated Effect Contribution" (SEC). An example of the passage from one part to the other is sketched in Fig. I.3 as block diagram. It allows a "Sequential Enlargement Combination" (SEC) of the "separated effects" and the "Side-by-side Experimental/ Numerical Checking" (SEC) of the appropriate characterization of the field obtained by the introduction of new "separated effect". The terminology in the quotations marks may be only partially appropriate because they are forced in a synthetic acronym, but the general meaning of the procedure should be straightforward by following the sketch in fig. I.3.

Such strategy could be named "MultiSECtioning" Process Evaluation Strategy since it refers to a Multidimensional, Multiscale, Multicomponent and Multiphysics process (Sorrentino G. et al. 2011).

The first part of the acronym emphasizes the multiple repetition of the acronym SEC in this type of strategy, but it refers also to the intrinsic multi-faceted nature of combustion processes.

The acronym evokes that the procedure consists in sectioning the whole process in parts, by means of both geometrical sectioning of the control volumes and/or selection of a subset of physical effects, which can be modelled and validated when added ones at the time to the process.

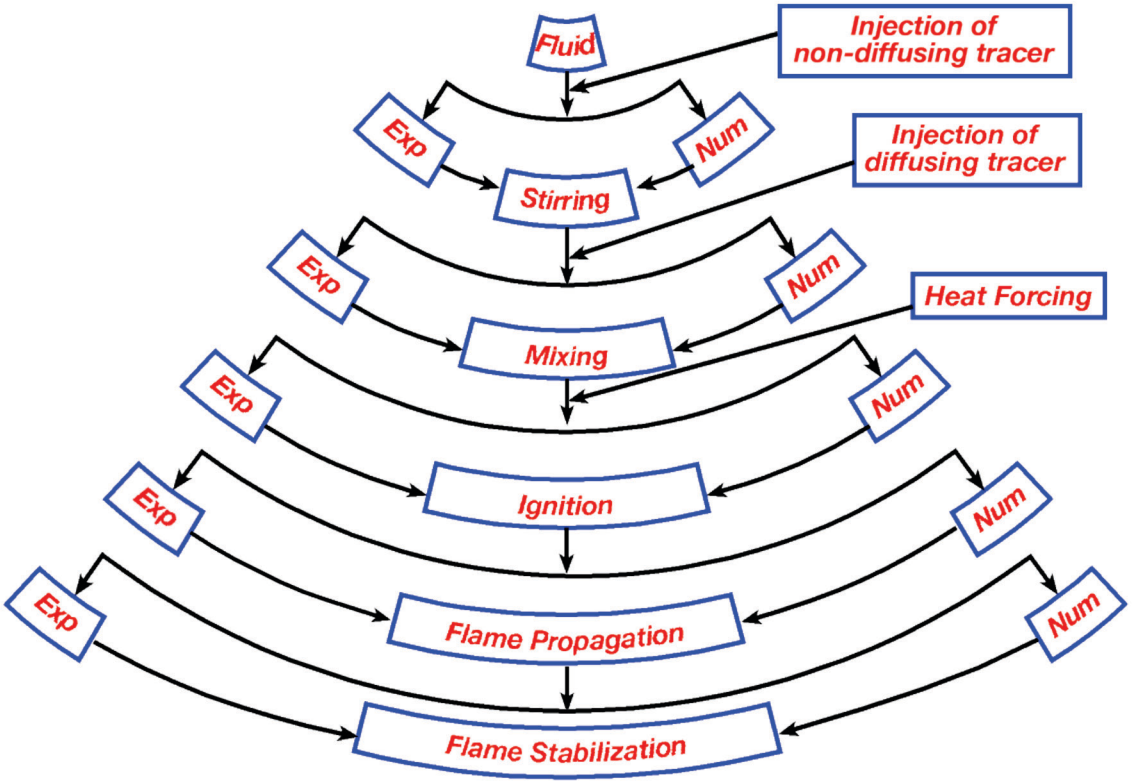

Figure I.3. Flow-chart of MultiSECtioning strategy

This approach has been followed in a rigorous way only in some passages from one level of complexity to a higher one or in empirical way in the whole process analysis. It deserves, thus, a systematic review work of both the possible steps for its application and the sparse information that can be inserted in such framework. Furthermore a more explicit and proper classification of all the effects to be evaluated for such strategy is needed because this can affect in turn subsequent choices along the complexity enlargement process.

The first part of the procedure is a fluid-dynamic characterization of the patterns of interest when not reacting flows are introduced in fixed control volume, for fixed boundary-initial conditions, for fixed external parameters. It does not include mass distribution of the reactants, but only pure fluid-dynamic quantities. For instance it could be the characterization of the fluid-dynamic pattern of a single component reactant, which is usually the oxidant, since in a great number of applications its mass/volume flow is much greater than that of the fuel. Alternatively it is also possible to envisage conditions in which the two reactants are injected separately and they affects the fluid-dynamic pattern only for their different densities. The fluid dynamic database, generated in this first step, has to be suitable for the characterization of the effects generated by considering the injection of not-diffusing tracers in the control volume. This is the second step of the strategy, which is reported in fig I.3 in the block quoted as “stirring”. It is anticipated here that it can be obtained from experimental point as smoke streak-lines, which in turn yield interface between the two reactants and that the prediction of the location of such surface is the object of the numerical codes which are “enlarged” in order to include also the convective transport of an inert, passive not-diffusing material. Then a new database is generated which can be analyzed in terms of local or integral stirring quantities (interface location) either for mutual validation between experimental and numerical determinations or for evaluating the efficiency of stirring in relation to the whole combustion process (Sorrentino G et al. 2011, Sorrentino G et al. 2012).

The second step, reported in the figure as “mixing” is obtained by injecting a diffusing tracer into the control volume. In this case the experimental characterization is done in terms of some types of species concentration, which are representative of the reactants inter-diffusion. Similarly the numerical model has to incorporate an additional equation for

the mass balance of a species that is not reacting. Model should also predict the spatial distribution of air/fuel ratio. In other words, the charge stratification has to be characterized by means of both the mutual experimental-numerical validation and their complementary contribution. In this case a new database is originated which includes temporal-spatial field of the air fuel ratio in not reacting conditions (Cavaliere A et al. 1995, Cavaliere A and Ragucci R 2002).

The third step, quoted in the figure as “ignition” can be obtained through spark ignition or autoignition in turbulent flowing mixtures.

Also in this case this process can either be predicted in a numerical model or be experienced in a physical model. In particular in this step the information content of both numerical and experimental implementations can be exploited cooperatively in terms of whole characterization of the database that they refer to.

Finally, flame propagation from the selected ignition kernel and the possible combustion stabilization has to be modelled or experimentally observed. The two steps (propagation and stabilization) are kept separated in fig. I.3 in order to stress that only part of the ignition domain, from which flame propagates, can generate combustion processes. This reduction of the database from one step to the other is not represented in fig. I.3. In fact it should be clear that in the same figure the increase of the geometrical area passing from the box representing propagation to the box representing stabilization is only referred to the number enlargement of both quantities and equations, which should be taken into account passing from the not- reacting to the reacting conditions.

A special situation of flame propagation may arise if the flame kernel has been generated through autoignition. In this case, the fluid ahead of the flame may be partially-reacted already, or even locally auto-ignited. This situation may correspond to the so-called

premixed phase of conventional diesel engine combustion. We shouldn't confuse this situation with forced ignition in stratified-charge engines, where flow temperatures are low enough so that autoignition does not happen. Moreover, in non-conventional autoignition processes (for example MILD combustion conditions) it is not possible to have a propagation stage, so the stabilization mechanism in this case follows different paths.

In this sense, the MultiSECtioning strategy seems to be a very flexible methodology. In particular, the interface characterization is the basic-step of this approach because it permits to adapt the presented procedure to different ignition events (i.e. forced ignition or autoignition) in relation to the different chemical-physical time scales that are involved in the process.

Some of the procedures outlined here will be described in details in the following sections, which are devoted to some of the steps reported in fig I.3. Some of the “Separated Effect Contributions” will be qualified in terms of operative procedures and their “Sequential Enlargement Contribution” to the complete stable combustion process will be discussed. Then the anticipated synthesis of the procedure presented here will be discussed more deeply on the ground of the specific state of art in the fields related to the different steps.

I.4 Objectives and outline

The methodological procedure discussed in the previous sections is based on the fact that a combustion process is the non-linear combination of many physics. This implies that the characterization of each combustion process seems to be very difficult.

Therefore, a sequential approach can be used to split the different sub-processes and to validate and characterize them step-by-step.

The possibility of this splitting is very dependent on the definition of peculiar surfaces which represents a sort of "skeleton" of this approach.

More specifically, in this thesis a complete characterization of the stirring process will be carried out in order to study the evolution of the interface and to quantify it.

In particular, the main quantities that characterize the stirring process are evaluated as a function of the different flow conditions.

The results lay the foundations for future developments in this direction concerning semi-empirical models for interface evolution and prediction.

Moreover, the other steps of the MultiSECtioning strategy will be discussed and some results concerning the ignition part will be shown by evaluating the diffusion-controlled ignition processes in simple cases.

The characterization of the mixing step is not a specific objective of this PhD thesis because it is well-reported in literature and it is directly characterized as a consequence of the stirring process

Furthermore the strength of such a procedure will be discussed in order to show its potentiality and applicability also to non-conventional combustion processes.

It is here worthwhile to note that the single parts of the presented procedure are not reported in this thesis according to the logical path shown in Fig. I.3 because of clarity reasons. In fact the different "ignition events" that may occur in a combustion chamber are reported in chapter II and the various combustion regimes are discussed in relation to simple diffusive layers structures.

Relevant contributions to autoignition processes in Mild Combustion conditions are reported to show that the MultiSECtioning strategy can be adapted also to non-conventional ignition processes.

The characterization of the stirring process is discussed in the third chapter in relation to a proper test rig.

Some digital image processing technique have been reported in the fourth section and they have been applied to obtain the results shown in the chapter V.

The VI chapter has been devoted to some discussion about the main limits of the presented approach and the diagnostic apparatus.

The discussions are related to future modeling developments of this work and to show the robustness and feasibility of the presented methodology.

Chapter II
Reactive structures in non-premixed flames

As in most branches of the physical sciences, the ultimate goal of research on turbulent combustion is an accurate and tractable theory or model, which encapsulates the attained knowledge and understanding of the phenomenon.

One procedure is to develop models applicable to the geometry of practical combustion devices, including various kinds of sub-models. As our knowledge and computer power increase, the sub-models can be improved in their scope and accuracy. While this line of attack is extremely valuable, it has to confront two difficulties. First, the quality and quantity of experimental data for model validation in such applications are quite limited. Second, when there are discrepancies between simulations and experimental data, it can be difficult to determine which sub-model (or combination of sub-models) is to blame.

A different, complementary line of attack is, to the extent possible, to separate and isolate the different phenomena involved, and to study them in laboratory experiments in relatively simple geometries.

With this kind of approach (reported in chapter I as “MultiSECtioning”), much more comprehensive and accurate measurements are possible.

As specified in the first chapter, the latter line of attack has been used in this thesis by focusing on the essence of the turbulent combustion problem, namely the interacting processes of reaction, molecular diffusion and turbulent stirring of the flow field. Furthermore, the attention has been focused on non-premixed turbulent combustion.

The viewpoint is that underlying physics and chemistry should satisfy the requirement of “tractability”.

In order to overcome the challenges of small scales and many species, it seems unavoidable that any tractable computational approach must include two ingredients:

1) a description of the fluid-dynamics pattern by means of characterization of the stirring process in gaseous flows;
2) a description of the reactive structures in terms of gaseous diffusion flames.

In the context of this approach, therefore, the identification and description of the interface seem to be the sinews of a MultiSECtioning strategy.
Therefore, after the characterization of these advected-surfaces, the second step can be carried out following two different paths:

2-a) kernel expansion process following spark ignition in a stratified mixture.
2-b) analysis of the elementary reactive diffusion layers that can be obtained in the single lamellar structures related to the interface.

In particular, the path 2-b can be obtained as a consequence of an autoignition event.
One of the aim of this thesis, i.e. the identification and description of the interface related to the stirring process, will be treated in the following chapters, while the purpose of this chapter is to provide a brief outline on spark ignition (path 2-a) and autoignition (2-b) in turbulent flowing mixtures with particular emphasis on the initiation of turbulent non-premixed gaseous fuel combustion. This is identified as the second ingredient of a MultiSECtioning analysis of the diffusion flames and it represents a “critical” point of the proposed methodology. Specifically, the ignition step has been reported in this chapter (the PhD thesis does not follow the logical path of Fig. I.3) in order to show that the proposed

approach should be able to adapt itself to both ignition processes, i.e. spark ignition and autoignition.

It is useful to categorize various practical situations involving turbulent non-premixed autoignition and spark ignition into simpler problems that can be used to focus the different aspects related to the "ignition" step in the MultiSECtioning approach.

They allow the passage from a state in which only a not yet reacted stratified medium is distributed in the reactor to a state in which the reactor is occupied also by combustion products.

The main objective of this chapter is to consolidate existing knowledge on the autoignition and spark ignition of turbulent non-premixed combustion of gaseous fuels.

The key phenomena can be understood as sub-problems constituting the full problem and are hence important to analyze them, in a first approximation, separately. In this chapter relevant results from premixed systems and from laminar studies that affect the behaviour of the turbulent non-premixed systems will be reported.

The first part of this chapter includes a brief review of turbulent spark ignition and autoignition of gaseous fuels by emphasizing the many outstanding questions that need to be addressed.

The second part reports the original contribution of this thesis work on this problem by providing insight into the reactive diffusion layers structure under autoignition conditions also in non-conventional combustion conditions.

II.1 State of the art

Fig. II.1 schematically shows a turbulent fuel jet into oxidizer (in the following, the index 1 denotes the fuel-carrying fluid, while index 2 identifies the oxygen-carrying fluid; the index 0 denotes condition far from the mixing region). The oxidizer stream could be air

or air mixed with hot combustion products or even air enriched with radicals (Mastorakos E. 2009) . When $U_{2,0}$=0 and $U_{1,0}$ is high, the flow pattern is akin to the usual turbulent jet. If $T_{1,0}$ is low and $T_{2,0}$ is high, the flow may correspond to gaseous fuel injection into a stagnant hot environment, such as that in a natural gas direct-injection compression-ignition engine. If the fuel is originally injected in liquid form but the atomization and evaporation processes are very fast, then Fig. II.1 may be considered conceptually as the pre-auto- ignition part of diesel engine combustion. If $U_{2,0}$ is high and $T_{2,0}$ is high (but perhaps not so high that autoignition happens quickly), the flow mimics the premixing duct of an LPP gas turbine. Confinement and the co-flow turbulence are important in this case, as they determine how quickly the fuel mixes with the oxidizer.

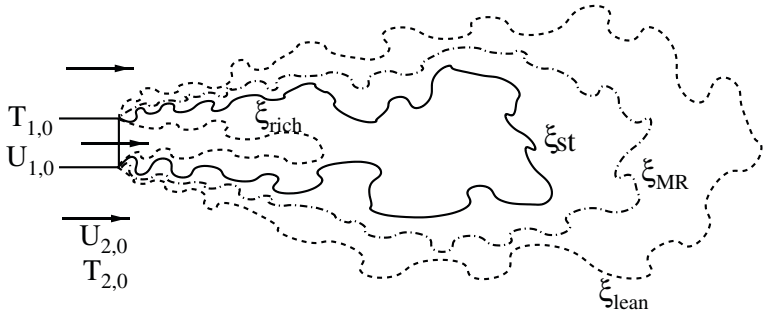

Fig. II.1 *Schematics of a fuel jet in air co-flow. 1: fuel; 2: oxidizer. Adapted from Mastorakos E. (2009)*

This type of flow has been considered experimentally for various combinations of temperatures, velocities, fuel and oxidizer stream compositions, and for both confined and open flows and will be reviewed in paragraph II.1.1 of this thesis.

The opposed-jet flow (Fig. II.2), with fuel impinging on air or combustion products has been used to study autoignition mostly for laminar, but also for turbulent flows. This flow involves uniform strain and can demonstrate directly the effects of strain rate on the

ignition process and hence forms an important building block in our understanding of initiation of non-premixed combustion.

In Figg. II.1 and II.2., isolines of the stoichiometric mixture fraction, ξ_{st} , are shown, together with the isolines corresponding to the lean and rich static flammability limits (ξ_{lean} and ξ_{rich} , respectively). These limits are available for most of the fuels at atmospheric conditions.

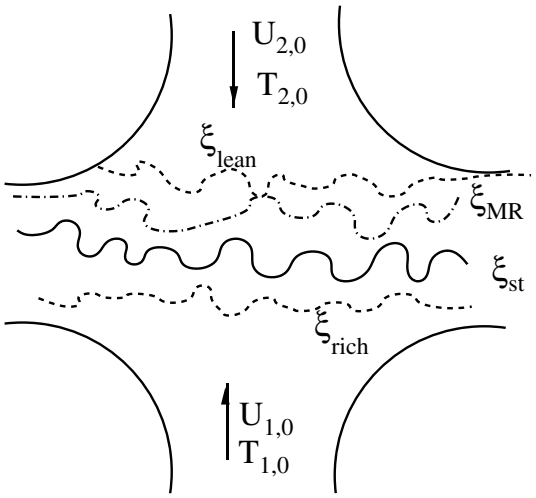

Fig. II.2 *Schematics of opposed-jet flow. 1: fuel; 2: oxidizer. Adapted from Mastorakos E. (2009)*

However, they are not always available for the conditions corresponding to autoignition (e.g. the high pressure, high $T_{2,0}$ of an LPP turbine duct or a diesel engine) or to some practical spark-ignition problems (e.g. at the low pressure, low temperature characteristic of high altitude relight situations). A fourth curve, denoted as ξ_{MR} is meant to show the so-called *most reacting mixture fraction*, we don't imply that $\xi_{MR} < \xi_{ST}$ necessarily. For cold fuel in hot oxidizer ($T_{2,0} >> T_{1,0}$), autoignition happens somewhere along the ξ_{MR} isoline,

and in particular where the mixture fraction gradients, quantified through the scalar dissipation N , are low $\left(N = D\left(\partial\xi / \partial x_i \right)^2 \right)$ (E. Mastorakos et al., 1997).

II.1.1 Spark ignition of turbulent non-premixed flames

In this section are reported fundamental findings for the forced ignition of turbulent non-premixed flows. Despite its practical significance, this is a new topic of research in turbulent non-premixed combustion and hence has not been studied as extensively as autoignition. However, new technologies such as the gasoline direct-injection spark-ignition engine and lean gas turbines have some difficulties with ignition and hence this topic has recently become a focal point of research.

II.1.1.1 Reactive mixing related to stratified medium with external source ignition

Some features of the forced ignition in turbulent non-premixed flames are demonstrated in Fig. II.3, which shows schematically the flame expansion in a turbulent fuel jet in cold air (i.e. low $T_{2,0}$) after a successful spark. The most reactive mixture fraction is not a relevant quantity here because autoignition does not occur due to the low temperature and hence only the isolines of ξ_{st} , ξ_{lean} and ξ_{rich} are indicated. Assume that a spark of high enough energy has been deposited in a region comprising flammable mixture, for example between ξ_{st} and ξ_{lean} .

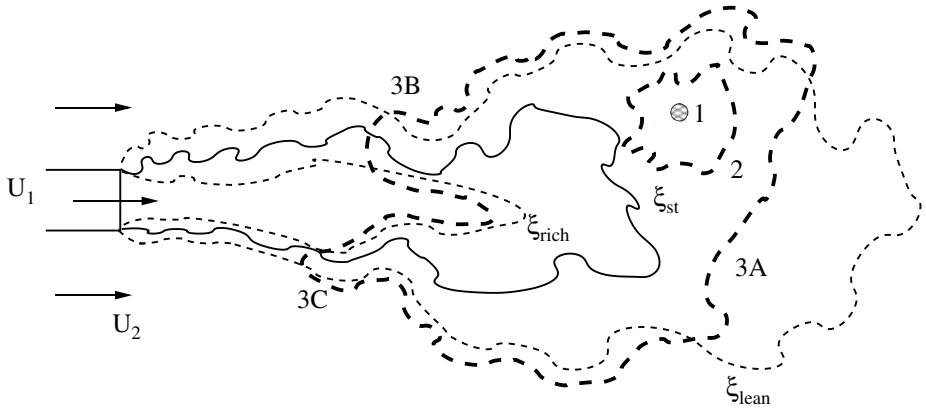

Fig. II.3 *Schematic of the kernel expansion process following localized ignition. Adapted from Mastorakos E. (2009)*

Immediately following the spark, a small kernel has been generated, with an approximately spherical reaction zone (1). The flame then expands (2). This flame is of a premixed nature, but spans a finite range of flammable equivalence ratios since our flow is non-premixed; we can call this situation *premixed flame propagation in a stratified mixture*, implying that the turbulent mixture fraction fluctuations fall within the flammability limits. Bilger et al. (2005) have used this term for a situation where fluid is either only fuel-lean or only fuel-rich and we will partly follow this practice here. Flame element 3A is also of this kind. As the flame continues to expand upstream, it includes stoichiometric mixture fraction, and it may eventually propagate along the isoline and hence assumes characteristics more akin to non-premixed edge flames, whose behaviour will depend on the local mixture fraction gradient. For low gradients, the flame may have three distinct fronts (triple flame: 3B) and for high gradients the fronts will have merged (edge flame: 3C). Such flames will be denoted collectively as turbulent non-premixed edge flames. Some authors (Bilger et al., 2005) have used the term premixed/non-premixed for these flames, but we prefer the explicit inclusion of the word edge because tracking the physical flame edge has been used to measure the statistics of their propagation. However, if the mixture fraction gradient is very low, no clear edge may be discernible. The final outcome of the flame expansion

process will be a stable turbulent jet flame, attached to the nozzle or lifted, depending on the jet and co-flow velocity (Lyons KM 2007).

II.1.1.2 Concentrated ignition

The stratified medium created in the not-reacting condition can be in principle be ignited either with direct injection of thermal energy and/or reactive species or some other form of energy or material which induces their local formation.

Laser ignition has been reviewed by Ronney (1994), which also reported a short literature review on spark ignition, wile some more details on the flow structure around the laser spark is given in Refs. (Bradley D et al. 2004, Beduneau JL 2003). Ignition by a flame jet (Murase E, et al. 1996) or puff (Pitt PL et al. 1984) has been suggested to improve ignitability of the mixture due to the increased initial surface area of the kernel. More recently, a detailed study (Sadanandan R et al. 2007) of a transient hot gas jet into a quiescent hydrogen-air mixture showed that the first site of ignition appears at the tip of the hot gas get. Plasma jets have been proposed as effective igniters for gas turbines (Cote T, et al. 1986) and their action is not only thermal, but also chemical, since they release significant amounts of radicals. A situation called "radical-induced ignition" has been observed in numerical simulations (Campbell CS et al. 2005) of autoignition of uniform mixtures starting from cold temperatures with large amounts of radicals present initially. If their concentration is such that they do not decay due to recombination reactions occurring before than they can trigger the generation of more radicals, the system will eventually autoignite.

For most practical purposes, the overall energy deposited by the spark is the most important factor. Measurements reveal that there exists a minimum ignition energy (MIE) for initiating a self-sustained front. If the energy deposited is too low, the flame kernel

decays rapidly because heat and radicals diffuse out of the kernel faster than their rate of production inside the kernel can sustain. The MIE depends on parameters such as electrode diameter and gap and the spark duration because not all of the electrical energy is absorbed by the gas due to heat losses that depend on geometric parameters and on the proximity of the flame kernel to the electrodes.

Fig. II.4 shows schematically some of the parameters involved in the forced ignition of a laminar non-premixed one-dimensional flame.

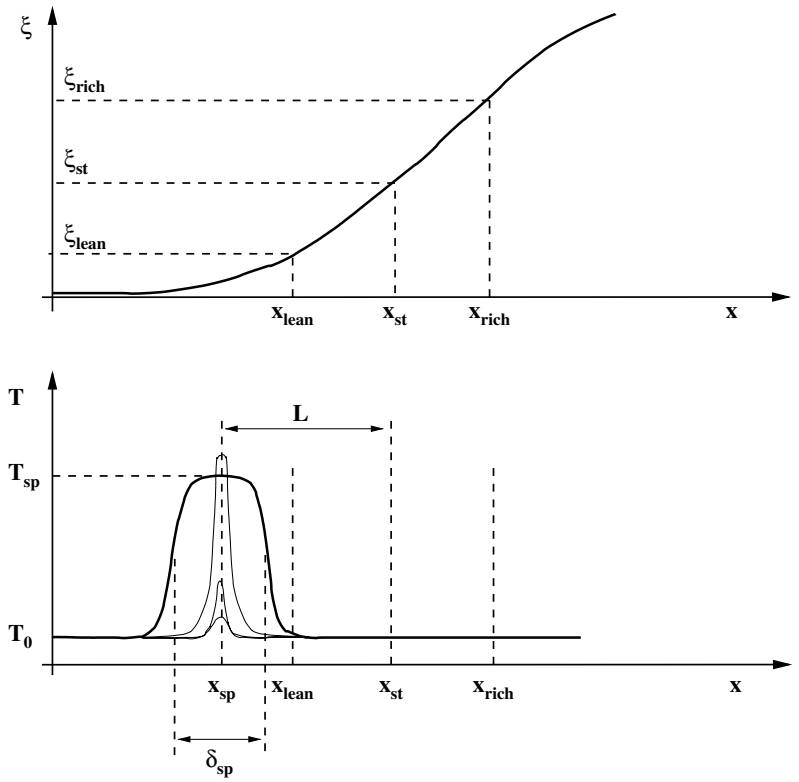

Fig. II.4 *Schematic of the parameters appearing in the forced ignition of a non-premixed flame. Upper: mixture fraction distribution. Lower: The thin lines denote possible temperature profiles during the fast combustion initiation at the spark position.*

Intuition suggests that in contrast to the forced ignition of a homogeneous mixture, here the spark's location relative to the positions of the stoichiometric mixture fraction and of the nominal lean and rich flammability limits must play a role in the success or not of the ignition process. A systematic study of these effects has not been performed yet.

Rashkovsky (1999) may have been the first to numerically analyze the problem of flame ignition in a strained counterflow mixing layer between cold fuel and cold air by a source of energy at a given location across the layer. All the energy E_{sp} was delivered at a point; molecular diffusion then caused the region of high temperature to spread. One-step chemistry was used and a constant-strain field was assumed. Detailed examination of the results of numerical calculations revealed some important characteristics of the process. First, there is a critical Damköhler number for successful flame establishment. Second, this critical Damköhler number increases sharply with decreasing E_{sp} and, third, it increases sharply with increasing distance of the spark position from the location of the stoichiometric mixture fraction.

The above reported chaacteristics have been confirmed with laminar counterflow flame simulations of methane with the GRI3.0 mechanism (Richardson ES and Mastorakos E. 2007).

In these simulations, the initial condition for the scalars was the inert distribution corresponding to the set strain rate, while the temperature was set at 293 K everywhere except for a slab of gas that was set at T_{sp}, as shown in Fig. II.4. The use of detailed chemistry and transport allows a better representation of the reaction initiation at both lean and rich mixture fractions, while the use of flame-derived mechanisms for this problem is reasonably reliable as long as T_{sp} is not too high. Fig. II.5 shows the evolution of the temperature with time for three sparks, differing only in their position across the mixing layer which was at a strain rate less than one half of the extinction strain rate. It is evident that not all sparks are successful.

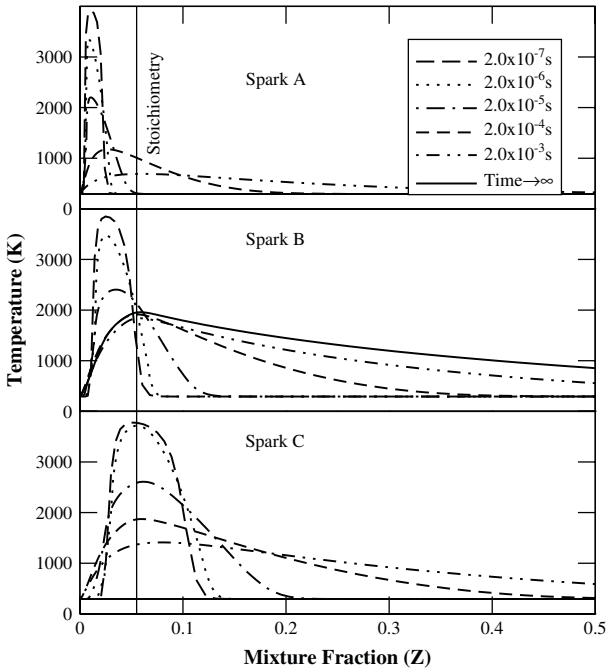

Fig. II.5 *Transient temperature profiles in a laminar non-premixed counterflow layer between methane and air with a spark represented by a slab of gas set at T_{sp}=4000 K at t=0. For all, the strain rate was 0.4S_{ext}, with S_{ext} the extinction strain rate. The centre of spark A was located in a region leaner than x_{lean}, B was at x_{lean} and C was at x_{st}. B was successful, while A and C were not.*

Failure may occur at strain rates $S_{cr,sp}$ even lower than the extinction strain rate Sext of the non-premixed flame we are trying to ignite.

These simulations confirm the complicated picture of forced ignition of non-premixed flames. In addition, detailed studies of the initial spark processes of the type performed for homogeneous mixtures, such as those in Refs. (Kono M et al. 1984, .Kravchik T et al. 1995), must be performed for situations with inhomogeneous fuel distribution in the electrode gap.

There are very few experimental studies focused on the forced ignition processes of laminar non-premixed combustion. Laser- induced ignition kernels in laminar hydrogen (Phuoc X et al. 2007) and methane (Qin X et al. 2004) jets have been visualized to determine ignition success and the positions along the jet that resulted in successful jet flame establishment.

The probability of initiating a flame kernel from a spark in a turbulent axisymmetric jet has been measured for a range of fuels in a pioneering series of experiments by British Gas (Birch AD et al. 1981).

The creation of a kernel was judged visually. In these experiments, the electrode gap was 3 mm and the spark had energy 100 mJ, which was higher than the MIE of homogeneous mixtures over the whole flammable range. The spark duration was 20 ms. Natural gas, propane and simulated town gas (50% H_2, 30% natural gas, 20% N_2 by volume) were examined. Mixture fraction measurements were performed with Raman scattering (Birch AD et al. 1978) and the data were analyzed to give the pdf of the mixture fraction, at every point. From this, the flammability factor was defined from:

2.1) $$F = \int_{\xi_{lean}}^{\xi_{rich}} P(\eta) d(\eta)$$

The experiments showed that:

- the region where $P_{\mathrm{ker}} > 0$ extends further than the region bracketed by the isosurfaces $\langle \xi \rangle = \xi_{lean}$ and $\langle \xi \rangle = \xi_{rich}$, thus implying that the mixture fraction fluctuations play a role;
- $P_{\mathrm{ker}} \approx F$ along the centerline of the jet.

With ‘‘ignition’’ defined as the initial kernel generation plus successful flame propagation upstream to ignite the whole jet flame, the probability P_{ign} (called ‘‘conditional light-back probability’’ by Smith et al. 1986) can be different from P_{ker}. The results showed that P_{ign} sharply reduces to zero downstream of a certain distance. For example, for natural gas issuing at 20m/s, P_{ign} decreased from unity to zero between 80 and 100 jet diameters, while P_{ker} decreased gradually to zero at about 180 jet diameters. The results also showed a

reduction in P_{ign} with jet velocity. In good agreement with our expectations from the self similar behaviour of an axisymmetric jet, F did not change with velocity. It is not fully clear from the data whether P_{ker} was dependent on the jet velocity or not. The overall findings from these studies have been confirmed from experiments with large-scale natural gas releases with drive pressures up to 100 bar.

Similar data for a methane jet, including radial distributions of P_{ign} and the effects of spark parameters on P_{ign} have been reported in Ahmed SF and Mastorakos (2006). Fig. II.6 shows snapshots from a high-speed movie showing the flame propagation process (McCraw JL et al. 2007).

Failure of the overall process was associated either with failure to initiate a flame kernel (no visible flame after the spark ended) or with a kernel that was convected downstream. Once a flame started propagating upstream, it was likely to propagate upstream all the way up to the stabilization point.

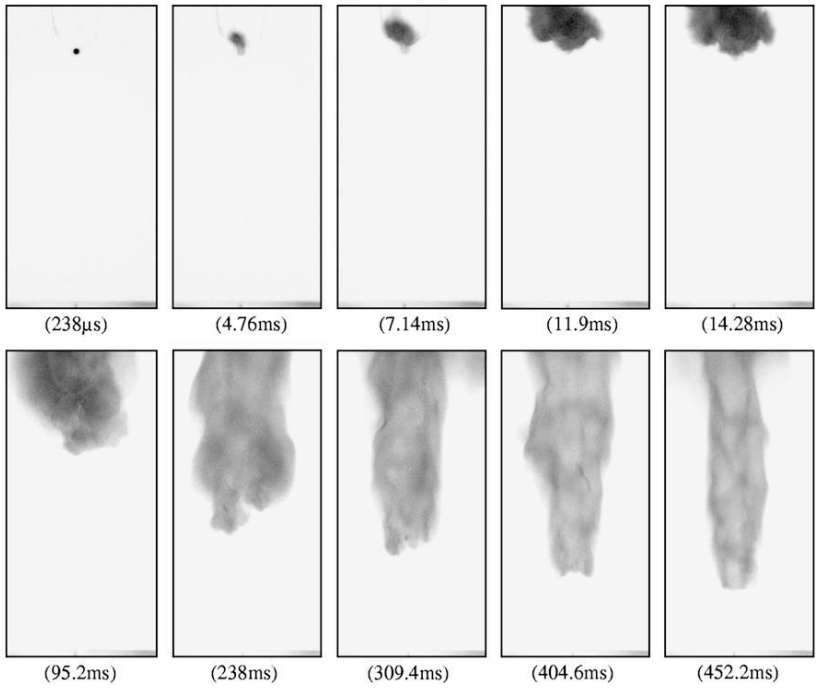

Fig. II.6 *Flame evolution following spark ignition at 40 jet diameters on the centerline in a jet issuing methane partially-premixed with air (30% by vol.) from a 5 mm nozzle at 25.5 m/s.*

These observations are consistent with the earlier studies (Smith MTE, et al. 1986). Contours of P_{ign} , obtained in that case, are reproduced in Fig. II.7. It is evident that:

- P_{ign} decreases sharply downstream of the estimated position where the mean stoichiometric mixture fraction of the inert jet closes on the centerline;
- $P_{ign} < 1$ even along the mean stoichiometric isoline;
- P_{ign} is reduced with increasing velocity.

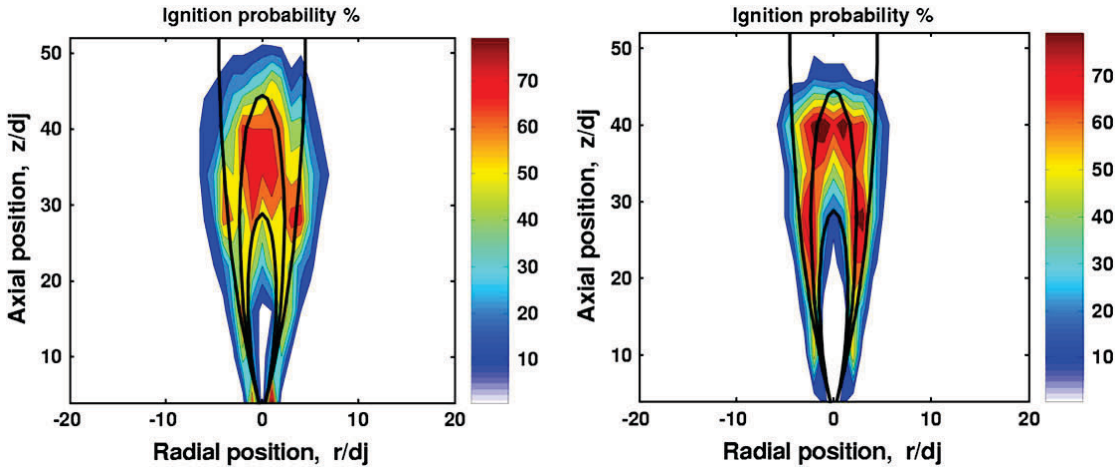

Fig. II.7 *Ignition probabilities (defined as successful kernel generation plus upstream flame propagation) as a function of spark position. The jet velocity was 12.5 m/s for the left contour and 25.5 m/s for the right.*

It is understandable that P_{ign} is reduced when the jet velocity is high, since the flame kernel will have to propagate against a higher velocity to ignite the whole jet. The local velocity measured by Laser Doppler Anemometry in the spark region during discharge had a negative correlation with ignition success, with failed events associated with high positive (downstream) velocities and successful events with lower velocities. The limiting downstream distance, beyond which upstream flame propagation in the jet does not occur, has been determined also by using a pilot flame as the ignition source (McCraw JL et al. 2007). These authors called this distance "Upper Propagation Limit". This limit is equivalent to the downstream location where P_{ign} falls to zero in Fig. II.7. For a range of jet

and co-flow velocities, the data are correlated with the estimated mean flow speed at the stoichiometric surface. The existence of a downstream location beyond which ignition does not result in a flame but simply in kernels that are blown-off has also been observed in tests concerning the ignitability of hydrogen leaks (Swain MR et al. 2007).

II.1.1.3 Flame propagation in stratified medium following forced ignition

In order to achieve good ignitability of the flame, we need to generate the kernel ($P_{ker} > 0$) and to allow this kernel to expanding and igniting the whole combustion chamber. The various flame propagation phases are shown qualitatively in Fig. II.3. Some information on this topic is discussed in this paragraph along with some further comment on the overall flame ignition.

In an effort to classify the nature of flames involved in the transition from a kernel to the fully-established non-premixed flame, consider Fig. II.8, which shows various shapes of the pdf of the mixture fraction relative to the nominal lean and rich flammability limits. Let's assume this pdf homogeneous in space in the direction of flame propagation.

If a flame propagates in mixture associated with a pdf of type S1 or S2, we may speak of a *stratified-charge premixed flame* borrowing the terminology from spark-ignition engines. If a flame propagates in mixture associated with a pdf of type E, then we can call it non-premixed edge flame (or triple flame). This distinction is consistent with that suggested by Bilger et al. (2005). In view of Eq. (2.1) that defines the flammability factor F, we may call *non-premixed edge flames* those in regions with $F < 1$, while premixed stratified flames those with $F=1$.

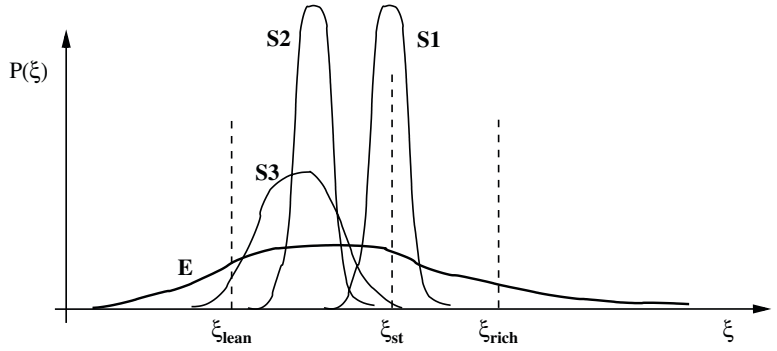

Fig. II.8 *Schematic of mixture fraction pdf's relative to the nominal lean and rich flammability limits, which can help distinguish between stratified-charge premixed flames (S1–S3) and non-premixed edge flames (E).*

A flame in a mixture fraction pdf around stoichiometry with F=1 (denoted as S1 in Fig. II. 8) could also be thought of as an edge flame, but the relatively small mixture fraction fluctuations in this case would probably suggest that such flames are best understood from premixed flame concepts. A flame such as S3, which includes mixtures with compositions leaner than ξ_{lean} and hence has F < 1, is mostly of premixed character. Combustion in mixtures with $\xi < \xi_{lean}$ in this flame may be facilitated by diffusion from the vigorously-burning mixtures with $\xi > \xi_{lean}$, which implies that we should treat ξ_{lean} and ξ_{rich} only as nominal values. The distinctions discussed here are mostly of a qualitative nature. Turbulent flame propagation in both types of stratified mixtures is an important constituent of the problem of forced ignition of non-premixed combustion.

II.1 Background on autoignition of non-premixed flows

The purpose of this section is to give a general overview of autoignition background; from early knowledge and observations of the phenomenon, to the most recent advances in the more complex, turbulent inhomogeneous case.

A variety of previous autoignition studies are appraised, from the theoretical treatment of homogeneous, stagnant mixtures with simple chemistry, to Direct Numerical Simulations (DNS) and experiments of inhomogeneous counterflow and co-flow configurations.

The earliest investigations of autoignition, during the late 19th century, were aimed at determining the 'autoignition temperature' of a combustible mixture.

This has remained the 'traditional' form in which autoignition is studied, with the bulk of recent experiments and analyses continuing to be aimed towards understanding the chemical kinetics of oxidation of various fuel–oxidizer systems in homogeneous reactors. Much work is required before it can be claimed that a complete understanding of oxidation kinetics has been attained and the community still struggles to come to a consensus over several issues. Still, corpus of knowledge on these chemical processes has been greatly expanded.

In the aftermath of the advent of the Homogeneous Charge Compression Ignition (HCCI) engine and Lean Premixed Pre-vaporized (LPP) gas turbine concepts and the increasingly strict emission regulations for diesel engines, the immediate practical needs concerning autoignition in the presence of strong turbulence and mixture inhomogeneities served as a renewed driving force for research in this field, with inhomogeneities making their first, reluctant appearance. Initially, the 'conventional' approach towards inhomogeneous autoignition resulted directly from the pre-existing work concerning autoignition delay times in the various homogeneous configurations, on account of the considered increased importance of the chemistry (Pedersen and Qvale 1974).

An argument was put forward that attempted to explain inhomogeneous autoignition once again in terms of a residence time and envisaged the possibility of separating the total autoignition delay time into a fluid-mechanical 'mixing time' (set by turbulent mixing) and a 'chemical delay time' (set by the chemistry as before), the latter of which was believed to

be the most important, or 'controlling', parameter. According to this idea, the initially inert inhomogeneous mixture will need some 'mixing time' before becoming a reactive homogeneous mixture, after which it will need a further (homogeneous) 'chemical delay time' to autoignite.

Currently, the autoignition of a turbulent mixing flow is a problem of great fundamental importance and practical interest. The further development of combustors for HCCI engines and LPP gas turbines, in terms of improved performance and efficiency and reduced emissions, can be significantly aided by a better understanding and ability to predict the phenomenon of autoignition in the presence of considerable fluctuations of velocity, composition and temperature, whose effect must be understood. In parallel, turbulent autoigniting flows in which the chemical and fluid-mechanical timescales are of the same order, are a theoretically challenging problem, due to the non-linear coupling between complex chemistry and turbulent mixing, that is interesting to explore. The phenomenon of inhomogeneous, turbulent autoignition involves the dynamic interplay between several underlying mechanisms, such as:

- the turbulent, fluid-mechanical mixing processes of oxidizer and fuel;
- the chemistry of the slow pre-ignition reactions between the reactants;
- the thermodynamical fate of the heat released from these reactions, leading to thermal runaway in localized sites called autoignition kernels.

With each one carrying equal importance, the convenient assumptions of scale-separation cannot be applied and so it can be said, that turbulent inhomogeneous autoignition truly stands on the boundaries where the disciplines of chemistry, fluid mechanics and thermodynamics meet. These phenomena can be complicated and immensely diverse,

highlighting the many possibilities for non-linear interaction between the equally important aspects.

The major advances in this field have come from all aforementioned disciplines. They have been borne out of experimental, theoretical and computational approaches and by considering a wide variety of configurations: homogeneous and in-homogeneous, gaseous fuels and evaporating sprays, simple and complex chemistries, constant volume/pressure vessels and continuous flows; laminar and turbulent, two and three-dimensional.

In each of these configurations it has been possible to isolate and treat different aspects of the phenomenon, from the chemistry to the mixing patterns of passive scalars in turbulent flows, but also to progressively examine more complex cases of autoignition in a turbulent reacting flow.

The phenomenon of turbulent inhomogeneous autoignition is dominated by turbulent scalar mixing, set up by the non-uniformities and turbulent flow.

For the autoignition of a homogeneous mixture in the absence of temperature fluctuations, the fluctuations of the velocity field cannot give rise to scalar fluctuations. Hence, this case is of little fundamental importance. In the turbulent autoignition of homogeneous mixtures, even the inclusion of temperature fluctuations is of reduced fundamental importance.

In the absence of turbulent mixing, which is by definition non-existent for a homogeneous mixture, an important part of the turbulent transport processes is not treated. A true understanding of turbulent autoignition in the presence of mixture inhomogeneities should come from dealing with the full, turbulent inhomogeneous situation.

For this reasons, the following sections are a brief introduction to inhomogeneous autoignition in laminar and turbulent flows respectively.

II.1.2.1 Laminar Inhomogeneous Autoignition

Laminar inhomogeneous autoignition includes the classical problems of the laminar (most commonly planar) co-flowing mixing layer and strained counterflow. Due to its simplicity, the laminar mixing layer has been approached mostly from an analytical and theoretical point of view. On the other hand, the autoignition of non-uniform counterflow mixing layers has been explored analytically, experimentally and with simulations.

This latter flow involves uniform strain and can demonstrate directly the effects of strain rate on the ignition process and hence forms an important building block in our understanding of initiation of non-premixed combustion.

Here only the laminar counterflow configuration is treated.

II.1.2.1-a Laminar Counterflows

Steady and unsteady counterflow flames of cold fuel and oxidizer have been extensively studied both analytically and numerically. Analytic, asymptotic approaches include those of Liñan (1974) for large activation energy thermal autoignition, and Mellado et al. (2000) for chain-branching autoignition. Generally, the literature focuses on hydrogen chemistry. Yet numerous experimental investigations have been performed, for a variety of hydrocarbon fuels and hydrogen and over a wide range of conditions. Another situation that has been considered is that of a premixed fuel–oxidizer stream being ignited by an inert, opposed hot nitrogen flow.

The counterflow, or strained mixing layer, is a boundary-value problem and as such can be described by an elliptic set of partial differential equations.

A potential (inviscid) flow stream-function transformation can be used, based on an aerodynamic strain rate (a), such that $u_x = ax$ and $u_y = -ay$. For the species in steady

counterflow mixing layers diffusion is balanced by species advection that brings the reactants together in the mixing zone. Mathematically for species i :

2.2) $$u_x \frac{\partial Y_i}{\partial x} + u_y \frac{\partial Y_i}{\partial y} - D_i \left(\frac{\partial^2 Y_i}{\partial x^2} + \frac{\partial^2 Y_i}{\partial y^2} \right) = \frac{\dot{\omega}}{\rho}$$

with D_i its diffusion coefficient.

It becomes straightforward to define two characteristic timescales; one for the fluid-mechanics (left-hand-side) and sometimes called the 'diffusive time', and, one for the chemistry (right-hand-side). A Damköhler number (which compares the chemical time scale to the flow time scale) can be defined from the inverse of the scalar dissipation rate (χ) since in this flow, a is proportional to χ according to eq. 2.3.

2.3) $$\chi = \frac{a}{\pi} \exp(z^{-2})$$

with z a non-dimensional length (Lińan, 1974).

Seen otherwise, a acts as a 'scaling parameter' for the conditional χ ,

2.4) $$\chi|_{\xi} = \frac{a}{\pi} \exp\left\{-2[erfc^{-1}(2\xi)]^2)\right\}$$

where ξ is the mixture fraction and $erfc^{-1}$ is the inverse of the error function *erfc* (Peters, 2000).

Lińan (1974) obtained solutions of the form of an S-shaped curve, as illustrated in Fig. II.9 and studied the ignition regime at lower *Da*. He found that critical straining conditions exist, beyond which a low temperature, frozen solution is not possible and a diffusion flame temperature exists instead. This means that autoignition (i.e. transition to flame in this context) can occur only if *Da* is above a certain value, whereby the mixing rate is

below a critical value. The autoignition delay time, was found to increase with increasing mixing rate (Liñan and Williams, 1993). Theory, numerical simulations and experiments have indicated, that indeed, autoignition is not possible for $a > a_{crit}$.

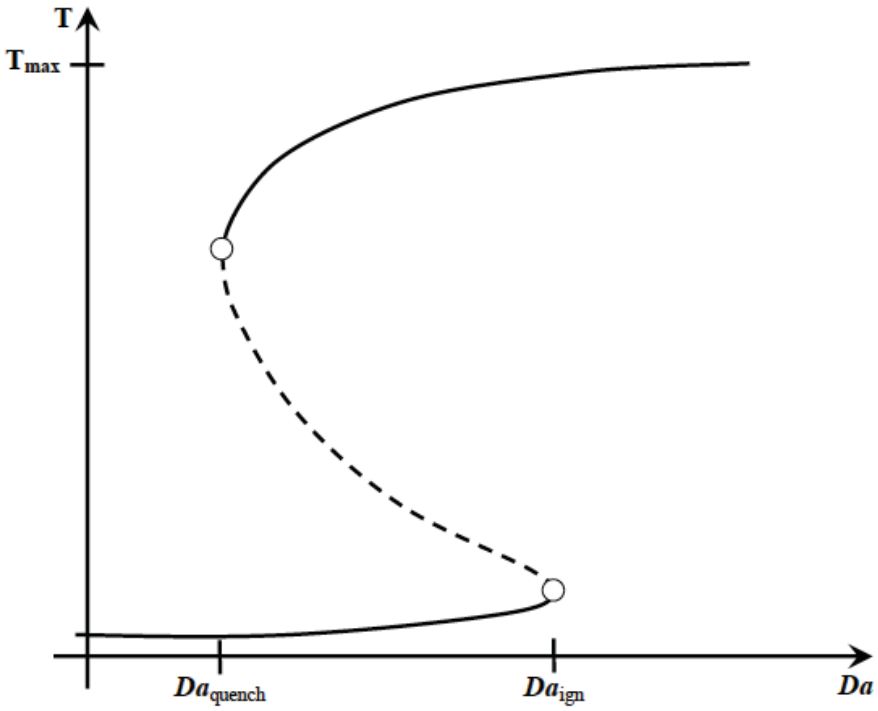

Fig. II.9 Maximum Flame Temperature versus Damkohler Number

More detailed treatment of the hydrogen autoignition chemistry in the laminar counterflow configuration was possible by computational (Kreutz and Law, 1996, Mason et al., 2002) and experimental/computational (Fotache et al., 1998, Zheng et al., 2002) investigations. Various hydrocarbons such as methane, ethylene, ethane, propene, propane, butane and n-heptane have also been investigated, with numeric studies (Liu et al., 2004) and experiments/simulations (Humer et al., 2002). These studies have provided an excellent understanding of autoignition chemistry in the presence of strain rate and have revealed the existence of complex thermokinetic/diffusive effects. On the ground of these studies it has been possible to develop reduced chemical kinetic mechanisms.

In laminar inhomogeneous autoignition the existence of critical conditions, in terms of a strain-rate, scalar dissipation rate or Damkohler number, has been verified. The observed influence of the non-uniform flow on the emergence of autoignition highlights the fact that, on a fundamental level, autoignition does not follow directly from expectations based on the homogeneous case (Humer et al., 2002).

II.1.2.1-b The flamelet assumption and its limitations

In this context, following the earlier ideas of Peters (2000) introduced a turbulent combustion model based on the flamelet concept. This term now designates a variety of physical models in which the turbulent flame is viewed as a collection of infinitely thin laminar flame elements embedded in a turbulent flow and interacting with it. The main advantage of the flamelet concept is that it decouples the complex chemical structure of the flame from the flow dynamics, which can be modeled independently.

In fact, under flamelet assumptions, the flame surface density concept may be used (Vervisch L and Poinsot T 1998). In this approach, the flamelet library contains only the total (i.e. integrated across the flame front) reaction rate, and the mean reaction rate is written as:

2.5) $$\overline{\dot{\omega}_k} = \overline{\Omega_k(\chi_{st})}\Sigma$$

where Ω_k is the integrated reaction rate averaged along the flame front, only dependent on the scalar dissipation, and Σ is the mean flame surface density defined as:

2.6) $$\Sigma = \overline{|\nabla Z|}_{Z=Z_{st}} p(Z_{st})$$

In the above formulations, one single parameter (χ_{st}) is used to describe the flamelet library. It allows to correctly describe flames in the high Damkohler number limit, but it is

not sufficient to capture additional effects such as curvature, ignition or extinction, flame history and transient effects.

The flamelet structure is either described with a simplified analytical formulation or with a flamelet library involving the detailed chemical structure of the flame. For non-premixed combustion, it corresponds to the laminar counterflow flame, which determines a steady diffusion flame structure. The flamelet is therefore submitted to strain only and curvature is ignored, although it may have non negligible effects (Van Kalmthout E et al. 1996).

It is generally believed that the flamelet concept is valid in the range of high Damkohler number.

High Da corresponds to fast chemistry compared to the turbulent time scale. In this case, the chemistry is fast enough to adapt instantaneously to the flow changes and unsteady effects can be neglected. Another condition is that the flame thickness is sufficiently small compared to the turbulent length scales, so that vortices can not disturb the inner structure of the flame. Even if chemistry is fast, i.e. the reaction layer is thin, the diffusive flame thickness is larger and may be perturbed by the flow.

Both space and time-scale ratios are usually recast in two non-dimensional numbers: Da and the turbulent Reynolds number Re_t. It can be shown that the time ratio condition corresponds to $Da = Da_0\sqrt{\mathrm{Re}_t}$ where Da_0 is a critical value under which unsteady effects appear. This value can be determined either with asymptotic analysis or Direct Numerical Simulation of turbulent diffusion flames. A typical regime diagram is shown in Fig. II.10, using a log-log scale for both Da and Re_t. In this diagram, the different regimes are separated by lines corresponding to $Da \propto \sqrt{\mathrm{Re}_t}$ (Veynante D and Vervisch L, 2002).

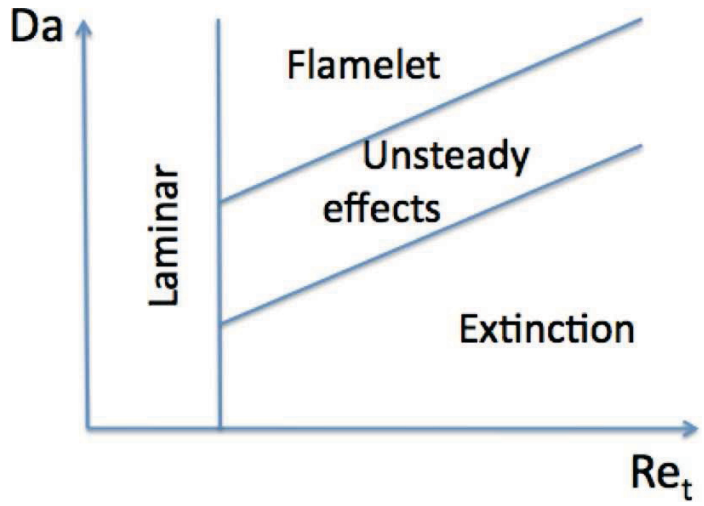

Fig. II.10 Regimes for turbulent non-premixed combustion

There are different approaches to turbulent flamelet models, but they all include the same ingredients:

- A laminar flamelet description, as presented above, describing the local flame structure,
- A turbulence model, describing the unclosed terms of the averaged or filtered equations,
- A coupling model to describe the interaction of the flame with the turbulent flow.

As mentioned above, the flamelet approach is based on steady-state assumptions that is, however, less efficient in 'low' temperature regions.

At high temperatures many chemical processes are fast and can be assumed to be in partial equilibrium. At lower temperatures the number of slow chemical processes increases and less species can be assumed to be in quasi-steady state. At these lower temperatures, convection and diffusion become important and the local mixture composition is determined by a balance between convection, diffusion and reaction.

For example in Mild or Flameless combustion processes the differential diffusion effects are found to have a strong influence on the accuracy of the predictions and therefore should always be accounted for (Christo F.C. and Dally B.B. 2005).

The modeling of these combustion processes needs specific attention. In fact, the conditions of uniform temperature distribution and low oxygen concentration lead to slower reaction rates and enhance the influence of molecular diffusion on flame characteristics, particularly when hydrogen is present in the fuel. These two effects, in particular, challenge the applicability of scalar-based models (such as flamelet approach) that assume fast chemistry and neglect the effects of differential diffusion (Coelho P.J. and Peters N. 2001).

Hence this turbulent combustion approach should be used with great care and only in particular conditions. Some strong assumptions have been introduced in its derivation.

II.1.2.2 Turbulent Inhomogeneous Flows

An appreciation of the fundamental issues of turbulent autoignition must come from truly dealing with the turbulent case. Theoretical approaches are extremely difficult because of the complex chemical kinetics of the slower chemistry of autoignition, the turbulent closure problem and the coupling of the chemistry and turbulence. Experimentally there has been a lack of interest in treating this problem, perhaps inhibited by the difficulty of performing well-characterized measurements in the 'hostile' and strongly sensitive to conditions turbulent autoignition environment. It is well known that the underlying physical and chemical processes of this phenomenon and their mutual cross-interference is sensitive to initial conditions. As a result, there is currently little data available concerning the effect of the local turbulence character on autoignition. It is only recently, with the increase in residence times associated with the low emission LPP industrial turbines and

the increased interest in controlling the autoignition timing in HCCI engines, that this issue has become relevant. Improved understanding of turbulent autoignition has come from Direct Numerical Simulations (DNS), even though there are the issues of the low Reynolds numbers that have been examined and/or the simplified description of the chemistry. Moreover, and crucially, the validity of the DNS results has not been experimentally verified.

II.1.2.2-a Stagnant Mixing Layers

Knowledge in this field has been recently expanded with the help of DNS (Domingo and Vervisch 1996, Echekki and Chen 2003) which have amply emphasized the importance of the mixture fraction field in determining the location of autoignition.

Current, 'state of the art', understanding of the autoignition of an inhomogeneous mixture, in a turbulent flow, stemmed from the observation of Mastorakos et al. (1997), who re-examined autoignition in isotropic, homogeneous, decaying two-dimensional turbulence in a shear-less mixing layer with a simple chemistry model, in terms of the original observations of Linan and Crespo (1976) for the laminar mixing layer and concluded that:

1. Autoignition always occurred at a well-defined mixture fraction ξ_{MR}, termed the *most reactive mixture fraction*. The value of ξ_{MR} could be determined a priory from knowledge of the initial conditions and the chemistry. At any instance, there were many such possible locations in the layer.
2. The fluid particles that eventually autoignited were the ones associated with small gradients of the mixture fraction, i.e. experienced lower values of conditional scalar dissipation rate, $\chi|_{\xi=\xi_{MR}}$.

Plots of the reaction rate versus $\chi|_{\xi=\xi_{MR}}$ were demonstrated to be very well correlated as far as the first autoignition location was concerned.

Since then, evidence to support these findings has come from simulations with different codes (Sreedhara and Lakshmisha 2000) and with detailed chemical mechanisms for hydrogen and a reliable four-step reduced mechanism for n-heptane. An extension has been made to three-dimensional simulations with complex hydrocarbon chemistry (Sreedhara and Lakshmisha 2002), agreeing fully with the earlier results.

It is significant to mention that, according to the latest understanding, a residence time until autoignition cannot fully define the problem in the absence of information on the mixture fraction field. It is surprising that even today, the number of autoignition experiments that are being performed in turbulent flows for which the mixture fraction field has been directly characterized, or at least for which an attempt has been made to estimate the mixing quantities based on accurate turbulence measurements, is very scarce indeed.

A point is being reached, whereby the location of autoignition can be reasonably predicted, but these predictions can only be confirmed by experiment. On the other hand, the effect of the turbulence character, length and timescales on the magnitude and randomness of τ_{ign} is far from understood.

II.1.2.2-b Turbulent Counterflows

Recently, autoignition experimental study in counterflow configuration have been extended to turbulent counterflows of hydrogen (Blouch and Law 2003). These experiments and successful Probability Density Function (PDF) modelling have produced the very interesting result that, as with the laminar counterflows, depending on the temperature of

the air stream autoignition may not occur at all (at least during the residence time available, as determined by the mean bulk strain rate).

The existence of critical conditions in the case of the counterflow is an interesting outcome, in that the DNS have not shown that such a limit exists for autoignition in turbulent mixing layers. Going back to the laminar mixing layers, both co-flow and counterflow, τ_{res} is completely determined by χ and vice versa.

The novelty of the turbulent case is that χ does not completely determine τ_{res}.

For the counterflow it is known that the criticality holds, but then the allowable τ_{res} is not arbitrary and it is relevant to approach the problem in terms of a consistently high bulk that can be achieved in practice by having high bulk strain rates. On the other hand, for the co-flow τ_{res} can still be arbitrarily long. This means that it is possible to have a 'hypothetical' situation in which χ is sustained above a critical value such that autoignition fails. Physically this would mean that the flow always has the ability to diffuse heat and radicals away from the reaction zone, promoting heat losses and depleting the radical pool and thus precluding autoignition.

For the turbulent counterflow it was also shown experimentally, that increased turbulence in the air stream resulted in a higher critical temperature necessary for autoignition, suggesting a delaying effect of turbulence on the pre-ignition reactions.

This finding is in subtle contrast to the DNS, that have shown that turbulence may accelerate autoignition. This discrepancy is most interesting and so the reasons behind the DNS finding will be reflected on briefly. It has been stated above that the DNS results have revealed that, locally, autoignition occurs at ξ_{MR} and at regions with low values of $\chi|_{\xi=\xi_{MR}}$.

The simulations did not last very long relative to the turbulence turnover time and also had

to resolve the fuel–air interface. Hence, the autoignition time was found to depend strongly on the initial condition (i.e. the initial value of χ), with the turbulence affecting autoignition time only insofar as it affected the emergence of the lowest value of the conditional $\chi|_{\xi=\xi_{MR}}$. Therefore, autoignition was promoted by fast mixing, due to the earlier emergence of well-mixed ξ_{MR} spots. It becomes essential to experimentally clarify this disparity and to validate or not the theoretical results from DNS regarding turbulent autoignition in parabolic flows.

II.2 Original Contribution

The purpose of this section is to report the basic properties of 1D reactive structures in steady and unsteady conditions.

The only 1D structures considered are planar since they show with sufficient details the main fluid-dynamic influence on the diffusion flames.

The counterflow configuration involves uniform strain and it forms an important building block in our understanding of autoignition of non-premixed combustion.

In particular the different reactive structure stabilized in a diffusion layer as a function of the different feeding configurations will be shown.

In the analysis of reactive structure some synthetic characteristics will be pointed out as discriminative for the occurrence of different combustion regimes.

II.2.1 HDDI in Counter-Diffusion flow reactor

Combustion processes in which the reactants are separated in feedback combustion yield diffusion flames. It is possible to analyze the simple reactor in which this processes are

stabilized that is the counter-diffusion reactor fed with oxidant and fuel in opposite directions along the same axis.

They include a set of processes according to the different boundary conditions pertaining temperatures and dilutions of the reactants.

Therefore, it is possible to envisage four configurations listed below, each with a simple acronym of self-explaining terms. Specifically, H, D, O, and F stand for hot, diluted, oxygen, and fuel (CavaliereA and de Joannon M 2005).

The first two processes are characterized by dilution of the oxidant. In the first case, the oxidant is also heated to high temperature, whereas in the second process, the fuel is heated. This process (HFDO) is less interesting than the other three because the fuel is preheated to such temperatures that the fuel undergoes a classical pyrolysis, which may generate heavier and denser aromatic products. Consequently, the HFDO process will not be discussed in this section because it would likely generate undesired pollutants.

Configuration Name	Description
HODO	Oxidant is hot and diluted
HFDO	Fuel is hot and oxidant is diluted
HFDF	Fuel is hot and diluted
HODF	Oxidant is hot and fuel is diluted

Table 2.1

Hence, the other three processes will be treated in the next sections and they are, in turn, ordered according to the number of terms present in the balance equations, by considering the steady and/or unsteady nature of the diffusive layer.

II.2.1.1 Steady diffusion ignition processes

Following one of the classical approaches in the study of diffusion flames, the Hot Diluted Diffusion Ignition has been analyzed by means of opposed jets configuration.

In dependence on the pre-heating and/or dilution of fuel and/or of oxidant jets, four cases of inlet conditions can in principle lead to an oxidative structure related to HDDI.

In the first part of this section the attention has been focused on the system where the undiluted, pre-heated air stream is fed in counter-flow toward a diluted fuel jet, identified in literature as Hot Oxidant Diluted Fuel condition (de Joannon M et al. 2009).

Moreover the characteristics of the reactive structure will be shown when diffusion ignition takes place in the other feeding configurations.

The system was schematized in the sketch reported in Fig. II.11. A methane-nitrogen flow, characterized by an inlet temperature (T_o), velocity (V_o) and a fuel molar fraction (X_f), is fed toward an opposed flow of air at high temperatures (T_{in}). The flow rates of the two jets were set in such a way that their kinetic energies were equal, so that the stagnation point occurs in the middle of the two inlet sections, at x = 1 cm.

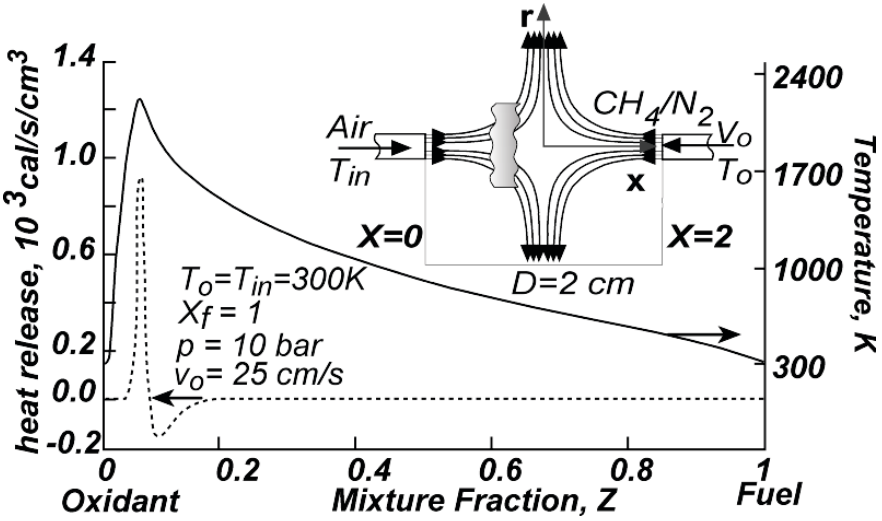

Fig. II.11 Schematization of hot diluted diffusion ignition configuration

Numerical analysis was carried out by means of Oppdif application of ChemKin (Kee RJ et al. 2002) package by using the GRI 3.0 mechanism (Bowman CT 1999).

The general approach used in this section is to analyze the behaviour of the reactive layer by evaluating temperature (T) and heat release rate ($\dot{h}$) profiles as function of the mixture fraction (Z). In the case of standard inlet conditions, corresponding to undiluted jets fed at $T_{in} = T_o = 300$ K, the profiles of these quantities were reported in Fig. II.11 as function of the mixture fraction with solid and dashed lines, respectively. Starting from $T_{in} = 300$ K at Z = 0 the temperature rapidly increases up to the maximum value of about 2220 K at Z = 0.055, which corresponds to the stoichiometric mixture fraction (Z_{st}). Hereafter, T smoothly decreases with Z up to reach T_o at Z = 1 (i.e. in correspondence of fuel inlet section at x = 2 cm).

The related heat release profile, reported in the same figure with a dashed line, better highlights the range of Z where reactions take place.

Therefore, starting from Z = 0, $\dot{h}$ sharply increases up to a maximum that occurs in correspondence of the maximum temperature, at $Z_{st} = 0.055$. This trend testifies a prevalent reaction activity toward the formation of species with heat of formation lower than that of reactants, i.e. intermediate or product of oxidation reactions.

Then $\dot{h}$ drops toward a negative minimum, which occurs at about Z = 0.08. It becomes zero for Z = 0.17 and keeps this value up to Z = 1. In contrast with what occurs where heat release is positive, the range of Z corresponding to the negative values of $\dot{h}$ identifies the region where recombination reactions overcome the oxidation ones.

Several simulations were performed over a wide range of T_{in} at different dilution level of fuel jet and strain rate $K_0 = \frac{V_0}{D}$ in adiabatic conditions in correspondence of 1 and 10 bar.

The pre-heating of the air as well as the dilution of fuel affects the flame structure in dependence of its magnitude. A synopsis of such variations in flame structure is reported in Fig. II.12 where temperature (upper part) and heat release rate (lower part), computed for a pre-heating temperature of 1400 K, V_0 = 100 cm/s and p = 10 bar, were reported as a function of Z on curves parametric in X_f, which ranges from 1 to 0.05.

Both T and $\dot{h}$ are represented by solid lines that increase their thickness with X_f. On the same figure, frozen temperature is also reported with a dashed line. The temperature profile obtained for $X_f = 1$, i.e. when no dilution is considered, is very similar in shape to the one reported for standard conditions in Fig. II.12, although it covers a wider range of values.

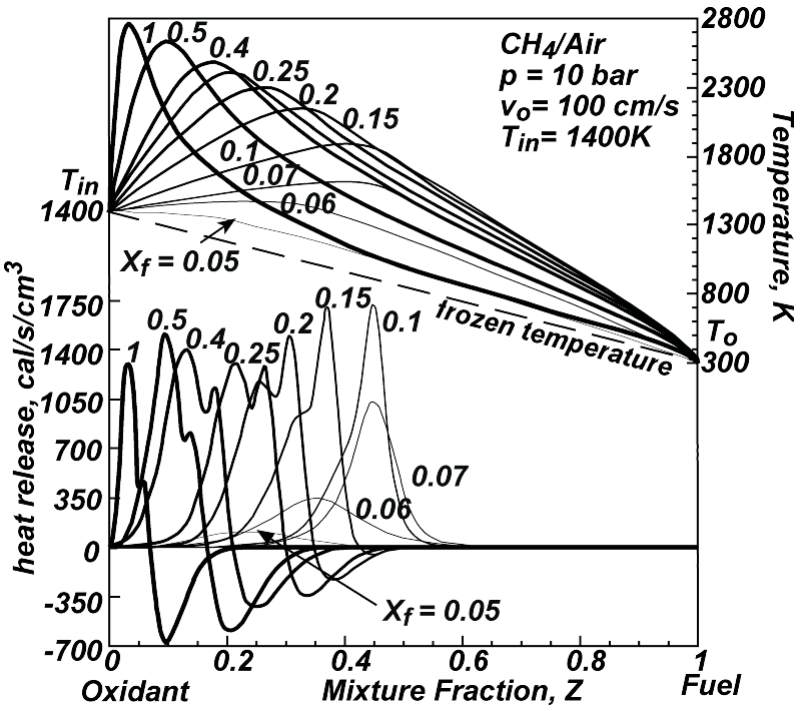

Fig. II.12 *Temperature (upper part) and heat release rate (lower part) versus mixture fraction, parametric on Xf at To= 300 K, Tin = 1400 K and p = 10 bar.*

As expected due to the preheating, the temperature reaches a higher maximum value of 2740 K for Z = 0.033, then decreases toward the frozen line.

The corresponding heat release profile sharply increases up to a first absolute maximum at Z = 0.033. Then it decreases in direction of a second relative maximum which occurs at Z = 0.057. This occurrence makes the oxidative region slightly enlarge toward higher Z, which also results in a shift of the subsequent pyrolytic region. In fact, the minimum of heat release rate occurs at Z = 0.095 then it comes back to zero at Z = 0.2. The presence of a more complex structure is obviously related to the effect of the highly preheated flow. It supplies thermal energy to the mixing layer making the ignition of mixture occurs at lower Z with respect to the standard conditions.

This leads to the stabilization of a predominant oxidative structure where the most part of the conversion occurs, as also showed by the maximum temperature that is simultaneous with the first maximum of the heat release rate.

The fuel dilution stresses the differences with respect to the standard conditions.

For X_f = 0.5 the maximum of temperature profile shifts toward higher Z (Z = 0.094).

The subsequent temperature decrease toward the frozen line is smoother than what happens in the absence of dilution. Consequently, the oxidative region in the related $\dot{h}$ profile shifts and widens.

It is again characterized by the presence of two positive maxima.

The pyrolytic region slightly enlarges toward higher Z, although the main effect due to dilution is a decrease of the absolute value of the minimum heat release rate.

This behavior is even more evident by decreasing X_f , making the pyrolytic region vanish for X_f lower than 0.15.

More complex behavior is related to the evolution of the structure of the oxidative region by varying the dilution level. Decreasing X_f it persists to shift toward higher Z following the shift of Z_{st}.

As expected, temperature profiles behave as $\dot{h}$ profiles, thus showing the maximum at higher Z. The most relevant effect of dilution increase is the variation of relative intensities of the two maxima. A further depletion of X_f makes it overcome the first maximum that, in turn, slowly reduces up to be embedded in the remaining structure
for $X_f = 0.1$. Contemporaneously, the pyrolytic region disappears. The increase of dilution level makes the part of the mixing layer where the composition allows for the ignition, shift toward region characterized by lower frozen temperature.
Therefore, the oxidative structure principally due to the air pre-heating reduces its strength. Starting from $X_f = 0.1$, $\dot{h}$ profiles exhibit only a single maximum that decreases in intensity with X_f. However, as most remarkable effect of a further dilution increases, the oxidative region moves backward toward lower Z, in opposite direction with respect to that naturally increases with dilution of fuel jet. For very high dilution levels, falls outside the reaction zone as shown by the heat release profiles for $X_f = 0.05$.

For lower pressures, the temperature and heat release rate profiles keep the main characteristics, although minor differences can be found, as shown in Fig. II.13 where the data computed for p = 1 bar were reported.
In contrast with the data reported for p = 10 bar, the value of the first maximum, occurring at $Z < Z_{st}$, is always lower than the value reached by the maximum at Z = Zst.

Starting from X_f = 0.25 the first maximum turns into a shoulder on the left side of the curves that seems to persist up to X_f = 0.07.

As evident from the Fig. II.13, also in this case the oxidative region shifts toward higher Z up to X_f = 0.07. For lower X_f the oxidative region again moves backward toward lower Z leaving outside the reaction zone.

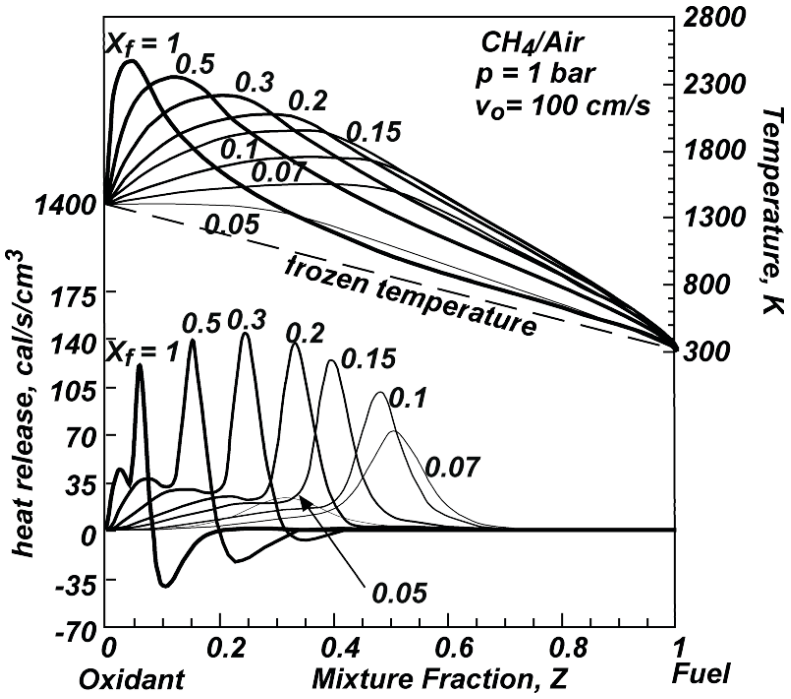

Fig. II.13 *Temperature (upper part) and heat release rate (lower part) versus mixture fraction, parametric on X_f at To= 300 K, T_{in} = 1400 K and p = 1 bar*

The inversion in the displacement of maximum of temperature and heat release profiles by increasing the dilution level is present in a wide range of inlet temperatures. This is shown in Fig. II.14 where the mixture fraction at which the maximum of heat release rate closest to occurs Z_{st} (Z_h max) is reported on curves parametric in T_{in} for p = 1 bar (upper) and p = 10 bar (lower), as a function of Z_{st}.

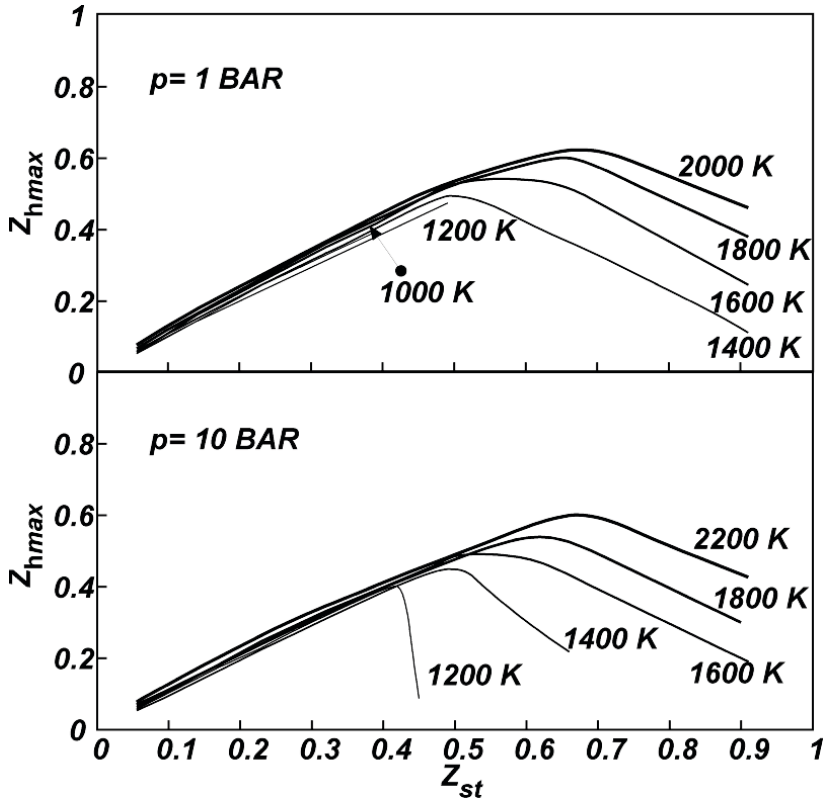

Fig. II.14 *Temperature (upper part) and heat release rate (lower part) versus mixture fraction, parametric on X_f at T_o= 300 K, T_{in} = 1400 K and p = 1 bar*

As already described by analyzing the previous profiles, at 10 bar Z_{hmax} is very close to, up to a certain value in correspondence of which Z_{hmax} decreases with respect to Z_{st}. This decrease occurs at higher by increasing T_{in}. For instance, at T_{in} = 1400 K the inversion occurs at Z_{st} = 0.5 (X_f = 0.1) whereas at T_{in} = 2000 K it occurs at Z_{st} = 0.7 (X_f = 0.0415).

At p = 1 bar the same behavior can be pointed out for temperatures higher than 1200 K. In fact, up to this Tin an increase of dilution let the oxidative structure disappears before the occurrence of inversion.

In a restricted range of temperature, the system can work in two different steady states, which correspond to different oxidative structures. This is shown in Fig. II.15 where the heat release profiles obtained for T_{in} = 1000 K, X_f = 0.5 and p = 10 bar were reported. The solid line represents the solution corresponding to a high fuel conversion as the maximum

value reached by the heat release shows. In this case, the flame structure shows two maxima in correspondence of the oxidative region and one minimum in pyrolytic region. The profile related to the very low fuel conversion, reported in the figure with dashed line, is very different. In this case the heat is released in correspondence of very low Z values with a rate that reaches the maximum at Z = 0.027. Then it decreases to zero, never assuming negative values due to the absence of the pyrolytic region. Moreover the characteristic values reached by heat release rate in this case are order of magnitude lower than the one obtained for high fuel conversion.

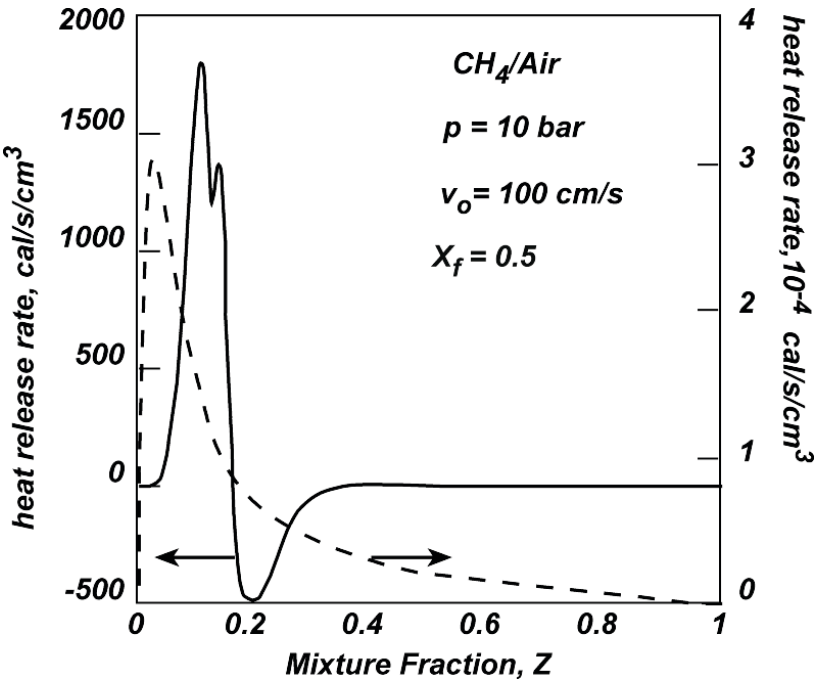

Fig. II.15 *Heat release rate profile for high and low conversion solution, T_0 = 300 K and T_{in} = 1000 K.*

On the basis of the considerations reported so far, the different shapes of heat release profiles are related to different combustion regimes that can establish in dependence of the initial conditions. They can be used for pointing out a comprehensive classification by building up a map of behavior on a $T_{in} - \Delta T$ (ΔT = maximum between allowable temperature and frozen temperature) plane where the regions corresponding to the different

combustion regimes were identified. In Fig. II.16 the map obtained for K_0 = 50 s^{-1}, T_0 = 300 K and p = 1 bar was reported. T_{in} was changed from 600 to 2400 K whereas ΔT ranged from 300 to 2200 K.

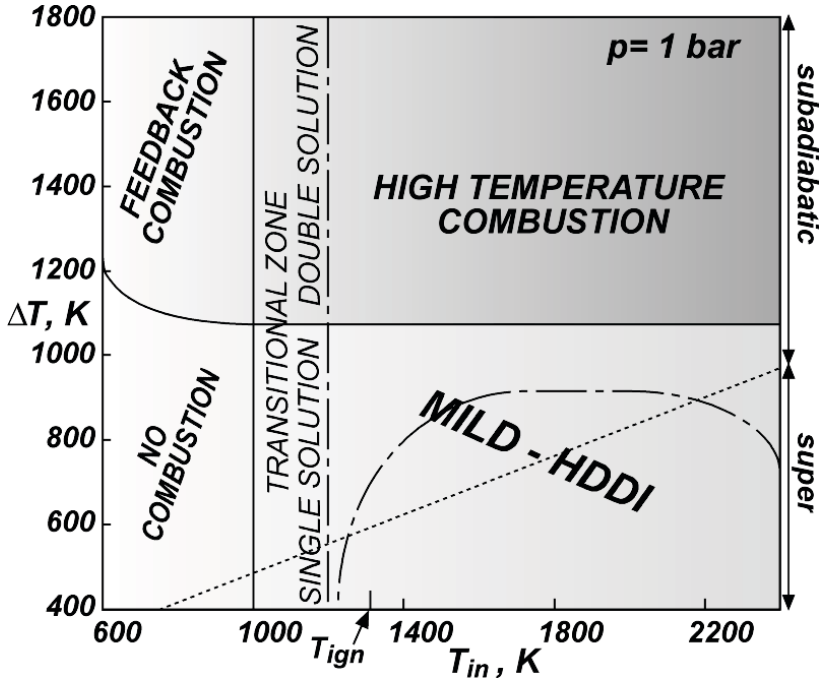

Fig. II.16 Combustion regimes at p = 1 bar, T_0 = 300 K, T_{in} = 1400 K and K_0 = 50 s^{-1}.

The map was divided in four main regions. In the lower left region the "no combustion" zone, where the fluid-dynamic and temperatures of the two jets do not allow the combustion to take place, is reported.

The upper left part of the map, i.e. the "feedback combustion" region, identifies the conditions in correspondence of which traditional flame structures stabilize. In this case the maximum of the heat release rate occurs for Z very close to the stoichiometric value and the oxidative region is followed by a well-defined pyrolytic region.

The "high temperature combustion" area, in the upper right part of the map, is the region where very high maximum temperatures are reached due to the pre-heating and the flame structure can be assumed to be similar to the rough structure of "feedback combustion".

Therefore, both an oxidative and pyrolytic regions are present in the heat release profiles that in this case show two maxima in correspondence of the oxidative region.

The lower left area of the map, namely the ‘‘Mild-HDDI” represents the condition in which the diffusive structure no longer exists in its standard aspect. In this combustion regime only the oxidative structure is visible in the heat release profiles. An additional, not secondary characteristic is represented by the occurrence of maximum heat release rate at Z very low with respect to Z_{st}. As described above, the lower X_f the lower the Z at which the maximum occurs is, in contrast with what happens in the ‘‘high temperature combustion” and ‘‘feedback” regimes. This feature occurs in the lower part of Mild-HDDI area, delimited with the dashed-dotted line.

The boundaries among the different regimes are represented by transitional regions where the behavior of the system can not definitely associated to one controlling process but it has to be analyzed with more detail.

These results presented until now in the previous section can be summarized in a synthetic frame, which is outlined by taking into account the parameter plot of Figs. II.16.

1. A significant change of spatial distribution of heat release is associated to oxidant temperatures higher than the auto-ignition temperature of homogeneous charge for a characteristic time comparable to the convective characteristic time of the system. The most striking change is the broadening of heat release profiles in the mixture fraction plot, which entails also a broadening of the spatial region where the heat release occurs. This result supports the conceptual model of ‘‘distributed oxidation” in contrast to the thin flame in the mixture fraction domain.
2. Inside this region the asymptotic condition with undiluted or nearly undiluted fuel identifies the sub-domain of High Temperature Combustion (the region above the

dashed line), in which a double peak of heat release is clearly identified, one at nearly stoichiometric condition and one on the high temperature side. The former can be thought in terms of the ‘‘classical” diffusion flame structure whereas the latter can be explained in terms of the expected increase of the heat release just taking into account an Arrhenius-type dependence on the temperature.

3. In the same region for air temperature higher than the auto-ignition one, the asymptotic condition with very diluted fuel identifies the subdomain ‘‘Mild-HDDI” Combustion (the region under the dot-dashed line), in which the position of the maximum heat release is completely uncorrelated with the stoichiometric mixture fraction. In this case oxidation takes place only where the autoignition can develop inside constrain of the residence time of the fuel in the system.

4. The two aforementioned regimes are extended to a well-defined boundary that separates the two regions. This consists of the loci where a negative heat release, i.e. a pyrolytic region, is present or not present on the rich side of stratified charge.

5. The separation between the High Temperature Combustion and Mild Combustion can be performed by means of a single parameter, i.e. the maximum allowable temperature increase in the system. This is the most striking phenomenological aspect of the results since it shows the important role of fuel dilution. It is also of great interest that this constancy allows for neglecting any relation of this transition with the superadiabatic condition of the system. In other words it is not necessary that the air temperature is higher than whatever possible temperature in the system to yield Mild Combustion condition.

6. The transition from Feedback Combustion to High Temperature Combustion occurs through a region of the parameter plot, in which two possible solutions are present. It

is clear that the high conversion solution is related to the extinction of Feedback Combustion and the low conversion solution is related to continuous enhancement of the heat release of the autoignition solution of the High Temperature Combustion with the temperature increase.

7. The transition from the ‘‘No-Combustion” region to the Mild Combustion one occurs in a more gradual way passing through a region where methane is increasingly more converted by oxidation by increasing the air temperature. This reflects also the behavior of the system in terms of increase of stretch rate, which is not shown in the paper. In fact no abrupt transition from combustion/no combustion conditions has been identified in the explored regimes. This is similar to what it has been revealed for well stirred reactor conditions and it is consistent with the noiseless characteristics of such types of regimes (de Joannon M et al. 2005).

The aforementioned characteristics of MILD combustion change when diffusion ignition takes place in a structure where the non-diluted fuel diffuses into the diluted hot oxidant (HODO configuration).

The flow high initial enthalpy and the low oxygen concentration can drastically modify the structure of the oxidative and pyrolytic region due to change of the physical and chemical kinetics respect to conventional diffusion flame (de Joannon M et al. 2012).

In order to extend the previous results to HODO configuration, an analysis has been carried out using the same tools to those used for HODF-case.

In particular, the oxidant flow and the fuel flow are characterized by inlet temperatures, respectively T_{in} and T_0. The fuel has a inlet velocity V_0, while the oxidant flow velocity comes from the assumption that the kinetic energies of the two flows are equal so that the stagnation point is located, in any case, in the middle of the two injection planes, located at a relative distance D equal to 2 cm. The asymptotic strain rate K_0 is defined with respect to

the fuel flow velocity as V_0/D. For the HODO configurations the dilution degree is expressed respectively by the oxygen molar fraction XO_2. The diluent species is nitrogen while fuel is pure methane.

The structure of reactive zone was analyzed always in the same way, i.e. by a simple evaluation of temperature T and heat release rate H profiles as a function of mixture fraction Z along the axial coordinate of the system.

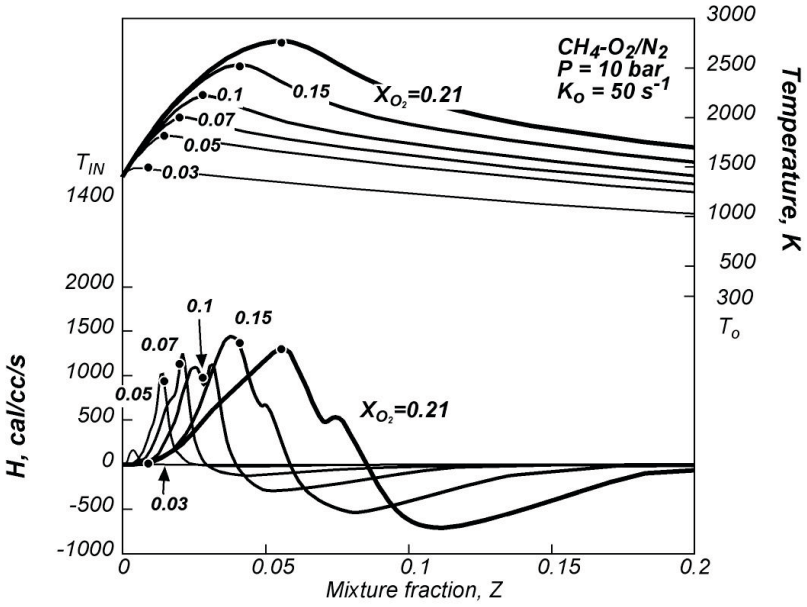

Fig. II.17 *Temperature (upper part) and heat release rate (lower part) versus mixture fraction, parametric on XO_2 at T_0 = 300K, T_{in} = 1400K and p = 10 bar, for the system CH_4- O_2/N_2.*

Figure II.17 shows the temperature (upper part) and the heat release (lower part) profiles along the coordinate Z on curves parametric in the dilution level of the N_2/O_2 pre-heated flow. The inlet temperature T_{in} is equal to 1400K, while the pressure is 10 bar. Methane is fed at environmental temperature with an inlet velocity V_0 equal to 100 cm/s. This means a strain rate K_0 equal to 50 s^{-1}.

Solid lines, representing T and H, decrease their thickness with XO_2, whereas black dots indicate, once the two flows completely mix, the stoichiometric values of the parameter Z.

The analysis of numerical results have been realized on the basis of the consideration that positive values of H are symptomatic of oxidation reaction occurrence, whilst negative values suggest the establishment of pyrolytic reactions or the overcoming of decomposition reactions with respect to oxidation ones.

Since the reactive region in the Z coordinate develops in the neighborhood of the oxidant injection plane the analysis of the results have been restricted in the range 0 - 0.2 of the mixture fraction.

Profiles at $XO_2 = 0.21$ corresponds to the case where the oxidant flow is just air. In such a case the temperature slightly increases up to reach a maximum value equal to 2750 K, then it slowly decreases down to 300 K towards the methane injection plane.

At the same time, the heat release profiles shows two relative maxima values, the former, in correspondence of the maximum value of temperature, located at $Z = Z_{st} = 0.055$, the latter, with a lower value, at Z = 0.06. At Z = 0.11 it shows a minimum negative value. Afterwards it slowly increases towards the fuel injection plane and becomes zero.

As soon as nitrogen content in the oxidant flow is enhanced, in general the temperature and the heat release profiles show the same trend but the maxima and minimum values occur for lower values of Z and the region, in the Z space, where reactions occur becomes narrower with respect to the case with no oxidant dilution.

For $XO_2 = 0.15$ the maximum temperature ($T_{max} = 2675$ K) occurs for at $Z = 0.0404 = Z_{st}$. The H absolute maximum is localized at the same position, while the second one at Z = 0.0505. Both the two maxima heat release values are higher than the ones showed in the previous case, whereas the negative minimum is lower in absolute value.

When the oxidant stream dilution degree is 90%, the decrease of the mixture calorific value leads to a lower system temperature. The maximum allowed temperature is positioned at Z = 0.0275 which corresponds to Z_{st}. The heat release profile is similar to the previous cases

described earlier, but the absolute maximum is not located in correspondence of the stoichiometric Z value. As matter of fact the first maximum is sited at Z = 0.025, whereas the second one at Z = 0.031. It means that the maximum heat release rate occurs in correspondence of a mixture with a fuel lean composition. In such a case the two maxima are of comparable magnitude, furthermore the extension of the negative heat release region is reduced and the minimum absolute value is diminished in comparison with the previous considered systems.

For $XO_2 = 0.07$ the temperature further on decreases in congruence with the mixture lower calorific power due to the dilution degree enhancement. The temperature maximum falls in correspondence of the stoichiometric Z value. At the same time heat release profile maxima change their relative importance, in particular the former becomes lower that the second one that almost disappears. The stoichiometric mixture fraction falls on the left side of the maximum heat release rate value. The pyrolytic region extension diminishes congruently with the trend found out in the previous conditions in dependence of the dilution level.

A further depletion of oxygen causes a merging of the heat release maxima values and the disappearance of the negative heat release region. As matter of fact in case of $XO_2 = 0.05$ the H profile shows a single positive maximum in correspondence a Z value slightly $Z = Z_{st}$, while the pyrolytic region is negligible.

In the last case the molar fraction of oxygen is equal to 0.03. For such dilution the temperature increase is very limited and the maximum temperature is 1475 K, while the heat release presents one single maximum very low in comparison with other cases. Neither the maximum temperature, neither the maximum heat release are correlated with Z_{st}.

The heat release profile shapes have been considered as indicative of the structure of the oxidation region. In particular profiles that show two positive peaks and a negative minimum value are indicative of high temperature combustion, where the composition of the mixture ensures high heat release and high system temperatures so that the oxidation process is self-sustaining. On the other hand, whereas heat release profiles that present a single positive peak and no negative values are symptomatic of Mild Combustion. In such case oxidation reactions occur just by means of the high enthalpy content provided by the hot oxidant flow.

Similarly to the HODF-case, the heat release profile can be used for pointing out a comprehensive classification by building up a map of behavior on a $T_{in} - \Delta T$ plane where the regions corresponding to the different combustion regimes were identified.

In Figure II.18 the map obtained for K_o = 50 s^{-1}, T_0= 300 K and p = 10 bar was reported for a pressure equal to 10 bar and a strain rate equal to 50 s^{-1}. T_{in} was changed from 500 K up to 2500 K.

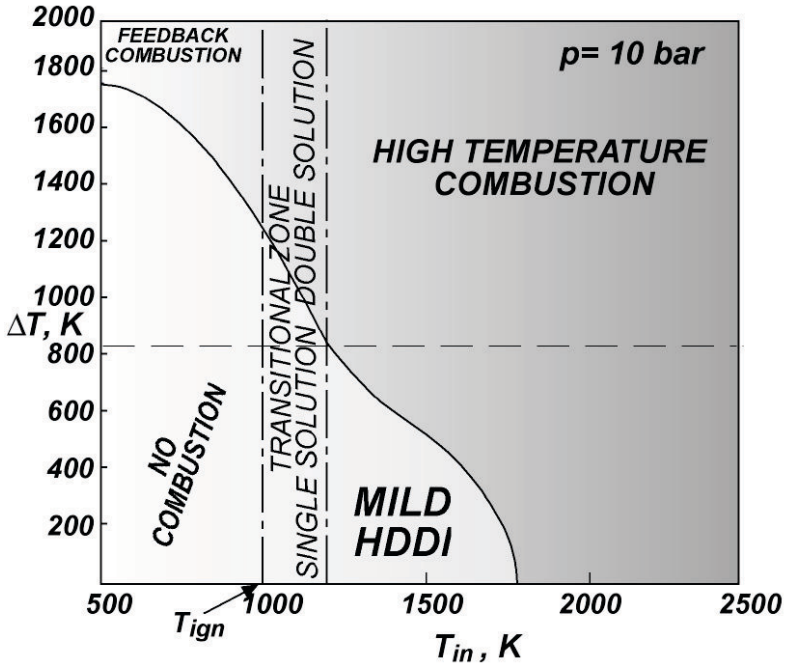

Fig. II.18 Combustion regimes at p = 10bar, T_{in} = 300K, Tin = 1400K and K_0 = 50 s^{-1}

The numerical results are similar to those obtained in the HODF-case.

In particular they can be reassumed as follows:

i) The oxidation processes can be sustained just because the pre-heating temperature of one of the two flows is high enough to promote the auto-ignition of the system.

ii) The maximum local temperature of the systems is lower with respect to the undiluted traditional diffusion flames even though one of the reactant is pre-heated. This implies a reduction of undesired by-products such as NOx species.

iii) The double heat release peak, typical of High Temperature Air Combustion, disappears as the dilution degree is increased leading to a single peak profile and to the absence of the pyrolytic region, associated to Mild Combustion processes. Such condition implies the reduction of soot precursor species.

iv) Once approaching Mild operative conditions, the temperature maximum always occurs in correspondence of the stoichiometric value of mixture fraction whereas the heat release maximum is uncorrelated with Z_{st} and occurs for leaner compositions respect to the stoichiometric one. The region in the Z space where reactions occur decreases as the highly diluted (Mild combustion) conditions are reached.

In addition to the results shown so far, further simulations have been carried on in the HODO configuration in presence of water and carbon dioxide.

In fact, in industrial furnaces a common practice to ensure Mild Combustion conditions is by means of a recycling of hot exhausted gases since they provide for both the sensible enthalpy required for the fresh inlet mixture pre-heating and the mixture dilution (Katsuki M. et al. 1998). Exhausted gases are mainly composed by steam and carbon dioxide. Therefore the analyses of the oxidative structure in condition typical of Mild Combustion in systems diluted in H_2O and CO_2 is very interesting.

Figure II.19 reports the T and H profiles versus the mixture fraction Z for the system composed by a oxygen flow diluted in water and pre-heated up to 1400K, while the fuel flow is fed at environmental temperature. The inlet velocity V_0 equal to 100 m/s, thus the asymptotic strain rate is equal to 50 s^{-1}. Curves are parametric in the oxidant flow dilution level specified by the oxygen molar fraction XO_2.

The numerical simulations have been carried on varying the XO_2, from air composition to very diluted conditions.

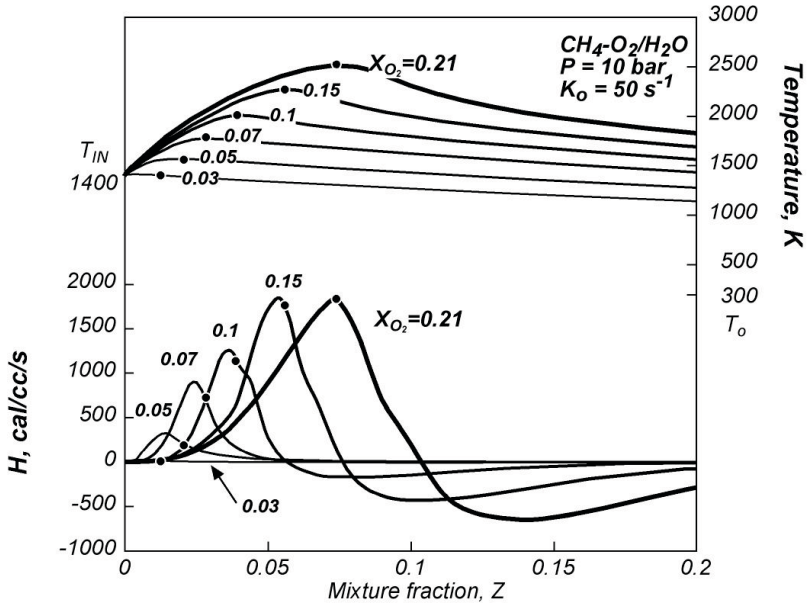

Fig. II.19 *Temperature (upper part) and heat release rate (lower part) versus mixture fraction, parametric on XO_2 at T_0 = 300K, T_{in} = 1400K and p = 10 bar, for the system CH_4- O_2/H_2O.*

As soon as water content in the oxidant flow is enhanced, the temperature and the heat release profiles show the same trend but the maximum and minimum values occur for lower values of Z and the region, in the Z space, where reactions occur, is narrower with respect to the case with no oxidant dilution.

For XO_2 = 0.15 the maximum temperature (T_{max} = 2300 K) occurs for at Z = 0.0563 = Z_{st}. The H absolute maximum is localized at a Z value slightly lower than the stoichiometric

one. The maximum H release intensity is comparable with respect to the previous case but the negative minimum is lower in absolute value.

In case of $XO_2 = 0.1$, the enhancement of the heat capacity of the system leads to a lower system temperature. The maximum allowed temperature is positioned at Z = 0.0396 which corresponds to Z_{st}.

The heat release profile is similar to the cases described earlier, but the absolute maximum is not localized in correspondence of the stoichiometric Z value. As matter of fact the maximum is sited at Z = 0.038, whereas the maximum at Z = 0.0396. The pyrolytic region disappears.

In the other cases (XO_2=0.05, 0.03) the temperature increment and the heat release are relatively modest. The maximum temperature always occurs for the stoichiometric mixture fraction, while the heat release is uncorrelated with Z_{st}.

Figure II.20 shows the temperature and heat release profiles relative to the system CH_4-O_2/ CO_2. The approach to the problem is similar to the previous cases so the operative conditions, the dilution levels as well as the nomenclature are equal to the HODO configurations numerically exploited earlier in this section.

In general, as the CO_2 concentration is increased, from 85% up to 97%, the temperature maximum decreases and shifts towards lower mixtures fraction values, while the two maxima as well as the absolute minimum value diminish their magnitude. The oxidative and pyrolytic regions shift to lower Z values while diminishing their extension.

Starting from $XCO_2 = 0.1$ the heat release shows just a maximum value while the absolute minimum becomes zero.

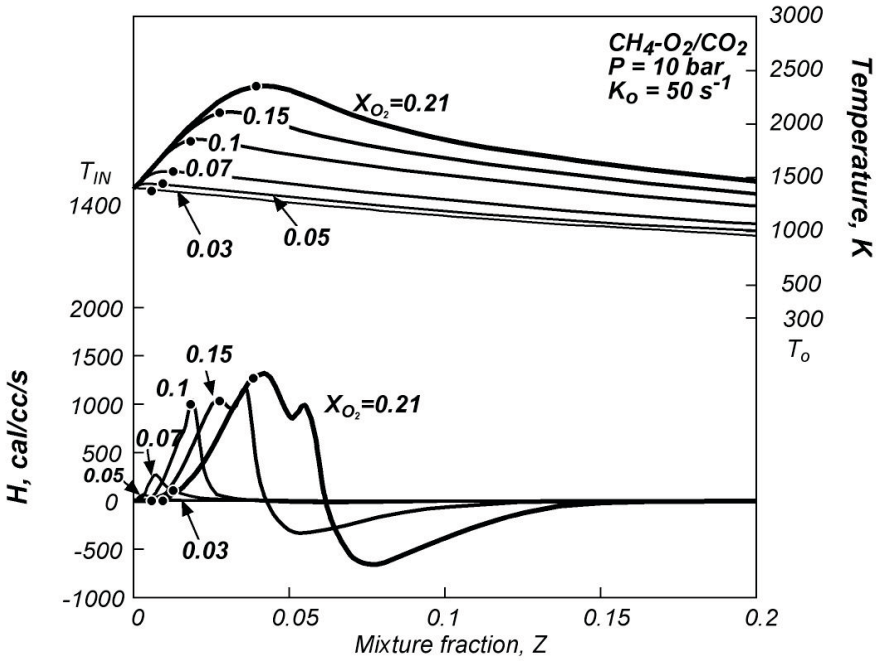

Fig. II.20 *Temperature (upper part) and heat release rate (lower part) versus mixture fraction, parametric on XO_2 at T_0 = 300K, T_{in} = 1400K and p = 10 bar, for the system CH4- O2/CO2.*

In highly diluted conditions the heat release is uncorrelated to the position of the stoichiometric mixture fraction.

All the HODO systems numerically analyzed have shown the same features relatively to the modification of the reactive structure of the combustion process in dependence of the dilution level increase.

In particular, the nature of diluting species affect significantly the reaction region structures, affecting both the temperatures and the heat release profiles extension and shape in the Z coordinate. Due to higher thermal capacity of the system with respect to nitrogen diluted system, the maxima temperature are lower, thus the production of undesired species, such as NO_x and soot, is mainly suppressed.

The last steady-HDDI process analyzed is obtained when the fuel is injected at high temperature and is diluted. This process is known as a hot fuel-diluted fuel (HFDF) process.

The categorization and characterization of the reactive structures in the diffusive configuration, dealing with a fed condition corresponding to the Hot-Fuel-Diluted-Fuel counter flowing jets has been done by following the same approach on HODF and HODO conditions previously reported (de Joannon M et al. 2012).

In particular, the effects of dilution and pre-heating of the fuel flow can be seen at a glance by analyzing the synopsis of the temperature and heat release profiles reported in Figs. II. 21 and II.22. In Fig. II.21, the T and $\dot{h}$ profiles, computed for a pre-heating temperature of 1400 K, V_0 = 100 cm/s and p = 10 bar, are reported as a function of Z on curves parametric in X_f , over a range from 1 to 0.02. Both T and $\dot{h}$ are represented by solid lines that increase their thickness with X_f . The dots reported on the heat release curves indicate the value of $\dot{h}$ at Z_{st} for each X_f considered. On the same figure, the frozen temperature is also reported with a dashed line. In the temperature profile obtained for X_f =1, i.e., when no dilution is considered, T reaches a higher maximum value of 2340 K for Z = 0.053, due to fuel preheating. The $\dot{h}$ profile at X_f =1 sharply increases up to an absolute maximum at Z=0.053. It then decreases and exhibits a small shoulder at Z=0.062, which is slightly higher than the Z_{st} = 0.055 that makes the oxidative region slightly larger toward a higher Z. This difference also results in a shift of the pyrolytic region.

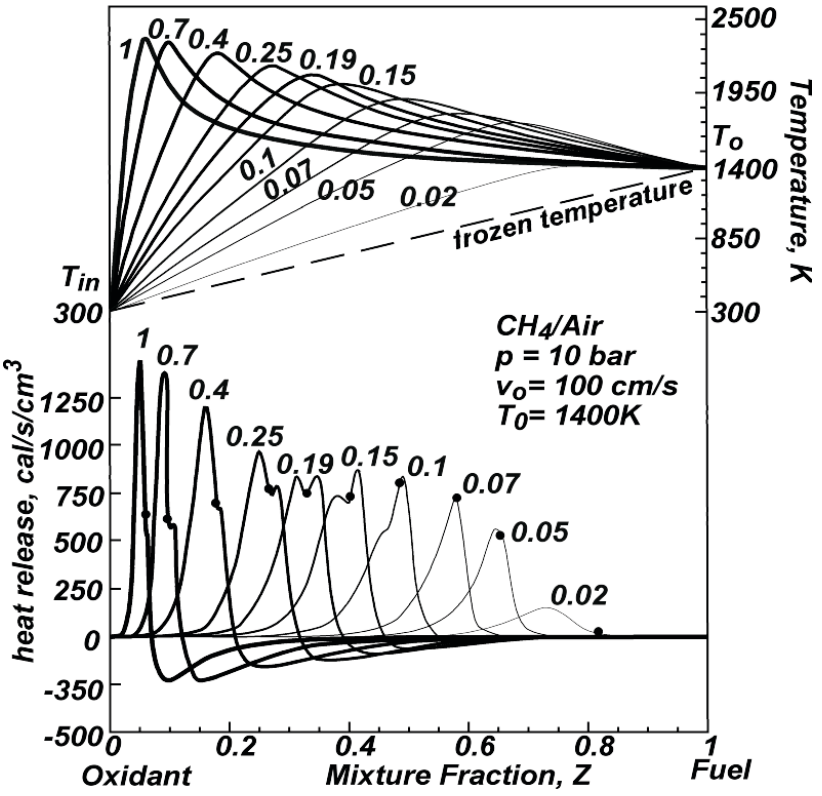

Fig. II.21 *T and $\dot{h}$ vs. Z, parametric on X_f at p = 10 bar.*

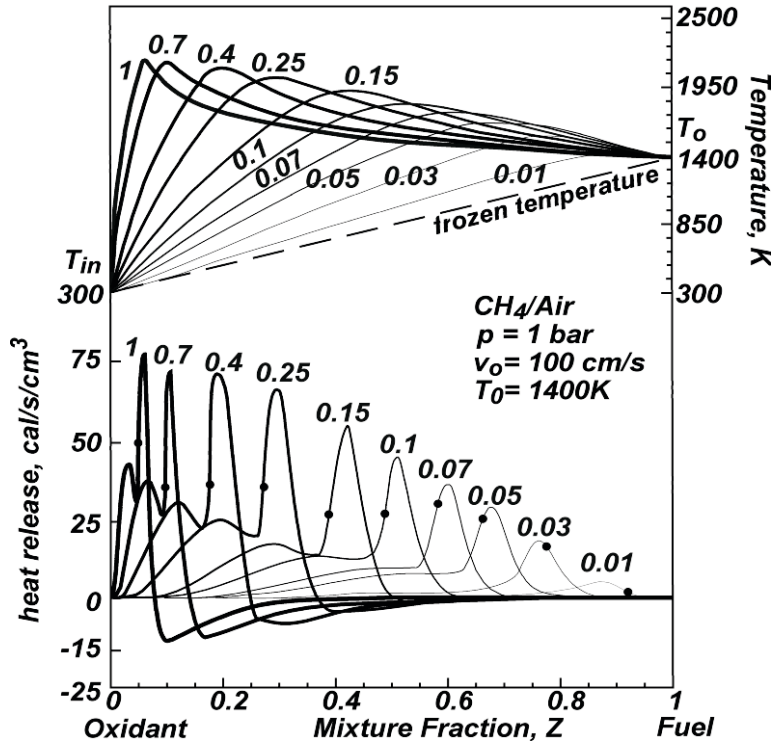

Fig. II.22 *T and $\dot{h}$ vs. Z, parametric on X_f at p = 1 bar.*

Increasing fuel dilution enhances the differences with respect to the standard conditions. The evolution of the oxidative structure becomes more complex when varying the fuel dilution.The reactive structure continues to shift toward a higher Z following the shift of Z_{st} by decreasing X_f .The most relevant effect of the dilution increase is the evolution of the shoulder at the right side of the maximum of heat release. For $X_f = 0.25$, this shoulder gains in magnitude and becomes a relative maximum that reaches the same value of the first maximum for $X_f = 0.2$. A further decrease of X_f makes the second peak the largest. The first peak, in turn, slowly reduces to be embedded in the remaining structure for $X_f =$ 0.07. Simultaneously, a significant flame thickening occurs while the pyrolytic region disappears. The increase of dilution level makes the part of the mixing layer where the composition allows for ignition, shift towards a region characterized by a higher frozen temperature.For still higher dilution levels, $\dot{h}$ profiles exhibit only a single maximum that decreases in intensity with X_f .

However, the oxidative region moves toward a higher Z, and this shift occurs in the same direction with respect to Z_{st}.

At 1 bar, the T and $\dot{h}$ profiles retain their main characteristics, although minor differences can be found in Fig. II.22.

Based on the typology of the heat release profiles above reported, an overall characterization of the combustion regimes occurring under the different feed conditions was carried out. This analysis follows the same approach that was applied in the Hot-Oxidant-Diluted-Fuel and Hot-Oxidant-Diluted-Oxidant inlet conditions. Thus, it produces a map of behavior as a function of the inlet parameters, i.e., T_0 and the dilution level.

The $T_0 - \Delta T$ plane obtained for T_{in} =300K, K_0 =50s^{-1} and p=10 bar is reported in Fig. II.23.

In both cases, T_0 ranged from 600 K to 2400 K, whereas ΔT ranged from 600 K to 2000 K. At p = 10 bar (Fig. II.23), the map is divided in four main regions.

From the high temperature combustion regime, a decrease of ΔT leads to a further widening of the reactive structure to reach the MILD combustion area, where the pyrolytic region is no longer noticeable in the reactive structure. These two characteristics are related to ‘‘flameless’’ combustion, as indicated by the map.

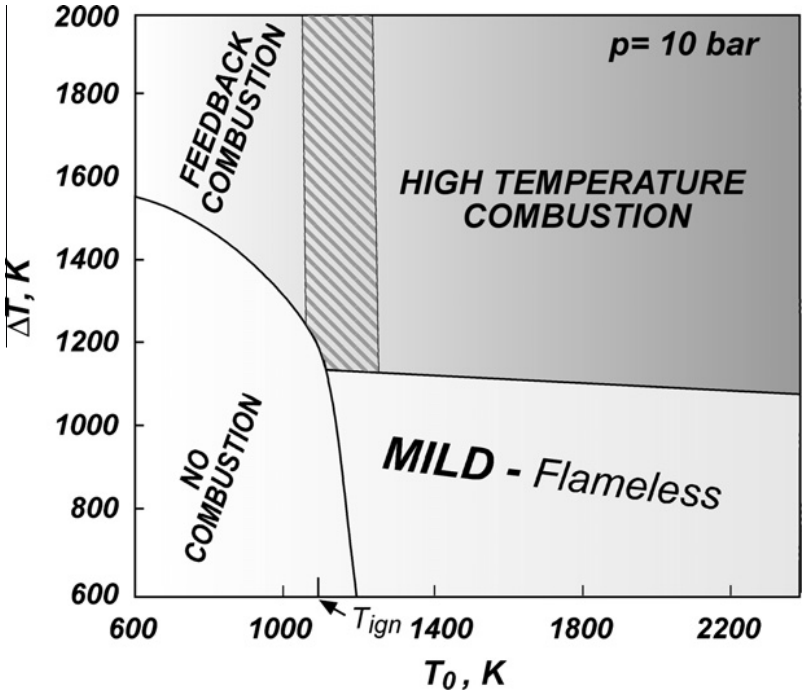

Fig. II.23 Combustion regimes at p = 10 bar, T_{in} = 300 K and K_0 = 50 s^{-1}

Moreover, a map of combustion regimes for p = 1 bar is shown in Fig. II.24.

It clearly indicates that the ranges of parameters corresponding to the different regimes change to some extent while keeping the characteristics of the four main regions. Compared to the case of p = 10 bar shown in Fig. II.23, a new feature is the transitional

zone that is present at this pressure between the feed-back combustion and the no-combustion region.

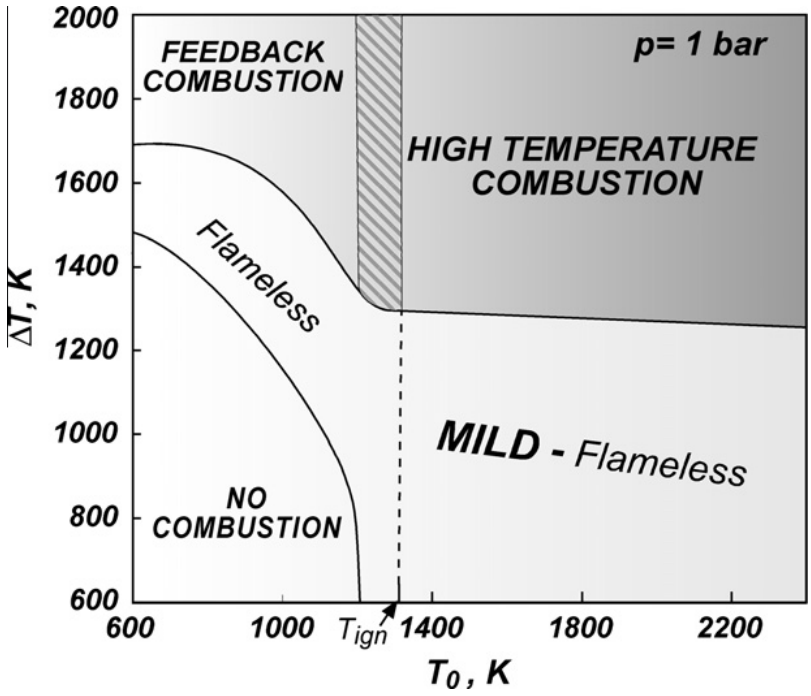

Fig. II.24 Combustion regimes at p = 1 bar, Tin = 300 K and K_0 = 50 s-1

The flame thickening and the absence of pyrolytic region justify the identification of such a transitional zone as ‘‘flameless’’ but the inlet temperatures that are lower that the ignition one, thus, not fitting the MILD combustion conditions by definition. The significance of this classification will be better clarified below in this section.

The peculiar feeding conditions make it reasonable to expect that outstanding properties (e.g., flameless, noiseless, and pollutant free) should occur. Several attempts have been reported to show this assumption under all possible feeding configurations.

Among these relevant for not premixed conditions are those that were obtained in counterflow conditions for different combinations of heating and dilution of the reactants (de Joannon M et al. 2009).

It has been shown that, when the two feeding conditions (dilution and pre-heating), are obtained separately for the two reactants, the local heat release spatial structure is quite different from the processes that are known as ‘‘diffusion flames’’. In fact, in contrast from diffusion flames, they are characterized by three outstanding characteristics:

- Pyrolysis depression.
- Flame thickening.
- No correlation of the stoichiometric and maximum heat release conditions.

All of these characteristics are signatures of a special situation that can occur in MILD combustion conditions. In particular, it is relevant that the control of the process relies on the heating of one reactant and not on the autocatalytic conditions generated by the heat released due to oxidation. This peculiarity has been emphasized by the use of a specific name when all of these characteristics occur: Hot-Diluted-Diffusion-Ignition (HDDI) (de Joannon et al. M 2009).

In this context, the Hot Fuel Diluted Fuel process is a very peculiar process that does not coincide with a HDDI process in the whole range of occurrence. In fact, the pyrolysis depression and the flame thickening characteristics have been shown to occur in subregions in the regime diagrams reported in Figs. II.23 and II.24 approximately in the parameter range in which MILD combustion is defined. Instead, the third characteristic, i.e. the no correlation of the stoichiometric and maximum heat release conditions, is only occasionally present in a limited part of the domain.

The data indicate that HDDI is a subregion of MILD combustion region for the HFDF-case. In fact, pyrolysis depression is a necessary condition to yield colorless products (Tsuji H et al. 2002)

However, flame thickening is a necessary condition to support distributed flame processes. These two properties (colorless and distributed flame) have been frequently reported in relation to combustion regimes that are classified as flameless combustion (Wünning J and Wünning J 1997). In these regimes, both the typical ‘‘traditional’’ features of visible emissions and the ‘‘front-like’’ structure of oxidation disappear. Thus, these two properties (flame thickness and pyrolysis depression) are coincident with flameless properties; therefore, the domain over which they occur has been classified as flameless regimes.

In the HFDF configuration it has been found the presence of the flame thickening/ pyrolysis depression outside the MILD combustion region. This factor is clearly indicated in Fig. II.24, where the ‘‘flameless’’ area extends in the narrow peninsula on the left side relative to the region where MILD combustion is defined. This feature is relevant to emphasize that the main effect of the dilution is to slow down the chemical kinetics of both pyrolysis and oxidation, as well as to lower the adiabatic flame temperature and the concentration of the reactants. To be more precisely, on one hand, the dilution effect slows all kinds of reactions (oxidation and pyrolysis), leading to flame thickening. On the other hand, the lowering of the concentration of the reactants exerts a more significant effect on the third order reaction, which controls CH_3 recombination, and on the post combustion reactions. In summary, flame thickening and pyrolysis depression are independent effects of dilution. This peninsula in the regime diagram is absent in the HODF counter-flow feeding condition that was analyzed in relation to the other MILD combustion conditions. This difference is due to the effect of the dilution of the fuel on the stoichiometric value of the mixture fraction (Cavaliere A. et al. 2008) in relation to the frozen temperature distribution.

In general, the results obtained in Hot-Fuel-Diluted-Fuel conditions are consistent with and extend those achieved for Hot-Oxidant-Diluted-Fuel and Hot-Oxidant-Diluted-Oxidant

conditions, supporting the assertion that these inlet parameters are a suitable choice for the definition of MILD combustion.

II.2.1.2 Unsteady autoigniting layerlet

In the previous sub-sections, they were shown two important aspects related to some limitations of the flamelet approach for turbulent non-premixed flows:

- it is not capable of modeling unsteady effects of ignition
- flame thickness should be sufficiently small compared to the turbulent length scales.

Hence if chemistry is slow, i.e. the reaction layer is not thin (for example in Mild combustion processes), or unsteady effects are relevant, the flamelet assumption is not valid.

To overcome these limitations, a different approach, named "*layerlet*", is here introduced (Sorrentino G. et al. 2012).

A layerlet is an unsteady diffusive layer characterized by a finite value of its thickness δ_m

(that tends to zero if a layer degenerates into an infinitely thin layer).

Unsteady combustion regimes are of interest for many combustion processes because they describe part of the stabilization process. A system with internal recirculation is one of the possible examples of unsteady combustion process. In fact, heated fuel injected in an exhausted flue gas stream with residual oxygen present yields hot fuel diluted oxidant (HFDO) conditions. Eventually, air mixed with an inert high-temperature flow (such as from a recirculated flow) yields hot oxidant diluted oxidant (HODO), which can be mixed with fuel at room temperature. Of course, among these exemplificative asymptotic conditions, all intermediate and mixed conditions can be created with partial preheating and dilution of both streams.

Some of these configurations, specifically HODF and HFDF, have been addressed in this section in unsteady conditions (Sorrentino et al. 2012), because they can be compared directly with the steady results previously presented.

The analysis has been performed following the same approach. It consists of detailed simulations of the thermo-chemical patterns in a dense grid of input parameters synthesized in regime diagrams, and it differs from the other approaches only in the inlet conditions. Therefore, the results are highly comparable with each other, and the discussion on their implication extends the previously outlined conceptual framework.

The study of an unsteady one-dimensional diffusive layer was performed by means of the opposed jets configuration. The attention has been focused on the system in which an undiluted air stream is always fed in counter-flow toward a nitrogen-diluted methane jet with a different fuel molar fraction X_f. Three types of preheating conditions were established:

- Preheating of the air (room temperature for the fuel), referred to as a hot oxidant diluted fuel (HODF) condition.
- Preheating of fuel (room temperature for the air), referred to as a hot fuel diluted fuel (HFDF) condition.
- Preheating of both streams with the same temperature, referred to as a isothermal (ISO-T) condition.

A structured 2D mesh, generated with Gambit, was used. It consists of 4x1000 quadrilateral cells with a uniform spacing of 10^{-5} m. Velocity inlet boundary conditions have been used to define the flow velocity at the fuel and oxidant inlets, while outflow boundary conditions were used to model flow exits. Numerical analysis has been performed with Fluent software by using, as ChemKin-import mechanism (Kee RJ et al.

2002), the GRI 3.0 mechanism implemented without the NO_x reactions (Parente A. et al. 2008). The flow regime is laminar, so there is no need to introduce a turbulence model.

Simulations have been performed at atmospheric pressure for a CH_4/N_2 jet with a fuel molar fraction of 1, 0.5, 0.3, 0.15 and 0.07, T_0 = 300 K, and T_{in} which ranges from 1000 to 2200 K. The initial distribution of the mixture fraction, velocity, temperature and species mass fractions has been set equal to a step function from the inlet values.

The structure of the reactive zone has been analyzed by an evaluation of temperature (T) profiles as a function of the mixture fraction (Z) along the axial coordinate of the system evaluated on the nitrogen mass fraction, which is conserved in the kinetic scheme used in this case.

The ensemble of the temperature/mixture fraction profiles for each preheating and dilution condition allow three relevant characteristic times, partially used previously by other authors (Mastorakos E 2009), reported in Fig. II.25 :

- the minimum ignition time (τ_{IGN})
- the temperature-maximization time (τ_{MAX})
- the stabilization time (τ_{STAB}).

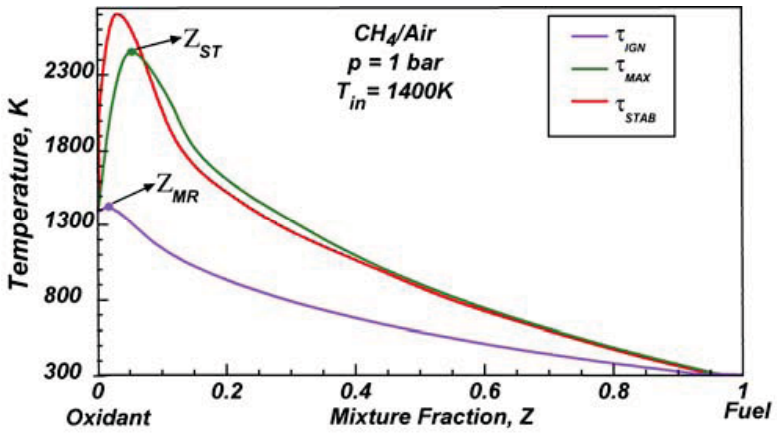

Fig. II.25 Characteristic times for P=1 bar and T_{in}=1400K.

The minimum ignition time (τ_{IGN}) reported in this paper is the time at which the system reaches a threshold of 10 °C above the temperature of the frozen state for the first time, due to heat release. This minimum occurs at a mixture fraction defined as the most reactive one (Z_{MR}).

The temperature-maximization time (τ_{MAX}) is defined as the time at which the peak temperature in the T–Z plot is localized at the stoichiometric mixture fraction value. Its computation is straightforwardly obtained by the temporal evolution of temperature at a fixed mixture fraction.

Lastly, the stabilization time (τ_{STAB}) is defined as the time at which the system reaches its steady-state temporal profiles. It is evaluated by searching the maxima of the temperature differences between the current values and the corresponding steady-state solutions at fixed times.

The overall behavior of the unsteady MILD combustion process is shown in Fig. II.26.

The figure consists of nine plots, which refer to nine selected feeding conditions: three for each type of preheating condition at different fuel dilution levels. More specifically, the first three plots in the first left column refer to the HODF condition with an air temperature of T_{in}=1400 K; the three central ones refer to isothermal (ISO- T) conditions in which the fuel jet and the oxidant jet are fed at the same initial temperature (1400 K); and the three plots on the right column refer to the HFDF with an inlet temperature of the diluted fuel of 2200 K. The choice of such a high temperature is related to the use of the results for exemplificative purposes. In fact, at lower temperatures, the HFDF condition does not always present ignition for different dilution levels.

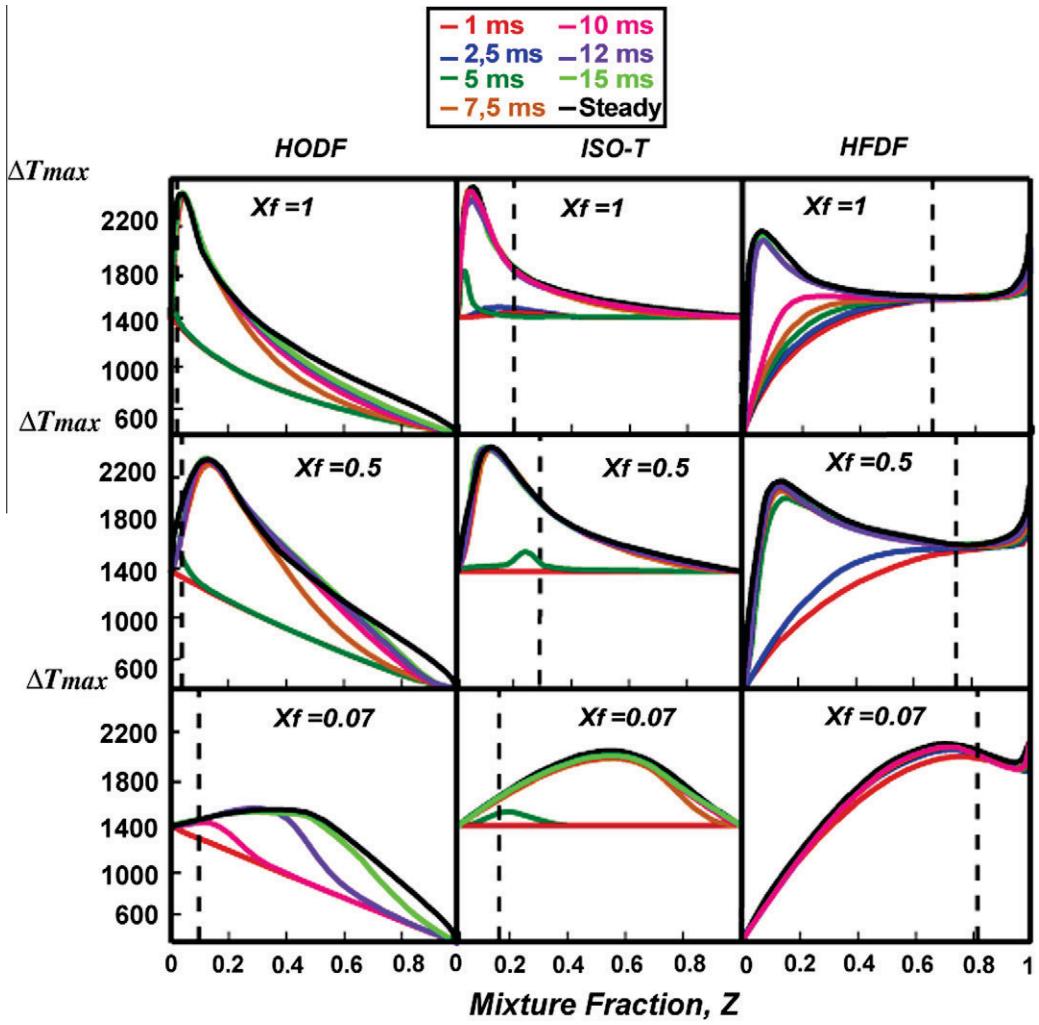

Fig. II.26 *Temperature profiles with respect to time, which refers to nine selected feeding conditions at different fuel dilution levels (X_f = 1, X_f = 0.5, X_f = 0.07).*

The plots aligned on a single row have the same dilution level. The first one is the undiluted case at X_f = 1, the second row is an intermediate dilution case with X_f = 0.5, and the third row reports very diluted cases (classified as MILD conditions) at X_f =0.07.

Temperature versus mixture fraction profiles are reported; in each individual plot, the profiles are parameterized for eight values of the time delay (with respect to the initial condition) uniformly distributed between 1 ms and 15 ms and are color-coded, as shown in the inset. The steady-state profile is also reported with pale black line.

The first plot in the left top corner shows the ensemble of the temperature profiles divided into two main sub-sets of profiles. The first ensemble of profiles before the ignition is fused into a nearly rectilinear line, which approximates the frozen mixing line. The first (and only) colored profile that clearly detaches from the asymptotic lines pertains to the temperature profile evaluated at 5 ms after the initial time. This profile can be considered representative of the autoignition process, even though the temperature increase is much higher than that used in the definition (10 °C), which cannot be appreciated in this representation because of the choice of temperature scale. The profile reported in the figure for 7.5 ms cannot be distinguished from the others and from the steady-condition profiles when Z is less than 0.2. It is fused with the other profiles of the mixture fractions less than 0.2, i.e., the temperature profiles show a "jump" when passing from autoignition conditions to the stabilized combustion conditions in a temporal range between 5 and 7.5 ms.

As matter of fact, a slow shift from the temperature profile at 7.5 ms to the temperature profile at 15 ms can be appreciated in the mixture fraction range greater than 0.2. In particular, at Z = 0.5, the maximum increase of 300 K is shown in the figure, and three profiles are distinguishable from each other.

In the second row of HODF cases, the methane is diluted with nitrogen at a molar fraction of X_f = 0.5. The general behavior of the temperature profile is quite similar to those reported for X_f = 1, as previously described. The main difference is the shift in the maximum at Z = 0.15, which is consistent with the shifts observed for stoichiometric mixture fractions, which also shift from 0.05 in the undiluted case to 0.15 for the diluted one. Furthermore, the bottom line, which represents the frozen mixing condition, is significantly different. It is positively curved at $X_f = 1$ and is nearly straight at $X_f = 0.5$. This behavior is due to the influence of the specific heat capacity, which, for methane, is

more than double that of air. The frozen mixing line is straighter for more diluted fuels. In fact, the dilution with nitrogen makes the specific heat capacities similar, and the mixing rule is no longer valid for such mixtures.

Lastly, the ignition time for this partially diluted case is 5 ms. Additionally, in this case, the isolated curve reported with a green color is distinguishable from the other curves whose frozen and steady-state curves are fused.

The similar behavior described for these two plots is not confirmed under the highly diluted condition at X_f = 0.07, which is representative of a MILD combustion process, reported in the third row of the HODF column. In this case, the temperature profiles show a gradual increase in the maximum temperature with increasing time, starting from the first profile at 10 ms, which can be considered representative of the autoignition process. The times for the temperature profiles reported in the figure were purposely chosen to make the curves distinguishable from each other and uniformly spaced. This stresses the slowness of autoignition process, particularly when the profile distribution is compared with those in other plots. This comparison is possible by virtue of the use of the same times for which the temperature curves have been reported for all the plots, i.e., the fusion of the temperature profiles on one of the two limit conditions (frozen and steady-state) is itself informative when the two times between which the "jump" occurs are identified. This fusion of the profiles is the case for the three plots reported in the central column (ISO-T), which refers to the three cases in which the fuel jet and the oxidant jet are fed at the same initial temperature (1400 K) so that the frozen mixing line is horizontal and straight. The first two plots, at X_f = 1 and X_f = 0.5, are similar to the corresponding plots on their left in HODF. The temperature profiles show a "jump" within the same time range. In contrast, for ISO-T conditions, the profile distribution is significantly different under the diluted

condition at $X_f = 0.07$. The "jump" is observed only under the ISO-T conditions, reported in the central lowest plot, whereas the aforementioned "slow graduality" is observed under HODF conditions. A different behavior is shown for the hot fuel diluted fuel (HFDF) conditions, as reported in the third column on the right in the figure. The most diluted conditions in the lowest row show that the early reactivity is due to the pyrolysis process. In fact after 1 ms, all the temperature profiles show values lower than those shown in the frozen profile on the right of Z = 0.8. Then, a positive temperature increase is shown in the temperature profile at 2.5 ms for the mixture fraction range centered around Z = 0.6. For the less-diluted conditions at X_f = 0.5 and X_f = 1 (in the center and in the top of the column, respectively), the pyrolysis region (identified by the zone with temperature less than the frozen one) develops over a wider range, and the first oxidation activity is shifted toward the stoichiometric values. The plots of the combustion regimes, in terms of the maximum allowable temperature increase (ΔT_{max}) and inlet temperature of the preheated reactant (T_{in}), are reported in Figs. II.27 and II.28 such that they are outlined for both the HODF and HFDF regimes under the steady-state conditions reported previously in this section. The pink, red and blue regions represent the feedback regime, the high-temperature combustion processes and the MILD combustion processes, respectively. It is worthwhile to note that in MILD combustion the process cannot be sustained without preheating the reactants. The black dashed areas are the transitional regions where the existence of multiple steady states has been identified with ΔT_{max} values greater or less than $\Delta T_{max} / MILD$, as also reported in Figs. II.27 and II.28. Isolines at the fixed autoignition time, the maximization time and the stabilization time have been drawn on these plots with solid, dashed and dashed/dotted lines, respectively.

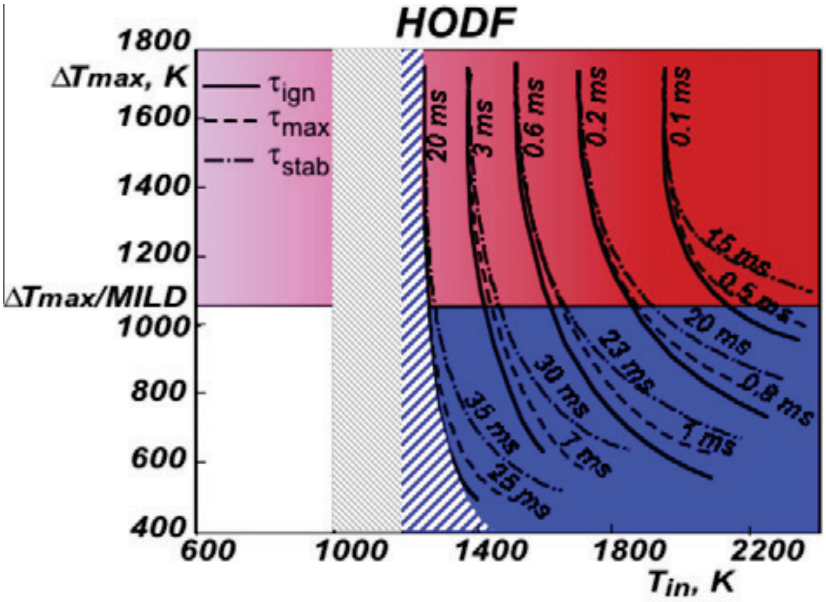

Fig. II.27 *Map of the behaviors under HODF conditions for P = 1 bar and K_0 = 100 s^{-1}. Isolines at the fixed autoignition time, the maximization time and the stabilization time have been drawn with solid, dashed and dashed/dotted lines, respectively.*

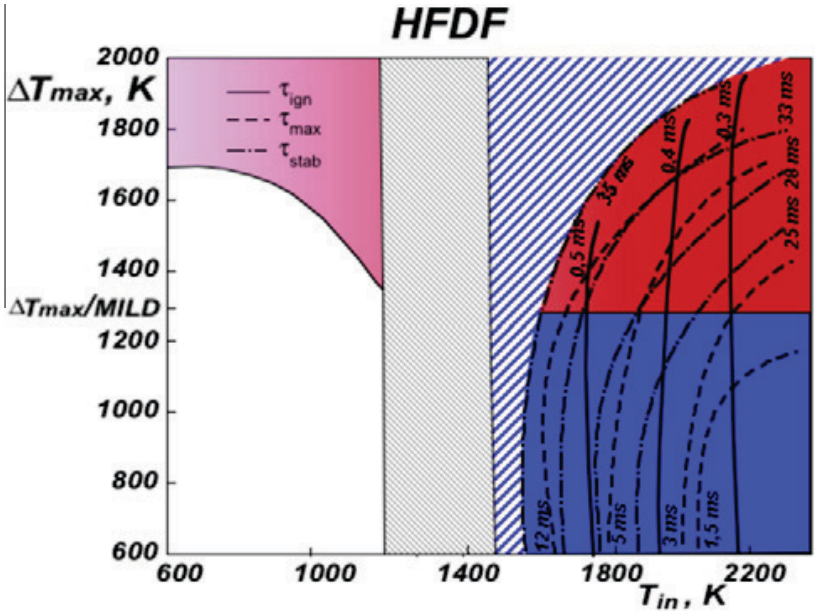

Fig. II.28 *Map of the behaviors under HFDF conditions for P = 1 bar and K_0 = 100 s^{-1}. Isolines at the fixed autoignition time, the maximization time and the stabilization time have been drawn with solid, dashed and dashed/dotted lines, respectively.*

The autoignition-time isolines for the HODF case, shown in Fig. II.27, exhibit nearly hyperbolic behavior with an easily identifiable vertical asymptote. These isolines also

exhibit a tendency to become more horizontal for inlet-temperature values. This tendency, in turn, indicates that τ_{IGN} depends only on Tin in the high-temperature combustion (red-colored) region, whereas it tends to depend on ΔT_{max} and Tin in the MILD combustion (blue-colored) region. The value of τ_{IGN} is less than one millisecond for T_{in} values greater than 1600 K; it then increases exponentially and attains τ_{IGN} = 20 ms for T_{in} = 1300 K, passing through τ_{IGN} =3ms for T_{in} =1400K.

It is interesting to note that for inlet temperature lower than those on the left of the autoignition isolines at 20 ms, no ignition occurs. This region is shown in Fig. II.27 with a dashed blue color, which extends the black-dashed transitional area into the high-temperature combustion and MILD regions.

The maximization times τ_{MAX} , i.e., the time required to develop the reactive mixing layer in correspondence of the stoichiometric mixture fraction, exhibit similar trends and range within the same order of magnitude as the autoignition times.

In contrast, for the stabilization time τ_{STAB} , even though their isolines have similar trends as those of the other two time values, their values are significantly higher and always range within the same interval between 15 and 35 ms.

The behavior of the characteristic times for HFDF is different with respect to those of HODF. In fact, for HFDF, all of the times are approximately perpendicular to the abscissa in the MILD combustion region, which shows that all of them can be considered to depend only on the inlet temperature Tin. In contrast, two of the characteristic times, specifically the maximization and stabilization times, bend in the high-temperature combustion region (red-colored region) in such a way that they are dependent on both T_{in} and ΔT_{max} .

Different from the HODF case, the autoignition time is nearly the same over the whole studied region, with a slight dependence only on the inlet temperature, as indicated by the vertical isolines. Similar to the HODF case, the overlapping of the steady (feedback and no-combustion zone) and unsteady regimes is not perfect in the case of HFDF. The two domains differ from the blue dashed area, which partly covers the transitional black-dashed area also shown in Fig II.28.

The results reported above show that he domains of MILD combustion of the unsteady reactive mixing layer are smaller in comparison to the corresponding domains under steady HODF/HFDF conditions. The maximum ignition delays reported in Figs. II.27 and II.28 were 20 ms and 0.5 ms, respectively. None of the regions on the left sides of these autoignition delays yielded any transient reactive mixing layers. Therefore, steady MILD combustion processes can be stabilized in these regions only if additional heat is provided through recirculation or through a piloted source (Abtahizadeh SE et al. 2012).

The extensions of the regions that cannot be reached by any autoigniting combustion process consist of the black and blue dashed areas in Figs. II.27 and II.28.

Notably, the boundaries of the areas, including the high-temperature combustion regions, where a combustion process could be stabilized only under steady conditions, are much wider for the HFDF than for the HODF, and they closely follow the trends of the characteristic times of the processes.

The most reactive mixture fraction, Z_{MR}, is always positioned on the high-temperature side with respect to the stoichiometric mixture fraction for both HODF and HFDF.

The process evolution rate of unsteady MILD combustion is not universal.

In fact, at least in the two of the analyzed cases, the process evolution rates are just the opposite. In HODF conditions, the overall rates slow down passing into the MILD combustion domain as shown by the characteristic times reported in Fig. II.26. The

characteristic autoignition, maximization and stabilization times are all longer than those in high-temperature combustion processes. This situation is the opposite for HFDF conditions. The unsteady diffusive autoignition is always shorter than those in the corresponding HODF conditions. Furthermore, the subsequent part of the process accelerates the passage into the MILD combustion domain.

The autoignition delay times in MILD combustion regimes also vary according to external parameters (preheating temperature and dilution level), in agreement with the trends presented by previous authors (Liu S et al. 2004, Mastorakos E et al. 1997).

In conclusion, it is possible to emphasize that the results reported here support the inclusion of an additional property for the characterization of MILD combustion, i.e., a property that accounts for the fact that this process can be auto-sustained with autoignition. Nevertheless, the whole process must be analyzed not only in terms of the autoignition time but also in terms of the evolution of the oxidation. The presumed slowness of the autoignition process is not universal because it depends on which part of the reactants is under the high-temperature conditions.

Chapter III
Identification of advected-surfaces

In the study of mixing and reaction in turbulent flows, there are several phenomena that can be usefully described in terms of surfaces (Hawkes ER and Cant RS 2001). For example, in the flamelet regime of turbulent combustion, reaction is confined to the flame sheet, a surface that can be highly wrinkled and possibly disconnected.

The most basic is the material surface. By definition, a material surface moves with the fluid: every point of the surface is a fluid particle.

For premixed combustion the flame sheet is a propagating surface: each point on the surface moves at the local flame speed in the direction normal to the surface. For non-premixed flames, the reaction sheet is a constant-property surface: at each point on the surface the mixture is stoichiometric. In the appropriate limits (vanishing flame speed or diffusivity) both propagating surfaces and constant-property surfaces become material surfaces.

Various measures of the surface geometry, such as surface-to-volume ratio or volume-fill fraction, and their relation to the distribution of spatial scales, are, as a consequence, important to our understanding and modeling of mixing, chemical reactions, and combustion in turbulent flows.

In turbulent reactive flows, accurate simulation of mixing and reaction processes is an important challenge. For fast mixing flows, the length scale of the concentration field rapidly becomes smaller than practical grid sizes leading to numerical diffusion errors.

If we consider mixing segregated fluids in the absence of diffusion, the mixing process is described by the location of the interface between the fluids (Roberts E 2010). For a fast

mixing flow such as a chaotic or turbulent flow, this interface stretches at an exponential rate (Cerbelli S et al. 2002).

The consequence of this exponential stretching rate for mixing simulations is that the data storage capacity required to describe the interface rapidly becomes excessive. Ottino JM (1989) and others (Clifford MJ et al. 1998) have suggested that the mixing rate can be characterized by the stretching rate of infinitesimal lines advected by the flow.

Moreover, in the turbulent mixing of a passive scalar, surfaces of constant mixed-fluid concentration, or isoscalar surfaces, are highly convoluted in turbulent-jet flows (Catrakis HJ et al. 1996), as well as other high-Reynolds-number turbulent flows (e.g. Sreenivasan KR & Meneveau C 1986). Knowledge of the geometry and topology of these iso-surfaces is necessary for an understanding of the turbulent mixing process. In particular, molecular mixing occurs across such surfaces.

Characterizations of the geometry of interfaces and iso-surfaces in turbulence, in particular, and of other complex structures encountered in natural phenomena, in general, require extending notions of Euclidean geometry.

The behavior of surfaces in turbulence is an issue with many practical implications.

The simplest problem of stretching of microstructures corresponds to the case of passive material elements (Aref H and Tryggvason G 1984).

In this case, the connectedness of material surfaces suggest a way of incorporating the effects of stretching on diffusion and reaction processes. In particular, all the topological features are conserved and cuts of partially mixed materials reveal a lamellar structure. The striation thickness s, serve as a measure of the mechanical mixing. The approach used here wish to preserve a similar structure for the case of diffusing fluids in such a way that a properly defined striation thickness can be thought to act as the underlying fabric on which the transport processes and reactions occur.

In this thesis, this typology of surfaces are named as “advected-surfaces” and they represent the morphological building blocks of arbitrary flows.

In the first part of this chapter, the local geometry of regular surfaces is described by the surface element properties: position; normal to the surface; curvatures, volume fraction and, fractional area increase. Exact evolution equations for these properties are derived which reveal the effects of various processes as advection and stretching for example.

However, the second part of this chapter reports an experimental test rig that has been built to perform the characterization of the aforementioned reference-surfaces.

In particular, we will confine our discussion to the basic parts of the apparatus (and the relative optical diagnostics) that were necessary to carry out the experiments.

In the next section, the image analyses procedures and the software employed to perform this kind of study are presented and discussed in their general aspects.

III.1 Definitions, properties and kinematic relations of advected-surfaces

Mixing is intimately related to stretching and folding of advected-surfaces, and theory can be couched in terms of kinematical description.

Definitions of the more conventional eulerian (like interface and scalar surface) and lagrangian surfaces (material and intermaterial surface) are given in the following section together with more common properties and kinematics aspects.

III.1.1 Definitions and topological features

The analysis of stirring/mixing processes needs the definition of some quantities, which are here preliminarily defined.

A variable is conserved if it obeys a source-free balance equation; i.e. it is relative to a quantity, which can not be created or destroyed, but only convected and diffused. This statement is expressed in differential form according to the following equation as reported in many text books (Williams 1985):

3.1) $$\rho\frac{\partial\beta}{\partial t}+\rho\underline{v}\cdot\underline{\nabla}\beta-\underline{\nabla}\cdot(\rho\ \mathcal{D}_{\beta}\ \underline{\nabla}\beta)=0$$

in which " β " represents a conserved variable per unit mass.

The sum of the first two terms in eq. 3.1, divided by the density, is designated in the literature as material or substantial derivative. It is cited in the following as $D(\cdot)/D(t)$ and it defines a "material" variable, " β_M " when eq.1 can be written as:

3.2) $$\frac{D\beta_M}{Dt}=\frac{\partial\beta_M}{\partial t}+\underline{v}\cdot\underline{\nabla}\beta_M=0$$

An example of material variable, which will be used in the following, is the mass fraction of a tracer (Cavaliere A and Ragucci R. 2002).

In agreement with Ottino (1982) the tracer should not only be non-diffusing but should also be transported at mean field velocity. In this way the tracer's mass fraction, Y_t, will be constant in time, and therefore the material derivative of Y_t will be zero.

It is quite difficult to produce this kind of tracer under experimental conditions in order to seed a gaseous fl¯ow also because the tracer cannot be a gas, as gases, by definition, diffuse. Neither can the tracer be a solid particle of such large dimensions to be unable to immediately respond to accelerations in the average flow. In effect the only tracer, which has features which are close to those described in the definition above, is a particle for which the Stokes number is less than unity (Crowe CT et al. 1988) and for which the Schmidt number is greater than 1000 (Rosner DE 2000).

A particle, for instance, between 0.1 and 1 μm is sufficiently large in dimension to ensure that Brownian diffusion is low, but it is sufficiently small to immediately follow the flow.

III.1.1.1 Eulerian surfaces (interface, isosurface)

When a non-diffusive tracer is introduced into part of the flow it determines an interface. This is the surface of the flow where the concentration of the tracer is discontinuous, that is where it passes from zero to a finite value on an infinitely thin surface. In other words, an interface is the place of the points in space where ∇Y_t is infinite.

Examples of interfaces are shown in Fig. III.1 (Cavaliere A et al. 1995). They are obtained by seeding the central part of a 2D plane jet by means of TiO_2 sub-micronic particles. The concentration of the particles is measured by means of elastic light scattering. White corresponds to an area in which the tracer concentration is zero. Black corresponds to an area in which the tracer concentration is equal to that fixed at injection. It is interesting to note that the tracer substance concentration in a material volume cannot, by definition, vary in time. In contrast an Eulerian, fixed, non-infinitesimal volume may contain a tracer quantity which is different according to the volume filling with the part of the flow, which has been 'traced'. If the resolution, through which the spatial dispersion of the tracer is observed, is limited, the concentration itself seems to change point by point and even the interface appears as a continuous variation of the tracer concentration. It is also possible that, in practice, the tracer concentration is so weak that its presence is hardly detectable. This happens when the tracer is transported in filamented structures so thin that its continuous distribution does not occur. Despite these experimental difficulties, the interface is a characteristic of the dispersion of one gas into another which is easily measurable, because it possesses a clearly Eulerian nature. In fact, it is possible at any time

to obtain a measurement without worrying about the intricate Lagrangian evolution of the particles.

Usually the term ‘stirring’ is applied to the process that leads to extension and dispersion of the interface, in as much as diffusion processes are not used because stirring is purely convective.

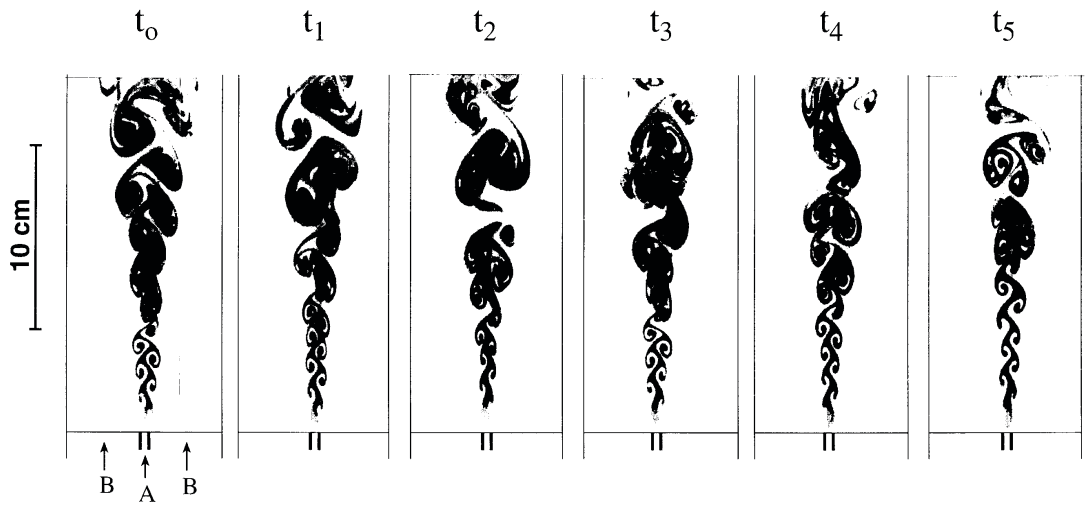

Fig. III.1 Interfaces sequence of a transitional isothermal jet (after Cavaliere et al. 1995).

Isosurfaces, or isolevel surfaces (Pope SB 1988; Gibson CH 1968) are surfaces on which scalars are constant. Isobars or isotherms, which refer to pressure or temperature isosurfaces, are commonly used.

The study of the behavior of iso-scalar surfaces is crucial in understanding turbulent mixing and combustion (Kim SH and Pitsch H 2007).

Iso-surfaces in turbulent flows are quite complicated due to stretching and folding by random velocity fluctuations with a broadband spectrum of time and length scales (Candel SM & Poinsot J 1990; Trouvé A & Poinsot T 1994). Increased surface area and scalar gradients due to the turbulent motions result in the enhanced mixing of the scalar. Overall reaction rates in turbulent non-premixed combustion increase with the turbulent mixing rate, when there is little local extinction.

For the sake of brevity in this section, iso-surfaces will be referred to the scalar mixture fraction, Z. Iso-surfaces move with respect to the fluid that transports them at a relative propagation speed $\underline{w}_Z$ whose orientation and direction are given by the unit vector $\underline{n}$, perpendicular to isosurface and oriented toward lower values of Z. Its absolute value is given by the material derivative, with respect to a reference moving with the fluid velocity, of the position of the material point (Dx/Dt), divided by its gradient ($\underline{\nabla}Z = DZ / Dx$). According to this position, Gibson (Gibson CH 1968) has derived a relation which is also discussed by Pope (Pope SB 1988)

3.3) $$\left|\underline{w}_Z\right| = \frac{Dx_n}{Dt} = \mathcal{D}_Z \frac{\underline{\nabla}^2 Z}{\underline{\nabla} Z}$$

In fact, the material derivative of the mixture fraction, DZ/Dt, in Eq. 3.3) is equal to $\mathcal{D}_Z \underline{\nabla}^2 Z$ for incompressible flows. A second relation between the propagation speed $\underline{w}_Z$ and the mixture fraction field is obtained by expliciting the gradient $\nabla Z = -\underline{n}\left|\underline{\nabla} Z\right|$ in Eq. 3.3).

The divergence of the product $\underline{n}\left|\underline{\nabla} Z\right|$ is, then, expressed according to the following equation:

3.4) $$\left|\underline{w}_Z\right| = -\mathcal{D}_Z \frac{1}{\left|\underline{\nabla} Z\right|} \frac{\partial x}{\partial x_n} \cdot \underline{\nabla} Z - \mathcal{D}_Z C$$

This equation is relevant because it shows that the isosurface propagates by means of two mechanisms. The first is driven by the mixture fraction inhomogenity perpendicular to the isosurface and to its non-linear distribution. The second is related to the curvature of the isosurface, expressed by $C = \underline{\nabla} \cdot \underline{n}$. Kinematics of isosurfaces is fully described in the

papers from Pope (1988) and Trouvé et al. (1994), where possible discontinuity and annihilation of these surfaces are also discussed.

There are two complementary routes to study isomixture fraction surfaces (Vervisch L and Poinsot T 1998).

First, by studying the behavior of a set of instantaneous iso-Z surfaces, the shape and the wrinkling of these surfaces may be measured in DNS. This was done for example in the case of an initially planar and unstrained laminar diffusion flame interacting with a freely decaying homogeneous turbulence (Kollmann W and Chen JH 1994). In particular, the wrinkling of mixture fraction surfaces is reduced by heat-release effects for surfaces defined for values of Z near Z_{st}. The impact of heat release diminishes, however, for surfaces defined for Z much larger or smaller than Z_{st}. This suggests that the effect of heat release on the dynamics of micromixing is localized around the stoichiometric surface.

A second approach is to consider the average properties of the surface and measure $\Sigma|_{Z_{st}}$, the density of area of the iso-Z_{st} surface per unit of volume. $\Sigma|_{Z_{st}}$ is a one-point quantity widely used in turbulent combustion modeling (Bray KNC 1996). Figure III.2 shows the simulation of a constant-density (ϱ = cst) “flame” (van Kalmthout E et al 1996), where turbulent fluctuations of velocity are injected at the inlet of the computational domain according to a prescribed energetic spectrum.

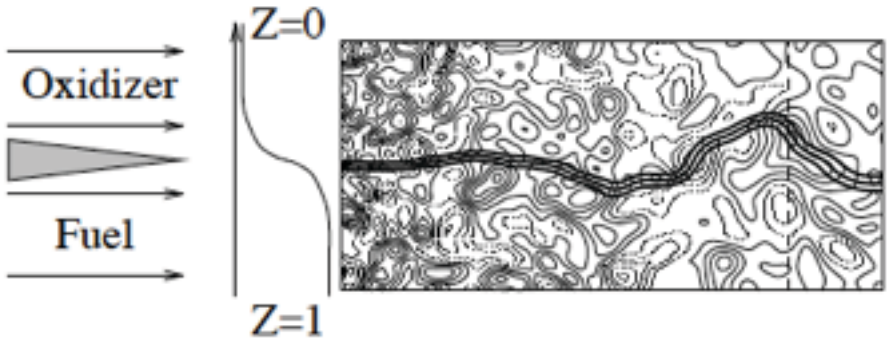

Fig. III.2 *Two-dimensional simulation of a constant-density mixing layer without velocity shear (van Kalmthout E et al 1996).*

At a particular streamwise location, $\Sigma|_Z$ is collected for different points in the spanwise direction, averaged over time and plotted versus Z (Figure III.3). Depending on the equivalence ratio ϕ, different distributions of $\Sigma|_Z$ are observed: a symmetric profile for ϕ = 1, and profiles shifted either toward the fuel side, when the oxidizer is in excess ($\phi < 1$), or toward the oxidizer side, when the fuel is in excess ($\phi > 1$). The mixing between fuel and oxidizer results from the motion of iso-Z surfaces relative to the fluid. In particular, the local amount of mixing depends on the relative progression velocity of the surface measured in the direction normal to the surface (Vervisch L et al. 1995).

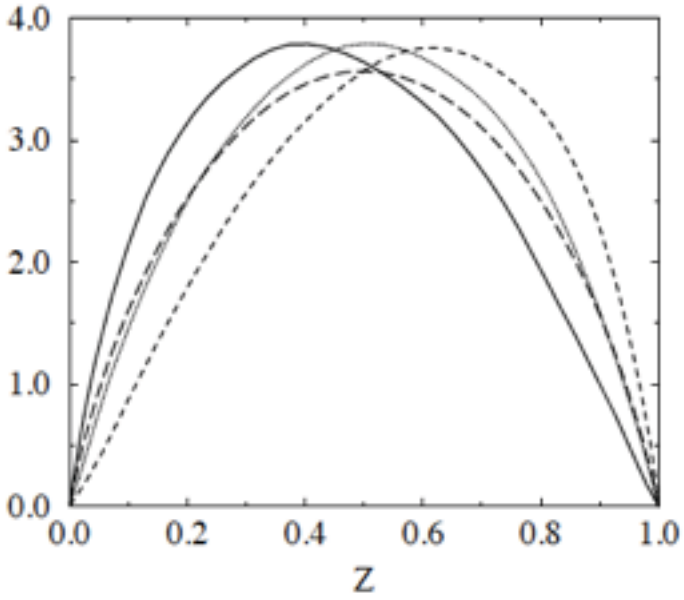

Fig. III.3 *Flame surface density $\Sigma|_Z$ plotted versus mean mixture fraction Z for various values of the equivalence ratio: ϕ = 3 (solid line); ϕ = 1 (dotted line); ϕ = 0.33 (short-dashed line); $|\overline{\nabla Z}|$ for ϕ = 1 (long-dashed line) (van Kalmthout et al 1996).*

This relative progression velocity is defined by the difference between the velocity of the surface and the fluid velocity. It is not constant along the isosurface. In the case of iso-Z surfaces, the two quantities determining this velocity are the curvature of the surface and the diffusive flux in the direction normal to the surface.

III.1.1.2 Lagrangian surfaces (material, intermaterial)

Surface is considered material when it is made up of points identified by a tracer. In other words a surface is material when it follows a material evolution (Gibson CH 1968). As this kind of surface is stretched and bend, its topology does not change. The surface cannot intersect itself; holes are not created; and a singularity (infinite curvature) cannot develop in finite time. A material surface is defined by its initial condition (e.g. a specified plane at t = 0), and by the condition that every point on the surface moves with the local fluid velocity (Pope SB et al. 1992). Following are provided two examples to illustrate the

physical significance of these surfaces. Figure III.4 shows a sketch of the mixing of two bodies of water (A and B) in a closed vessel. Initially (t=0) A contains a trace solute of concentration $\phi = \phi_0$ while B is pure water $\phi = 0$. Here is considered the material surface that is initially coincident with the interface between A and B. The water is set in turbulent motion and as a result the material surface is convected, bent and stretched. In the first stage of mixing, the concentration is uniform everywhere except in the immediate vicinity of the material surface where there is a thin diffusive layer. Locally, the behaviour of the diffusive layer is the same as a plane layer in a uniform strain field. Consequently, the mixing process can be completely analyzed in terms of the statistics of straining on the material surface (Batchelor GK 1959, Pope SB 1988).

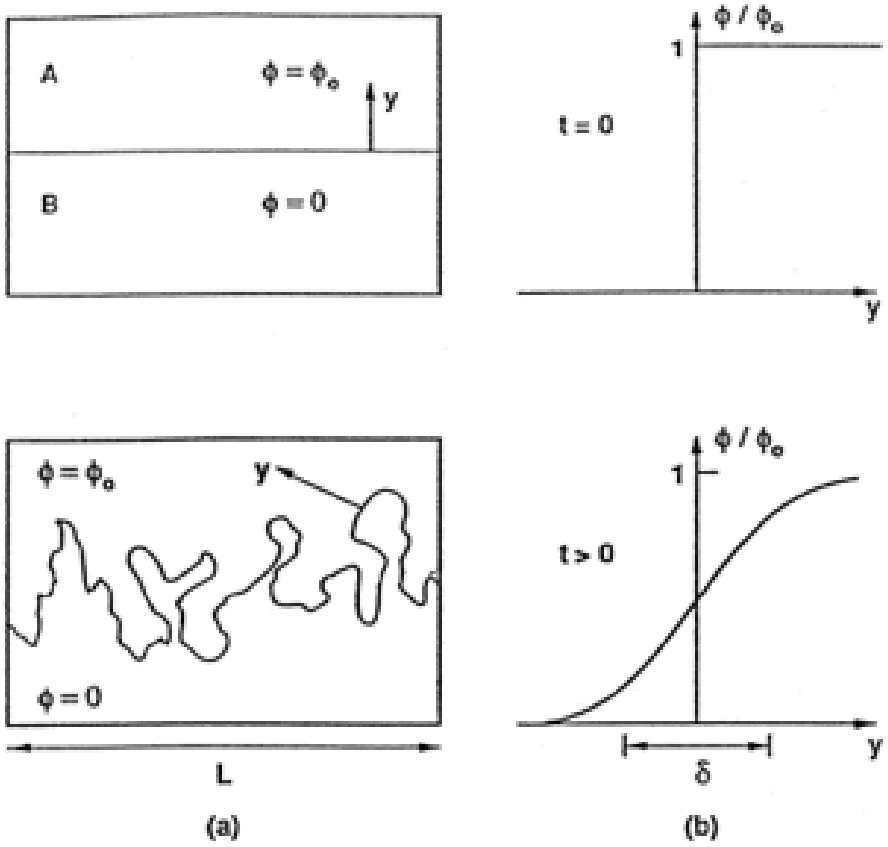

Fig. III.4 *Mixing between two bodies of water. Sketch of the mixing phenomena :*
a) The material surface that initially (t=0) separates A from B.
b) Normalized concentration profiles normal to the surface

The second example is an idealization of a turbulent premixed flame. Under appropriate conditions (Pope SB 1987), there is a thin flame sheet that forms a connected but highly wrinkled surface that separates reactants from the products (see Figure III.5).

This flame surface is convected, bent and strained by the turbulence, and propagates at a fixed speed. If the propagation speed is small compared to the turbulent velocity scales, then the flame surface behaves like a material surface.

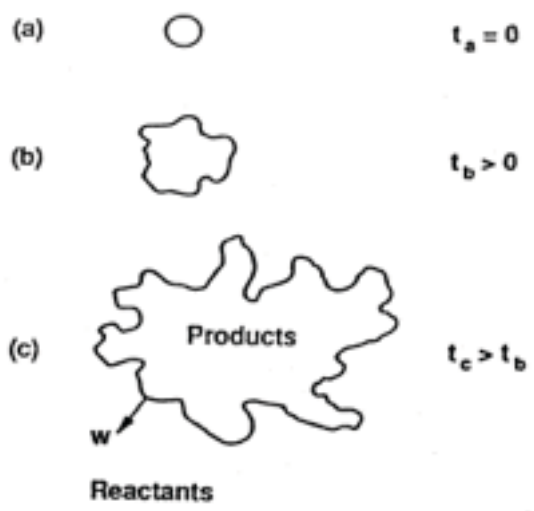

Fig. III.5 Sketch of a turbulent flame sheet developing from an initially spherical kernel.

In general, concerning material surfaces, it is possible to assume that:

- straining is persistent (i.e. the time scale of change of the strain rate is large compared to the time scale of strain itself);
- the material surface becomes aligned with the principal axes corresponding to the two greatest principal strain rates;
- the radii of curvature of a material surface are no smaller than the smallest turbulence scales.

Following the previous examples, a 2D material surface at time t_0 is sketched through its linear section in Fig. III.6-a. Every point of the surface follows a definite trajectory. At time t all these points together will make up a new surface which besides being translated and

rotated is also extended or contracted. In the aforementioned figure material surfaces are sketched starting from a surface arbitrarily fixed at the point t_0. In theory a material surface cannot became discontinuous even if in practice its detection can be subject to the limits already discussed in conjunction with the interface.

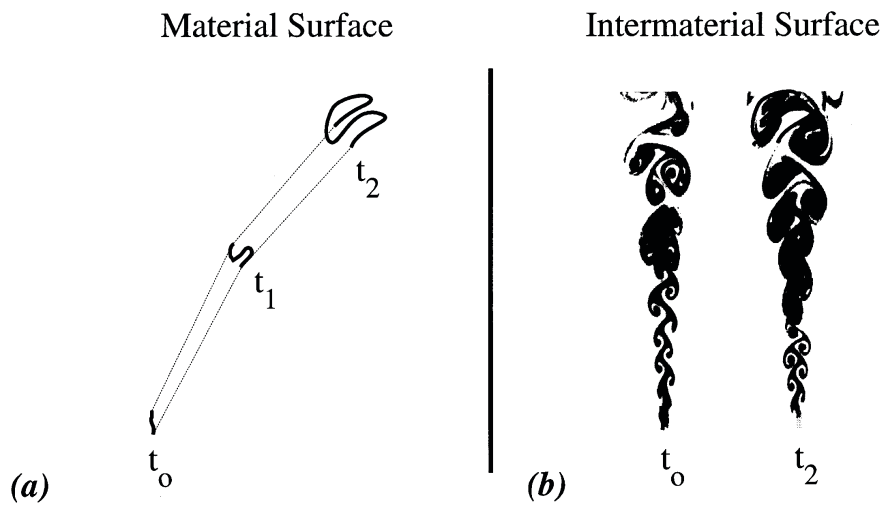

Fig. III.6 *a) Example of material surface evolution. b) Schematic of intermaterial surface evolution. Two material surfaces are selected on the interfaces at time t_0 and t_2.*

An intermaterial surface is a material surface defined at time t_0 on the interface.

In general intermaterial surfaces of practical interest are those partially limited by the first contact point (or line). The first contact point (or line) is the point (or line) of the interface through which the tracer passes with the shortest residence time. In a jet, for instance, the first contact line is the border of the jet's exit orifice. In fact all the possible interfaces, obtained by plotting the jet, pass through the side of the jet's orifice at residence time of practically zero. In the opposite jets the first point of contact is the stagnation point.

An example of an intermaterial line is shown in Fig. III.6-b. The same lines, used as example of material surface sections on the left side, are shown again together with the interfaces at time t_0 and t_2, sketched as red lines between the seeded (black) and unseeded (white) flows.

III.1.1.3 Interface density, tracer volume fraction and interface extension

It is possible to define various important quantities, that results very useful for the theoretical description of material surfaces (Sorrentino G et al. 2011).

Surface weighted value $Q_{\Delta A}$ of whatever quantity is defined according to eq. 3.5 with respect to a generic surface ΔA:

3.5) $$Q_{\Delta A} = \frac{\iint_{\Delta A} Q dA}{\Delta A}$$

3.6) $$Q|_{\Delta A} = \iint_{\Delta A} dQ$$

where $Q|_{\Delta A}$ is the local value of the quantity Q with respect to the surface ΔA.

Moreover, ensemble average quantities $\hat{Q}$ are defined in the eq. 3.7, as the expected value of $Q_{\Delta A}$

3.7) $$\hat{Q} = \langle Q_{\Delta A} \rangle = \langle \iint_{\Delta A} Q dA \rangle \frac{1}{\langle \Delta A \rangle}$$

Similarly to surface weighted value, is possible to define respectively volume weighted average ($Q_{\Delta V}$), local ($Q|_{\Delta V}$) and ensemble quantities ($\tilde{Q}$).

3.8) $$Q_{\Delta V} = \frac{\iiint_{\Delta V} Q dV}{\Delta V}$$

3.9) $$Q|_{\Delta V} = \iiint_{\Delta V} dQ$$

3.10) $$\tilde{Q} = \langle Q_{\Delta V} \rangle = \langle \iiint_{\Delta V} Q dV \rangle \frac{1}{\langle \Delta V \rangle}$$

The local surface-to-volume ratio σ is defined as the ratio between the infinitesimal surface area dA with respect to the infinitesimal volume dV.

3.11) $$\sigma = \lim_{\Delta V \to 0} \frac{\Delta A}{\Delta V} = \frac{dA}{dV}$$

The volume-average of σ^* is defined in eq. 3.18.

3.12) $$\sigma_{\Delta V} = \frac{\iiint_{\Delta V} \sigma dV}{\Delta V} = \frac{\iiint_{\Delta V} \frac{dA}{dV} dV}{\Delta V} = \frac{\iiint_{\Delta V} dA}{\Delta V} = \frac{A|_{\Delta V}}{\Delta V}$$

The expected value of $\sigma_{\Delta V}$, at fixed Eulerian position, is here named as "*interface density*" Σ and it is defined by eq. 3.13.

3.13) $$\Sigma = \left\langle \sigma_{\Delta V} \right\rangle = \left\langle \frac{A|_{\Delta V}}{\Delta V} \right\rangle = \frac{\left\langle A|_{\Delta V} \right\rangle}{\Delta V} = \tilde{\sigma}$$

It is important to underline that interface density Σ is conceptually different from the flame surface density $\Sigma|_Z$ firstly introduced for the coherent flame model (Marble FE and Broadwell JE 1977) and then identified by other authors (Van Kalmthout E et al. 1996) , with the stoichiometric iso-surface $Z=Z_{st}$.

A physical interpretation of Σ , is that its inverse is a striation thickness (Ottino JM et al. 1981).

The striation thickness is related to the amount of area between the fluids (Ottino JM. 1990).

This quantity can be interpreted as a structured continuum property; thus, if the surface is multiply folded so that locally it appears like parallel planes (i.e. the structure is lamellar and uniform), then the mean distance between the planes is Σ^{-1} .

This quantity is useful in describing mixing with diffusion and reaction (Chella & Ottino 1984).

Interfaces are determined by means of a non-diffusive tracer that is introduced into part of the flow. With respect to this fact, a local "*tracer volume fraction*" is defined by eq. 3.14 as the local ratio of a non-diffusive tracer volume dV_{Tr} with respect to the infinitesimal volume considered dV:

3.14) $$\varphi = \lim_{\Delta V \to 0} \frac{\Delta V_{Tr}}{\Delta V} = \frac{dV_{Tr}}{dV}$$

Analogously to interface density; also for the tracer volume fraction is possible to define respectively volume averaged ($\varphi_{\Delta V}$) and ensemble quantities (Φ):

3.15) $$\varphi_{\Delta V} = \frac{\iiint_{\Delta V} \varphi \; dV}{\Delta V} = \frac{\iiint_{\Delta V} \frac{dV_{Tr}}{dV} dV}{\Delta V} = \frac{\iiint_{\Delta V} dV_{Tr}}{\Delta V} = \frac{V_{Tr}\big|_{\Delta V}}{\Delta V}$$

3.16) $$\Phi = \left\langle \varphi_{\Delta V} \right\rangle = \left\langle \frac{V_{Tr}\big|_{\Delta V}}{\Delta V} \right\rangle = \frac{\left\langle V_{Tr}\big|_{\Delta V} \right\rangle}{\Delta V} = \tilde{\varphi}$$

It is worth noting that the volume fraction Φ is directly related to the concentration of the tracer in the considered volume. In particular, a unit value of Φ would correspond to a cell full of tracer, while a zero value would indicate that the cell contained no tracer.

Finally, it is possible to define a characteristic length for the stirring process (ψ), as the inverse of the ratio between the quantities previously defined:

3.17) $$\psi = \left(\frac{\sigma}{\varphi} \right)^{-1}$$

Analogously to interface density and volume fraction; also for ψ is possible to define respectively volume averaged ($\psi_{\Delta V}$) and ensemble quantities (Ψ):

3.18) $$\psi_{\Delta V} = \left(\frac{\sigma_{\Delta V}}{\phi_{\Delta V}} \right)^{-1}$$

3.19) $$\Psi = \left\langle \psi_{\Delta V} \right\rangle = \tilde{\psi}$$

Ψ is named here as "*interface extension*" and represent a measure of the mean thickness of the interface.

This quantity allows to unify, in a fascinating way, concepts on mixing and atomization.

In fact, the interface extension is a sort of analogous of the Sauter mean diameter for the atomization process (Lefebvre AH 1989).

III.1.1.4 Stretching, curvature and coherent structures of material surfaces

Surface stretching is defined as the temporary evolution of the surface area.

The stretch ratio, or SR, is the ratio between the material surface area ΔA at time t and the area at time t_0, for which

3.20) $$\mathrm{SR} = \frac{\Delta A(t)}{\Delta A(t_0)}$$

The stretch rate $K_{\Delta A}$ is the relative change of the stretch ratio, SR:

3.21) $$K_{\Delta A} = \frac{\mathrm{D}}{\mathrm{D}t} \ln \mathrm{SR} = \lim_{\Delta A \to 0} \frac{1}{\Delta A} \frac{\mathrm{D}\Delta A}{\mathrm{D}t}$$

The surface stretch rate is linked to the velocity pattern of the flow, in which it evolves, by the following kinematic relationship,

3.22) $$K_{\Delta A} = \underline{\nabla} \cdot \underline{\mathrm{v}} - \underline{\nabla}\underline{\mathrm{v}}:\underline{\mathrm{n}}\underline{\mathrm{n}}$$

where $\underline{\mathrm{n}}$ and $\underline{\mathrm{v}}$ are the normal unit vector and the velocity vector of the surface ΔA, respectively. This expression can be read in a heuristic way as the difference between a volumetric stretch, $K_{\Delta V}$, and a linear one, $K_{\Delta l}$, bearing in mind that the stretch rate is additive by virtue of its logarithmic nature. The definitions of volumetric and linear stretch rates and their kinematic expressions are given below for completeness (Cavaliere and Ragucci 2002):

3.23) $$K_{\Delta V} = \lim_{\Delta V \to 0} \frac{1}{\Delta V} \frac{\mathrm{D}\Delta V}{\mathrm{D}t} = \underline{\nabla} \cdot \underline{\mathrm{v}}$$

3.24) $$K_{\Delta l} = \lim_{\Delta l \to 0} \frac{1}{\Delta l} \frac{\mathrm{D}\Delta l}{\mathrm{D}t} = \underline{\nabla}\,\underline{\mathrm{v}}:\underline{\mathrm{n}}\underline{\mathrm{n}}$$

It is also possible to demonstrate:

3.25) $$K_{\Delta A} = \underline{\nabla}_t \cdot \underline{\mathrm{v}}_t + \mathrm{v_n} C$$

Where $\underline{\mathrm{v}}_t$ and $\mathrm{v_n}$ are the projection of the velocity vector $\underline{\mathrm{v}}$ on the surface ΔA and the modulus of the projection $\mathrm{v_n}$ along the normal to the surface, respectively, $\underline{\nabla}_t$ the divergence operator on the surface ΔA and C is its curvature. This last expression shows that the stretch rate consists both of a contribution related to the "planar divergence" of velocities on the surface and of a contribution related to the mean surface curvature.

Moreover, it is possible to consider average values of surface stretch rate and flow velocity as reported in the following equations:

3.26) $$\widehat{K_{\Delta A}} = \left\langle K_{\Delta A} \right\rangle$$

3.27) $$\underline{\mathrm{v}}_{\Delta A} = \frac{\iint_{\Delta A} \underline{\mathrm{v}}\, dA}{\Delta A}$$

3.28) $$\hat{\underline{\mathrm{v}}} = \left\langle \underline{\mathrm{v}}_{\Delta A} \right\rangle$$

The aforementioned quantities are referred to area-weighted ensemble averages and their equivalent form in terms of kinematic and scalar field variables are also reported in eqs. 30-31. It is worth noting that the velocity can be decomposed in the Reynolds averaged and the fluctuating component.

3.29) $$\hat{\underline{\mathrm{v}}} = \frac{\left\langle \iint_{\Delta A} \underline{\mathrm{v}} dA \right\rangle}{\langle \Delta A \rangle} \cong \bar{\mathrm{v}} + \left\langle \mathrm{v}'_{\Delta A} \right\rangle$$

3.30) $$\widehat{K_{\Delta A}} = \widehat{\underline{\nabla} \cdot \underline{\mathrm{v}}} - \widehat{\underline{\nabla}\underline{\mathrm{v}} : \underline{\mathrm{n}}\underline{\mathrm{n}}} = \widehat{\underline{\nabla}_t \cdot \underline{\mathrm{v}}_t} + \widehat{\underline{\mathrm{v}}_n \underline{\nabla} \cdot \underline{\mathrm{n}}}$$

In eq. 3.29 the surface mean of the first is the average itself under the hypothesis of ergodicity, while the ensemble average of the fluctuation may be different from zero, because it is area-weighted.

Moreover it is worthwhile to note that eq. 3.30 is the ensemble average of eq. 3.25. The first term on the right side is the, so-called, area stretch and the second consists both of a contribution related to the "planar divergence" of velocities on the surface and of a contribution related to the surface curvature. ΔA can be, for example, an element of a material surface or an iso-scalar surface. The mean curvature, C of ΔA corresponds to $\nabla \cdot \underline{n}$ by eq. 31:

3.31) $$C = \nabla \cdot \underline{n} = (k_1 + k_2) = \left(\frac{1}{R_1} + \frac{1}{R_2} \right)$$

where k_1 and k_2 are the principal curvatures and R_1 and R_2 the principal radius of curvature. k_1 and R_1 (and, similarly, k_2 and R_2) are positive for a convex surfaces towards $\underline{n}$.

The investigation of the mixing features under the action of a turbulent flow, in terms of surface curvatures, k_1 and k_2, is an attempt at relating these phenomena to the small-scale topology of the scalar field. Using k_1 and k_2 instead of C tries to unveil the three dimensional structures which are hidden by the essentially two-dimensional diagnostic techniques. Moreover, when C = 0 there exists an ambiguity as this might imply either a flat surface or a saddle point with $k_1 = -k_2$.

DNS have been used by several authors (Brethouwer G 2000; Haworth DC et al. 1992) in order to investigate the stretching, rotation and folding of material and iso-scalar surfaces. Chen and Im (2000) have used a 2-D DNS with detailed chemical kinetics for unsteady premixed hydrogen/air flames in order to investigate the dependence of the burning velocity with tangential strain, curvature and stretch. Haworth & Poinsot (1992) unveiled through DNS the significant influence of the Lewis number upon premixed flame characteristics. Pope et al. (1989) obtained via DNS the curvature of material surfaces in isotropic turbulence, finding that the most probable structures with large curvatures are cylinders. Echekki & Chen (1996) numerically simulated turbulent premixed stoichiometric methane/air flames, evaluating, among other things, the effects of strain rate and mean curvature upon radicals concentration and heat release. Chakraborty & Cant (2004) have used DNS to investigate the influence of unsteady tangential strain rates and mean curvatures on premixed flame propagation.

Iso-surface curvature can also appear explicitly in the molecular diffusion term in the scalar conservation equation (Dopazo C 1994).

It is relevant to scrutinize the importance of that curvature upon scalar molecular diffusion, as modelling the latter gives rise to a difficult closure problem in turbulent mixing (Vervisch L et al. 1995).

Another relevant topological feature of the advected-surfaces in three-dimensional fluid flows is intimately linked to the presence of coherent structures (Haller G 2001).

For the purposes of characterizing Lagrangian motion, the problem of locating the boundaries of coherent structures is of special importance. Indeed, one of the fascinating elements of fluid motion is that it may be so heterogeneous despite the near homogeneity of the fluid medium itself: long-lived nonlinear jets and vortices that may transport fluid great distances, either by advection within a jet or by translation of a fluid-trapping vortex, may coexist side by side with relatively quiescent regions of flow in which the fluid parcels move, if at all, only in weak, nearly linear wavelike oscillations.

Previous work on flow structure identification has been primarily Eulerian, i.e., it has been concerned with the spatial structure of quantities derived from the instantaneous velocity field and its gradient. The resulting Eulerian coherent structure criteria have been broadly used in flow structure identification, although none has emerged as a definitive tool of choice (Green MA et al. 2007).

The notion of a coherent structures is usually related to the identification of vortex in a fluid flow.

Vortical structures are often thought of as regions of high vorticity, but there is no universal threshold over which vorticity is to be considered high. More alarmingly, vorticity may also be high in parallel shear flows where no vortices are present.

Definitions requiring closed or spiraling streamlines for a vortex are also ambiguous, because streamline topology changes even under simple Galilean transformations such as constant speed translations.

Jeong & Hussain (1995) stress the need for Galilean-invariant vortex criteria, i.e. criteria that remain invariant under coordinate changes of the form $y = \boldsymbol{Q}x + \underline{a}t$, where $\boldsymbol{Q}$ is a proper orthogonal tensor and $\underline{a}$ is a constant velocity vector. For a three-dimensional smooth velocity field $\underline{v}(x,t)$, available Galilean-invariant vortex criteria use the velocity gradient decomposition:

3.32) $$\nabla \boldsymbol{v} = \boldsymbol{S} + \boldsymbol{\Omega}$$

where $\mathbf{S} = \frac{1}{2}[\nabla \mathbf{v} + (\nabla \mathbf{v})^{\mathrm{T}}]$ is the rate-of-strain tensor, and $\Omega = \frac{1}{2}[\nabla \mathbf{v} - (\nabla \mathbf{v})^{\mathrm{T}}]$ is the vorticity tensor.

In historical order, the first three-dimensional vortex criterion using eq. 3.32) is the Q-criterion of Hunt et al. (1988) which defines a vortex as a spatial region where

3.33) $$\mathrm{Q} = \frac{1}{2}\left[|\boldsymbol{\Omega}|^2 - |\mathbf{S}|^2\right] > 0$$

i.e. where the Euclidean norm of the vorticity tensor dominates that of the rate of strain.

Another well-known Galilean-invariant definition is the Δ-criterion of Chong et al. (1990), who define vortices as regions with :

3.34) $$\Delta = \left(\frac{\mathrm{Q}}{3}\right)^3 + \left(\frac{\det \nabla \boldsymbol{v}}{2}\right)^2 > 0$$

In these regions, the velocity gradient $\nabla \boldsymbol{v}$ admits complex eigenvalues, thus local instantaneous stirring is a plausible assumption.

Finally, according to the λ_2-criterion of Jeong & Hussain (1995), vortices are regions where:

3.35) $$\lambda_2(\boldsymbol{S}^2 + \boldsymbol{\Omega}^2) < 0$$

where $\lambda_2(\mathbf{A})$ denotes the intermediate eigenvalue of a symmetric tensor $\mathbf{A}$. Under appropriate adiabatic assumptions, this last criterion guarantees an instantaneous local pressure minimum in a two-dimensional plane for Navier–Stokes flows.

In an unsteady flow, other criteria like the Galilean-invariant one give consistent results in frames that move at constant speeds relative to each other. The same criteria, however, fail to be invariant under more general changes of frame such as rotations.

III.1.2 Properties of non diffusing surfaces

The analysis of advected-surfaces has to be pursued on the ground of the following basic properties of the interfaces, which are:

- interfaces are continuous
- interfaces are non intersecting
- interfaces are oriented

III.1.2.1 Interface continuity

The continuity infers that an interface can be drawn as surface track without any solution from the inlet to the outlet. In a discretized volume the track can passes from an elementary volume to the adjacent one. The volume characteristic size can be adjusted in order to have only a single passage of the interface through it. This occurs when either the volume is so small that the smallest interface convolution can be resolved or, on the opposite, when it is larger than the largest interface convolution length scale. An example of this behaviour is shown in fig. III.7, in which three different grids are superimposed to the same two dimensional interface.

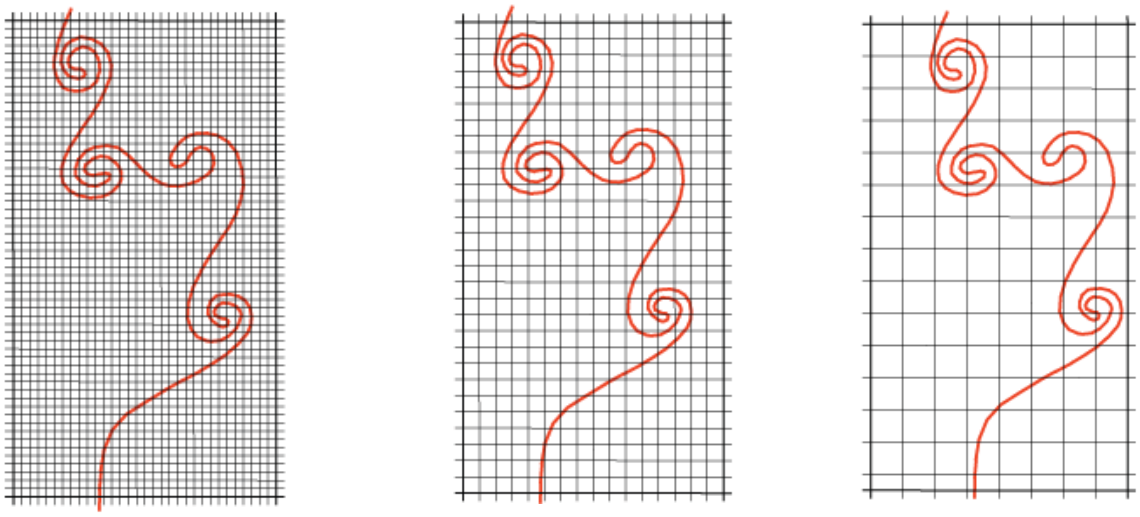

a) b) c)

Fig. III.7 *Example of three different grids that are superimposed to the same two dimensional interface.*

In the first case (fig. III.7-a) the grid size is so small that every bending and convolution of the surface is resolved. The length of the curve inside a box, which represents a surface extension in each elementary volume in this two dimensional example, is comparable to the characteristic box length. In the second case (fig III.7-b) the grid size is larger than that of fig III.7-a and it is smaller than an average curvature radius of the interface. Therefore the bending is responsible for the recursive crossing of the interface through the box and it fixes the number of adjacent boxes which the interface has to cross between two passages through the same box. In the third case (fig III.7-c) the grid size is so large that the bending develops inside one single box and the possible stretching extends the interface inside each cell. In respect to the first case the interface is similar in the fact that it is *single-box-crossing* but it differs from the first example of interface in the localization of its generation. In fact it is *local-box-stretching* in the last case whereas it can be generated outside the box and transported diffusively inside it in the second case.

A further example of the interface distribution on a discretized space is reported in the vast literature on the interface characterization in turbulent condition (Sreenivasan KR and Meneveau C 1986, Cavaliere A et al. 1993, Sreenivasan KR 1991) in terms of fractals by means of counting box technique.

Figure III.8 shows one of these examples in which an interface for a turbulent condition is reported on the left side and its counting box surface distribution on the right side.

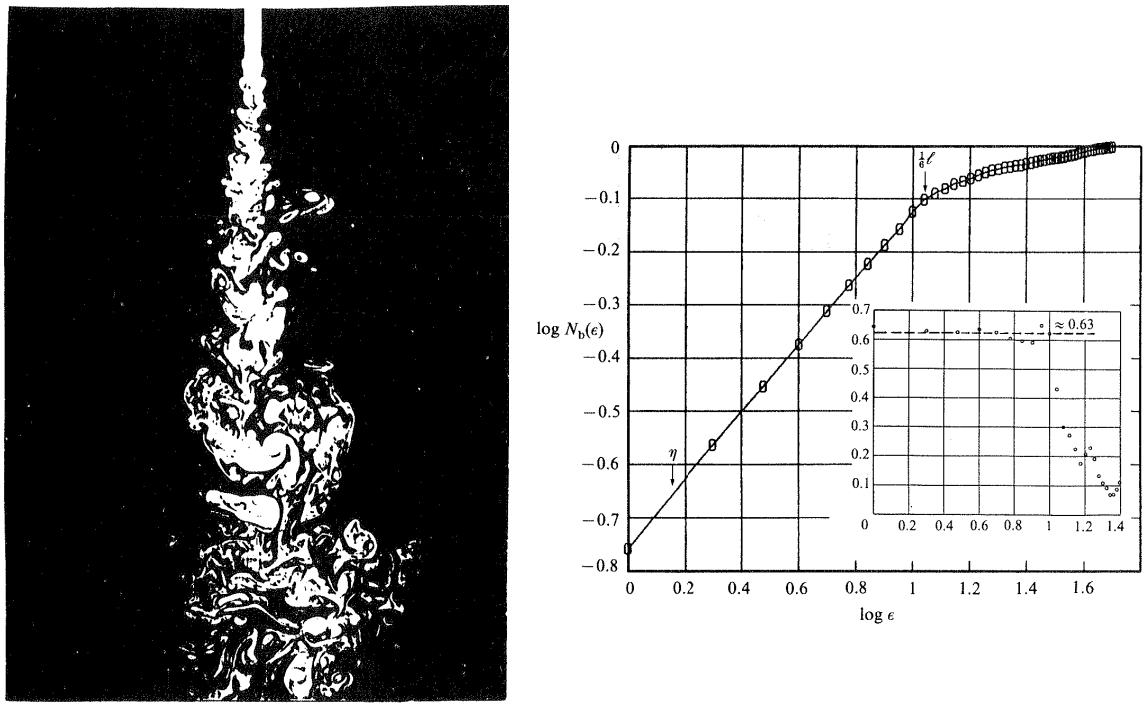

Fig. III.8 Example of Box counting in turbulent conditions

In this type of procedure it is possible to show that the box number is invariant with the box size when it is greater or smaller than the largest and smallest characteristic curvature respectively. When the curve is interpolated by a single slope in log-log plot this slope describe the fractal dimension of the surface.

In any case every model which aims to predict the interface evolution can exploit several submodel in order to evaluate its subgrid distribution according to different fluid-dynamic conditions.

III.1.2.2 Non-intersection

The interface can not intersect itself for a basic principle. It is a material surface so that each point can not be the place of different material for the mass conservation principle. This property is not relevant in the prediction of the interface itself, but it is of interest because it infers that there is not annihilation of interface and that it can be very near to an another piece of interface without violating any principle. This consideration will have in turn some interest in the analysis of the mass fraction distribution of any conservative diffusing species. For instance possible models of continuous, not intersecting interface in two dimensional are shown schematically by means the four sketched reported in fig.III.9.

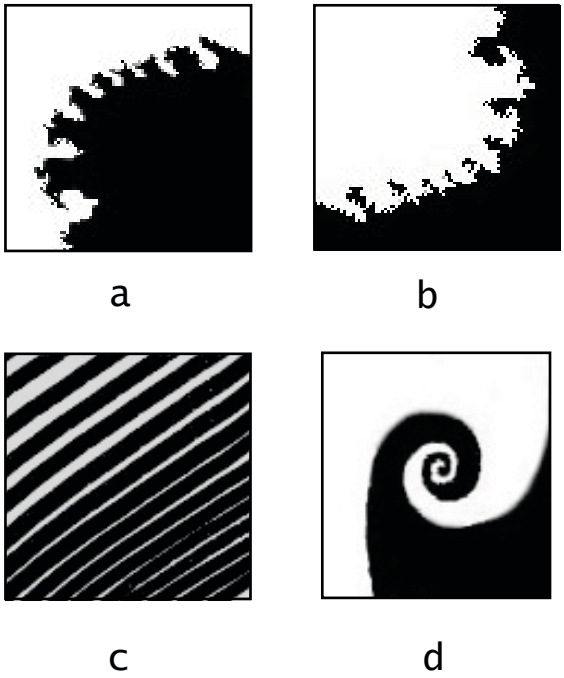

Fig. III.9 Models of interface distribution in two-dimensional field (taking into account the property of not-intersection)

They pertain to limit models which could be defined as interface :

- Convex
- Concave

- Stratified
- Convoluted

The meaning of each regime and of its correspondent sketch is straightforward. In fig III.9-a and fig III.9-b the interfaces are convex or concave surfaces, generated at different length scales, with the self-similar recursive procedures, as it is done in the yield of fractal surfaces. It is a matter of fact that one image is the negative of the other. In other words the only difference between the two is that the air and fuel exchange each other, so that the air-fuel interface on the air side is concave and convex respectively. There are stirring characterization of such type also in immiscible liquid-liquid interface. On the contrary the stratified interface, shown in fig. III.9-c, is similar to the regimes reported in the literature with “lamellar”, that is the product of aged stirring in which the interface undergoes several bendings as it occurs in the baker-transformation (Clifford MJ et al. 1998). In gaseous system the convoluted surface reported in fig. III.9-d is the very common shape of two-dimensional vortical structure. The inner parts of the interface around the apex are closer than those parts on its periphery, the change of curvature passing from the outer to the inner core makes the distribution of the characteristic lengths different and in particular make the fractal dimensions obtained with counting box comparable to those one obtained with self similar recursive procedure.

It is a matter of fact that any kind of stirring process relies on such type of interface, even though some elongated vortex structures which are obtained when stretching affect very small vortex can be confused with the lamellar stirring mentioned before. This similarity can occur in the central parts of the two structures, whereas on the their periphery the bending of the interface makes the two quite different. In one case the bending is around the interface itself in the other case the bending is external to the other parts. Nevertheless the spacing between the interface are quite similar.

These two dimensional interfaces have to be considered section, projection or analogous of the tridimensional interface. Very few works report some information concerning the three dimensional structure, (Galaktionov OS et al. 2001) but most interesting features are captured also in the low dimensional level.

Furthermore sectioning of the interface in two or several parts ensure that these parts cannot intersect each other even they are entangled in convoluted ways in some part of the stirring process. This is a quite interesting feature, since it allows to section the whole mixing process and to identify a criterion for distinguish regimes. In fact for a fixed sectioning of the boundary interface in parts and for a fixed grid distribution it is possible to define "sectional" a stirring process, in which in each elementary volume there is only one part of the interface.

III.1.2.3 Orientation

The interface is an oriented surface. This means that the normal versor to the interface is always oriented according to a conventional rule to one of the two species which it separates. For instance the unit normal versor can be chosen to be positive when is oriented forward the oxidant and it is negative when it oriented forward the fuel. In this case the distance between two positive sides of the interface, Δ^+ , is that separating fuel parcels, whereas the distance between two negative sides, Δ^- , is that representing the fuel parcel characteristic size. The average of the two distances is the reciprocal of the interface density in a "stratified" or "lamellar" stirring process. The interface is n times l^2 and the volume is l^3. Therefore the surface density is

3.36) $$\Sigma = \frac{n \times l^2}{l^3} = \frac{1}{l/n} = \frac{1}{\Delta}$$

where Δ is the average distance between interfaces. Δ is in turn the average between the average distance of the positive side Δ^+ and of the negative side Δ^-.

In some particular cases the two distances at an interface position are equal and the stirring can be said “uniform” or “regular", but this is a very peculiar situation in which the volume fraction of the two species is 0.5.

Other topological features can be obtained by the analysis of interface orientation when preferential directions of the stirring process are identified. For instance in coflow jet stirring the vectorial average of the unit positive versor should be at most a unit versor in one direction. In other words positive and negative side of the interface have to be balanced, apart the most external part of the interface which gives the orientation of the area inside which the stirring process takes place.

III.1.3 Evolution and conservation equations of advected-surfaces

The kind of surfaces previously defined can be properly exploited in a framework which included all their relations both with kinematic properties and with semi-empirical characteristics which can be obtained either by experimental or numerical analysis partly presented in the following. This type of methodological approach has been first introduced by Marble and Broadwell (1977) and explored in a systematic way by Candel and co-workers (Veynante D et al. 1991) in order to show the potentials of coherent flame description. The ensemble of these works has yielded a framework which in time has given the evolution equation of the surface density following the works of Pope (Pope SB 1988) and Trouvé et al. (1994).

In particular, the evolution equation of interface density , eq. 3.37, is also reported as it has been obtained by the authors referenced before.

3.37) $$\frac{\partial \Sigma}{\partial t} + \underline{\nabla} \cdot \left(\hat{\underline{v}} \Sigma \right) = \widehat{K_{\Delta A}} \Sigma$$

It is quite similar to any balance equation with a transport term analogous to the convective one, in which the fluid-dynamic velocity is substituted with the area-weighted ensemble velocity $\hat{\underline{v}}$. The interface density production is reported on the right side of the evolution equation as the product of itself and the stretch rate .

The evolution equation can be derived only in absence of singularities, critical points, internal edges, self-intersection (properties of surface regularity).

All the aforementioned quantities concerning interface density evolution equation, are referred to area-weighted ensemble averages and their equivalent form in terms of kinematic and scalar field variables are also reported in eqs. 3.26-3.30.

By analyzing the interface density equation it is worthwhile to note that stretching and curvature effects can be represented directly in the evolution equation by using suitable model for the interface density production.

In this context, the need for realistic turbulent combustion models motivated first developments of closure-approach based on the flame surface density (FSD) concept.

In particular the flame surface density (FSD) concept is well established in the context of RANS simulation of turbulent premixed combustion (Veynante D and Vervisch L 2002).

By contrast, extension of the FSD concept for LES combustion modelling is relatively recent (Pitsch H 2006; Knikker R et al. 2005; Chakraborty N & Cant RS 2007).

Straining and curvature effects can be represented directly in the FSD transport equation by using suitable models for the displacement speed of the flame.

At present, most FSD modelling does not account for the strain rate and the curvature dependence of displacement speed. In the thin reaction zone regime, the curvature contribution to displacement speed cannot be ignored.

Recent works, has provided a detailed examination of the curvature and propagation terms of the FSD transport equation (Chakraborty N and Cant RS 2007) and has indicated the importance of the displacement speed in closing these terms.

Modelling of the unclosed terms of the FSD transport equation in the context of LES has been addressed in the light of a priori DNS analysis (Chakraborty N and Cant RS 2009) by comparing the proposed model with the actual quantities obtained from DNS data. The model has significant advantages under unsteady flow conditions and it could form the basis of a future LES study of unsteady combustion in real engineering combustion devices.

It is important to note here that the FSD approach is not the aim of this thesis.

As a matter of fact, the interface density is conceptually different from the FSD.

In fact, in the FSD-approach, the reference-surface is not a material one, but a propagating-surface.

Another very important quantity which rules the whole stirring/mixing process, together with Σ , is the volume/mass ratio of the two species. Therefore a specific conservation equation should be written for such quantity together with the surface evolution equation. This is eq. 3.38, reported here again in compressible condition:

3.38) $$\frac{\mathrm{D}\rho\beta_M}{\mathrm{D}t} = \frac{\partial\rho\beta_M}{\partial t} + \rho\underline{\mathbf{v}}\cdot\underline{\nabla}\beta_M = 0$$

where β_M is the mass fraction, which is in turn the volume fraction Φ when the density of the two species is the same.

On the other hand, a transport equation for the local volume fraction φ must be considered.

Since φ is passively advected with the flow, we can expect its material derivative to vanish:

3.39) $$\frac{\partial \varphi}{\partial t} + \underline{\nabla} \cdot (\underline{v}\varphi) = 0$$

this, along with the assumption of a zero divergence for the velocity field (in an incompressible flow):

3.40) $$\frac{\partial \varphi}{\partial t} + \underline{v} \cdot (\underline{\nabla}\varphi) = 0$$

Equation 3.39 is the same for any passively advected scalars. However, the conservative form (3.40) is taking also into account a discontinuous nature of φ.

An equivalent form of eq. 3.39 is possible to obtain if volume weighted ensemble averages quantities are considered:

3.41) $$\frac{\partial \Phi}{\partial t} + \underline{\nabla} \cdot (\widetilde{\underline{v}\varphi}) = 0$$

If the convective term is replaced with the tracer velocity ($\underline{v}^{Tr} = \underline{v}\varphi$), the eq. 3.41 can be written as:

3.42) $$\frac{\partial \Phi}{\partial t} + \underline{\nabla} \cdot \widetilde{\underline{v}^{Tr}} = 0$$

It is straight to link the volume fraction Φ to the surface density Σ and to the positive and negative interface distance (Δ^+, Δ^-). For instance in the case of stratified stirring the eq. 3.43 takes into account that only half of the surface density is the base of a parallelepiped with the third side equal to Δ^-. It becomes eq. 3.44 taking into account eq. 3.36 and eventually it becomes 3.45 taking into account eq. 3.37:

3.43) $$\Phi = \frac{1}{2}\Sigma \cdot \Delta^-$$

3.44) $$\Phi = \frac{1}{2}\frac{\Delta^{-}}{\Delta}$$

3.45) $$\Phi = \frac{1}{2}\frac{2\Delta - \Delta^{+}}{\Delta} = 1 - \frac{1}{2}\frac{\Delta^{+}}{\Delta}$$

The previous equations show some relations between the interface density, volume fraction and interface distance. Therefore, only two of these three quantities must be defined in order to describe in the right manner the stirring/mixing process.

Moreover, it is worthwhile to note that the local value of the interface extension (i.e. the average thickness of the interface) is univocally related to σ and φ as reported in eq. 3.17.

It results as a characteristic length of the stirring process.

III.2 Experimental facility and diagnostics

This thesis may be included within the broad context of the characterization of passive interfaces in turbulent flows. In this respect one of the objectives of this thesis is to recognize advected-surfaces in transitional/turbulent flows.

In particular the attention has been focused on the identification of this kind of surfaces and their characteristics quantity.

Experimental measurements have been carried out using a proper test rig that has been built to permit the visualization of material surfaces in transitional or turbulent flows.

This statement triggered the basic design of the experimental facility described in the following. The other design constraint is the possibility to have full optical access to the test section, in order to explore the characteristics of the seeded jet issuing from a square duct and interacting with the airflow.

The feeding section has been designed with the intent to ensure optimum mixing conditions. A thorough description of the system will be given in the next paragraphs.

In the case studied here, it must be stressed that the main focus of the next chapter is not placed on the investigation of the flow field inside the chamber but on the measurements of the main properties of the surfaces.

As a consequence, the study has been focused on transitional flows because of diagnostic limitations.

Experimental evaluation of the interface is discussed in the next sections in relation to an experimental test rig, which has been purposely designed in order to be suitable for the experimental/numerical comparison. The techniques of particle seeding and of optical characterization on the interface are thoroughly described in order to stress the constraints and difficulties, which have to be faced to obtain both single and statistical characterization of the interface.

III.2.1 Experimental facility

The main features of a model experiment which should keep the main characteristics of a turbulent mixing pattern are the following:

- low dimensionality; i.e. the final target of a quasi-2D, time dependent fluid-dynamic pattern.
- small range of length scales of fluid-dynamic structures; i.e. low Reynolds number so that the fluid-dynamic pattern can be described both by full numerical simulation and two-dimensional imaging. As first choice this number has been fixed to be lower than some hundreds (at the inlet of the honeycomb structure), even though the relation between it and the scale range can be predicted only in simplified conditions.

- perturbation of the pattern that should be able to generate high level of velocity gradient.

This latter requirement conflicts with the second one. In fact high velocity gradients related to high level of vorticity imply large velocity scales, whereas low Reynolds number requires low value of velocity. a possible way of satisfying both conditions is the superimposition of a strong perturbation with small-length scales on fluid-dynamic pattern. Also the perturbation quasi-2D ad space-periodic in order to keep the advantage obtained by the dimensional reduction.

An experimental apparatus, sketched in Fig. III.10, has been designed with the purpose to satisfy the aforementioned conditions.

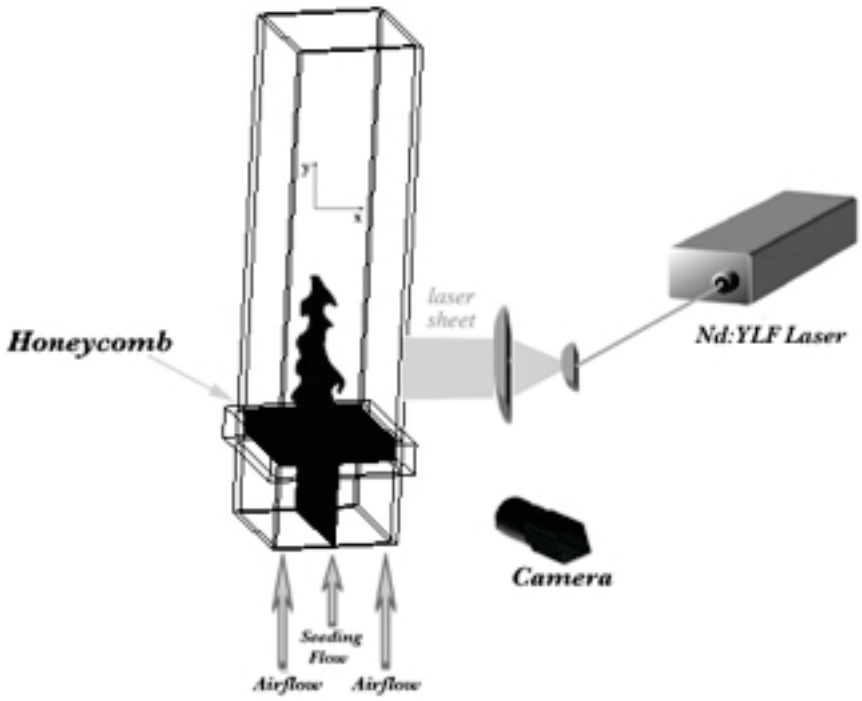

Fig. III.10 Sketch of the experimental apparatus.

The test rig used in this work was built to reproduce the stirring/mixing characteristics of gaseous jets under the perspective of the theoretical analysis of the problem. The test

section of the system is a glass windowed channel with 140 x 128 mm cross-section, designed to operate at atmospheric pressure and environmental temperature conditions.

In order to face the difficulty previously mentioned, the first requirement of the experimental flow to be investigated was fulfilled by choosing a flow configuration which is 3-D planar symmetric. The feeding system of the gaseous flows was designed in order to achieve both a high degree of turbulence level control and repeatability of inlet conditions. Design process has been strongly guided by feasibility criteria (Sorrentino G et al. 2012). In addition, the design of the mixing test was such that both the building of the experimental apparatus and the numerical simulations were possible and meaningful. In this respect the most important features were considered to be the turbulent and three-dimensional character of the flow, as well as the choice of well defined, stable and easy to implement boundary conditions. A further characteristic, i.e. the spatial periodicity of the flow, is quite desirable in a numerical simulation of the fluid-dynamic pattern. A honeycomb (reported in Fig. III.11-a), formed by square channels with a cell size of 2 mm, is used to obtain the desired fluid dynamics conditions in the test section. This structure has 35 channels along the x- direction and 32 channels in the other one. Therefore, the cross section of the test duct has a very large aspect ratio (10). The length of any duct (30 mm) is much larger than its width (H >> L) so that self-similar velocity profiles can develop. Furthermore the duct widths are small enough to ensure that, for the employed average velocities, relatively low Reynolds numbers are obtained and laminar Poiseuille-type flows can be reasonably supposed to develop in every duct of the honeycomb structure. This means that natural boundary conditions are used.

Moreover, the fact that the cross section of the test duct has a very large aspect ratio (L*>>L as reported in Fig. III.11-b) permits to have transitional/turbulent flow conditions in the main test chamber.

Finally, in order to control the streak-lines roll-up process, the ducts in the central row of the honeycomb structure are independently fed with a seeding flow (Fig. III.11-a) and the airflow velocity can be varied independently from the velocity in the other ducts.

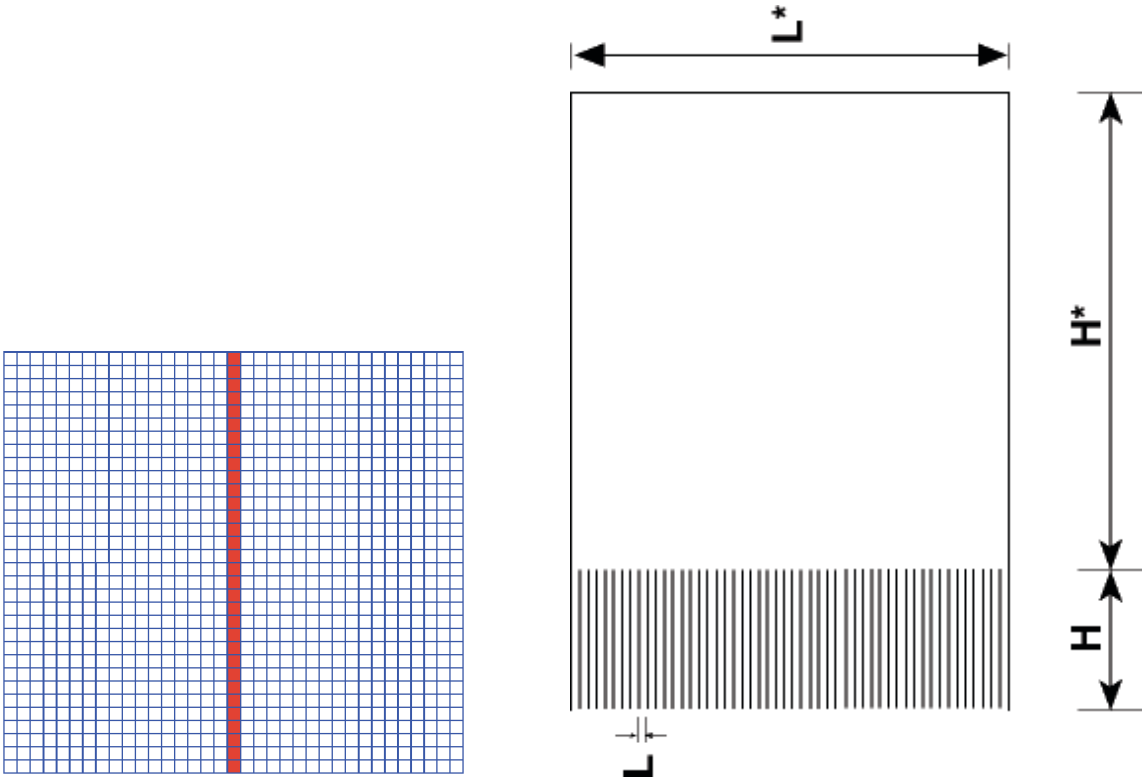

a) b)

Fig. III.11 a) Details of the feeding configuration; b) Frontal view of the chamber

Special care is devoted to assure an even distribution through the remaining ducts. The test section of the experiment is a rectangular channel, made of optical grade glass in order to have optical accessibility on all the four sides (see Figure III.12).

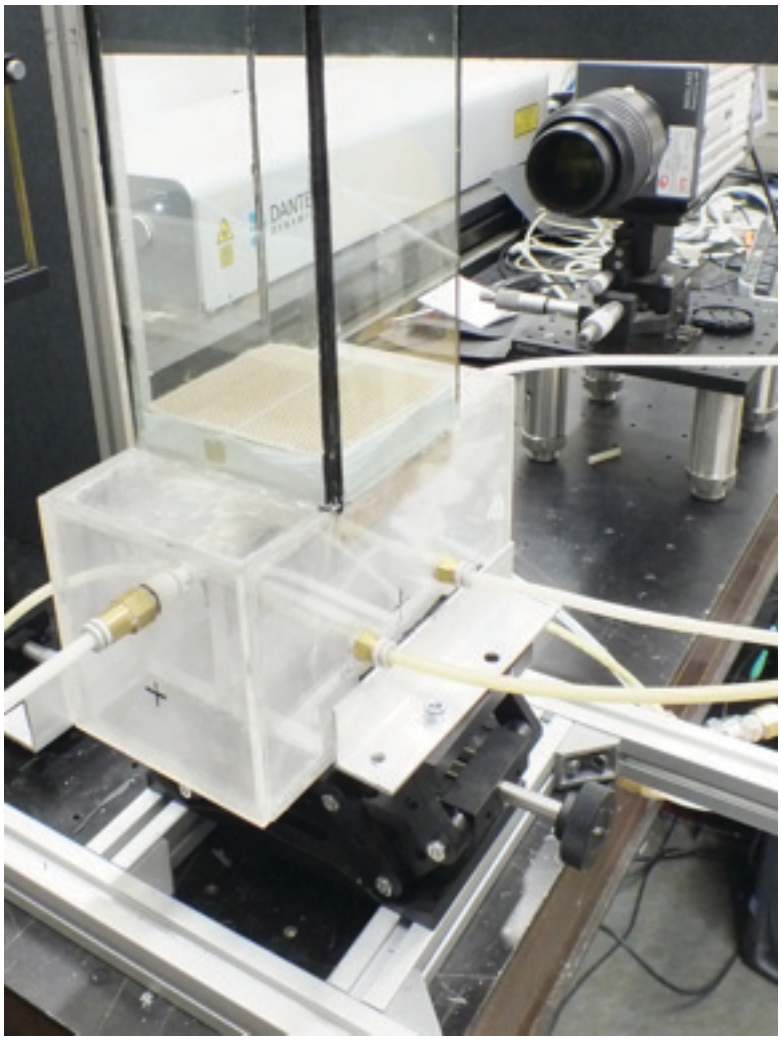

Fig. III.12 Experimental apparatus for the study of the mixing of gaseous jets

In order to analyze the stirring characteristics, interfaces from two flows have been generated by means of some devices later described. In this case, the diagnostics problem is the same (Cavaliere A et al. 1994).

It consists of detecting the concentration of some tracers, which could be submicron particles produced by various types of methods.

For this reason, the generation of the interface is obtained by seeding the central part of the flow with submicron particles. The seeding particles are illuminated by a laser light sheet perpendicularly crossing the test chamber allowing for interface identification as the

discontinuity in the 2-D laser light scattering intensity due to the discontinuity of the tracer concentration.

For most experiments it is desirable that seeding particles be non-toxic, non-corrosive, non-abrasive, non-volatile and chemically inert. On the ground of these requirements, a wide variety of seeding particles is available for PIV experiments. In fact, an interface is formed by a tracer which, by definition, is a non-diffusing, fully convected material. In this case particles have to be dragged in such a way that they are representative of the gas displacement.

It is worthwhile to note, that the type of particles, for which Sc >> 1and St << 1, is the only possible choice of tracer in a gaseous system (Ottino JM 1982). A particle, for instance, between 0.1 and 1 μm is sufficiently large in dimension to ensure that Brownian diffusion is low, but it is sufficiently small to immediately follow a flow.

Moreover, intensity of the scattered light, as a direct measure of particle size has always been plagued with difficulties, as detected intensity is dependent on so many other parameters of a flow system (e.g., trajectory of particle through a shaped beam/sheet, obscuration of incident and scattered light, extinction), despite some early attempts to remove the necessity of calibration (Tropea C 2011). There is also the basic difficulty that, in the Mie scattering range, the intensity is not monotonically dependent on particle size (Figure III.13).

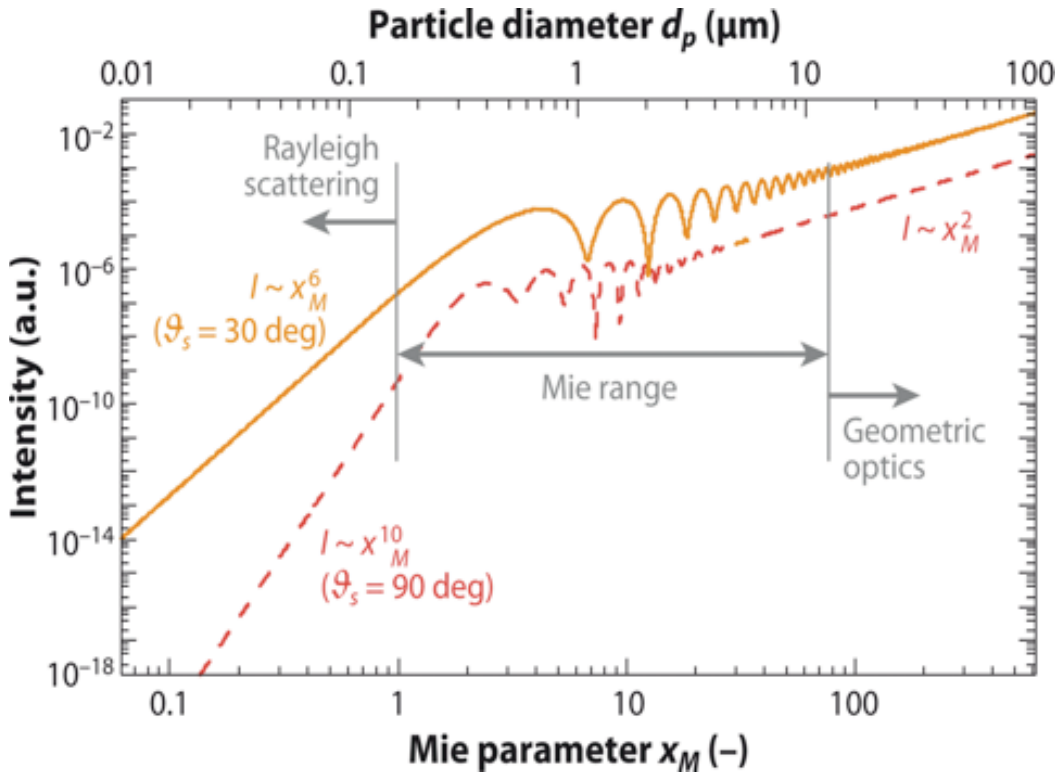

Fig. III.13 *Scattered intensity as a function of the Mie parameter for two scattering angles. Adapted from Tropea C., Annu. Rev. Fluid Mech., 2011*

For the previous reasons, the central gaseous flow was seeded with TiO_2 particles with a mean diameter of 2 μm, that correspond to an optimum between the not-diffusing tracer condition and an acceptable scattered light intensity.

For high quality PIV records a scattering particle concentration of about 15 particles per interrogation volume is necessary (Clemens NT 2002). The size of the interrogation volume depends in turn on the dimensions of the test section, but for many laboratory applications this condition corresponds to a concentration of 10^8–10^{10} m^{-3}.

Suitable generators to satisfy the particle size and concentration requirements in gas flows are twin-fluid atomizers (for droplets or solid particles in liquid suspension) and fluidized beds (for solid particles). Ideally the scattering particles should be distributed uniformly in the flow, but, with large volume flow rates, requirements for globally uniform seeding may exceed the particle generation capacity. If local seeding is adopted, uniformity of seeding

must be achieved in the region of investigation. In this work it has ben chosen to disperse the particles in the airflow by means of an ad-hoc realized elutriator, reported in Fig. III.14, based on a fluidized bed device (Melling A 1997), This solution allowed for the homogeneous dispersion of particles in the airflow and for a satisfying concentration of seeders.

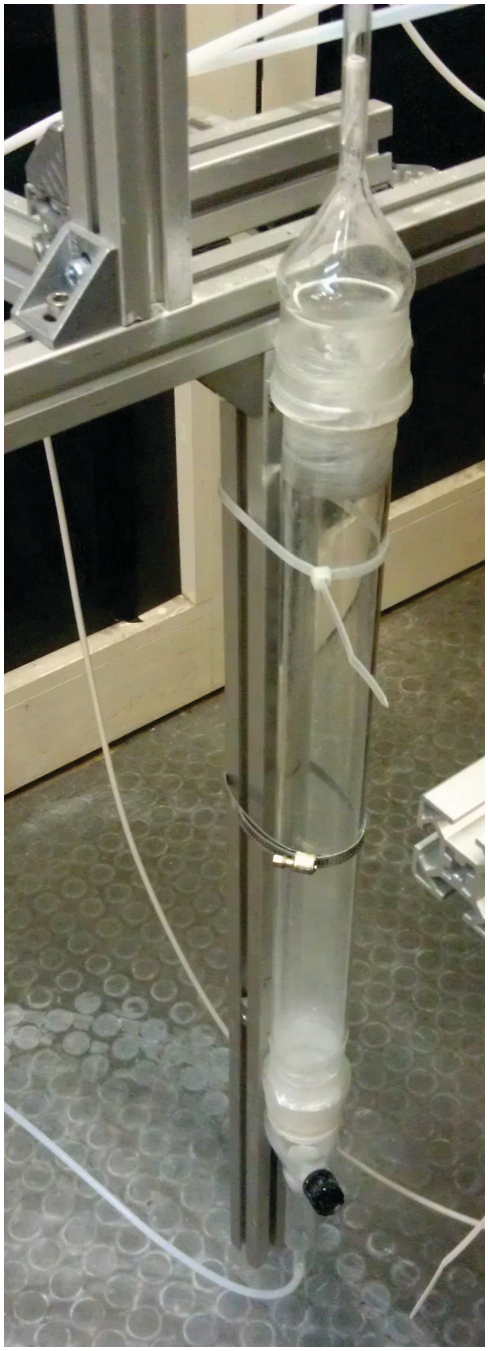

Fig. III.14 Fluidized bed that generates the seeding particles

III.2.2 Diagnostics

The measurement methodology must be able to evaluate the quantities defined previously, which are relevant with regard to stirring processes. Fluid-dynamics quantities, like $\hat{\underline{v}}$, $\widehat{K_{\Delta A}}$, and SR can be evaluated by means of PIV analysis. Other relevant quantities, like interface density and volume fraction, can be estimated through post-processing algorithms of images acquired by means of 2D laser light scattering technique.

For the aforementioned reasons, a satisfying characterization of the interface morphology would require the implementation of several on-line diagnostic systems.

The optical characterization of the surfaces is performed by recording the pattern of the light elastically scattered when a laser sheet illuminates the tracer. The Nd:YLF pulsed laser was tuned on the second harmonic wavelength (λ = 527 nm) and its beam was shaped by a set of cylindrical lenses to a sheet of constant thickness. It was varied in height by the extension of the objective field. Patterns of elastic scattered light was detected by a CMOS camera with a variable-focus telescope. Since each pulse is in a different frame, there is no directional ambiguity for the velocity vectors. The time and space scales were limited by the laser thickness and the tracer production time and therefore are not sufficient for measuring any range of length scales. Nevertheless, they are smaller than interface separation distances and the residence time needed to characterize the prototypal flows presented here. A shadowgraphic scheme has been adopted to collect images of the jets, with a proper system of lens. The pulsed laser frequency is 1000 Hz, the digital camera acquire 8-bit 1280 x 1024 pixel frames at 1000 Hz, and a BNC delay generator has been used for time base generation and synchronization. For each test condition a set of 3000 frames has been collected.

The diagnostic apparatus mainly consists of three units:

- Laser LDY Nd:YLF double head, (λ=527 nm), maximal frequency of 10 kHz and output Energy (at 1kHz and at 527nm per laser head per pulse) of 15 mJ.
- Camera NanoSense MkIII. Maximal resolution 1280x1024 pixels. Maximal frame rate= 2 kHz
- A BNC 575 delay generator that manage the timebase generation and synchronization between the devices.

Most imaging in fluid mechanics research involves planar imaging, where the flow properties are measured within a two-dimensional cross section of the flow. This is most often accomplished by illuminating the flow using a thin laser light sheet, as shown in Fig. III.15, and then recording the scattered light using a digital camera. The laser light is scattered from either molecules or particles in the flow. Quantitative imaging is substantially more challenging than simple visualization because a greater degree of knowledge and effort are required before the researcher can ensure that the spatial distribution of the flow property of interest is faithfully represented in the image.

The use of a laser sheet source (Nd:YLF Laser), already available in the laboratory, allow collecting shadowgraph of the turbulent flow, and so a more detailed description of interface behavior should be achieved.

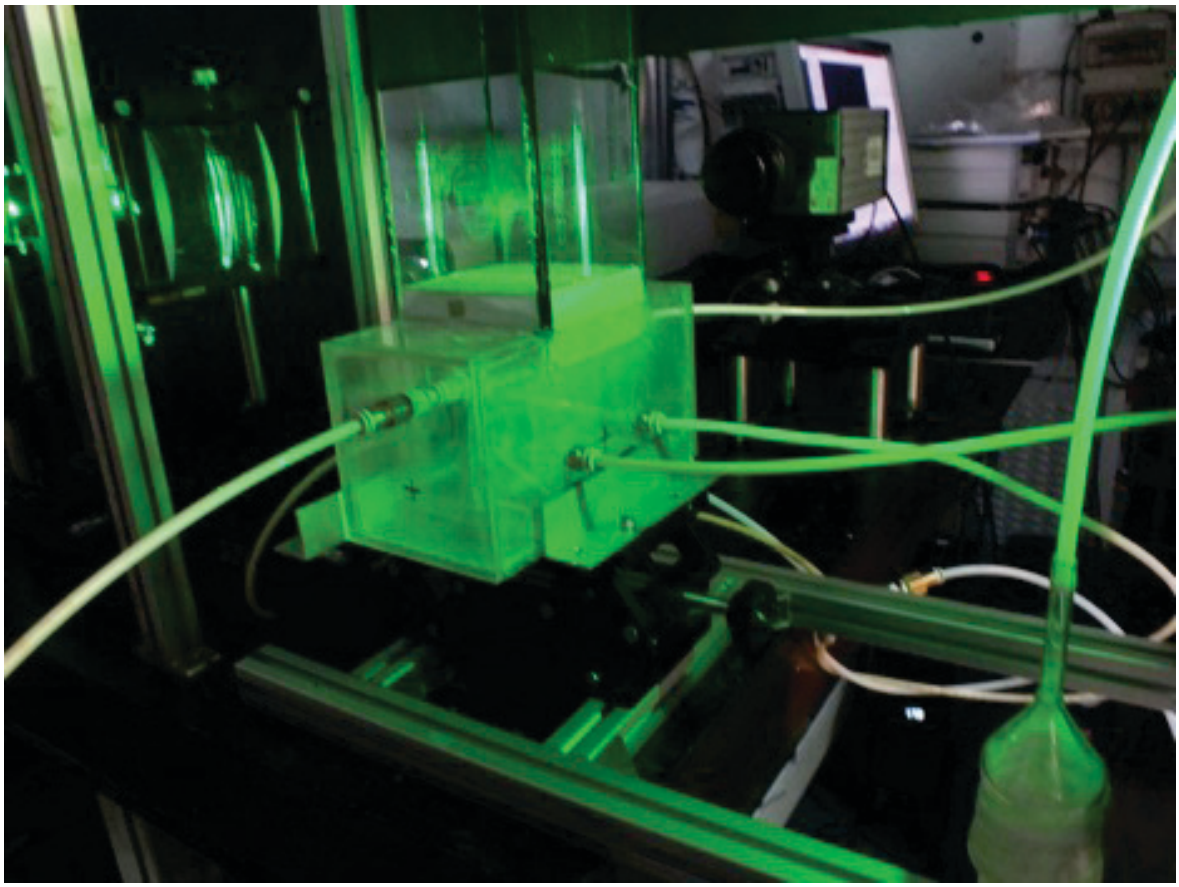

Fig. III.15 *Photograph of the test section during an illuminating of the flow using a thin laser light sheet.*

A side-view of the optical diagnostic apparatus is reported in Fig. III.16.

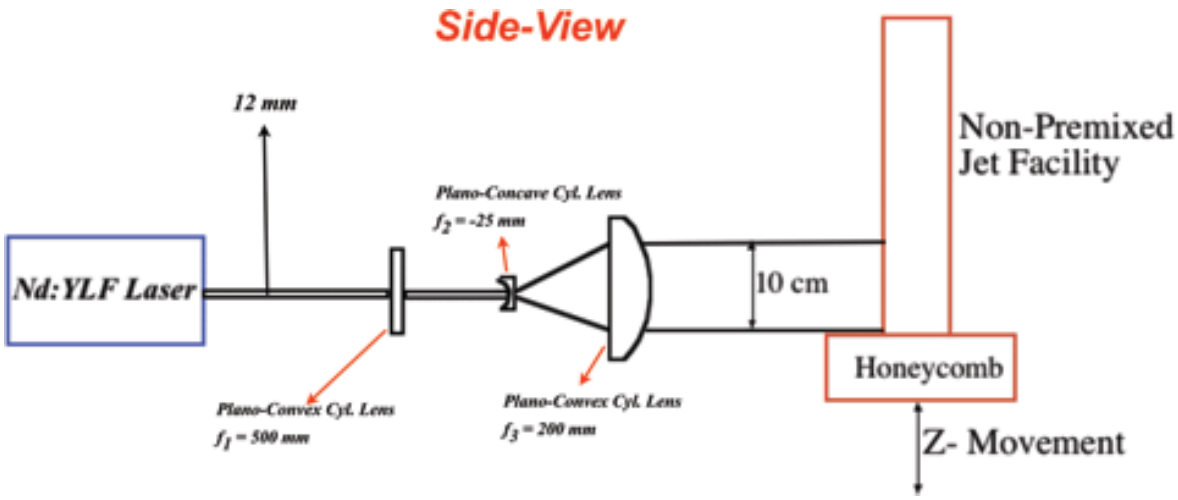

Fig. III.16 *Side-View of the optical diagnostic apparatus*

In planar imaging, the laser beam is formed into a thin sheet, which can be accomplished by several different techniques (Eckbreth AC 1988).

The method used in this thesis is shown in Fig. III.16, where a plano-convex cylindrical lens, that has a focal length of 500 mm, is used to focus the beam near the center of the field of view of the camera. Such long focal length lenses are used to increase the Rayleigh range, or the distance across which the beam remains focused. The larger Rayleigh range obtained from long focal length lenses permits also to have thicker sheets (in fact the final sheet thickness is 300 μm).

Figure III.17 also shows the use of a cylindrical telescope formed from a plano-convex lens of focal length f_2 and a larger plano-convex lens of focal length f_3. For high peak power laser beams, it may be best to use a negative (plano-concave) lens as the first lens to avoid a real focus and hence reduce the possibility of air breakdown. The reason for using two plano-convex lenses, where the convex sides are directed toward the collimated beam, is that this configuration minimizes the aberrations for a telescope formed from simple spherical lenses (Smith WJ 1990).

The cylindrical lenses expand the laser beam only in one direction, by a factor of f_3 / f_2 .

In this way is possible to obtain a laser sheet of about 10 cm starting from an initial laser spot of 12 mm.

Because the laser sheet height is determined by the height of the second cylindrical lens, producing large sheets (e.g., 100 mm) requires a large lens, which can be very expensive.

Spreading the laser beam into a sheet results in a large reduction in the intensity (or fluence); thus, when the intensity must be maximized, such as in Mie scattering imaging, the laser sheet can be formed by using a multipass cell. In this case, the laser beam is reflected back and forth between two confocal cylindrical mirrors. The main problem in

this technique is that the sheet intensity profile is very nonuniform, and the non-uniformity may be difficult to correct for on a single- shot basis. In this case, shot-to-shot fluctuations in the intensity distribution can be left as an artifact in the image. Another technique that can be used in low-velocity flows is the scanning method, where a CW laser beam is swept past the field of view by using a moving mirror. If time-resolved data are desired, then the sweep time must be short enough to freeze the motion of the flow. Because of this, the scanning technique is really useful only in liquid flows, which have relatively small characteristic flow timescales.

The double-pulsed, high-image-density images analyzed by digital spatial correlation analysis offered the best chance of achieving a large number of vector measurements per unit area and hence the best spatial resolution for studies of complex flows such as turbulence. At that time, images were necessarily recorded on photographic films that required chemical processing.

Subsequently, five developments combined to crystallize the form of the modern single-camera PIV system (Westerweel J et al. 2013):

- Digital computing power increased enough to permit the computation of two-dimensional (2D) spatial correlation functions using laboratory computers.
- The feasibility of digital PIV was established (Willert & Gharib 1991) and theory was developed that enabled optimal implementation and established the basis for further refinements (Keane & Adrian 1990, 1991).
- Digital cameras became available that were well suited to PIV by virtue of having more than 1 million square pixels.
- Special PIV cameras were developed that could separately store two images in close (<1 μs) succession.

- Double-oscillator solid-state Nd:YAG lasers became available with pulse energies sufficient to expose images of micrometer-sized scattering particles. Keane & Adrian (1990, 1991) defined a set of four simple "design rules" that provide guidelines to the optimal concentration of particles and exposure time delay Δt between the two light pulses with respect to the size of the interrogation domain, the light-sheet thickness, and the local variations in velocity.

This combination of a double-pulsed laser forming a light sheet, a single digital camera imaging light scattered from particles at 90° to the light sheet, and spatial correlation analysis of the images to determine their displacement in the image plane is a standard that has remained remarkably constant over the past two decades. A complete PIV system is shown schematically in Figure III.17. The laser pulses are separated by an easily adjustable time delay Δt , and the pulse durations are short enough, ~10 ns, to effectively freeze the images of submicrometer particles moving at all but the hypersonic velocities. Pulse energies range from 5 to 200 mJ, depending on the size of the illuminated region. The scattering particles are selected to follow the accelerations within the flow field with high accuracy (i.e., small velocity slip), to scatter light of intensity sufficient to form clear images, and to have relatively uniform size. Typically, ~1-μm aerosol particles, liquid or solid, are used in gas flows, and ~10-μm solid particles are dispersed into water flows. Images from the first laser pulse are stored in the first camera frame, and images from the second pulse go into a separate, second frame. This two-frame recording determines unambiguously the direction of the displacement between any pair of particle images, and it allows the analysis of overlapping images, thereby eliminating the need to employ image shifting.

The frames are divided into small interrogation regions, typically with dimensions of 32 × 32 pixels, and the displacement of the particle images in each interrogation region is measured by cross-correlating the images of the first and second frames to find the mean displacement that gives the maximum correlation. The correlation peak is located with subpixel accuracy by fitting a Gaussian or similar function to the tallest correlation peak, and this measurement gives an estimate of the mean displacement Δx of the particles residing in the volume that corresponds to the intersection of the interrogation domain with the laser light sheet. The velocity estimate, $\Delta x / \Delta t$, is assigned to the center of the interrogation region if the displacement is small compared to the interrogation region's size, or to the midpoint of Δx if the displacement is large, corresponding to a central difference estimate (Adrian & Westerweel 2010, p. 30). The analysis is performed on a set of interrogation domains that covers the flow field, typically with windows overlapping 50% or 75%.

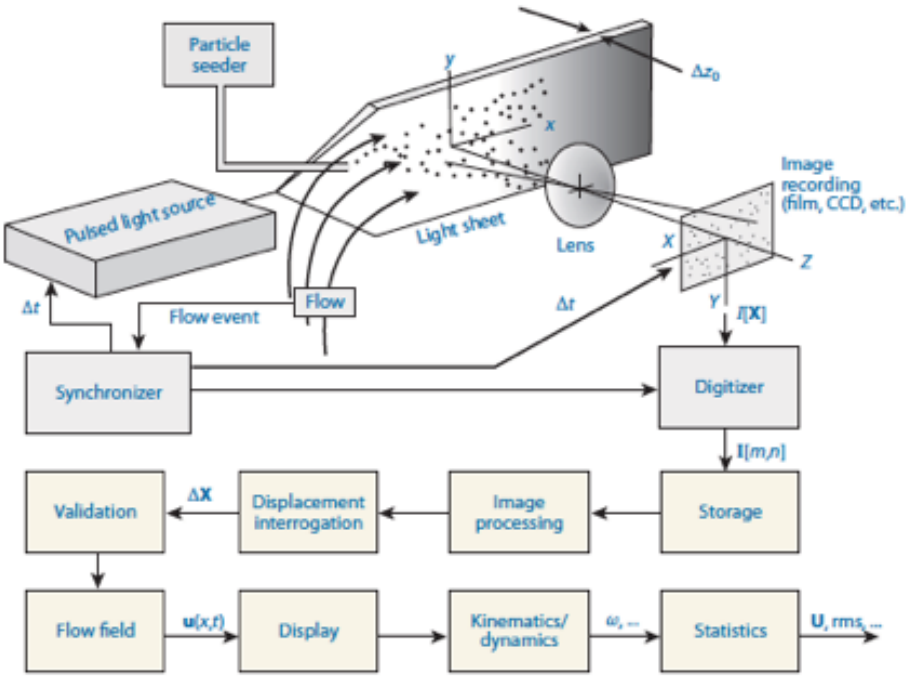

Fig. III.17 *Elements and processes in a planar, 2D particle image velocimeter system. Adapted from Westerweel et al. 2013.*

Eliminating the need to record on film simplified the PIV image acquisition and, more importantly, made it feasible to obtain the thousands of images needed for converged statistical averaging. Digital cameras have far fewer pixels than the equivalent number of pixels for film, so substantial resolution was lost in moving from film to digital cameras, but as cameras have grown larger (i.e., from 1 Mpixel to 14 Mpixel nowadays), they are approaching the performance of film, and the use of digital cameras is firmly entrenched in PIV.

The spatial resolution and velocity measurement error for a given exposure time delay Δt between the two recordings are defined relatively to the linear dimension l_x of the field of view and the maximum allowable particle displacement $\Delta x_{p.\max}$, which are represented as the dynamic spatial range (DSR) and dynamic velocity range (DVR); i.e.,

3.46) $$DSR = \frac{l_x}{\Delta x_{p,\max}} = \frac{L_X / M_0}{\Delta x_{p,\max}}$$

3.47) $$DVR = \frac{u_{\max}}{\sigma_u} = \frac{M_0 \Delta x_{p,\max}}{c_\tau d_\tau}$$

where M_0 is the image magnification, L_x is the linear dimension of the image sensor, u_{max} is the maximum measurable velocity within the interrogation domain, and $c_\tau d_\tau$ is the minimum resolvable difference in the particle image displacement for a given particle image diameter d_τ . c_τ is a dimensionless measure for the ability of the interrogation algorithm to accurately determine the particle image displacement, and it is typically of the order of 0.05–0.2 (Adrian & Westerweel 2010). From these expressions, it follows immediately that the product of DSR and DVR is a constant,

3.48) $$DSR \text{ x } DVR = \frac{L_X}{c_\tau d_\tau}$$

which defines the performance of a given PIV system.

This uncertainty principle states that a PIV system can achieve high spatial resolution only with the penalty of reduced relative measurement accuracy, and vice versa.

The image diameter cannot be made smaller than the diffraction-limited spot size with current technology,so it is not a practical means of improving performance. The physical size L_X of digital camera arrays has been increasing slowly from 1 Mpixel to 14 Mpixel over the past 20 years, and further slow improvement seems likely to continue. The value of c_τ depends on the algorithm used to measure the displacement (including the peak interpolator), the image noise and background noise, particle image aberration, the fill factor of the pixels, particle image overlap, and particle image clipping by interrogation window edges. Currently, the best value achieved for c_τ in real 3D flows is approximately 0.05. The development of many new algorithms to determine displacement has not resulted in any substantial reduction of c_τ . Of the effects that determine the value of c_τ , the fill factor probably offers the most room for improvement, but it may be difficult to approach a 100% fill ratio using PIV cameras, and a new design is probably needed.

On the basis of the requirement previously described for an optimal PIV system, a cartesian coordinate system is selected such that the transverse coordinate axis (y) is oriented in the jet injection direction. Nearly invariant spanwise distributions of velocity components are observed in the interest of measured sections. It ensures that the two-dimensional characteristics of the tested flows are preserved.

A two-dimensional double-pulse PIV system with cross-correlation estimation, which was manufactured by Dantec Dynamics, is used for the instantaneous measurements of velocity field. The PIV system consists of the aforementioned laser (Litron Lasers LDY302), software Dynamics Studio 3.14, a high-speed camera with a 105 mm Nikon standard lens, a synchronizing timing hub, and a personal computer for data acquisition.

In the test-case conditions, the f-number is set equal to 2.8 with a scale factor of 3.3.

As said previously, the light sheet thickness has been estimated to be 300 μm at its waist based on digital images of a black diffuse target illuminated by the light sheet at an angle of 10°.

According to Nyquist theorem (Bendat JS et al. 2000), the frame rate must be at least twice as fast as the frequencies of small turbulent eddies such as that of Kolmogorov scale eddy to avoid the problem of aliasing statistics.

The frame rate of CMOS camera (Model Nanosense MkIII) for capturing digital images is 1040 frames/s with full spatial resolution of 1280 x 1024 pixel^2.

Typical minimum spatial resolution of camera is 0.045 mm/pixel. Turbulent stirring occurs extends on a wide range of scales. The smallest scale of turbulence is characterized by the Kolmogorov scale η, which can be estimated for a jet from the well-known relation of Antonia et al. (1980):

3.49) $$\eta = LC_1 \mathrm{Re}_L^{-0.75}$$

Here L is the characteristic length of the system, while C_1 is a constant (for a non-reacting system), which for a cold jet is estimated to be 2.4.

The frequency of Kolmogorov-scale eddies is estimated to be around 100 Hz for transitional flows. It, thus, assures the accuracy of turbulent data obtained in the present experiments.

As said previously, the central flow is seeded with neutrally buoyant TiO_2 particles of nominal mean diameter 2 μm. Based on a bulk average velocity of 2 m/s (model scale) the Stokes number for these particles is St = 7 x 10^{-4}, ensuring accurate flow tracing. Since each pulse is in a different frame, there is no directional ambiguity for the velocity vectors.

Turbulence statistics are computed using 1000 frames to assure the statistically stationary results. Reliabilities of PIV measurements are estimated to be 1.4% and 6% for mean and

root-mean-squared (r.m.s) fluctuating velocities, respectively, through the repeated experiments. The particle density in the working fluid is set to give an average of 12 particle images in each 32 x 32 pixel interrogation window. Images for PIV were acquired at a rate of 1 kHz and the digitized images are cross-correlated using a recursive rectangular grid algorithm, which uses 32 x 32 and then 16 x 16 interrogation windows to find the mean pixel displacement. A Gaussian peak fit is used to determine the location of the cross-correlation peak to sub-pixel accuracy. Post-processing comprises a standard deviation filter to remove spurious vectors, followed by an interpolation to fill any empty locations and a Gaussian smoothing. All measurements reported in this article were made on the mid-plane of section.

The magnification, for the test conditions, has been set to achieve a field of view of 41 x 52 mm^2. The flow field was investigated in the regions downstream of the test-section inlet. The y coordinate is aligned with the main flow direction.

Spatial averaging across the light sheet thickness is intrinsic to PIV, and consequently the thickness of the light sheet is a limit on spatial resolution in measurement of three-dimensional flows.

Flow visualizations and PIV measurements have been conducted under various conditions, which differ only for the seeding flow velocity. In these conditions, the flow is rapidly accelerated from laminar state to a transitional flow.

The repeatability, or random, error is a statistical error. The uncertainty associated with the repeatability error can be assessed using the central limit theorem (e.g., Coleman HW and Steel WG 1999).

The random uncertainty of the mean velocity u_r can be calculated with:

3.50) $$u_r = \frac{1}{N}\frac{z_\alpha}{2}\frac{r_{RMS}}{R}$$

with N the number of samples , z_α a variable related to the chosen confidence interval, r_{RMS} the root mean square of the measured two-dimensional velocity in a point and R the mean two-dimensional velocity at the same location. For a confidence interval of 95%, the corresponding value of $z_\alpha/2 = 1.96$. The uncertainty of the measurement results is around 2–4% in the largest part of the test section and it is slightly higher in the interface as a result of the locally higher turbulence levels. Note that R is the local two-dimensional velocity and not the maximum jet velocity in this case.

The implementation of image analysis techniques allows getting information on various interface morphological aspects as will be shown in the following.

The need for a quantitative characterization of advected-surface behavior from the sampled images requires the implementation of a set of acquisition and elaboration procedures, written in LabVIEW programming environment and based on a standard library of image manipulation algorithms (Klinger T 2003).

Complete description of image analysis procedures is presented in the next chapter, after introducing, in the next paragraph, a survey of the investigated operating conditions.

III.2.3 Test Conditions

One of the major difficulties in flow imaging is achieving adequate spatial and temporal resolution. This is particularly the case when flows are turbulent because the resolution requirements are typically very severe if it is desired to resolve the smallest scales at which fluctuations occur. Laminar flows, however, pose substantially less stringent requirements on resolution, compared to turbulent flows. The primary issue when considering the resolution requirements is the gradient of the flow property that is being measured because the gradient determines the amount of averaging that occurs across the resolution volume.

In many laminar shear flows including boundary layers, pipe flows, wakes, jets, and mixing

layers, the maximum gradient is the same order of magnitude as the overall gradient.

Turbulent flows have substantially more severe resolution requirements than laminar flows, owing to the much larger gradients that occur at the smallest scales of turbulence. In turbulent flows, the spatial fluctuations in flow properties, such as velocity, temperature, or concentration range in scale from the largest physical dimension of the flow (e.g., the local width of the boundary layer or jet) to the scale at which diffusion acts to remove all gradients. The largest scales are often called the ‘‘outer scales,’’ whereas the smallest scales are the ‘‘inner’’ or dissipation scales because these are the scales at which the energy of fluctuations, whether kinetic or scalar, is dissipated.

Using scaling arguments, the Kolmogorov scale can also be related to outer scale variables through the relationship, $\eta \propto \mathrm{Re}^{-3/4}$.

For the test chamber here presented, the Re is the mean Reynolds number based on outer scale variables (such as U and L, respectively the mean velocity and the total width in the test section).

Buch and Dahm (K. A. Buch 1998) make explicit use of such an outer scaling by defining the strain-limited scalar diffusion scale λ_D, as

3.51) $$\frac{\lambda_D}{\delta} = \Lambda \mathrm{Re}^{-3/4}\, Sc^{-1/2}$$

where δ is the 5–95% velocity full width of the flow.

Some measurements in planar jets suggest a value of $\Lambda \approx 14$ (Su LK and Clemens NT 1999). The finest velocity gradient scale, analogous to the Kolmogorov scale, is the strain-limited vorticity scale, $\lambda_v = \lambda_D Sc^{1/2}$. The strain-limited diffusion scales can be related to

the Kolmogorov scale by using measurements of the kinetic energy dissipation rate. For example, using the data for the decay of the kinetic energy dissipation rate for gas-phase round jets and taking $\Lambda = 11$,it can be shown that $\lambda_D \approx 6\lambda_B$ and $\lambda_v \approx 6\eta$.

If the mean kinetic energy dissipation scales are about 6η, then accurate measurements of the gradients will necessitate better resolution than this. This is consistent with thermal-wire measurements of temperature and velocity fluctuations, which suggest that a resolution of about 3η is sufficient for correct measurements of the smallest scale gradients (Antonia RA et al. 1993). Therefore, it is recommended that the resolution of the imaging system be no worse than $\lambda_D/2$ and $\lambda_v/2$, if the smallest fluctuations in a turbulent flow are to be measured accurately. It cannot be emphasized enough that because of the nature of the modulation transfer function of the imaging system, it is too simplistic to speak of ‘‘resolving’’ or ‘‘not resolving’’ particular scales in the flow. Progressively finer scales will be increasingly affected by the imaging system, and any quantitative measurement of gradients must take this into account.

On the basis of this background, in this PhD thesis, for the correct measurements of the smallest scale gradients, a threshold of about $\eta/3$ has been used for the choice of the flow field conditions in the chamber. This condition allows to achieve a resolution of the imaging system no worse than $\lambda_v/2$.

In particular, for the reference diagnostic configuration, the high-speed camera is equipped with a 105 mm Nikon standard lens that gives a minimum spatial resolution of 45 μm/pixel.

For this reason, as reported in Fig. III.18, the smallest resolvable scale ($\eta \approx 135\,\mu$m) corresponds to a Reynolds number of about 3800.

Moreover, some comparisons will be shown in the next chapters to emphasize this diagnostic aspects.

The mean Reynolds number in the chamber is defined as:

3.52) $$\mathrm{Re} = \frac{\rho L^{*} \mathrm{v}_{mean}}{\mu}$$

Where v_{mean} is defined as the mean velocity in the chamber (i.e. it is weighted with respect to V_{air} and V_{seed}) and L^{*} is the total width of the chamber (see Fig. III.11-b).

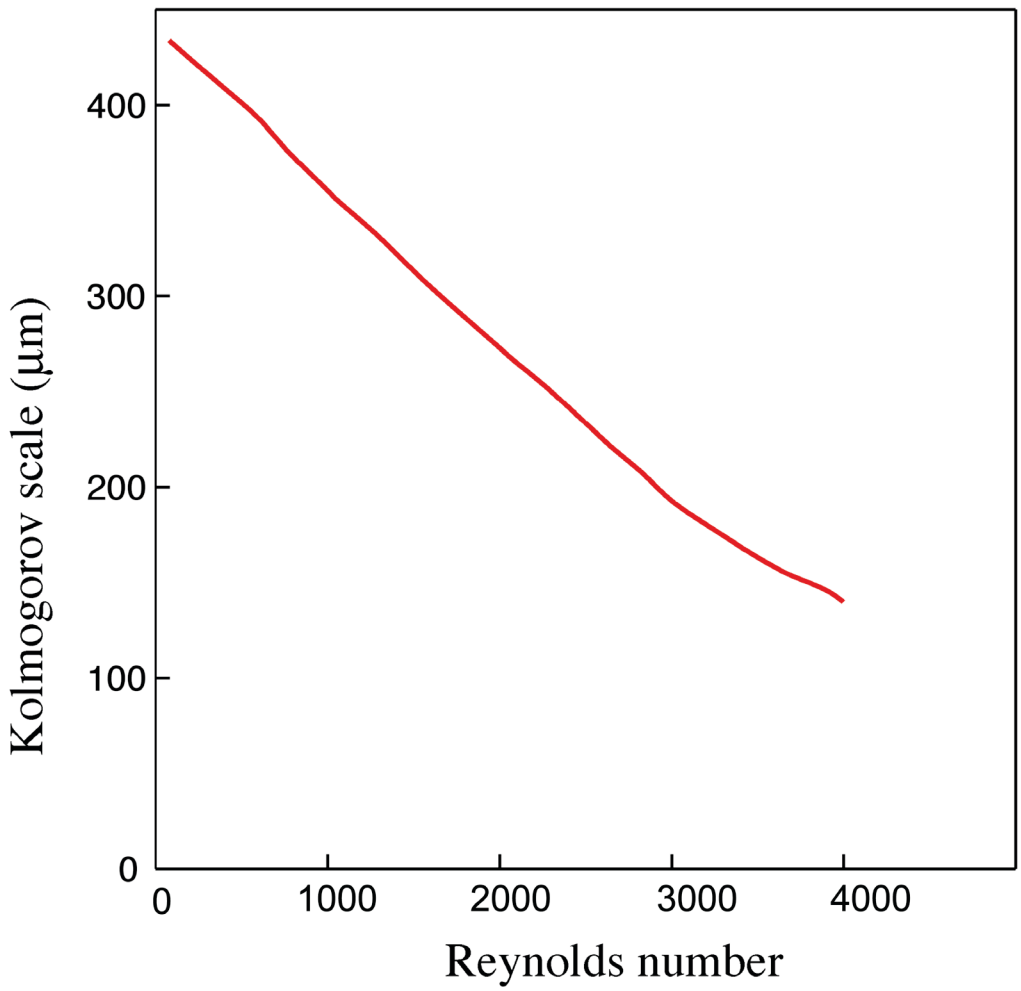

Fig. III.18 Kolmogorov scale vs mean Reynolds number

The pressure has been set at 1 Atm, while reference flow temperatures were 300 K.

In the following, test cases are defined by three elements: velocity of the seeding flow, velocity of the airflow and mean Reynolds number in the chamber.

Table 3.1 reports the matrix of the three investigated test cases.

Table 3.1

	Vair (m/s)	Vseed (m/s)	Re
A	***0,23***	***0,4***	***1000***
B	***0,31***	***1,31***	***2000***
C	***0,77***	***5,3***	***4000***

For each test case, an image analysis procedure has been performed, for evaluating interface density, tracer volume fraction and stretch rate. A comparison of the different trends will be shown in the next chapters for these three relevant cases.

It is here important to note that the case-C has been chosen to test the diagnostic capability of the optical apparatus. In fact, in this case the Reynolds number is 4000 which corresponds to a limit condition for the correct measurements of the smallest scale structures (see Fig. III.18).

Chapter IV
Digital image processing procedures

At present, there are relatively few reported images of the structure of the chemical reaction zones that occur within turbulent non-premixed flames. It has not been known if chemical reactions occur within thin layers or within thick distributed zones, or if the reaction layers are less wrinkled than the stoichiometric contour that exists within a non reacting jet.

However, the physical mechanisms of interaction between chemistry and turbulence is not well understood.

To overcome the intrinsic complexity of the problem, as reported in the first chapter, a sequential approach has been chosen for this non-linear process.

The building block of this strategy, named as “MultiSECtioning”, is the complete characterization of the “skeleton” of a non-premixed flame, i.e. the interface.

One of the goal of the work, reported in this chapter, has been to develop an image processing procedure to image the interface contour, which is located where the concentration of the tracer is discontinuous, that is where it passes from zero to a finite value on an infinitely thin surface, and to compute some numerical indicator of the ongoing of the stirring process.

The motivation for doing this were the following:

a. to measure quantities—such as the interface density, tracer volume fraction and stretch rate — that can be used to assess numerical model (for example LES);

b. to provide information about the evolution of the interface for testing the MultiSECtioning strategy;

c. to better understand the physical processes that occur in stirring/mixing processes.

Many fluid flows in nature are 'partly' turbulent, which implies that fluid regions in laminar and turbulent state often co-exist close to each other. One prominent feature of the non-turbulent flow region is that it is irrotational (Philip J and Marusic I 2012). Indeed, as confirmed in the recent studies of da Silva et al. (2011) and Westerweel et al. (2005), vorticity shows a very sharp variation at the interface.

Both vorticity and passive scalars were used for the identification of the outer bounds of the turbulent regions in a number of studies (Anand RK et al 2009).

The approach that is proposed in the next section is to use the sharp boundary between the seeded/not-seeded zone as a marker of the interface. This requires the elaboration of the interface images to determine:

- the structure of the material surface, including regions of high-curvature cusps, tracer concentration gradients, and interface contour;
- the interface density (Σ) and the tracer volume fraction Φ;
- the stretch rate conditioned on the interface location, by combining 2D laser light scattering and PIV techniques.

A purposely written algorithm which can be employed to determine the location of the interface from flow visualizations, without requiring any additional input, is thus proposed and evaluated in this chapter. Moreover, a method to obtain conditional sampling of the velocity field developed in order to evaluate the stretching rate of the interface is presented. Finally, a discussion about the limitations of these numerical procedures is provided.

IV.1 Interface density and tracer volume fraction evaluation

The characterization of advected-surfaces relies on the evaluation of relevant quantities as Σ and Φ and it is based on the implementation of an image analysis procedure, which visualize the seeded jet in the chamber and track the contour of the material surface.

The present chapter presents a fully automatic, and then repeatable, routine developed to evaluate the location of the interface contour.

With the post-processed image obtained from this procedure, interface density and tracer volume fraction can be evaluated.

A further advantage is the possibility of using a suitably large image set of images, reducing uncertainties due to statistical fluctuations.

IV.1.1 Detection of the interface location

Image processing is used for two somewhat different purposes:

a) improving the visual appearance of images to a human viewer,

b) preparing images for measurement of the features and structures present.

There are some important differences between human vision, the kind of information it yields from images, and the ways in which it seems to do so, compared to the use of imaging devices with computers for technical purposes. Human vision is primarily qualitative and comparative, rather than quantitative.

In this sense, an important difference between human vision and computer-based image analysis lies in the ways images are acquired.

Flow visualization (FlowVis) is one of the classic subfields of visualization, covering a rich variety of applications, from the automotive industry, aerodynamics, turbomachinery design, to weather simulation, meteorology, climate modeling, ground water flow and

medical visualization. Consequently, the spectrum of FlowVis solutions is very rich, spanning multiple technical challenges: 2D versus 3D solutions and techniques for steady or time-varying data.

Bringing many of those solutions in linear order is neither easy nor intuitive. Several options of subdividing this broad field of literature are possible. Hesselink et al., for example, addressed the problem of how to categorize techniques in their overview of research issues (Hesselink L et al. 1994) and consider dimensionality as a means to classify the literature.

According to the different needs of the users, there are different approaches to flow visualization. Figure IV.1 illustrates a possible classification of these approaches:

- *Direct flow visualization*: This category of techniques uses a translation that is as direct as possible for representing flow data in the resulting visualization. The result is an overall picture of the flow. Intuitive pictures can be provided, especially in the case of two dimensions. Solutions of this kind allow immediate investigation of the flow data.
- *Dense, texture-based flow visualization*: Similar to direct flow visualization, a texture is computed that is used to generate a dense representation of the flow. A notion of where the flow moves is incorporated through correlated texture values along the vector field. In most cases this effect is achieved through filtering of texture values according to the local flow vector.
- *Geometric flow visualization*: For a better communication of the long-term behavior induced by flow dynamics, integration-based approaches first integrate the flow data and use geometric objects as a basis for flow visualization. The resulting integral objects have a geometry that reflects the properties of the flow. A description of geometric techniques is presented by Post et al. (2002).

- *Feature-based flow visualization*: Another approach makes use of an abstraction and/ or extraction step which is performed before visualization. Special features are extracted from the original dataset, such as important phenomena or topological information of the flow. Visualization is then based on these flow features (instead of the entire dataset), allowing for compact and efficient flow visualization, even of very large and/or time-dependent datasets. This can also be thought of as visualization of derived data.

Note that there are different amounts of computation associated with each category. In general, direct flow visualization techniques require less computation than the other three categories, whereas feature-based techniques require the heavier computational efforts.

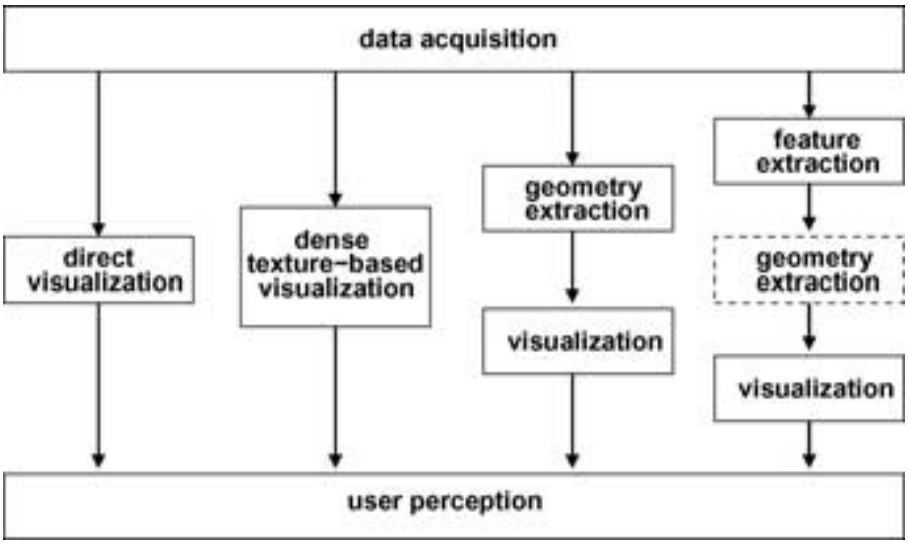

Fig. IV.1 *Classification of flow visualization techniques— (left) direct, (middle-left) texture-based, (middle-right) based on geometric objects and (right) feature-based.*

This classification provides a framework useful for placing the developed technique in a larger context.

The resampling tool that are here presented falls into the direct flow visualization category.

The instantaneous concentration field of the tracer is here used for the detection of the interface. The procedure described in this paragraph is aimed to detect the interface from flow visualizations and the routine will be here described for a reference image relative to the test case B.

The main steps of the procedure are summarized as follows:

- A background image is used in order to remove noise (single-pixel objects) in every processed image.
- Visually pleasing effects can be obtained when arbitrarily shaped field domains are addressed using contextual masking and defining a Region-Of-Interest for the source image (Gonzales et al. 2002)
- The gray level intensity images are transformed into binary images by means of a threshold, i.e. all pixels with a gray value above the threshold are labelled with '1', the remaining pixels are labelled with '0'. A fixed gray-value threshold (normalized by the maximum value of 255), is chosen using the technique proposed by Prasad and Sreenivasan (1989): in each image, the mean gray level intensity of all the pixels above the varying threshold is calculated. This conditionally sampled mean gray level intensity is shown in Figure IV.2-a, where the different curves correspond to different times (in the figure, the axes are normalized by the maximum gray-value). As the initially highly concentrated tracer is transported, the mean gray level is decreasing in time. We also computed the time averaged curve and used one fixed threshold for all images. In the time averaged curve shown in Figure IV.2-b, we detect two nearly linear regions indicated by two dashed lines. The intersection point of the two dashed lines determines the value of the threshold.

- The image is filtered using a linear filter that applies a convolution matrix to the image.
- In the binary images some patches of entrained fluid have been observed in the contour region (which appear as 'holes') and 'islands' of marked fluid outside of the continuous region. The detached patches of tracer are removed by means of morphological transformations and particle filters.

The boundary of the continuous object is obtained by means of a Sobel edge-detection filter (Wei GW 2007). The resulting discontinuous line is only a rough representation of the presumably continuous and smooth interface, reflecting mainly the large scales. However, for our purpose of analyzing the evolution of the material surface, this level of representation is regarded as sufficiently accurate.

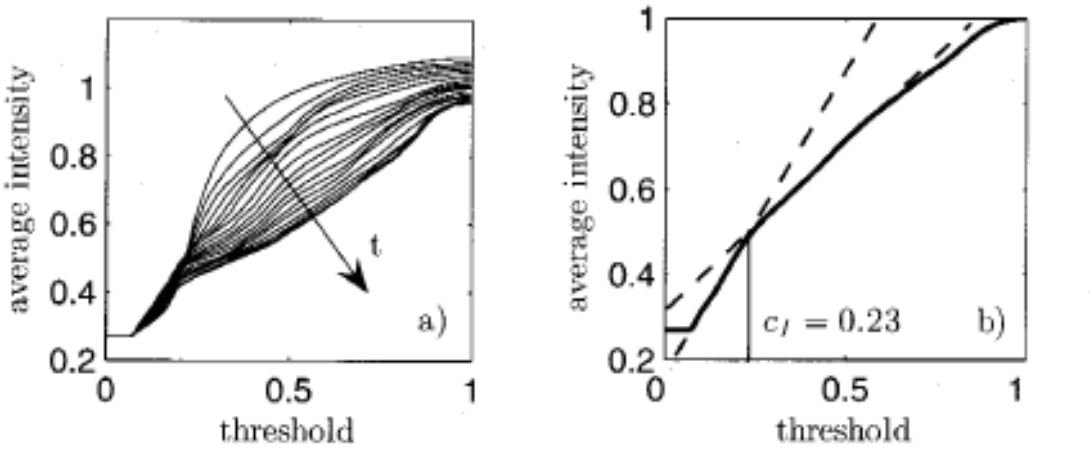

Fig. IV.2 *Average intensity of all pixels above the threshold as a function of the threshold, a) variation in time (0 — 20s) b) time averaged curve.*

The final processed images are achieved by averaging on the 3000 frames ensemble.

The image processing technique before described has been developed using IMAQ Vision Toolkit from National Instruments (Relf C 2003), and a snapshot of the control panel used for this algorithm is reported in Fig. IV.3. Furthermore, this procedure allows also for

calculate the profiles of tracer volume fraction and interface density along the transverse direction through a sum of pixels in the cleaned image and in the contour image, respectively.

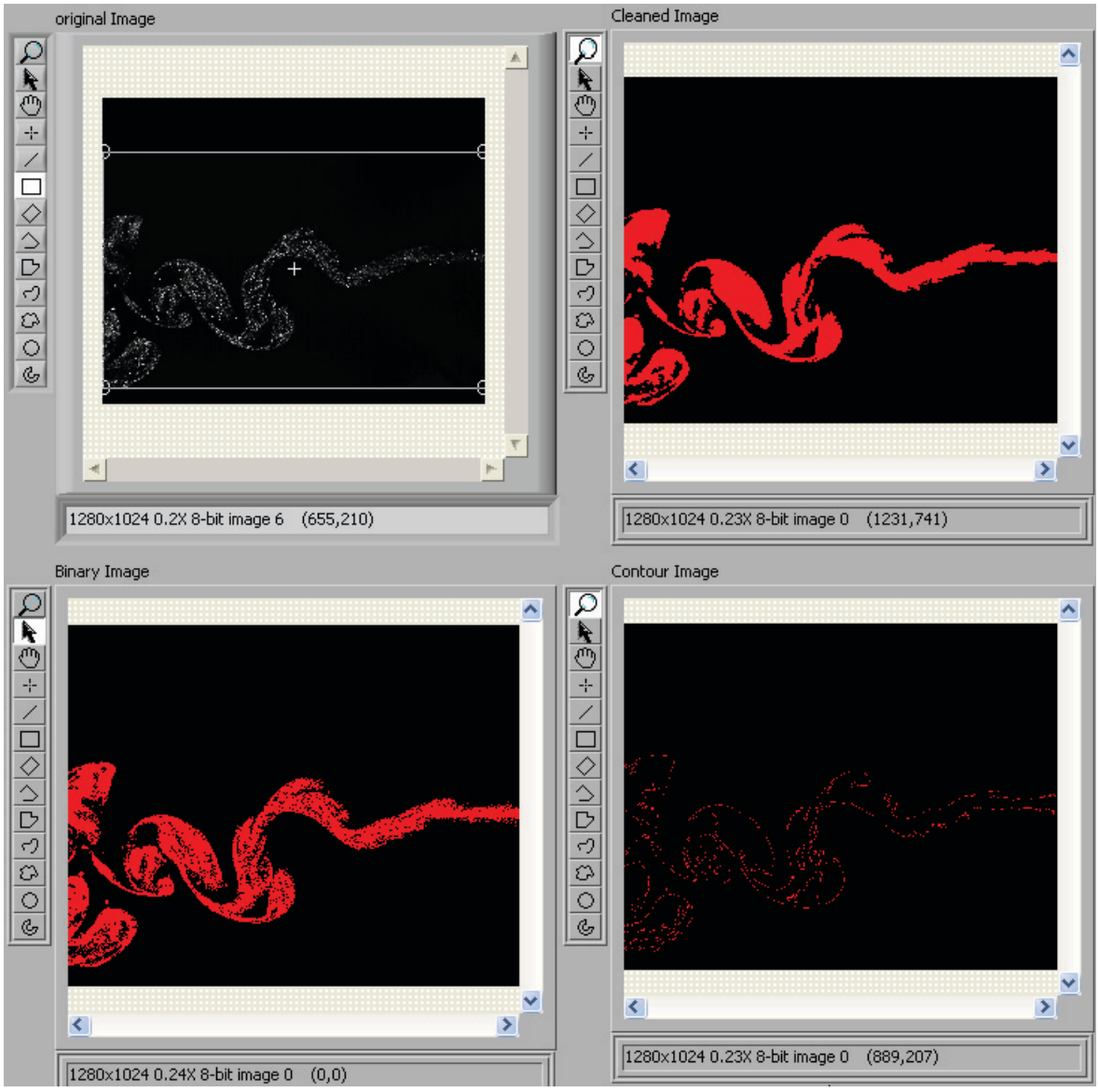

Fig. IV.3 Snapshot of the control panel used for the image processing algorithm

The main steps of the image elaboration procedure are briefly presented in the following sub-sections along with some elements on the image content modifications they introduce.

IV.1.1.1 Digital image processing fundamentals and background removal

An image is a two-dimensional array of values representing light intensity. For the purposes of image processing, the term image refers to a digital image. An image is a function of the light intensity: f(x, y), where f is the brightness of the point (x, y), and x and y represent the spatial coordinates of a picture element (abbreviated pixel). By convention, the spatial reference of the pixel with the coordinates (0, 0) is located at the top, left corner of the image. Notice in Figure IV.4 that the value of x increases moving from left to right, and the value of y increases from top to bottom.

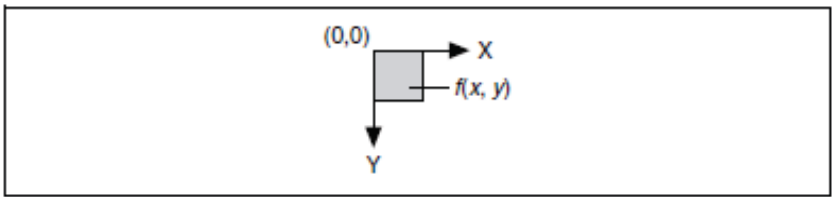

Fig. IV.4 Spatial Reference of the (0, 0) Pixel

In digital image processing, an imaging sensor converts an continuous image into a discrete number of pixels. Subsequently an analog-to-digital converter assigns to each pixel intensity a discrete value according to the selected encoding. This will produce a so-called grey scale picture which is, in essence, a matrix of numbers which is the digital translation of the analog intensity collected from the imaged field.

The precision of the numeric representation of pixel intensities depends on the dynamic range of the physical sensor and on the limits imposed by the available readout time (i.e. the time available to "translate" each pixel before a new exposure has to be taken). For the case of the camera used in the experimental work here reported the pixel depth is 8 bit (i.e. 256 grey levels). For this reason the original images are encoded using 8-bit unsigned integers that represent grayscale values between 0 and 255.

In the elaboration procedure it became necessary to use more detailed representations and thus alternative pixel depth were used according to the procedure requirements:
16-bit signed integers, representing grayscale values between –32,768 and +32,767;
Single precision floating point numbers (encoded using four bytes) representing grayscale values ranging from $-\infty$ to ∞.
Many different types of operations can be performed on digital images to produce new pictures. The following are some of the important types of picture operations:

Point operations: The output gray level at a point depends only on the input gray level at the same point. Such operations are extensively used for gray scale manipulations and for segmentation.
Local operations: The output level at a point depends only on the input levels in a neighborhood of that point. Such operations are used for de-blurring, noise cleaning, and edge and local feature detection.
Geometric operations: The output level at a point depends only on the input levels at some other point, defined by a geometrical transformation or in a neighborhood of that point.

Moreover it is possible to use some segmentation techniques to detect connected regions or groupings of pixels in an image and then make selected measurements of those regions. In particular, they classify pixels based on their gray levels.
In particular, thresholding consists of segmenting an image into two regions: a particle region and a background region. This process works by setting to 1 all pixels that belong to a gray-level interval, called the threshold interval, and setting all other pixels in the image to 0.

This kind of function converts the image from a grayscale image, with pixel values ranging from 0 to 255, to a binary image, with pixel values of 0 or 1.

The most simple threshold acts on the pixel intensity. Particles are characterized by an intensity range. They are composed of pixels with gray-level values belonging to a given threshold interval (overall luminosity or gray shade). All other pixels are considered to be part of the background.

The threshold interval is defined by the two parameters—Lower Threshold and Upper Threshold. All pixels that have gray-level values equal to or greater than the Lower Threshold and equal to or smaller than the Upper Threshold are selected as pixels belonging to particles in the image.

The gray level subpopulations corresponding to the different types of regions in a picture will often overlap. under these circumstances, segmenting the picture into regions by thresholding becomes difficult, since it is difficult to cleanly separate the overlapping subpopulations.

This overlap problem usually can be alleviated with the background removal, by cleaning the image before thresholding.

Poor illumination stemming from non-uniform tracer distribution results in blurred images with less brightness and low contrast as typically shown in the original image of Fig. IV.5, particularly in the overlapping region between the high-speed free stream region and the mixing layer.

As a first step for image elaboration, for each measurement a background image (acquired when there is no seeded flow in the field of view) is collected and then used to clean up the images, increasing the signal-to-noise ratio and removing the disturbance due to elements intercepting the light path by not belonging to the image. On the resultant image, a mask

operator, aimed at insulating the interesting portion of the image (i.e. the one containing the seeded jet) is applied for the successive step of thresholding.

Figure IV.5 shows an example of this procedure, which improves the image labeled as original, by subtracting pixel by pixel from the original image the background image. The result is reported in the right part of figure IV.5.

These pictures also show the loss of few seeded pixels at both top and bottom part of the image, due to the presence of stray light reflected by the channel sidewalls.

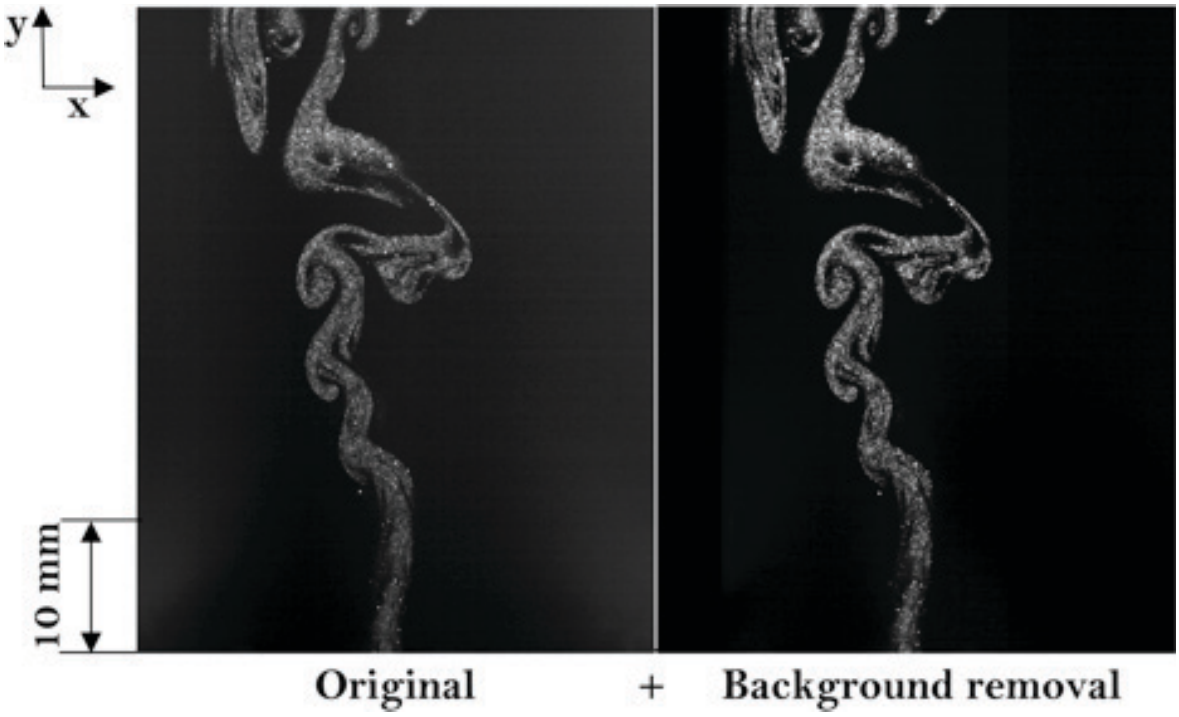

Fig. IV.5 Performances of the background removal on a reference image

IV.1.1.2 Image masking, thresholding, filtering and enhancement

A mask is a black and white image of the same dimensions as the original image (or of the region of interest).

An image mask isolates parts of an image for processing. Pixels in the image mask determine whether corresponding pixels in the inspection image are processed. If a pixel in the image mask has a nonzero value, the corresponding pixel in the inspection image is

processed. If a pixel in the image mask has a value of 0, the corresponding pixel in the inspection image is not processed.

An image masks is used when we want to focus the inspection on particular regions in the image. In fact, it is possible, using a mask to limit the area in which the function applies an image mask to the bounding rectangle of the region that we want to process. This technique saves memory by limiting the image mask to only the part of the image containing significant information.

To keep track of the location of this region of interest (ROI) in regard to the original image, an offset is used. A region of interest (ROI) is an area of an image in which we want to perform some image analysis. A ROI can be defined using standard contours, such as an oval or rectangle, or freehand contours.

Therefore, the second step of the algorithm described in this chapter, uses a masking operator of the image shown in the right part of the figure Fig. IV.5 with the definition of a ROI. Hence, by using the mean pixel intensities, binary images are obtained by threshold filtering with equal weight given to all pixels.

This process converts a grey image into a binary image: if the interesting pixels in the image are greater than or equal to the threshold value (k), then they are set to 1 while others in the image are set to 0 in order to obtain the object contour.

As said previously, the thresholding procedure is similar to that used by Prasad et al. (1989). In order to uniform the procedure of selecting the threshold value the ROI, where the computation of the averaged intensity value is made, is kept constant in all the sets of images elaborated.

The thresholded image should map object brightness into picture gray level in a monotonic fashion, and this mapping should ideally be the same at every point of the image. In practice, however, the mapping often varies from point to point.

Experimental images are subject to many different types of noise. Some of these are independent of the image signal, but others are not; some are uncorrelated from point to point, while other are “coherent”. If a thresholded image is too noisy, the black region may contain scattered white points, and the white region scattered black points.

To overcome these problems, some methods of noise removal, or more generally of image “smoothing” have been used. To this aim linear filtering procedures of the images have been applied in several sequential steps.

A linear filter replaces each pixel by a weighted sum of its neighbors. Averaging can be used to smooth an image without blurring it. A convolution matrix defining the neighborhood of the pixel also specifies the weight assigned to each neighbor. This matrix is called the convolution kernel. If the filter kernel contains both negative and positive coefficients, the transfer function is equivalent to a weighted differentiation and produces a sharpening or highpass filter. Typical highpass filters include gradient and Laplacian filters. If all coefficients in the kernel are positive, the transfer function is equivalent to a weighted summation and produces a smoothing or lowpass filter. Typical lowpass filters include smoothing and Gaussian filters.

Image degradation generally also involves some degree of blurring, the extent of which is described by the spread function of the degradation operation. Blurring is an averaging, or integration, operation; this suggest that it is possible to sharpen by performing differentiation operations. Blurring also weakens high spatial frequencies more than low ones; this suggests that images can be sharpened by emphasizing their spatial frequencies.

However, when an image is noisy as well as blurred, differentiation and high-emphasis filtering cannot be used indiscriminately to sharpen it, since the noisy generally involves high rates of change of gray levels, and it usually becomes stronger than the image signal at high frequencies.

When an irregular surface is affected by reflection light, holes often appear on the surface after image threshold processing. In this case, the detached patches of tracer can be removed by means of morphological transformations and particle filters. In particular, these binary morphological operations extract and alter the structure of particles in a binary image.

These operations have been used to improve the quality of the image. Therefore, inner holes and outer islands are removed according to their measurements.

As a consequence of such enhancement procedures, the image become cleaner, as reported in Fig. IV.6.

Fig. IV.6 Cleaned image after thresholding and filtering

The Figure IV.6 show a processed image of the seeded flow as collected by the digital camera for air velocity and seeding velocity of 0.31 and 1.31 m/s, respectively.

It is characterized by a regular development of instabilities along the jet, since the presence of unsteady phenomena, probably connected to eddy shedding, causes the jet to flutter. Moreover the camera frame rate is capable to capture the dynamics of both jet fluttering and surface growth, so that quantitative information can be obtained about volume fraction.

IV.1.1.3 Edge detection

Canny edge detection (Canny J 1986) with a Sobel operator has been used on the resulting binary images of Fig. IV.6 to obtain the regions of steep gradients corresponding to interface.

Technically, it is a discrete differentiation operator, computing an approximation of the gradient of the image intensity function. At each point in the image, the result of the Sobel operator is either the corresponding gradient vector or the norm of this vector. The Sobel operator is based on convolving the image with a small, separable, and integer valued filter in horizontal and vertical direction and is therefore relatively inexpensive in terms of computations. On the other hand, the gradient approximation that it produces is relatively crude, in particular for high frequency variations in the image.

In simple terms, the operator calculates the gradient of the image intensity at each point, giving the direction of the largest possible increase from light to dark and the rate of change in that direction. The result therefore shows how "abruptly" or "smoothly" the image changes at that point, and therefore how likely that part of the image represents an edge, as well as how that edge is likely to be oriented. In practice, the magnitude (likelihood of an edge) calculation is more reliable and easier to interpret than the direction calculation.

Since the intensity function of a digital image is only known at discrete points, derivatives of this function cannot be defined unless we assume that there is an underlying continuous intensity function which has been sampled at the image points. With some additional assumptions, the derivative of the continuous intensity function can be computed as a function on the sampled intensity function, i.e. the digital image. It turns out that the derivatives at any particular point are functions of the intensity values at virtually all image points. However, approximations of these derivative functions can be defined at lesser or larger degrees of accuracy.

The Sobel operator represents a rather inaccurate approximation of the image gradient, but it is still of sufficient quality to be of practical use in many applications. More precisely, it uses intensity values only in a 3×3 region around each image point to approximate the corresponding image gradient, and it uses only integer values for the coefficients which weight the image intensities to produce the gradient approximation.

Fig. IV.7 Contour image after edge detection

The resulting discontinuous line is only a rough representation of the presumably continuous and smooth interface, reflecting mainly the large scales. However, for our purposes this level of representation can be regarded as sufficiently accurate.

The Sobel algorithm uses a nonlinear filter which replaces each pixel value with a nonlinear function of its surrounding pixels. It extracts the contours (detects edges) in gray-level values. Like the linear filters, the nonlinear filters operate on a neighborhood.

The result of this operation is a 1-pixel-thick continuous curve that represents the surface boundary. The shape of the interface in Fig. IV.7 seems to be quite complex and with fractal features.

IV.1.2 Estimation of volumes and surfaces

We concentrate now on the geometry of the small scales of the scalar field inside the chamber whose global dispersion properties have been described in the previous section. Our aim here is to characterize how the volume occupied by the scalar and the surface of the interface, which separates the volume from the clear surrounding medium and in which it is enclosed, evolves in time. Since we only have access to a planar cut of the three-dimensional structures through the scalar jet, by 'volume' and 'surface' we actually mean 'area' and 'contour length' of the objects we visualize on a two-dimensional image.

As previously described, the passive scalar (i.e. the tracer concentration) is initially confined in a compact region whose front is further distorted into multiscale elongated structures. As the core of the jet is converted into thin sheets, the concentration distribution widens and the scalar elements with a concentration close to the injection concentration get less and less numerous.

As seen previously, to define the geometrical support of the scalar field, has been defined a given concentration threshold C_s (i.e. average pixel-intensity threshold) that is the largest

region of space occupied by the scalar. It is clear, in particular far from the injection point when the jet has appreciably diluted into the airflow, that the geometry of the scalar distribution is threshold dependent, because of the blurring action of mixing on the definition of the contours.

One might thus expect that both the surface and volume of the scalar support will present an average pixel-intensity threshold dependence and their sensitivity to the choice of C_s will be discussed later.

The sequence of operations for measuring volumes and surfaces as a function of time and of the stream-wise coordinate for a given threshold C_s is similar to that used by Villermaux et al. (1999) and and example of it is reported in Fig. IV.8. It divides the processed-image into N vertical rectangles (figure IV.8) that are then further elaborated.

Taking for example the processed-image reported in Fig. IV.6, we sum the images obtained by this procedure thereby obtaining the volume of the objects, the volume being defined here as the sum of the pixels within closed contours plus the pixels constituting the contour.

The number of pixels different from zero contained into the j-th rectangle of the images are the measure of the instantaneous volume of the material surface at time t_k and at location y_k. With this procedure it is also possible to obtain the profiles of the volume along y_k.

When these operations are applied at processed-images similar to that in Fig. IV.7, then a measure of the surface is obtained.

The mean values of the volume and surface are obtained by averaging over 3000 frames.

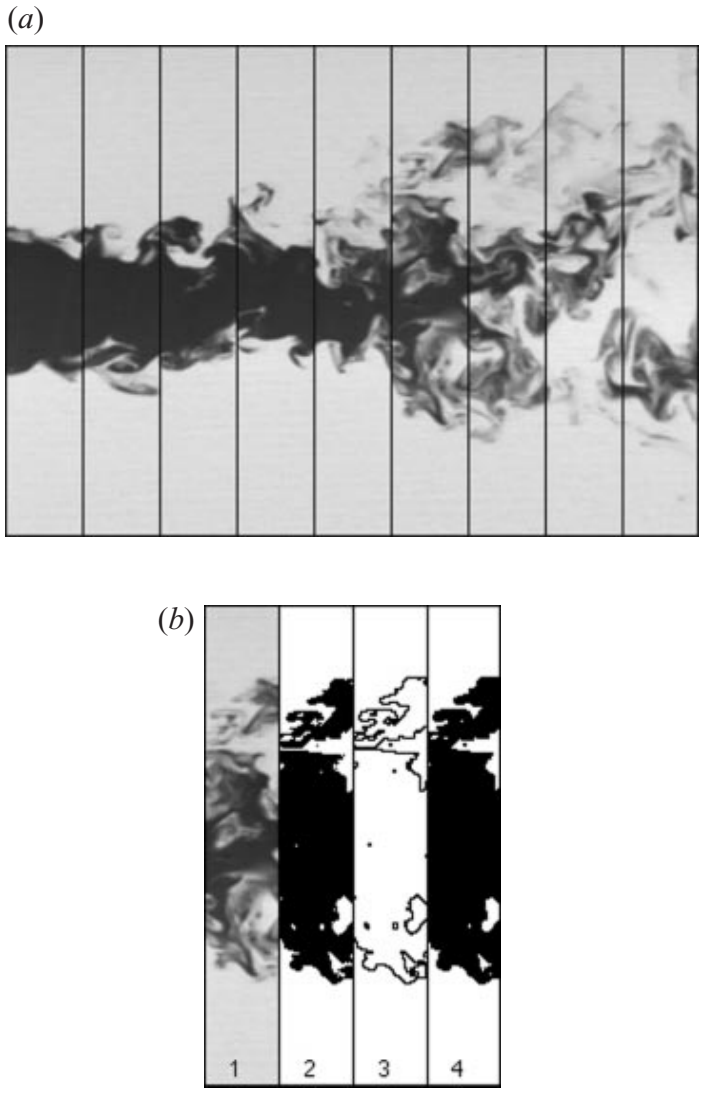

Fig. IV.8 *(a) Division of an image into nine equal rectangles.*
(b) Example of the procedure applied to the 6th rectangle of (a) to extract, after binarization (2), surface (3), and volume (4) of the object contained in (1).

Actually in the elaboration performed in this thesis work the size of the elaboration rectangles was 1 × 1024 pixels. Being the camera resolution 1280 x 1024 then N=1280. in figure IV.7 the size of the rectangles is larger to better clarify the procedure. It has to be stressed that elaborating the pictures with rectangles 1 pixel wide allows for a subsequent average over larger rectangle widths according to the needs.

The operations previously described allow to measure the values of volume and surface in real-world units when multiplied by the value of the resolution used for the acquisition.

Moreover, tracer volume fraction and interface density can be estimated simply dividing the volume and the surface by the area (in real-world units) of a j-th rectangle.

IV.2 Conditional flow field statistics

The relationship between the interface dynamics and the diffusion flame in turbulent fields is simple. In fact, the intermaterial surface can be considered as the skeleton of the process. The whole reaction process is concentrated in this structure, in the asymptotic limit, or part of it is centered in the reacting layer, where high-temperature oxidation takes place. The distribution of the stretch rates along the interface affects the oxidation rate in such a way that it determines the presence or absence of the flame and the partition of the material surface in reacting or non-reacting components.

Other elementary flame structures are related to single level interface.

In the previous section, an algorithm has been presented, in which some terms (Φ and $\sum$) involved in the interface evolution have been obtained by means of post-processing techniques.

Moreover, other quantities, defined in the third chapter, as $\underline{\hat{v}}$ and $\widehat{K_{\Delta A}}$ have to be evaluated to describe correctly the interface density evolution (see eq. 3.37).

The stretch rate along the interface is the sum of a contribution due to velocity gradient and another related to the mean curvature (see eq. 3.25).

In particular the strain is the primary mechanism responsible for the stretching of the surface area.

As the surface sheet becomes intensely folded, strain causes its surface area per unit volume to increase, and therefore, strain rate appears in the source term of the equation for interface density.

The total stretch rate can be separated into two components:

4.1) $$\widehat{K_{\Delta A}} = \widehat{K_{\Delta A}}\Big|_M + \widehat{K_{\Delta A}}'$$

where $\widehat{K_{\Delta A}}\Big|_M$ is the measured stretch rate and $\widehat{K_{\Delta A}}'$ is the contribution from unresolved small scales. The latter contribution is estimated to be small, relative to the measured one. This will be further discussed in the next chapters.

One problem that has prevented the measurement of interface strain rate is that one must first be able to identify the surface layer and then be able to record velocity along this layer.

The mean and instantaneous velocity field conditioned on the interface has been obtained by means of PIV measurements.

The partial derivatives of the velocity are determined using a three-point central differencing scheme on the regularly spaced velocity grid.

A contour extraction routine included in Labview has been used to obtain the couple of boundary point (x,y), i.e. the contour. Moreover the mean curvature is also evaluated with the same routine.

In the following paragraph, details of these operations will be given.

IV.2.1 Velocity field overlay

To sample the flow, a Dantec Dynamics two-component PIV system with a LDY Laser Nd:YLF laser operating at 527 nm was used.

A camera NanoSense MkIII with resolution 1280x1024 pixels is used to visualize the flow in a plane perpendicular to the model surface.

The operating parameters for the PIV system were kept constant throughout the study. The system operated in cross correlation mode using two images, which were correlated in the frequency domain. Before correlation, a 3x3 Low pass filter was used to widen the particle images. A 32x32 pixel interrogation area was used, and the images were processed with 75% overlap yielding a raw vector field of 317 x 253 vectors. The vector acceptance criteria showed a peak ratio of at least 1.2, and 25% maximum velocity variation from neighboring vectors.

This high overlapping is used only for conditioned velocity measurements, while for the whole flow field measurements is used an overlap of 25% between the interrogation windows (as reported in Fig. IV.9).

With a 75% overlap the instantaneous velocity field of the seeding-flow is measured with high-accuracy, as reported in Fig. IV.10.

This procedure is able to detect all the small-scale features, compatibly with the system resolution.

Fig. IV.9 Flow field in the jet with a 25% overlapping

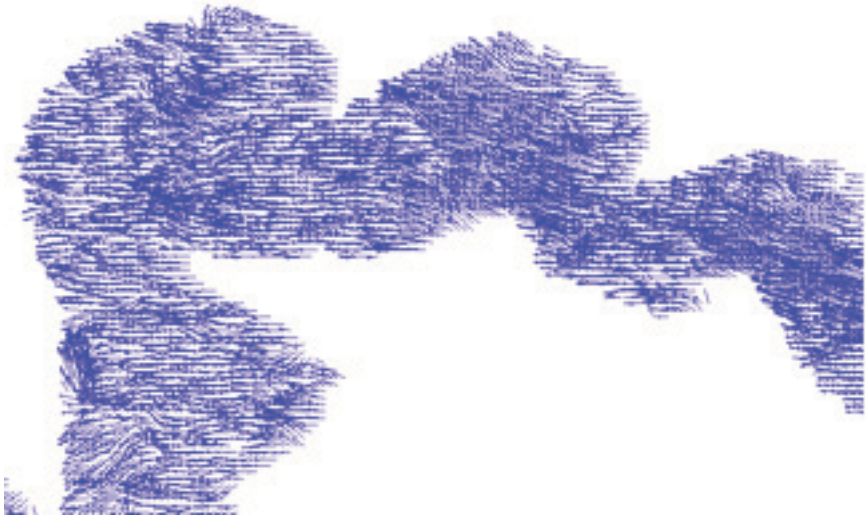

Fig. IV.10 Detail of a specific region of the flow field with a 75% overlapping

A subsequent treatment of this image allows to obtain a two-dimensional matrix related to each component of the velocity field.

After these operations it is possible to superimpose the flow field on the corresponding cleaned image (or contour image) that has been obtained with the algorithm showed in the previous chapter.

This step is obtained by means of an image overlay operation which is the projection of geometric models on to image planes using object pose.

Once some features are detected in the image, feature correspondence is carried out, i.e. associating a detected feature with the equivalent feature in the model. It is executed by generating a hypothesis of which features in the image correspond to which features in the model, and then doing verification based on the geometric relationship among them. This task is much easier in object tracking than in general object recognition, because feature correspondences in the last frame can be a very good initial estimate for the next frame in tracking. It is, however, necessary to verify successfully tracked features in the case of

tracking, because some features may be missed by illumination changes or for other reasons.

After the feature correspondence, object position and orientation are computed. In the case when object-centered coordinates in the models are used, the object pose can be calculated from an image and the problem is formulated as an inverse problem to solve the nonlinear relationship between object pose and feature positions in the image. Nonlinearity comes from perspective projection. This problem can be solved by recursive methods. If the visual tracking is at a relatively high rate, the change of object pose between cycles is not large and the algorithm tends to converge within a small number of iterations.

To overlay velocity informations on an image, both images (i.e the image that contains both the components of the velocity and the reference to the cleaned image) must have the same dimensions.

For this reason, the images that contain the velocity informations have been resampled in order to have the same size of the reference image. The resampling procedure has been implemented using a bi-cubic interpolation operator that reduces interpolation artifacts.

This procedure can be applied both to the cleaned image (Fig. IV.6) and to the contour one (Fig. IV.7) in order to obtain a visualization of the velocity field conditioned on the whole surface and on the contour, respectively.

The results of previous operations are shown in Figg. IV.11 and IV.12. Specifically, to obtain visualizations of the velocity vectors overlaid on the contour image, a masking operator has to be applied. This kind of operations allow to track the evolution of the seeded jet by visualizing both the large scale and small scale features. An appropriate threshold for the vectors and for the array interleave have to be chosen in order to have a correct visualization of the object.

Fig. IV.11 *Velocity vectors overlaid on the cleaned image*

Fig. IV.12 *Velocity vectors overlaid on the contour image*

Despite of the utility of these visualizations, they do not permit to have important informations about the conditioned flow field such as the location of the points on the contour and the velocity values for every contour point.

IV.2.2 Stretch rate estimation: contour extraction and curvature measurements

A focused characterization of strain rate in the vicinity of the interface between two jets does not appear to have been widely previously performed for material surfaces.

The objective of this sub-section is to show some digital image processing techniques in order to determine the key processes influencing surface generation.

It is useful to consider the expression for hydrodynamic strain under certain simplifying assumptions in order to illustrate some key points.

4.2) $$K_{\Delta A} = K_{planar} + K_{normal}$$

The manner in which these normal and planar deformation flow strain terms translate into surface strain is illustrated in Figure IV.13.

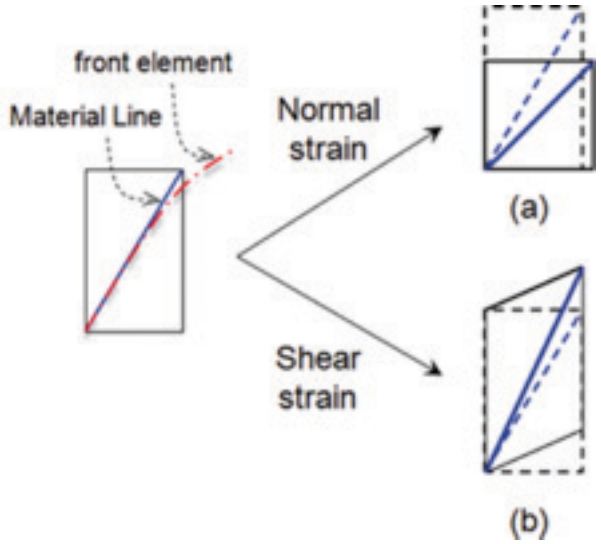

Fig. IV.13 Illustration of the manner in which (a) flow deceleration and (b) flow shearing causes compressive and extensional surface straining.

The left image illustrates a material line just upstream of the surface front. The right image shows the deformation of this material line due to flow strain an instant later.

The increase–decrease in length of this material line leads to surface strain, as detailed in Law (2006).

A second (t, n) coordinate system has been also defined that is parallel (t) and orthogonal (n) to the streamline at every point of the interface contour, which is indicated by the solid black line in Figure IV.14. The material surface contour has been determined with a contour extraction algorithm that will be clarified in the following. The corresponding velocities are given by v_t and v_n.

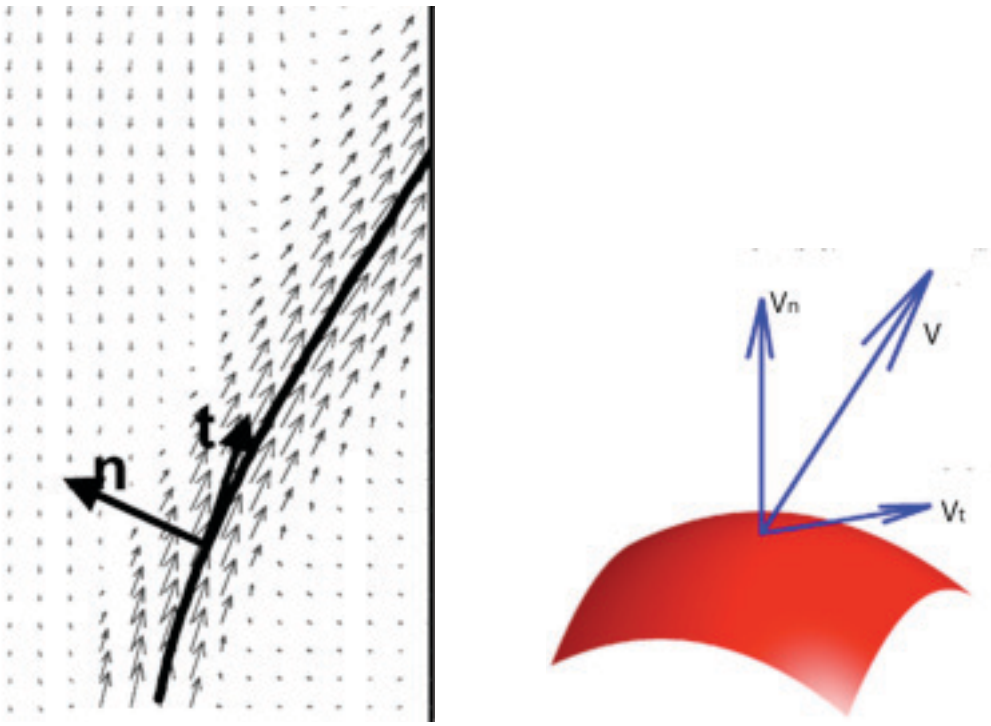

Fig. IV.14 (t, n) coordinate system on the contour.

IV.2.2.1 Contour extraction

Contour extraction involves the following steps:

1. Curves are extracted from the ROI.
2. Optionally, multiple curves are connected according to settings stored in connection parameters.

3. A single connected curve is selected to represent the contour.

Curve Extraction

A curve is a set of edge points that are connected to form a continuous contour. Curves typically represent the boundary of the parts in the image. In curve extraction, curves are the underlying information used to represent a template and to match the template in an inspection image.

The curve extraction process consists of finding curve seed points and tracing the curve.

A seed point is a point on a curve from which tracing begins.

To increase the speed of the curve extraction process, the algorithm visits only a limited number of pixels in the image to determine if the pixel is a valid seed point. The number of pixels to visit is based on the values that the user provides for the search step and ROI parameters. The larger the search step and the smaller the ROI, the faster the algorithm searches for seed points. However, to make sure that the algorithm finds a seed point on all of the curves, search step must be smaller than the smallest curve along the search direction.

The algorithm scans from the selected side of the ROI. Starting at the first pixel, the edge contrast of the pixel is computed. If the edge contrast is greater than the given threshold, the curve is traced from this point. If the contrast is lower than the threshold, or if this pixel is already a member of an existing curve previously computed, the algorithm analyzes the next pixel in the row to determine if it qualifies as a seed point. This process is repeated until the opposite side of the ROI is reached. The algorithm then skips search step pixels along the side of the ROI and repeats the process.

When it finds a seed point, the curve extraction algorithm traces the rest of the curve. Tracing is the process by which a pixel that neighbors the last pixel on the curve is added

to the curve if it has the strongest edge contrast in the neighborhood and the edge contrast is greater than acceptable edge threshold for a curve point. This process is repeated until no more pixels can be added to the curve in the current direction. The algorithm then returns to the seed point and tries to trace the curve in the opposite direction. the following figure illustrates this process.

Curve Connection

Curve connection parameters specify how the contour extraction algorithm connects individual curves to produce contours. To determine if two curves should be connected into a single curve, the contour extraction algorithm compares the endpoints of both curves. Each pair of end points is considered for connection until no more connections are possible. To connect, the endpoints must satisfy all of the conditions provided in the parameter array.

If the distance between the endpoints of a curve are within the distance specified by Max Endpoint Gap, the curve is considered closed. Closed curves cannot be connected to other curves. However, closed curves can be selected to represent the contour.

Contour Selection

After the curves have been extracted from the image and optionally connected, a single contour is selected from this set of curves based on contour selection parameters. You can select the first contour detected along the search direction, the longest contour, or the contour with the highest edge strength averaged from each point on the curve.

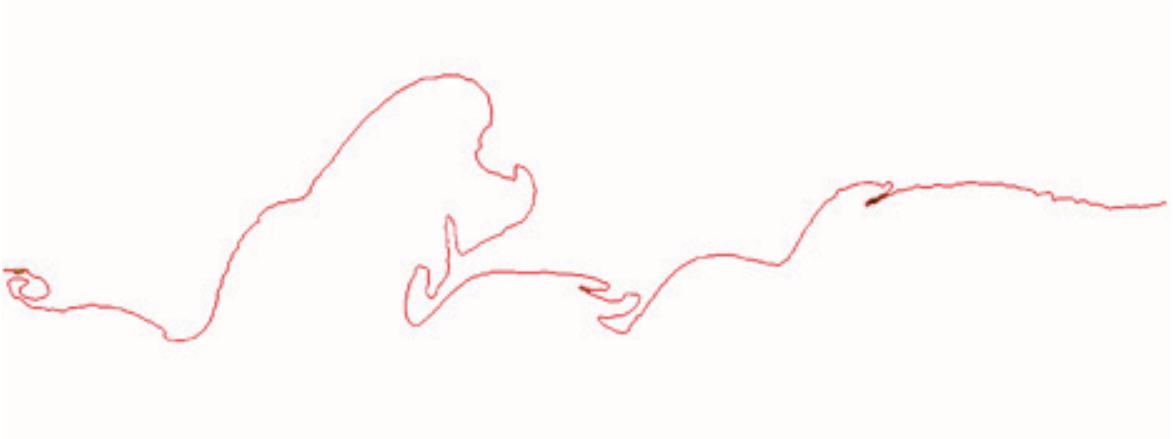

Fig. IV.15 Example of the extracted higher contour

The above presented procedure is automatic for extraction of upper/lower contours of 2D images. Obviously, some parts of the methods need improvement in terms of computational complexity.

When the present method is applied to the cleaned image reported in Fig.IV.6, the higher traced contour, reported in Fig. IV.15, is obtained.

For the sake of brevity, the procedures here reported are applied only to the higher contour. They can obviously be extended to the lower one.

In particular, once the contour has been extracted from the cleaned image, curvature can be measured on the single point that has been obtained.

Finally, velocity gradients on each contour point can be computed by applying numerical discretization schemes.

IV.2.2.2 Curvature measurements

The curvature of a contour is calculated from the edge points of the contour and by the input kernel size. For each point along the contour an algorithm selects two additional points at half the kernel width before and half the kernel width after the current point. The algorithm fits a cubic b-spline to the three points. Curvature represents the inverse radius of

the circle inscribed by the cubic b-spline at the current point. Curvature can be negative. A negative curvature indicate a curve to the left along the search direction. If the current point is too close to either end of the array to choose the additional points, the curvature is calculated as 0.

IV.2.2.3 Velocity gradients and stretch rate evaluations

Determining the velocity gradients requires getting as close as possible to the surface sheet in the strongly shearing flow, without allowing any bins to overlap the interface itself, which would induce bias errors in the measurement. For this reason, derivatives were estimated using a three-point central differencing scheme.

This method introduces systematic errors into estimation of the derivatives in the transverse direction. The errors are much smaller for derivatives in the flow direction.

A scheme of the derivative method is reported in Fig. IV.16.

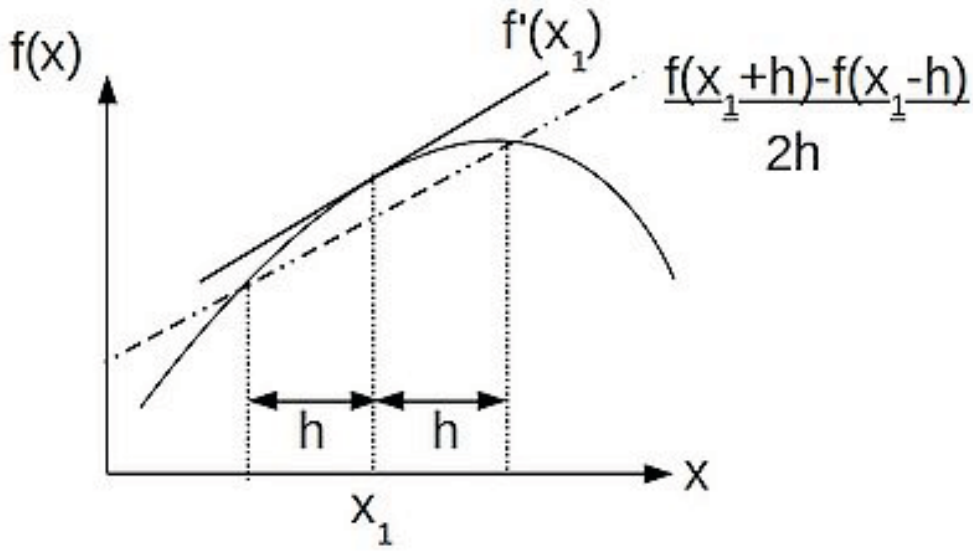

Fig. IV.16 Scheme of the three-point central differencing method

Stretch rate measurements has been obtained by means of equation 4.4 on the basis of the pre-estimated quantities.

In particular, ensemble average quantities have been obtained in each point of the contours (i.e. higher and lower contour).

4.4) $$\left\langle K_{\Delta A} \right\rangle = \left\langle \underline{\nabla}_t \cdot \underline{\mathrm{v}}_t \right\rangle + \left\langle \mathrm{v_n} C \right\rangle$$

The stretch rate profiles for some selected conditions are reported in the next chapter.

Chapter V
Experimental results and numerical validation

In this chapter, results relative to three test conditions, as mentioned in chapter III (and also reported in Table 5.1 for clarity), corresponding to three mean Reynolds number in the test section, are reported. The Reynolds number is based on the mean velocity pattern, as reported in eq. 3.52.

For these cases, profiles of interface density and volume fraction have been obtained and they will be shown in the next sub-sections.

The flow visualizations and velocity vectors for these three cases are reported in the following.

The behaviour of velocity magnitude has been obtained for each case from PIV measurements.

A first qualitative analysis of the scattered light patterns, collected using the previous-described diagnostic system, can help to clarify the general features of the interfaces generated in these cases.

Table 5.1

	Vair (m/s)	Vseed (m/s)	Re
A	***0,23***	***0,4***	***1000***
B	***0,31***	***1,31***	***2000***
C	***0,77***	***5,3***	***4000***

The evaluation of the aforementioned quantities will be reported in this chapter initially for the three reference cases to quantify the stirring process in relation to the different fluid-dynamics conditions. Then the analysis will be extended also taking into account Reynolds number values from 100 to 4000.

Moreover, the profiles of $\sum$ and Φ are also discussed in relation to the relative velocity (Δv) between the airflow and the seeding flow. The Δv, in fact, is directly related to the morphological behaviors of the material surface.

All the profiles reported in this chapter are relative to a fixed field of view of the acquisitions.

In fact, the high-speed camera is fitted with a 105 mm Nikon standard lens. The f-number is set equal to 2.8 with a scale factor of 3.3. The magnification has been set to achieve a field of view of 41 x 52 mm^2. The spatial resolution of this optical set-up is 0.045 mm/ pixel. The flow field was investigated in the regions downstream of the test-section inlet. The y coordinate is aligned with the main flow direction.

The effect of resolution on the evaluated quantities will be discussed in the next chapter, to point out the limits of the experimental procedures.

Moreover, some comparison between flow visualizations and Direct Numerical Simulation are reported at the end of this chapter.

V.1 Results from flow visualizations and Particle Image Velocimetry

The flow visualizations have been performed for seeding-flow velocity ranging from 0.4 to 6 m/s while the velocity in the outer channels has been varied from 0.23 to 1 m/s.

These values have been chosen to reproduce transitional/turbulent flow conditions into the test section. In fact, at environmental pressure and temperature conditions, the mean

Reynolds number into the chamber varies from 1000 to 4000 reproducing both laminar and transitional/turbulent conditions.

The images on the left of Figure V.1 shows instantaneous representative images of the flow inside the test-section, taken in the mid-plane for the cases reported in Table 5.1.

The images reported in the figure are only examples and are useful to give an impression of the great variety of structures, which can be established in 3D flows.

The visualizations has been obtained by means of a 2D laser sheet technique, which has been previously described, for detecting the interface. The sequence of consecutive visualizations is taken at a 1 kHz frequency.

The patterns show several vortical structures that can be identified together with the subsequent decay. In Fig. V.1, it is possible to observe the first region of the jet characterized by a short laminar zone followed by very weak undulation, which quickly generates a discrete vortex. The second region constitutes a zone of evolution of successive vortices moving downstream within the mixing layer and growing in size to end finally in a chaotic zone.

Furthermore, it is worthwhile to note that the optical diagnostic apparatus is able to follow the evolution of the small-scale structures in the aforementioned range of Reynolds number.

This fact is well shown in the Figure V.2 in which the temporal evolution of the interface in the Case B has been reported.

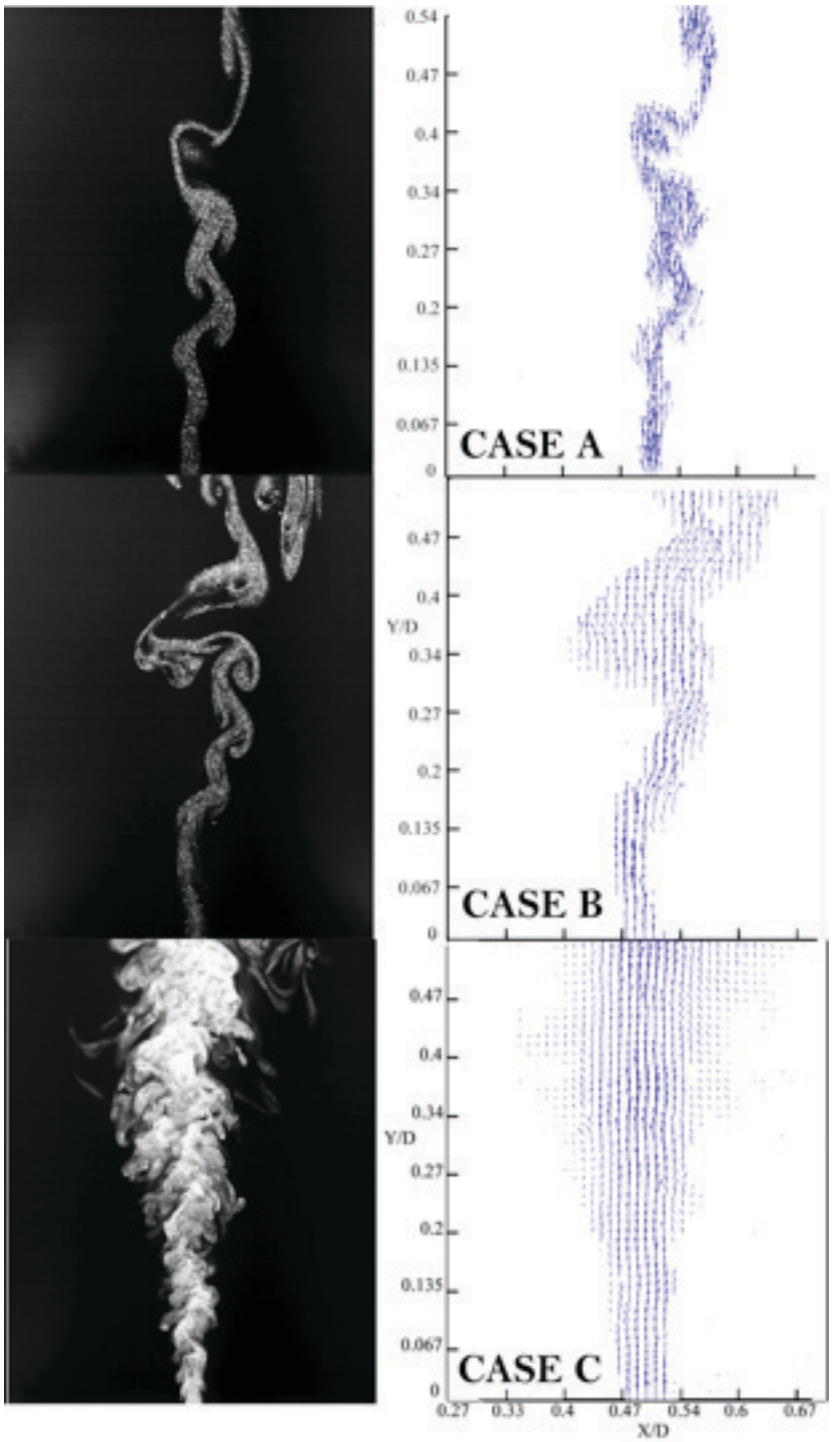

Fig. V.1 *2D Laser Light Scattering and velocity vectors patterns of the seeded jet for a selected time*

In this sequence of images, some background effects are evident on the side of the picture. They are eliminated in the image-processing phase when a background removal is performed.

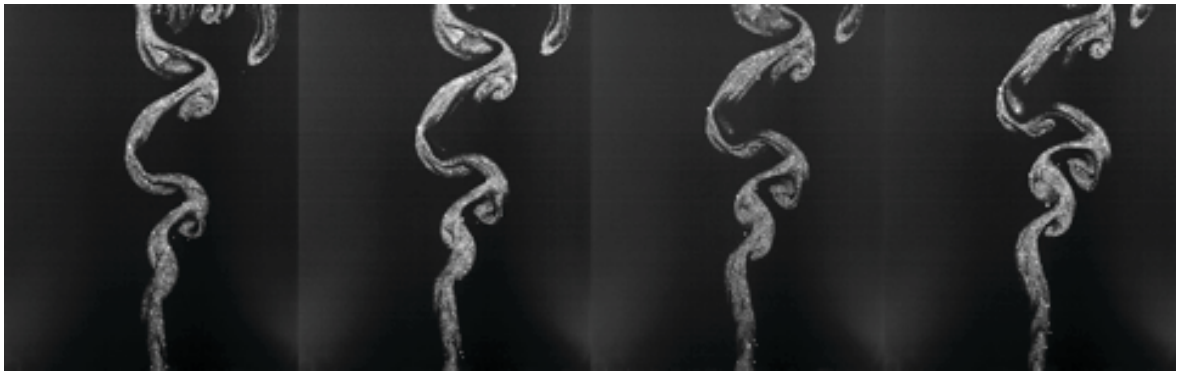

Fig. V.2 Interfaces sequence of a transitional isothermal jet

Moreover, in Figure V.3, in fact, is reported a snapshot of the evolution process of a vortex. A feature of the stirring process is the tendency of the streamwise vortices to move away from the core. This trend can be observed in the sequence of Figure V.3. It is associated with the curvature of the streamwise-vortex lines imposed by the primary-vortex velocity field.

The curvature induces a precessional motion which causes uneven spacing between the streamwise vortices on the periphery of the primary vortex. The resulting counter-rotating pairs have self-induced axial velocities directed outwards, away from the primary vortex core.

Based on the flow visualizations described in this section, PIV measurements were conducted for the same range of seeding-flow velocity, which is the range for which transitional flow is present.

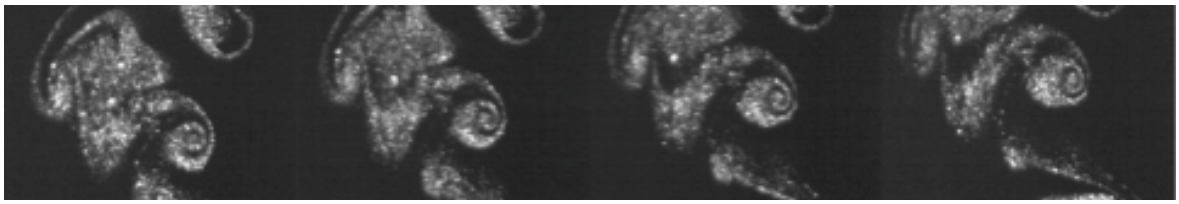

Fig. V.3 Snapshot of the temporal evolution process of a vortex

Some previous works (Cavaliere A et al. 1995, Cavaliere A et al. 1994) devoted to give an assessment of the great variety of structures which can be established in 2D flows, showed the presence of similar behaviour obtained here for a three-dimensional case. They provide a methodological framework, based on the evaluation of lagrangian quantities, by which turbulent diffusion flames might be classified by means of well-defined criteria.

Three typical instantaneous velocity magnitude contours (colored) at t=0.01 s between x/D = 0.27 and x/D = 0.7 are presented in Fig. V.4 to show the different features obtained when the Reynolds number is increased. For presentation purpose, a blanking operation was applied at the contours by fixing a threshold on the velocity magnitude. The oscillating behavior of the jet column is clearly demonstrated, reflecting the feature of entrainment of the seeded jet and its interaction with ambient airflow. The highest velocity contours (yellow-red) occur in the central region of the jet but are not continuous. The discontinuous nature of highest velocity fluid is expected to result from the induction of the ambient fluid by primary coherent structures.

The sub-scale vortical structures are evident in Fig. V.4. These structures result from the folding and stretching of the interface structure. It is worthwhile to note that these phenomena are more evident with the increasing of seeding flow velocity, i.e. of the local Reynolds number (Luo K et al. 2008).

The three instantaneous velocity contours in Fig. V.4 reveal a consistent trend of non-symmetry in the coherent structures and they also show the typical multifractal characteristics of these material surfaces.

The primary structures result from the roll-up of the initial mixing layer. They are known, where present, to engulf ambient fluid, and so to dominate the initial growth and entrainment of co-flow fluid in jets.

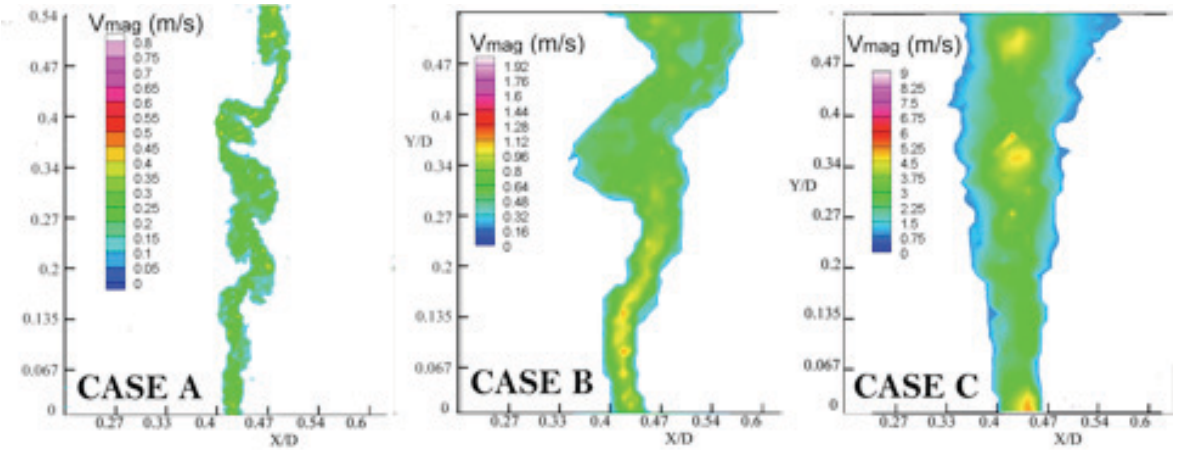

Fig. V.4 Instantaneous velocity magnitude contours at t= 0.01 s

The downstream propagation of coherent structures, even beyond the end of the potential core, is evident throughout the contours. The structure is complex, even if it is possible to identify a single core. Nevertheless, some important observations can be made, especially by comparing the different structures that were obtained by increasing the mean Reynolds number of the jet. With increasing the distance from jet inflow, the interface structure seems to become increasingly three-dimensional, and the streamwise vortices play a controlling role in the entrainment process. Self-induction, vortex stretching, and reconnection, which make the flow structure more three-dimensional, become the dominant fluid-dynamical processes involved in the stirring of these jets. The present measurements are only in one plane, so that it is not possible to directly assess the presence of streamwise vortices.

The turbulence intensities in the mixing layer are higher than at the centerline because the mixing layer generates highly energetic large turbulent structures.

The evolution of the structures close to the nozzle exit is due to the initial shear layer instabilities, which break down into vortical structures with kinetic energies of the order of the mean flow in the layer. Immediately downstream of the nozzle exit the initial turbulence energy decays before it increases under the effect of the growing large

structures that originate from the roll-up in the mixing layer. When the initial mixing layer becomes unstable, velocity fluctuations increase in amplitude, which result in the roll-up of the mixing layer into a train of azimuthally oriented vortex elements which pair-up to form large vortical structures and this occurs for any slight asymmetry in the spacing of two adjacent vortices, or inequality in their strengths.

V.2 Interface density and tracer volume fraction profiles

The two-dimensional scattering patterns showed before have been processed to smooth, and clean the images and to identify a digitized contour of these one. Each digitized contour has been obtained with image processing algorithms showed in the previous chapter.

The level of smoothing depends entirely on the threshold level for the light intensity.

The main advantage of this smoothing procedure is to preserve the surface front whereas quantization noise and small-scale errors of the Mie scattering measurements can be removed from the contours.

After these procedures, the local surface front length can be determined accurately for the purpose of $\sum$ and Φ measurements. It is here important to note that these evaluations are very dependents on the choice of the field of view, i.e. on the lens resolution that has been fitted on the camera. In this chapter all the presented profiles has been obtained with a spatial resolution of 0.045 mm/pixel.

The two-dimensional interface density and tracer volume fraction, have been obtained from the ensemble averages of the volume-averaged values, that have been evaluated with the image processing algorithm explained in the fourth chapter.

V.2.1 Interface density and volume fraction trend for test-conditions

The axial development of $\sum$ and Φ is shown in Fig. V.5 for three cases. Both the quantities are plotted versus the streamwise direction y.

$\sum$ is reported in mm^{-1}, while Φ is a dimensionless quantity that varies between 0 and 1.

The trend of these relevant quantities has been estimated with the procedure reported in paragraph IV.1.2

It appears that the generation of surface area is dominated by the length scale variations with the axial distance, and it depends on the increase of the turbulence intensity.

It is clear that the profiles of $\sum$ grow rapidly as the surface area increase.

The evolution of surface is a reversible process where fluid elements are transported across the domain, rotated, stretched and folded. Even for very simple velocity fields, the combined action of stretching and folding of fluid elements generates complex patterns, hence the name ‘chaotic advection’ or ‘stirring’.

In the absence of diffusivity, the advection homogenizes the distribution of the tracer at an exponential rate and blurs the structures present in the initial distribution as well as the patterns created by chaotic stirring.

If U and C denote a characteristic velocity and a typical tracer volume fraction, and if the tracer varies over length scales L, the stirring time is of the order UC/l.

From an initial macroscopic patch of tracer, or in a macroscopically forced tracer, the advection is the absolute ruler of the fate of the material surface. Nevertheless, the stirring stretches and folds the interface. Two fluid elements containing different tracer concentrations are stretched into long filaments that the velocity field brings together at exponential rates, creating higher gradients (Lekien F et al. 2007).

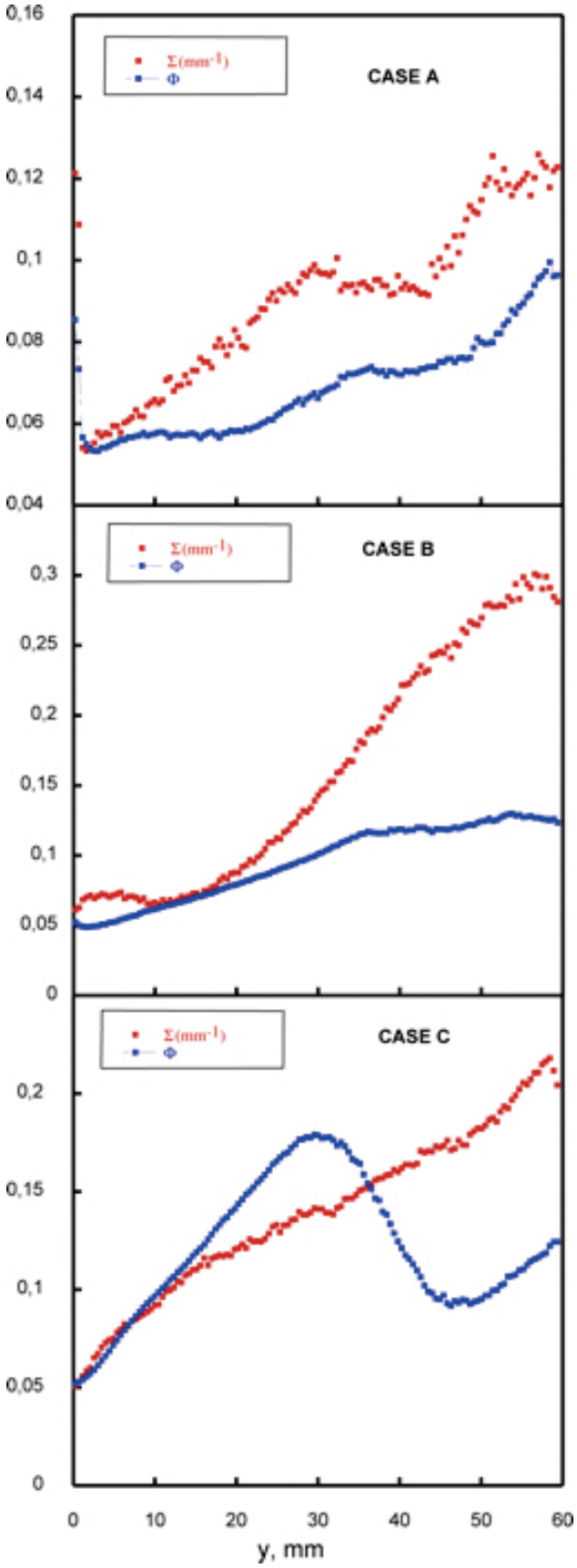

Fig. V.5 Profiles of interface density and tracer volume fraction along y-coordinate

These considerations partially justify the $\sum$ profiles along y which show the main effect of stretching and folding, i.e. a more than linear increase of interface density.

In particular, the interface density reaches a maximum value of 0.12 mm^{-1} when the flow is mainly laminar (A-Case) while it assumes higher values for the Case B.

On the other hand, the interface density shows smaller values for the C-case when it is compared with the B-case. This result has to be evaluated with some criticism.

In fact, as said before, by increasing the mean velocity in the chamber, the interface density should increase due to stretching and folding.

This fact is apparently in contrast with the results reported in Fig. V.5 in which the maximum value of $\sum$ for the case C is smaller than that for the case-B.

Such apparently anomalous behaviors can be explained by the fact that in the case C the detected values of surface and volume are probably underestimated. In fact, as discussed in chapter III, the minimum detectable scale is fixed by the spatial resolution (45 μm/pixel), while that characteristic of the small scale features increase with the level of turbulence.

This results, hence, show the limits of the diagnostic apparatus for the specified spatial resolution of the camera. These experimental limits will be better discussed in the next chapter.

Therefore, from a reference length scale L, chaotic stirring stretches the fluid elements containing the tracer in thin filaments (Giona M et al 2002). The duration of that process can be determined by following a reference trajectory $x(t)$ and a nearby particle $x(t)+\delta(t)$. The distance between the two particles follows eq. 5.1:

5.1) $$\frac{d\delta}{dt} = \frac{\partial v}{\partial x}\delta$$

The fast reduction of length scale, or hyperbolic stretching, is possible due to large negative eigenvalues in the velocity gradient. The magnitude of the velocity gradient determines how fast advection can shrink the length scale of the process.

Moreover, it is possible to understand from Fig. 5.1 that also relatively simple velocity fields can produce exponential area growth due to stretching and folding, and numerical tracking become numerically very expensive.

Integrable cases of the advection equations lead to what is called regular advection (Aref H 1984). Non-integrable cases implying motion are called chaotic advection or "lagrangian turbulence".

This last property is responsible also of the chaotic nature of these flows, because the dissipative regions, linked in a particular way through hyperbolic manifold, are the locations of positive exponential stretching of material line and surface. In other words, these regions are the locations from which trajectories of the material points with a high sensitivity to the initial conditions originate. In a broad sense these flows are related to the transitional regimes and the diffusion flames stabilized in them are named transitional flames. A thorough review of this subject is given by Takeno (1994) on the basis of numerical simulation.

The extension of the material surface with time (i.e with space) shown in Fig. V.5 reports that the extension of the three surfaces is different in dependence on the mean Reynolds number. It then increases at a slower rate in the A-case because the flow regime is prevalently laminar.

As the flow stirrers, the length of a contour bordering a fixed fraction of the interface increases in proportion to time.

Moreover, as reported in eq. 5.1, if a constant stretching rate is applied to the material surface, the surface area has to be increased exponentially.

This fact is partly confirmed for B and C cases.

Another important quantity, reported in fig. V.5, is the tracer volume fraction. It is directly related to the tracer concentration.

As well as discussed for the interface density, the tracer volume fraction shows a more than linear trend along the streamwise direction except for the C-case.

In fact the decreasing of Φ for y>30 mm in the case C is mainly due to underestimation of the small-scale features.

In fact in the tracer field evolution with a fixed spatial resolution the smaller vortices are not resolved, larger ones are slower and require a longer observation period. In incompressible velocity fields, exponential growth of scalar density gradients is due to exponential stretching of fluid elements, caused by stretching-folding motion of the fluid.

This aspect will be better discussed in the next chapter.

The concentration levels of the sheets show that the material surface deformation reflects the dispersion properties of the underlying flow.

It is observed that during the initial part of the jet instability development, the interface density increases very weakly. The increase reflects the slight oscillation of the interface owing to the instability development. However, from the vicinity of the first roll-up and beyond the surface area, in both the longitudinal directions interface density increases markedly.

This location also corresponds to the point where the stretching rate starts to decrease, indicating that, after the phase of production of the interfacial area, the onset of vortex-generation follows.

These observations offer a very simple picture of the early stages of the stirring between the streams. Sheets of scalar whose transverse size is of the order of the primary shear

instability wavelength are peeled off from the central jet and further stretched so that their linear dimensions in the streamwise and spanwise directions grow proportionally to time. Surface area and scalar concentration grow linearly in time, as they would if they were a material line spiralling in a vortex of constant circulation (Fung & Vassilicos 1991), or a material line stretched in a parallel shear flow (see e.g. Ottino 1989). In these simple flows, the length of a material line evolves as:

5.2) $$L(t) / L_0 = (1 + (\gamma t)^2)^{1/2}$$

where the rate of elongation γ clearly coincides with the velocity gradient between the streams, involving a length-scale which prescribes the steepness of the velocity jump $\left(u_{seed} - u_{air}\right)$ across the layer. Therefore the relative velocity between the flows plays an important role on the morphological evolution of the interface.

Note that such a linear dependence holds not only for the thickness of the layer, but also for the length of material lines, or isoconcentration contours within the layer. By contrast, a succession of stretchings and foldings would induces an exponential growth for the contour lengths, as shown in Fig. V.5 by increasing the y-coordinate.

Once produced by the primary instability, the structures are progressively elongated in the sustained shear between the streams. The maximal rate of shear, giving the separation rate of two material points initially close to each other is of the order of given in equation 5.2.

The progress of stirring phenomena is quantified by following the evolution of the tracer volume fraction in the course of time or equivalently for successive downstream locations in an advected flow.

In fact, the Φ -profiles are a consequence of the distribution of the cumulated stretch experienced by the different fluid particles in the flow at a given instant of time.

This behaviour has been already noted by several authors in the case of mixing of passive scalars, i.e. when diffusive effects are present (Shraiman BI et al. 1994, Villermaux E et al. 1998).

V.2.2 Effect of the Reynolds number

The profiles of interface density and tracer volume fraction has been reported in the previous sub-section for three selected reference cases to show the effect of the fluid-dynamics conditions on the main quantities affecting the stirring process.

To confirm the previously mentioned behaviours, profiles of interface density for 4 selected values of the mean Reynolds number are reported in Fig. V.6.

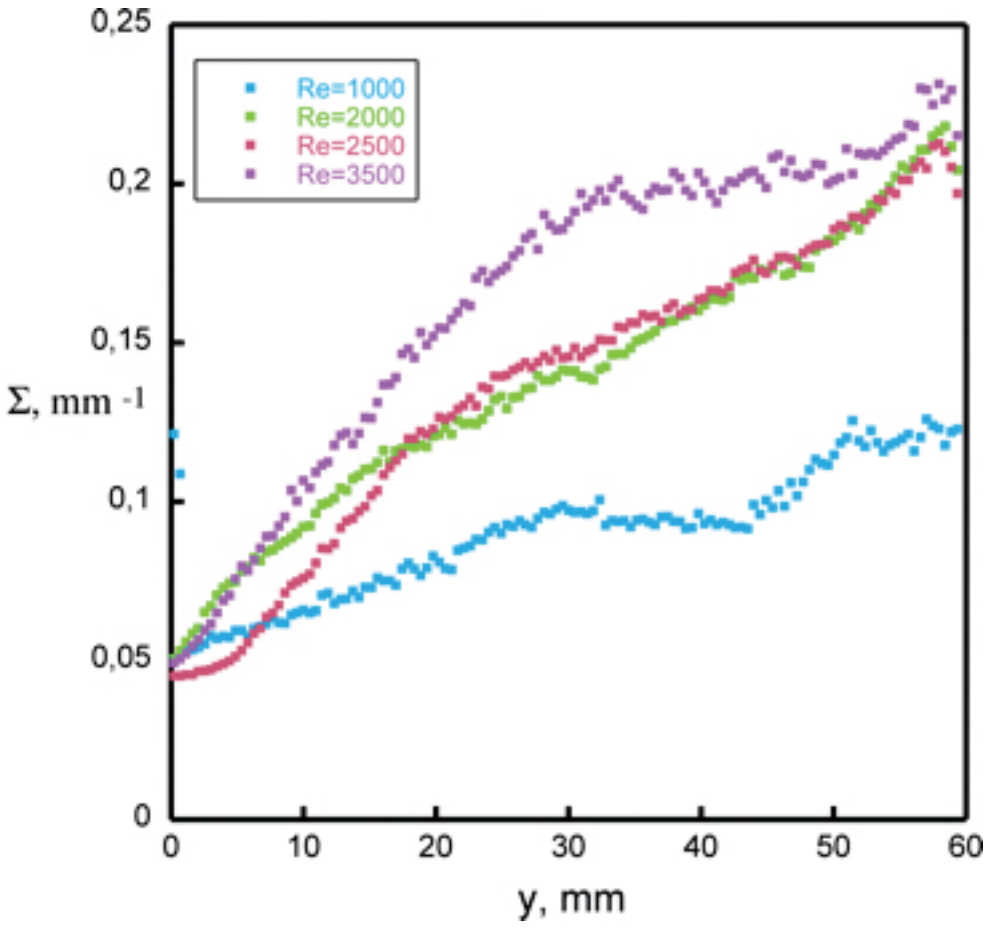

Fig. V.6 Profiles of interface density along y-coordinate parametric in Re

The profiles confirm the above considerations, i.e. that the surface area grows in a linear way only when the stretching is very low (mean Reynolds number lower than 2000).

Analogously, by increasing the mean Reynolds number, the interface density grows with a more than linear law. In fact, before the beginning of jet instability behaviours, Σ seems to depends linearly from the streamwise coordinate. Moreover, after this zone, the material surface increases following an exponential-like law, which remarks the well-noted trends reported in literature for the stretching of material lines and surfaces.

V.2.3 Effect of the velocity difference

In the mixing between two flows spanwise-organized, large vortical structures exist in this flow up to high values of Reynolds number. It is evident that the flow also contains smaller-scale structures, which form no particular patterns on edge views of the mixing layer but appear as distinctive streamwise streaks in plan view. It was speculated that the streaks delineate streamwise vortices which contribute in some way to the increased amount of interfacial area that occurs on the contour of a material surface. The primary, spanwise vortices and their amalgamations occur on both sides of the mixing transition, but the transition is characterized by the appearance, on its high-Reynolds-number or downstream side, of small-scale, three-dimensional structures and by an increased amount of mixing.

Further informations about the nature of the motions associated with the streamwise streaks are needed, in order to understand their contributions to mixing and growth of the layer.

Relevant to this is the role of the primary, spanwise-organized vortical structures in the growth of interfacial area. Those vortices are convected downstream during lifetimes that

are terminated when they interact or amalgamate with neighbouring vortices to form larger ones.

Analysis of flow-visualizations by increasing the velocity difference ($\Delta v = v_{seed} - v_{air}$) is used to understand the topology of the streamwise vortices and to obtain the effects of the streamwise vortex structures on the interface density and volume fraction. In this analysis the Reynolds number is kept constant at 2000.

Fig. V.7 Flow visualization at three selected values of Δv *and for Re=2000*

Quantitative data on the onset of the streamwise vortices have been obtained from 2D laser light scattering patterns of the planar jets. In particular the velocity difference increases passing from the image on the left of Fig. V.7 to that on the right.

It is clear that disturbances associated with the streaks are being amplified from their upstream origin until they reach levels at which they become visible on the image. The location of this visible threshold amplitude could be shifted upstream or downstream by variation of the Reynolds number or the velocity difference. These flow changes also resulted in changes of the number of streaks.

The streamwise streak pattern is caused by the gradients in the mean flow.

The interface density as a function of the velocity difference can provide additional insight into the underlying streamwise vortex structure. These measurements along the y-coordinate have been limited to the three flow conditions visualized in Fig. V.7, namely $\Delta v_1 = 1$ m/s , $\Delta v_2 = 3$ m/s and $\Delta v_3 = 4$ m/s and they have been reported in Fig V.8. The Reynolds number is fixed at 2000.

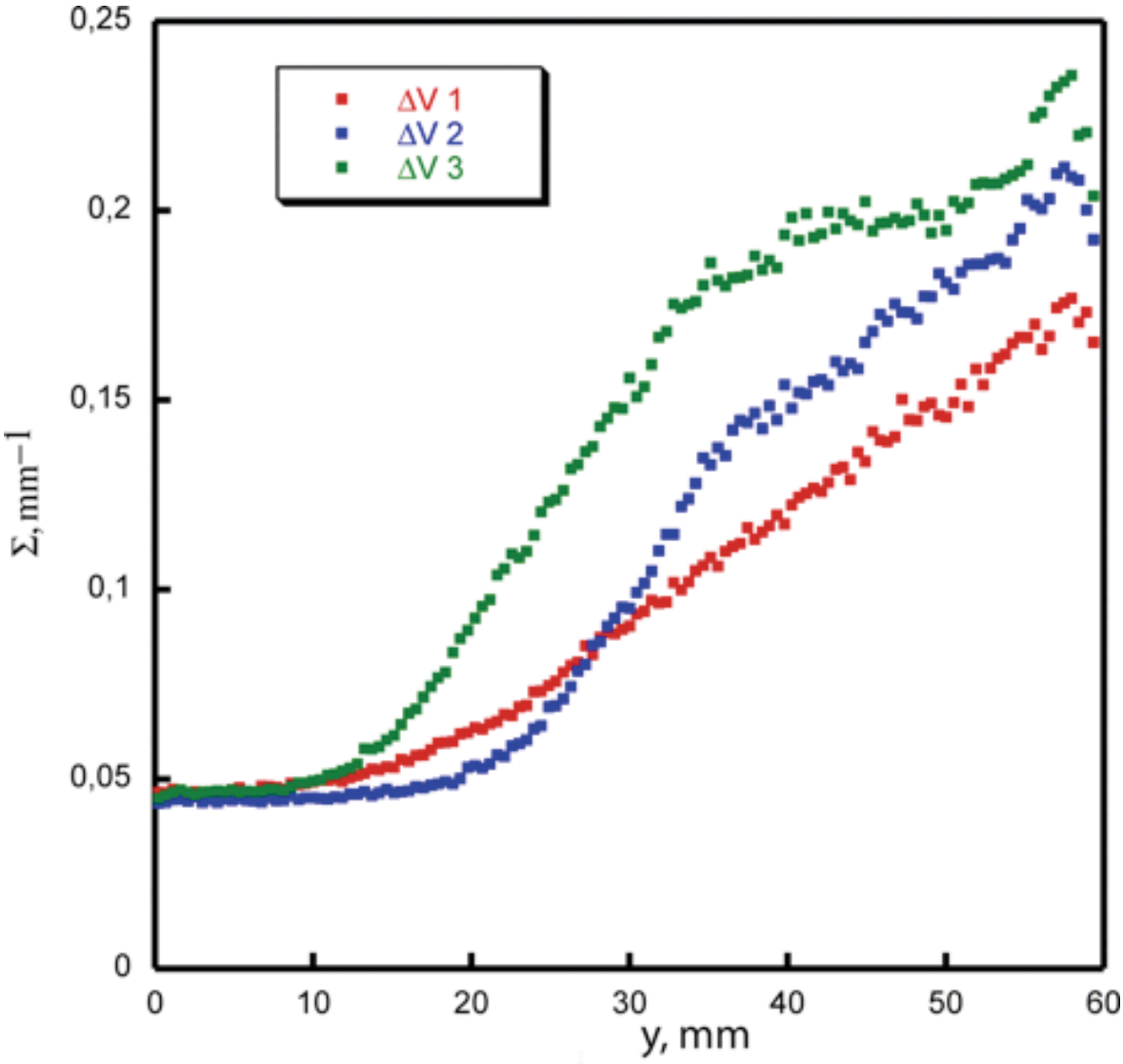

Fig. V.8 Profiles of interface density at three selected values of Δv *and for Re=2000*

The profiles in Fig. V.8 permit to understand the relation between the streamwise vortex structure and the mixing transition. The cross-section pictures obtained in this investigation

show that there is a direct contribution of the streamwise vortices to mixing owing to the increased interfacial area in the core of the vortices. The streamwise vortices play an indirect role in this process since stretched vorticity along the braids will become part of the spanwise vortex core after amalgamation. This mechanism suggests that the mixing transition should be completed downstream of the two-dimensional instability, after a number of amalgamations. Further, since in the early development the amalgamations can be traced back to the roll-up process and this process depends only weakly on the conditions of the low-speed boundary layer. Thus both, the two-dimensional instability and the amalgamation process play a role in the mixing transition. The instability generates the two-dimensionality, while the amalgamations redistribute it. Although these arguments provide an explanation for the scaling of the mixing transition, the possibility of additional internal instabilities cannot be disregarded.

Moreover, Fig. V.8 shows that the jet instability starts at a lower streamwise coordinate for the third case with respect to the other twos.

This is due to the higher velocity difference in the third case which generates high turbulence levels upstream with more vortical structures with respect to the lower velocity difference cases.

Furthermore, it is observable that the stretching rate (i.e. the growth of material surface) is higher in the last two cases with respect to the first one.

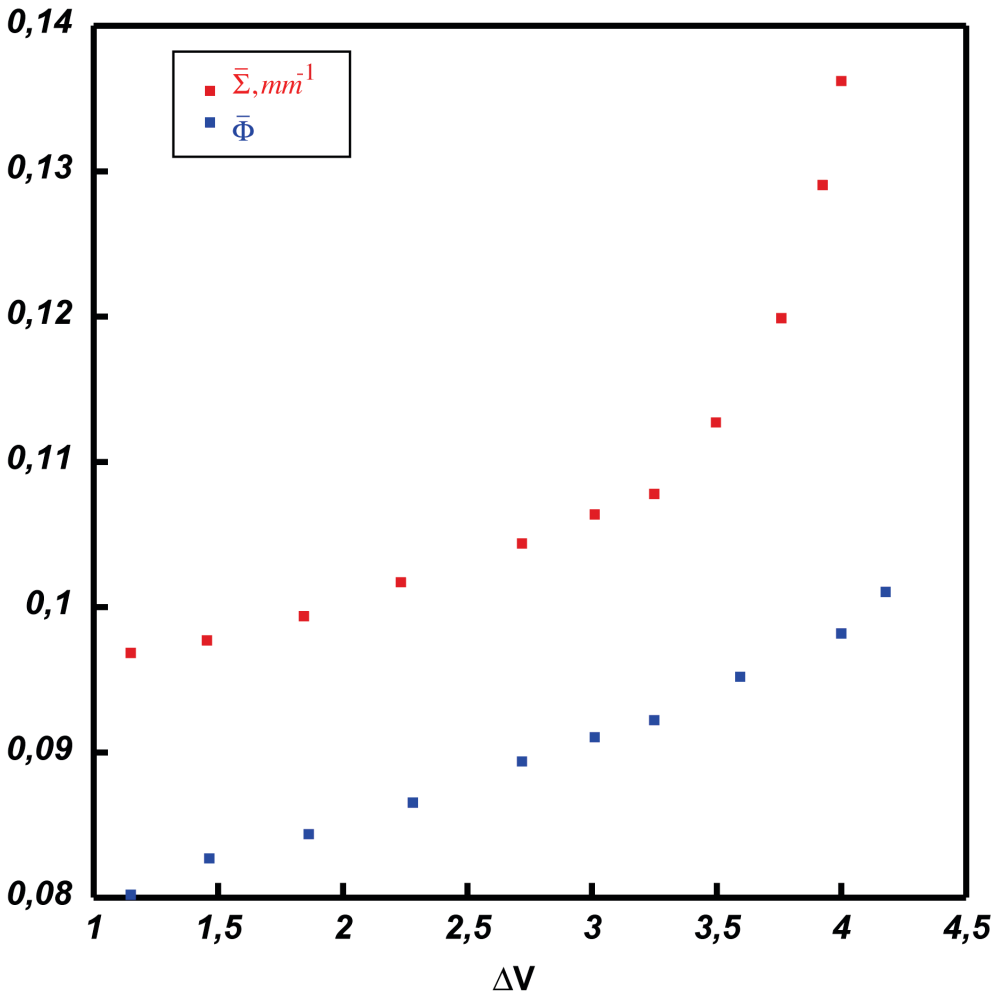

Fig. V.9 *Profiles of total interface density and volume fraction as a function of* Δv

Finally, Figure V.9 shows the trends of the total interface density and volume fraction with the increasing of the velocity difference at Re=2000.

The average quantities $\bar{\Sigma}$ and $\bar{\Phi}$ has been evaluated by integrating the interface density and the volume fraction along the streamwise direction (y).

The profiles permits to separate the effects of the mean Reynolds number from those related to Δv.

In fact, while the interface density follows the twofold behaviour also observed before (first stage of linear dependence and second one of exponential growth), the tracer volume fraction shows a linear profile with the increase of the velocity difference.

These observations lead to the important result that the velocity difference influences the interface density. More specifically the Δv changes the linear trend of the interfacial area increase.

On the other hand the velocity difference does not affect the linear increasing of the tracer volume fraction in time.

V.3 Stretch rate conditioned on the interface

In non-premixed jets, velocity gradients are the major parameter that governs the local surface area evolution.

In particular it quantifies the rate at which turbulence increases the material surface area. In terms of the velocity field u and flame-surface normal n, Candel and Poinsot have obtained the expression for the stretch rate.

One problem that has prevented the measurement of conditioned strain rate in the past is that one must first be able to identify the surface layer and then be able to record velocity along this layer.

Thus the image processing technique presented in the previous chapter have a double purpose:

- Identify the surface contour using flow visualizations
- Simultaneously measure the stretch rate along interface using Particle Imaging Velocimetry (PIV).

We decided to use the binary image contour as the location where strain is measured, as reported in the previous chapter.

In particular, the total stretch rate is the sum of two contributions, one related to the planar divergence and the other due to the mean curvature of the surface as reported in eq. 5.3:

5.3) $$K_{\Delta A} = \underline{\nabla}_t \cdot \underline{\mathrm{v}}_t + \mathrm{v_n} C$$

Both these contributions have been evaluated for the three test cases.

More specifically, for each processed-image, two contours of the image have been obtained and the total stretch-rate has been evaluated for both contour (namely upper and lower).

Fort the sake of brevity in the next chapter only the upper values of stretch rate will be reported, in fact the qualitative trends of both stretching function are similar because they have been obtained from ensemble-average.

Figures V.10 show results obtained for the test cases as a function of the curvilinear coordinate. Clearly, the fidelity of the stretch measurements is limited by the random error in measurements of both the velocity field and the surface normal.

The measurement inaccuracy is not so high because the profiles reported in Fig. V.10 has been obtained by ensemble averaging the velocity field, so the noise is limited.

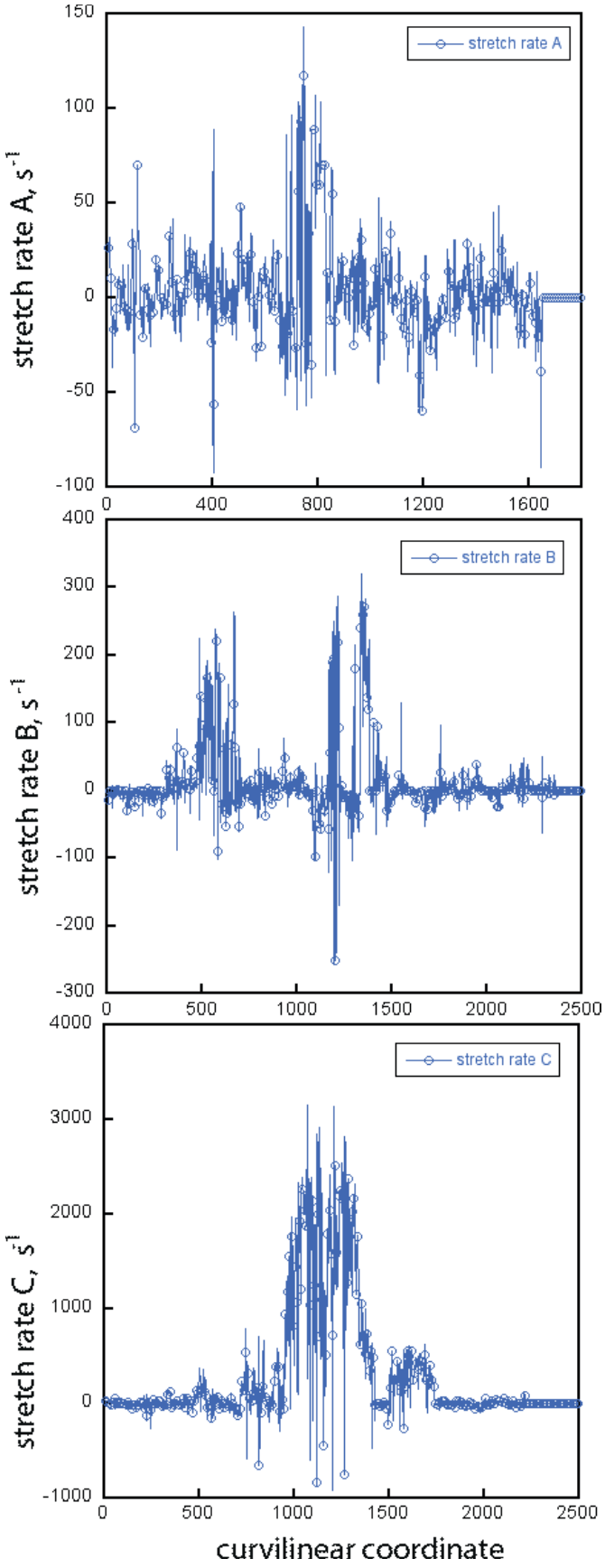

Fig. V.10 *Measured upper strain rate for the three test conditions along the curvilinear coordinate*

The profiles of V.10 are the resultants of the following phenomena:

- Surface rollup, resulting in an increase in flame area;
- Large curvature and cusps in certain regions;
- Surface stretching

One major feature observed in Fig. V.10 is that the strain is highly intermittent. The ensemble-average peak values are large for C-case, exceeding 3000 s^{-1}, but this high strain exists only for short distances. The mean strain rate at this location is 1000 s^{-1}, which is only one-third of the peak value.

Moreover, the mean stretch rate values in the A-case result lower than the other two cases. In fact when the Reynolds number is higher than 2000, the material surface is stretched until values of 3000 s^{-1} for the most turbulent case.

Nonetheless, here is important to note that the variations of surface area reported in Fig. V. 5, do not appear to correlate well with the variations in $\langle K_{\Delta A} \rangle$.

Thus, the interface density and the tracer volume fraction profiles apparently are not in phase with the high-frequency strain components.

Moreover, two mainly trends are displayed in Fig. V.10:

- the stretching slightly increase with y for the A-case;
- as the Reynolds number is doubled, $\langle K_{\Delta A} \rangle$ increases markedly.

It is only in part possible to compare these measured trends to theory, because few theoretical prediction exists of the strain rate along interfaces.

In particular, relevant results on Reynolds-number dependence of line and surface stretching in turbulence was obtained from Goto S et al. (2007).

These works demonstrated that the stretching rate, of sufficiently extended material lines and surfaces in statistically stationary homogeneous isotropic turbulence depends on the Reynolds number, in contrast to the conventional picture that the statistics of material object deformation are determined solely by the Kolmogorov-scale eddies. These numerical results can be understood from the following three facts. First, the exponentially rapid stretching brings about rapid multiple folding of finite-sized material objects, but no folding takes place for infinitesimal objects. Secondly, since the local degree of folding is positively correlated with the local stretching rate and it is non-uniformly distributed over finite-sized objects, the folding enhances the stretching rate of the finite-sized objects. Thirdly, the stretching of infinitesimal fractions of material objects is governed by the Kolmogorov-scale eddies, whereas the folding of a finite-sized material object is governed by all eddies smaller than the spatial extent of the objects. In other words, the time scale of stretching of infinitesimal fractions of material objects is proportional to the Kolmogorov time, whereas that of folding of sufficiently extended material objects can be as long as the turnover time of the largest eddies. The combination of the short time scale of stretching of infinitesimal fractions and the long time scale of folding of the whole object yields the Reynolds-number dependence.

These statements are partly confirmed from the results reported in Fig. V.10.

The fact that strain rate is very intermittent; leads to instantaneous values exceed 1000 s^{-1} and are significantly larger than the local mean. The strain rate oscillates at frequencies as high as 2–5 kHz, which approximately corresponds to the inverse of the convection time of integral-scale eddies across the interface.

V.4 Numerical validation

In order to give an assessment of the experimental results previously obtained, a comparison with some DNS results are here reported for a transition-flow case in which Re=2500.

They are relative to gaseous flows in which the average velocity of central channel is 5 m/s and the external velocity is 0.4 m/s. The upper row is relative to numerical predictions in which the interface has been identified by considering a lagrangian tracking of the flow field by injecting massless particles in the first contact point between the flows and by following their transport equation coupled with the unsteady flow field.

The lower row is relative to pattern of laser light scattered by a sub-micron seeding. The field of view is 10 cm x 4 cm. Both numerical and experimental results are reported in Fig. V.11 for five selected times.

Computational details and the choice of the boundary conditions are not relevant here and it will be briefly reported.

The finite-volume method is used to discretize the governing equations, which is employed to perform Direct Numerical Simulations. The geometric model setup and mesh generation is carried out by GAMBIT, which is the preprocessor of FLUENT.

A commercial CFD software, FLUENT, is employed for the numerical simulation.

The segregated implicit solver is used for all simulations. Second-order implicit temporal discretization is adopted. Time step of 0.00001 s is selected for the DNS to ensure that convergence can be obtained in each time step.

It is of great interest to underline that the comparison is quite satisfactory and that, in turn, this shows the two-dimensionality of the flows. Among the numerical predictions, the agreement are not so good in the high-convolution zones. Interfaces are quite convoluted,

as it is possible to observe in Fig. V.11. They undergo a relatively intense stretch rate. The stretch rate is sufficient for high level of convolution.

Blu particles indicate the right interface contour and red indicates the left one.

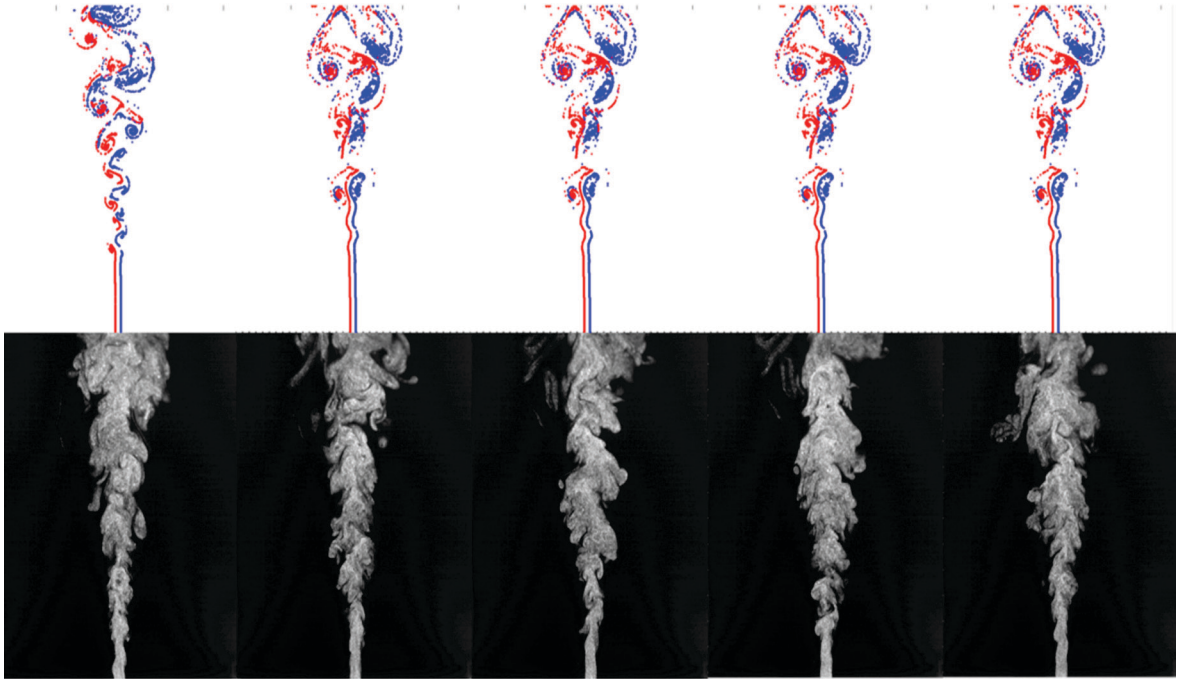

Fig. V.11 *Exp/Num Comparison of interfaces for a 2D transitional flow. In the upper row are reported the numerical prediction while in the lower row the laser light scattering images are reported in the corresponding conditions.*

Moreover, the interface contour at the downstream region in the numerical results is not well identified due to the high stretch rate. In general the agreement are quite satisfactory and they depict an important assessment of the experimental results.

A quantitative exp/num comparison for the patterns reported in Fig. V.11 has been obtained by comparing the mean velocity magnitude profiles along the axial direction (x) for three selected streamwise positions (y). They are reported in Fig. V.12.

The mean velocity magnitude has been obtained by means of ensemble average of the instantaneous velocity field.

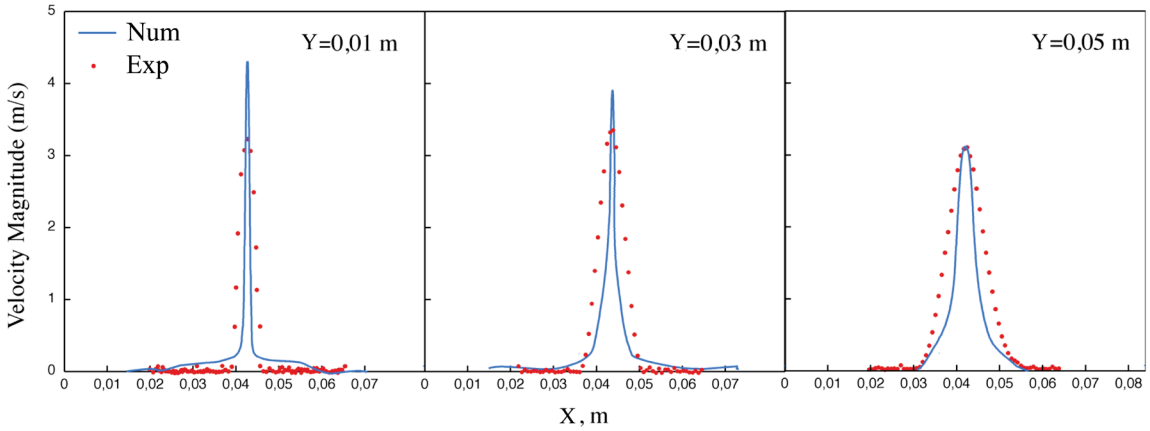

Fig. V.12 *Comparison of Average Velocity Magnitude profiles obtained from PIV measurements (red point) and DNS (blue curve) for Re=2500 and for three selected streamwise positions (y).*

A last comment is devoted to the assumption used for the exp-num comparison.

In fact, both LLS patterns and the DNS field has been obtained considering a two-dimensional flow field. This assumption for a quasi-2D flow (which is planar symmetric) seems to be quite realistic for transitional flows (i.e. Reynolds number up to 5000). In this case, in fact, the effect of the out-of-plane component on the fluid-dynamics patterns can be neglected. On the other hand, DNS of a 3D field is a very expensive computational task. Therefore the studies which are quoted here refer to complete 3D simulations of flow in control volume, whose dimension is only few orders of magnitude higher than the smallest resolvable length-scales. Low Reynolds number or transitional flows belong to this category. They may develop ensembles of structures in a narrow range of length scales so that they are suitable for some experimental validation too.

Relatively high Reynolds number turbulent flows, in which only the small length-scales are simulated, are also of interest. In this case initial turbulent kinetic energy spectra and periodic boundary conditions are generally prescribed and mixing-reacting fields are simulated in decaying turbulent fields.

Chapter VI
Discussion

Combustion is a mean of transforming primary energy into useful secondary energy such as heating, processed materials and mechanical and electrical power.

With some 100,000 years of development, it might be expected to be a mature technology. In fact, it is the least developed technology of modern engineering systems. Engineering systems with mature technology have computer models that are routinely used in analysis and can be used in the optimization of the geometry and operating conditions of new designs. The same can not be said for the new generation of combustion chambers. Computer modeling of combustors is still at a fledgling stage and is only used peripherally in the development of new combustors. Combustor development is still largely by cut-and-try testing in experimental rigs and in prototype and in-service engines and power plants (Mongia HC 2008).

The fledgling status of computer modelling of combustors comes not from the will of trying. More than forty years of effort by some of the leading scientists in the world has still not got us within close sight of achieving the goal of having soundly based predictive models for combustors that can be used in industry with confidence on a routine basis. This is because practical combustion systems involve multi-scale phenomena requiring advanced models for highly turbulent recirculating and swirling fluid flows, for gaseous and particulate fuel dispersion and mixing as well as for the extremely complex chemical kinetics involved in the oxidation of hydrocarbon fuels and the formation and burnout of pollutants such as soot, polycyclic hydrocarbons, carbon monoxide and oxides of nitrogen. Furthermore, these highly non-linear processes are inherently and strongly coupled together.

The multi-scale nature of this phenomena has led to the development of different kinds of models depending on the characteristic time-scale as reported in Fig. VI.1.

In particular, interaction between turbulent mixing and chemical kinetics is the key parameter which determines the combustion regime: only understanding such interaction may provide insight into the physics of the flame and support the choice and/or development of modeling tools.

In particular, most of the turbulent combustion models have proved to be not suitable for predicting new combustion technology processes (De A et al. 2011) such as Mild Combustion (Cavaliere A and de Joannon M 2004), in order to satisfy the requirements to design both efficient and clean combustion technologies.

A clear view of the autoignition process of these cases is however not yet available, although it is essential for practical applications of such cases (Abtahizadeh E et al. 2012).

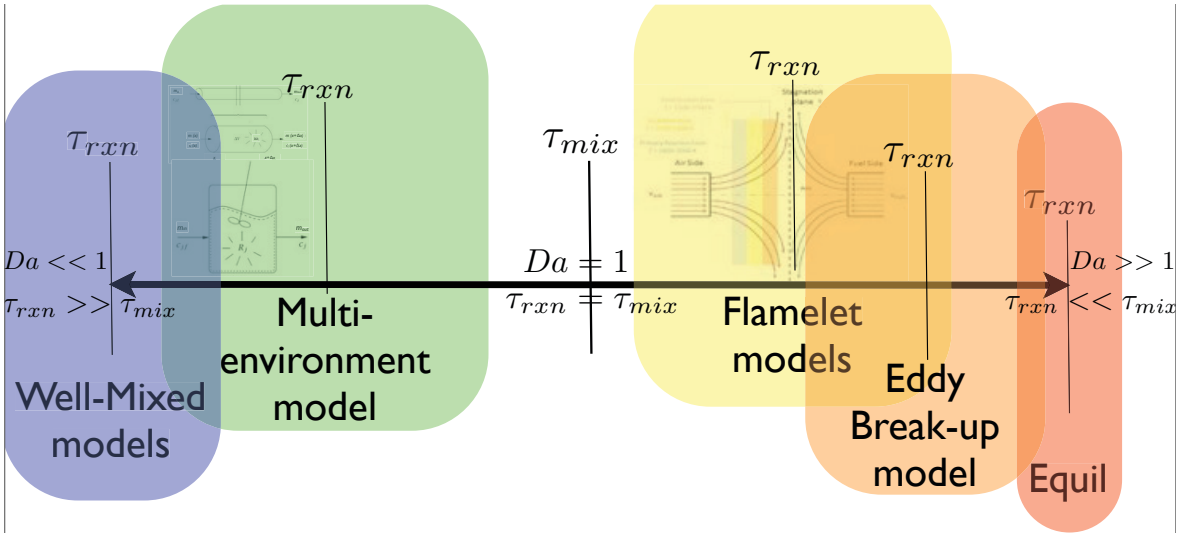

Fig. VI.1 Principal turbulent combustion approach based on the identification of time scales.

However, fundamental aspects of such combustion regime are still not completely understood and this generates uncertainties, especially from the modeling perspective.

In fact, in MILD combustion systems, combustion takes place in the midst of turbulent mixing of the reactants. Since the temperature of the reactants is above that of autoignition, a complex interplay between turbulent mixing, molecular transport and chemical kinetics occurs (van Oijen JA 2012).

In this sense, to reveal the fundamental reaction structures of emerging combustion technologies, high-fidelity numerical simulations are needed in which all scales of turbulent motion are resolved. Combined with detailed chemical reaction models, direct numerical simulation (DNS) is the appropriate tool to investigate these phenomena. The drawback of DNS, conversely, is that it is extremely expensive from a computational point of view.

Hence, it is evident that the fledgling status of computational modeling of combustors will be a severe handicap for the development of energy technologies involving combustion in the 21st century. The 2006 DOE workshop (McIlroy A et al 2006) pointed out the needs to "identified a single, overarching grand challenge: the development of a validated, predictive, multi-scale, combustion modeling capability to optimize the design and operation of evolving fuels in advanced engines for transportation applications." Such modeling capability is also sorely needed in the power generation and materials processing sectors of energy technologies.

As has already been stated in the first chapter, the fledgling status of turbulent combustion modeling comes despite much effort over many years. It is an extremely complex multi-scale problem. Important physics, including chemical physics, can be associated with any combination of these length and time scales.

Advances in computational power can be expected to continue. Even if the advances continue at present exponential rates, it is evident that full direct numerical simulation (DNS) is not possible for practical combustion systems in the foreseeable future.

It should be remembered that, to be an effective design tool in industry, a 20-hr turnaround time, or better, is needed. Perhaps new developments in computers, such as quantum computing (Aharonov D 1998), will become available in the longer term and be available to provide the computational tools in DNS that are needed before 2050. Such developments cannot be counted on, however.

Advanced computer methods for combustion will thus, inevitably, involve modeling of many of the important physical aspects of the flow that we cannot afford to resolve in our computations. The relative importance of these physical aspects to be modeled will depend on the application and on the information being sought.

A closer look at the situation, however, suggests that efficient coding and fast numerical algorithms are not the main limitations to advancement of combustion codes. These aspects can be quite significant. Of more importance, however, is the validity of the modeling approach and the sub-models that are used for the essential physics (including chemical physics) involved in the particular application.

The most important area is undoubtedly that of validation. All too often computer model predictions are 'validated' against sparse experimental data for full-scale combustors or for laboratory combustors that have some of the flow and other complexities of practical systems. Such data can often be adequately matched by choices made for boundary conditions that are unfettered by experimental measurement. Little information is gained about the adequacy of the modeling approach or of the combustion models used. A more scientific approach is to devise experiments in which the flow is simple enough for the boundary conditions to be adequately measured and for which the crucial physics that need modeling are dominant.

It is only with such an hierarchical approach to validation that sure progress on advanced computational modeling of combustion can be made.

The fledgling status of computational modeling of practical combustion systems will be a seriously limiting factor in the ability of combustion technology to meet the 21st century challenges of climate change, energy security and tropospheric pollution. The advances needed in such computational modeling for practical combustion systems will require considerable investment in modeling research in this area, including the new paradigms of multi-scale modeling. It will also need an increased emphasis on research directed at improving experimental data bases for model validation that are of an hierarchical nature and start with relatively simple problems that encapsulate the most important physics.

For such reasons, strategies which select particular sub-models and which exploit them in such a way that split effects can be separately introduced in more and more complex processes, should be preferred to other ones. In fact, this rational approach allows more sensible evaluation of their effects as well as of their interaction with more complex processes.

Such strategy could be named “MultiSECtioning” Process Evaluation Strategy and it refers also to the intrinsic multi-characteristics of combustion processes. The acronym evokes that the procedure consists in sectioning the whole process in parts, by means of both geometrical sectioning of the control volumes and/or selection of a subset of physical effects, which can be modeled and validated when added ones at the time to the process. The sequential structure of this approach is shown in Fig. VI.2. This strategy has an important feature, i.e. it is realistic and quantifiable in its realism. This is not a trivial requirement since the validation of high level model is rarely done without suitable adjustment of parameters or even adjustment of some of its components. In this strategy, the validation has been performed in a knowledgeable way by selecting representative samples of cases to be used for a thorough evaluation of carefully selected submodels sets on the basis of their features and of their potential interaction with the model core.

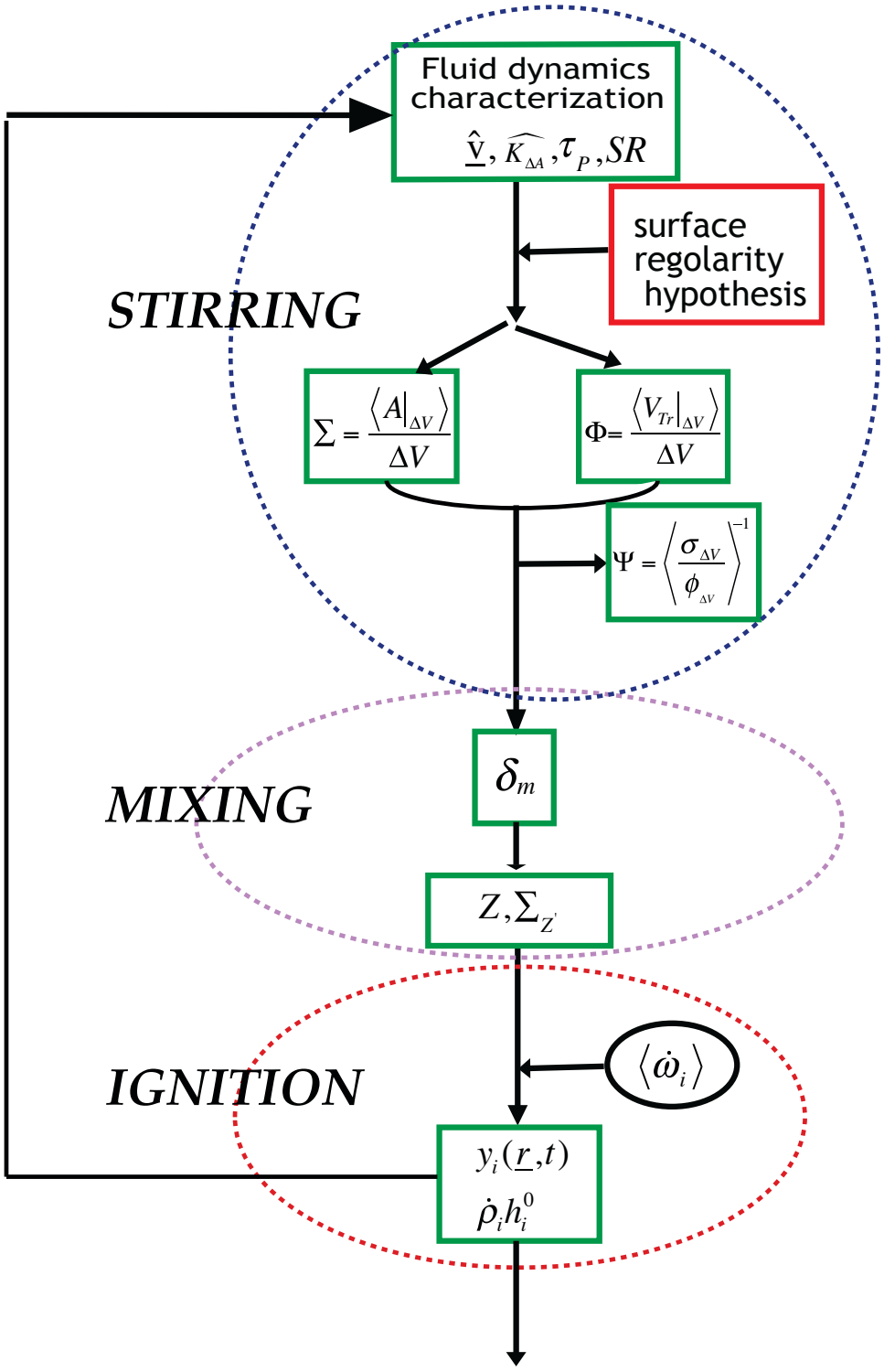

Fig. VI.2 *Main sequential blocks of the "MultiSECtioning" strategy*

The role of interlinking among different subprocesses has to be carefully evaluated since it can prevent the isolation of functional dependences on controlling parameters that has to

be studied by introducing unpredictable feedback mechanisms acting in different ways in physical and numerical models respectively.

The procedure consists in sectioning the whole process in parts, by means of geometrical sectioning of the control volumes or selection of a subset of one or more physical effects, which can be separately modelled and are, hence, separately validated.

In line of principle only for these sequential processes it is possible to check the accuracy of the numerical predictions through the comparison with the experimental data "side by side" for the two stages in which the whole combustion process has been sectioned. In other words, the validation, made separately for the two parts, is sufficient to ensure a reasonable prediction also for the whole process. Furthermore also the sensitivity analysis in respect to the initial and intermediate parameters is easy to be performed and the experimental and numerical results can support each other in the complete description of the system.

Of course, this is true only for sequential processes and in the case each single subprocess can be successfully described.

On the ground of these considerations, a MultiSECtioning methodology has been conceived because it allows for the analysis of the influence of single subprocesses.

The passage from one part to the other is sketched in fig VI.2 as block diagram and it allows a sequential combination of the separated effects" and the appropriate characterization of the field obtained by the introduction of new "separated effect".

The first part of the procedure is a fluid-dynamic characterization of the patterns of interest when not reacting flows are introduced in fixed control volume, for fixed boundary-initial conditions, for fixed external parameters.

The fluid dynamic database, generated in this first step, has to be suitable for the characterization of the effects generated by considering the injection of non-diffusing tracers in the control volume. This is reported in fig VI.2 in the block quoted as “stirring”.

A large part of this thesis work has aimed to the characterization of this sub-process, which in turn yield interface between the two reactants. In particular, the identification of these surfaces can be seen as the “sinew” of this approach.

This expression summarizes a twofold concept:

- the characterization of advected-surfaces is the “skeleton” of this strategy and it is connected to the other step;
- the interface identification is the mainstay of this kind of approach. The strength of MultiSECtioning is derived from this stage. In this sense, the subsequent steps are a consequence of the first one.

In fact, without a good prediction of the stirring phenomena, the whole combustion process cannot be analyzed in a correct way.

The approach in this sense is also cyclic, as shown in Fig. VI.2. In fact, local conditions of ignition/extinction influence the fluid-dynamic pattern.

Therefore in this PhD thesis, a new database, for the stirring-step, has been generated and it has been analyzed in terms of local or integral stirring quantities (interface location) either for mutual validation between experimental and numerical determinations or to evaluate the possibility of modeling this step in relation to the whole combustion process.

The main difficulties in the experimental evaluation of these quantities will be discussed in the following of this chapter and the main limits of the experimental measurements will be pointed out.

It is worthwhile to note that some quantities, reported in Fig. VI.2 in the fluid-dynamics characterization stage (stirring-block), such as the residence time (τ_P) and the stretch ratio (SR), have not been measured in this thesis because they are not useful for the stirring process itself. They in fact have to be evaluated to obtain the mixture fraction field once that the interface evolution has been completely characterized.

The second step, reported in the figure as “mixing”, is well reported in the literature. Specifically, the mixture fraction field characterization in a stratified medium will be discussed later.

The third step, quoted in the figure as “ignition”, can be achieved by means of two well-known processes, i.e. assisted ignition and autoignition.

A part of this PhD thesis has been devoted to the investigation of autoignition processes in non-conventional combustion conditions, to extend those already found in literature for standard cases. The main results has been reported in the second chapter and they will be discussed later.

Moreover, it is important to note that also “propagation” and “stabilization” steps has been reported in the first chapter for the MultiSECtioning. They play an important rule in such a strategy. Despite this fact, they have not been discussed in this thesis because they are a direct consequence of the main three steps reported in Fig. VI.2.

The procedure outlined here will be discussed in the following paragraphs, which are devoted to discuss each step reported in fig VI.2 and to show their limits.

VI.1 Reliability and validity assessments of the experimental results

An important part of this PhD thesis focused on experimental characterization of advected-surfaces by means of some diagnostics and image processing tools discussed in the previous chapters.

Some interesting results have been obtained which constitute an important database for the identification of these peculiar surfaces. The study has been also devoted to assessed the phenomenological aspects, in moderate turbulence conditions, related to the interface evolution. This qualitative and quantitative analysis corroborated the idea that different processes concur in the evolution of material surfaces.

In particular, it has been shown that stirring motions increase the length of material lines. We quantify the increase in the surface area from the two-dimensional slices through the field by a procedure illustrated in the fourth chapter.

For this purpose, the experimental trends of average interface density ($\overline{\Sigma}$) has been reported in Fig. VI.3 with blue points as a function of the mean reynolds number in the chamber.

The experimental profiles of $\overline{\Sigma}$ as a function of the Reynolds number have been compared with those obtained following the closure model for the interface density derived from fractal theories, leading to Gouldin et al. (1989).

The model is based on the assumption that the geometry of the interface (or in general of a material surface) can be represented by fractal surfaces with fractal dimension D that is bounded such that $2 < D < 3$.

The green dashed line in Fig. VI.3 marks a sort of separation zone between two different stirring behaviours. In fact, for Reynolds number less than about 3500, the interface

density evaluated with the fractal model increases linearly mainly due to weak oscillations of the jet.

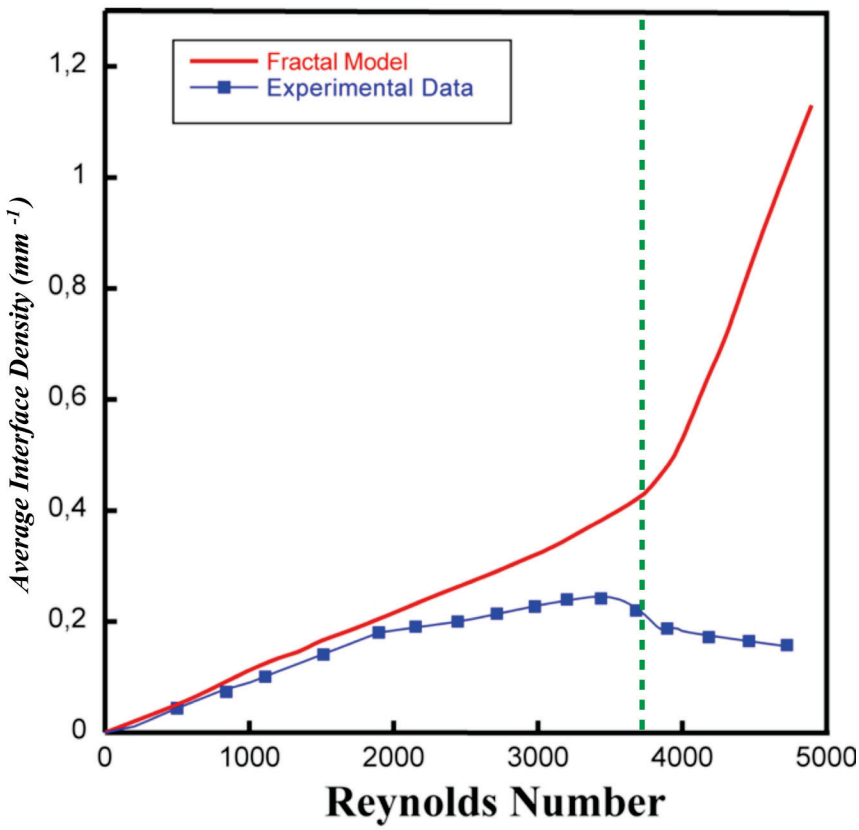

Fig. VI.3 *Average interface density versus Reynolds number. The profiles have been evaluated with experimentals (blue) and fractal model (red).*

Furthermore, starting from the green dashed line, the interface density presents an exponential growth in concurrence with the stretch rate increase.

This limits marks the onset of "Lagrangian turbulence", which is characterized by a more than linear increase of surface area with time. This phenomena is mainly due to the occurring of stretching and folding processes.

It is here important to note that the experimental profiles (blue points) reported in Fig. VI.3 shown a quite-good agreement with the fractal model up to the limit reported on the graph with the green dashed line. The unsatisfactory agreement for Re>4000 is due to spatial

resolution limits of the diagnostic apparatus that have been mentioned also in the previous chapter.

In this sense, the experimental results showed in Fig.VI.3, have been obtained by equipping the high-speed camera with a 105 mm Nikon standard lens, corresponding to a spatial resolution Res_1=0.045 mm/pixel.

To asses the validity of the experimental results and to compare them with the fractal model results, some 2D LLS patterns have been investigated by changing the minimum spatial resolution of the system, i.e. by equipping the camera with a 200 mm Nikon lens and achieving a resolution of Res_2=0.0015 mm/pixel.

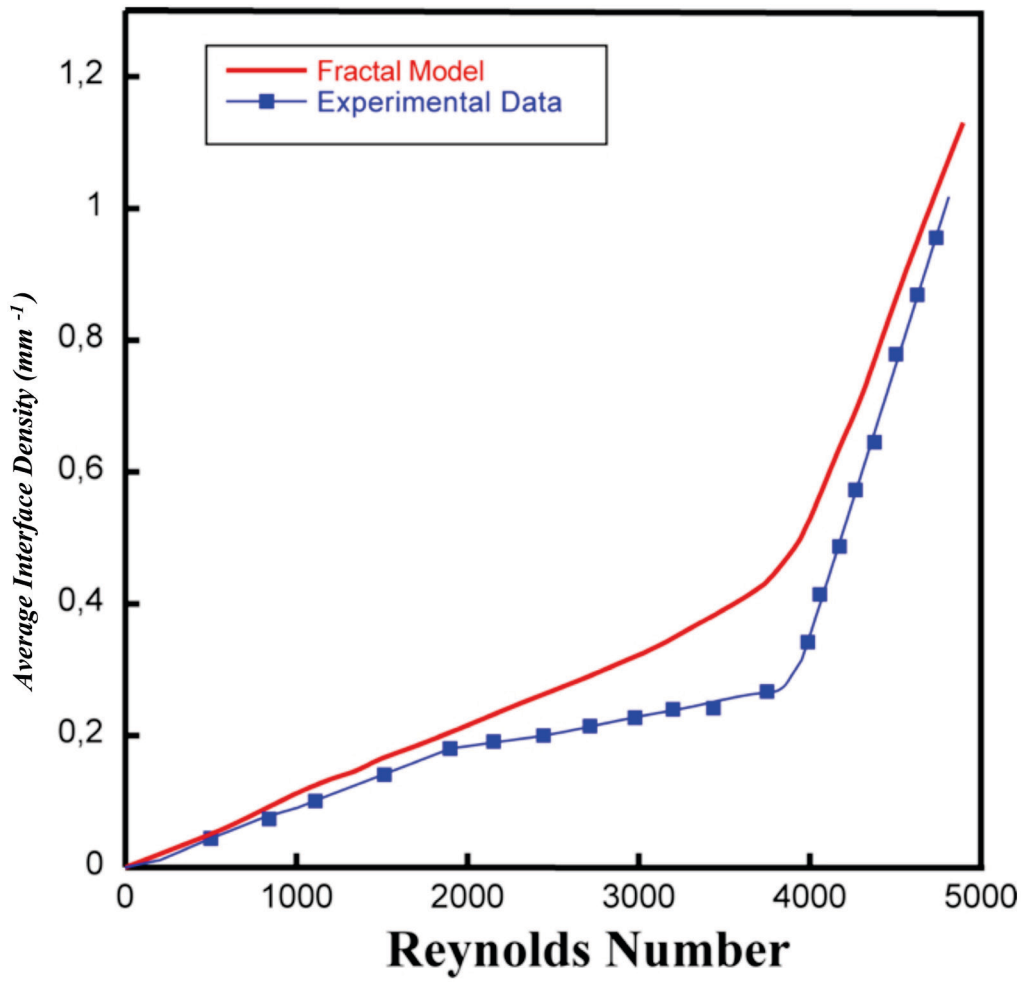

Fig. VI.4 *Average interface density versus Reynolds number achieved with Res_2. The profiles have been evaluated with experimentals (blue) and fractal model (red).*

The trends reported in Fig. VI.4 show better agreement with the fractal model than those obtained with Res_1 and reported in Fig. VI.3.

In this respect, the average interface density ($\bar{\Sigma}$) evaluated from experimental data fits very well the results obtained with the fractal model for the whole Reynolds number range analyzed. This results can be justified by considering an important aspect already reported in the third chapter. In fact, for a fixed spatial resolution of Res1, the smallest resolvable scale can be resolved up to a Reynolds number of about 3800.

This kind of considerations show that the evaluation of the quantities that affect the stirring process has to be done in a proper way considering the effects of the spatial resolution on the experimental results.

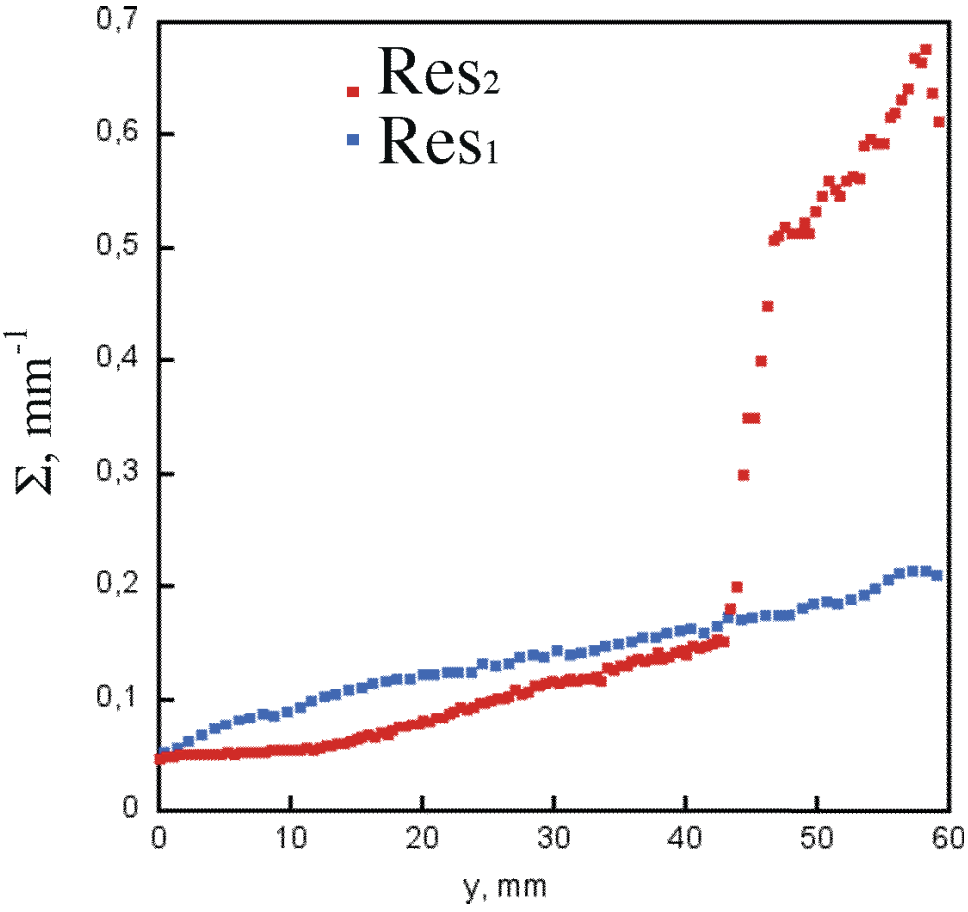

Fig. VI.5 Profiles of interface density for two different spatial resolutions for Case-C

In the fifth chapter, profiles of interface density along the y-coordinate have shown an anomalous trend with mean values in the case-B higher than that obtained in the C-case.

These apparently incorrect results are here justified by comparing $\sum$ profiles for two selected camera resolutions. In fact the Fig. VI.5 points out that for higher resolutions the interface density exhibits a different trend with respect to that observed for Res_1.

In particular, similar values have been obtained for y<40 mm (only few differences have been observed) whereas large differences are found when the local stretching phenomena are relevant (i.e. for y>40 mm). Specifically, the measured values of interface density in the higher resolution case are three times those obtained for a resolution of Res_1.

As discussed previously for Fig. VI.4, the quantities evaluated with the spatial resolution Res_1 do not take into account the interface density due to the unresolved scales, which is reported in eq. 6.1 as the term $\sum_{us}$.

On the other hand, with a spatial resolution equal to Res_2, small-scale structures are detectable up to Reynolds of about 20000.

Thus, the interface density measured in the C-case for higher resolutions, can be related to that obtained from a lower resolution of camera as reported in eq. 6.1:

6.1) $$\sum\Big|_{Res_2} = \sum\Big|_{Res_1} + \sum_{us}$$

where, as said previously, $\sum_{us}$ is the interface density contribution related to the unresolved scales.

This term is dependent on the local velocity gradients of the surface (Chakraborty N & Cant RS 2009) thus it can be related to the velocity field for modeling purposes in RANS or LES frameworks.

Similar profiles to those obtained in Fig. VI.5 can be obtained also for the tracer volume fraction in Fig. VI.6.

In this case the maximum value reached by $\Phi|_{Res_2}$ is 0.2.

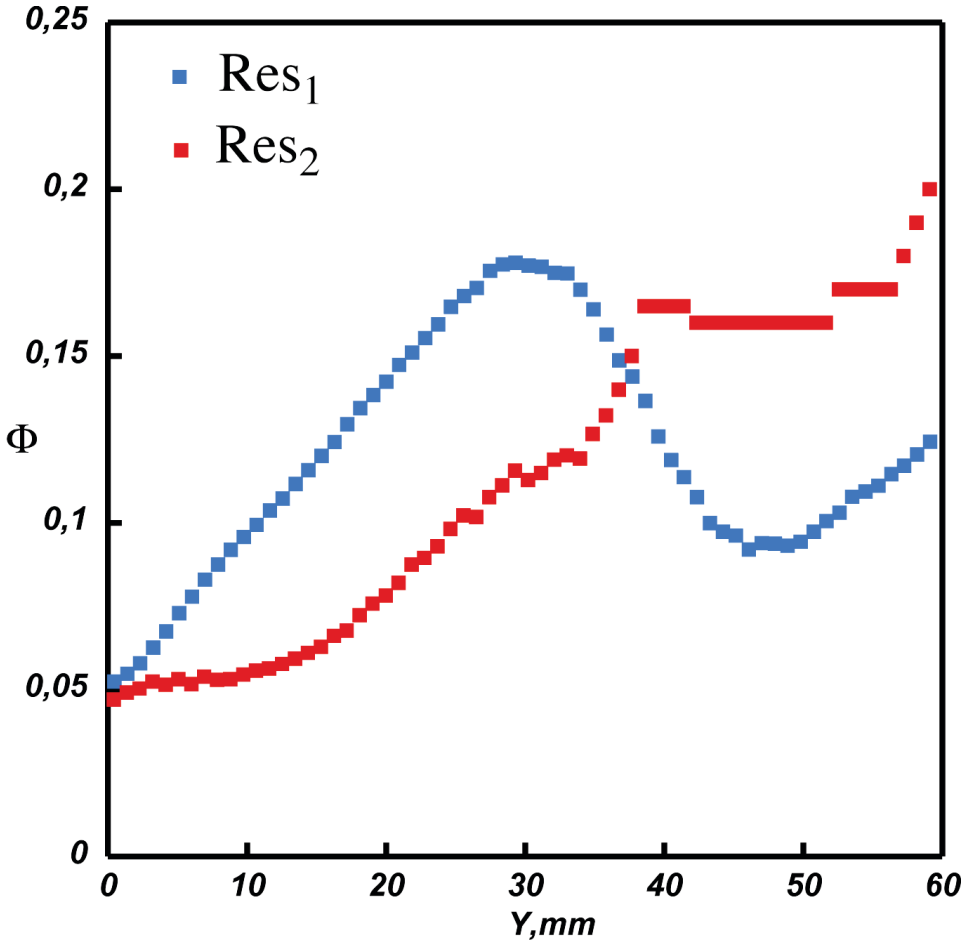

Fig. VI.6 Profiles of tracer volume fraction for two different spatial resolutions for Case-C

Another important quantity, affecting the stirring process is the interface extension Ψ .

In the following results, the interface extension has been evaluated for the three test conditions to study the dependence of this characteristic length on the fluid-dynamics conditions.

These profiles has been reported in Fig. VI.7.

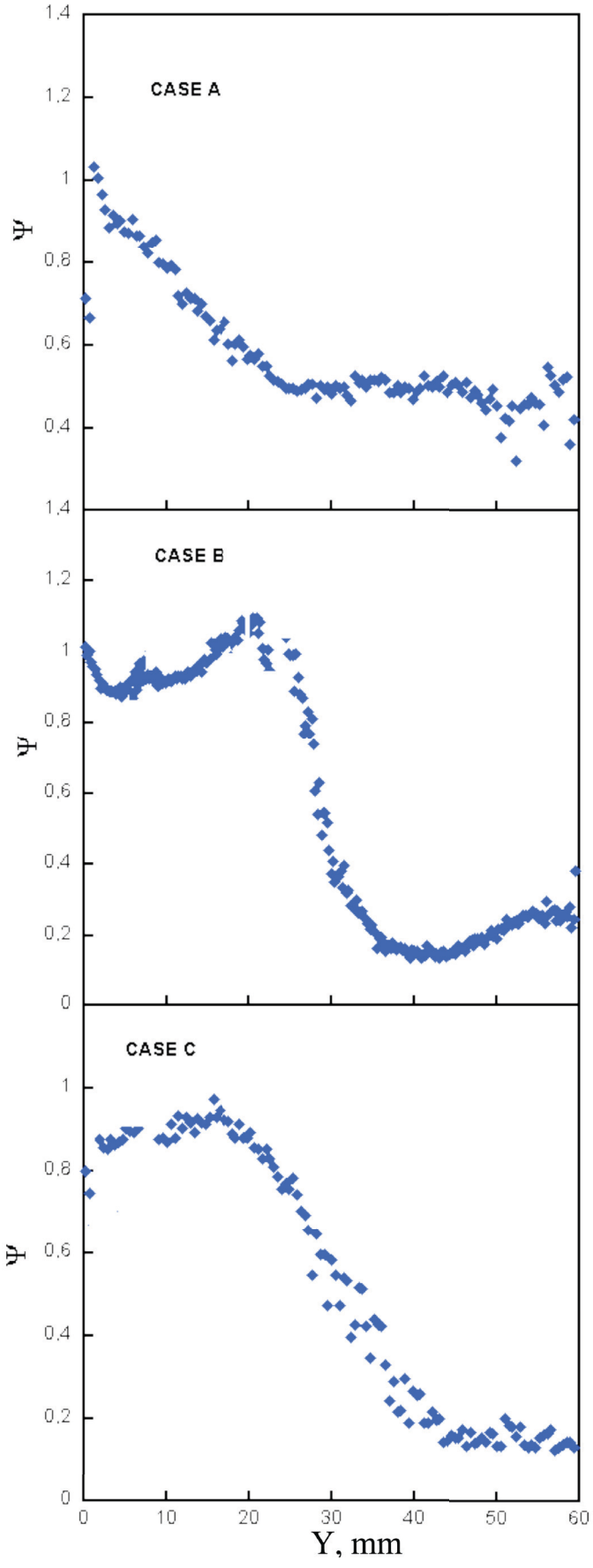

Fig. VI.7 Profiles of interface extension for three test conditions along the y-coordinate

The trends show an important feature of the Lagrangian Turbulence, i.e. a steep decay of the interface extension in the time (i.e. along y).

In particular, by increasing the turbulence level, the Ψ profiles show a gradual decrease in laminar conditions along the stream-wise while they show a fast decrease in transitional flow conditions.

The quantification of this interface property results very important for evaluating the performance of the stirring/mixing phenomena.

VI.2 Some aspects of mixing and ignition

The evolution of mixing layer is a well studied problem in different frameworks, referring to several geometrical constraints and to very broad field of applications.

A synthesis of one dimensional evolution (in a lamellar structure) is given here since this is a sufficient scheme to envisage the physics of the process and its insert in more complex models. The same information can be obtained for multidimensional conditions if this implementation is required, but it makes the analysis and the control of more complicated process.

Whatever conservative quantity, for instance the mixture fraction Z, can only be transported. In reference coordinates fixed in the origin on the interface and oriented with one axis perpendicularly to the interface, the mixture fraction along this coordinate is given by the folllowing equation:

6.2)
$$Z = \frac{1}{2}\left[1 + erf\left(\frac{x}{\delta}\right)\right]$$

where erf is the error function, x is the coordinate normal to the interface and δ is mixing layer thickness, defined in Cavaliere and Ragucci (2002), which is given by:

6.3) $$\delta = \sqrt{4Dt} \cdot \frac{\sqrt{\overline{SR^2}}}{SR}$$

where SR is the stretch ratio defined in chapter III.

The mixing layer thickness is function of time both explicitly as it is shown in square root and through the stretch ratio SR. It can be evaluated also when the complete characterization of stirring is obtained. In fact SR is the ratio between the surface density in whatever point of the field and the surface density at the inlet boundary if they refer to same control volume, whereas $\sqrt{\overline{SR^2}}$ is the root mean square of the stretch ratio. This last quantity can be evaluated if the residence time and the stretch rate tracked along the interface can be considered of the same orders of those developed on a intermaterial surface to which the stretch ratio refers. This position is more realistic in the case the interface density be, as it is , an average. Furthermore $\sqrt{\overline{SR^2}}$ is itself an average so that the correspondence between the intermaterial evolution and the track along a representative average surface is easier to be posed.

The mixing layer develops according to the previous equation when its thickness is smaller than one half of both the positive and negative interface distance, i.e. when $\delta \leq \Delta^{+}/2$ and $\delta \leq \Delta^{-}/2$. In fact it has been shown that in this case the mixing layer can be considered isolated and even the inner layer more adjacent to the interface are not affected by the presence of other mixing layers as it is shown by the negligible influence on the mass flux through the interface, when the aforementioned distance is kept (Cavaliere A et al. 1994). On the contrary when the mixing layer thickness is smaller then the semi-distance from an

another piece of interface, the mixture fraction distribution is given by the following equation:

6.4) $$Z = \frac{1}{2}\left[erf\left(\frac{x - \Delta^{-}}{\delta} \right) - erf\left(\frac{x}{\delta} \right) \right]$$

A more general relation when n stratified fuel layers are aligned perpendicularly to the x coordinate is given by the following equation which is easily derived as an extrapolation of eq. 6.4:

6.5) $$Z = \sum_{i=0}^{n} \frac{1}{2}\left[erf\left(\frac{x - n\Delta - \Delta^{-}}{\delta} \right) - erf\left(\frac{x - n\Delta}{\delta} \right) \right]$$

The comparison between the mixing layer thickness and the interface distance allow to identify a partition of the mixing field with different characteristics based on three main regimes (Cavaliere A et al. 1994):

- Isolated mixing layer
- Interacting mixing layer
- Saturated mixing layer

In the first one the mixing layer thickness is much smaller than the positive and negative interface semidistance, $\delta \le \Delta^{+}/2$,$\delta \le \Delta^{-}/2$. The mixing layer develops independently from any other mixing layer and it follows the temporal, spatial evolution described by the eqq 6.2 and 6.3 in one dimensional approximation. In fact it has been evaluated that the core of the mixing layer is unaffected by the presence of another mixing layer when its thickness is not in contact with another mixing layer thickness.

The interaction is effective when the two mixing layers touch each other, i.e. when $\delta \geq \Delta^{+}/2$,$\delta \geq \Delta^{-}/2$ and they evolve according to the eqq. 6.4 and 6.5, when one dimensional spatial distribution can be assumed.

The interaction is relevant up to the time, in which a significant inhomogeneity of the mixture fraction can be appreciated. On the contrary when the field is nearly uniform the gradient are so small that the mass diffusion is depressed. When the mixing layer thickness is much greater than the interface distance, say $\delta > 10\Delta^{+}$,$\delta > 10\Delta^{-}$, the mass diffusion on the interface is very negligible in respect to the isolated case, one thousand time smaller than the correspondent value in the isolated mixing layer. In this case the regime is said to be "saturated", because the presence of an interface in the neighborhood saturate the maximum possible values which a mixing layer can reach.

Other features of the mixing can be identified to make the local process deeply characterized taking into account also the possible reaction, which the medium can undergo. For instance it has been noticed that in particular convoluted structures the isosurface can separate each other and some of that can be imbedded on the interface side. In other words there is a "splitting" of the isosurface from the interface and the fate of the two surfaces is different, analogously to what happen in the annihilation of the isosurface. This "split" regime has only been hypothesized in turbulent conditions, therefore it has to be studied in complex fluid-dynamic pattern. Nevertheless it is easy to model as a lack of stretching of the isosurface and/or interface, because it delays their increase, since it is due to a stretch aligned normal to these surfaces. For this reason it should be of secondary importance in many practical mixing flows because these are built with the purpose to avoid such kind of alignment. Furthermore it is also unfavored because the probability that a linear stretch is parallel to one direction (normal to the isosurfaces) is half of the

probability that a linear stretch is parallel to a surface (the isosurfaces). In other words if there are not specific adjustment the probability of this alignment is only 0.33. and adjustment or realignment occur because the flow are built in such a way that they have to occur.

Finally it is worthwhile to underline that the interface density approach is a statistical approach, which is based on ensemble averaged weighted on the surface. The approach is also equivalent to others based either on the joint probability density function of the mixture fraction and gradient of mixture fraction or equivalently on the conditionally averaged quantity in respect to specific value of the mixture fraction (Meyers RE 1981). Nevertheless it is difficult to envisage the equivalence of single terms in evolution equation of surface density or of conditional average. Furthermore the meaning of each single quantity and the limit of their possible models are better evaluated in the framework of the first approach because it is based on topological characteristics which are easier to be visualized.

A final comment is devoted to emphasize an important characteristic of the MultiSECtioning procedure. It is suitable for different typologies of combustion processes. First of all it is very feasible in order to evaluate assisted ignition processes. In fact in this case it is possible to generate a spatial distribution of unreacted oxidant/fuel mixture, which can be ignited by an external source.

On the other hand there are processes that rely on the autoignition itself. Combustion in Diesel and Homogeneous Compression Compression Ignition (HCCI) engines, Mild Combustion and High Temperature Air Combustion (HiTAC) are examples for which the MultiSECtioning procedure follows a different path from that described for spark ignition processes.

The strategy also in this case relies on the identification of interface location. The advected-surfaces, in autoignition conditions, will be derived from a combination of fuel with the hot stream (or hot products). The quantities that affect the stirring/mixing processes also in this case are the same reported in the chapter III.

In some autoignition processes such as MILD Combustion, the reactive structures have *layerlet* features which degenerate in the classical flamelet picture when the system approach traditional diffusion flame behaviours.

Also in this case, it is possible to follow the evolution of the combustion process, as it is the case in the dynamical system with their time evolution. The procedure can converge or can not converge to stable (or unstable) state which is the combustion process as we are used to consider. Differently from the other procedure, the combustion process during this transition period has to be considered a diffusion controlled autoignition process, sometimes followed by a traditional diffusion flame. Therefore it is not a premixed (or partially premixed) propagation, as it is the case of assisted-ignition procedure.

Chapter VII
Conclusion

In the context of academic and industrial research concerning combustion systems, increasingly, advanced combustion modelling is finding application across a broad range of applications. Increasingly, such computational modelling is becoming more sound in its scientific base. There is still a long way to go until it enjoys the status of being an accurate predictive tool as is finite element analysis in elasticity and conductive heat transfer.

In the face of such difficulties for a direct analytical approach, engineering practice has traditionally resorted to empirical methods for combustor development. Thirty years ago, such empirical methods were all that were used by combustion engineers. Today, combustion engineers rely heavily on predictions from Computational Fluid Dynamics (CFD) codes incorporating models for the turbulence, for the kinetic, and for their interaction. Thirty years ago, empirical methods were sufficient for obtaining timely development of combustors using premium fuels and subject to moderate pollutant emission limits. Today, the market place demands rapid development of an increasingly broad range of products subject to even tighter pollutant emission controls. CFD is a very important component in the combustion engineer's toolkit. Empirical development is still necessary, but this is greatly aided by the insights gained from CFD studies, not only of the particular device of practical interest, but also of the simpler model problems that have been studied in detail by combustion scientists. Turbulent combustion research has also developed a wide range of combustion measurement techniques, especially those using lasers, that have not only been important in the development of the science of turbulent combustion but also are of direct use to combustion engineers. Combustion research has indeed been fruitful.

In this field, the fledgling status of computational modeling of practical combustion systems will be a seriously limiting factor in the ability of combustion technology to meet the 21st century challenges of climate change, energy security and tropospheric pollution.

The advances needed in such computational modeling for practical combustion systems will require considerable investment in modeling research in this area, including the new paradigms of multi-scale modeling. It will also need an increased emphasis on research directed at improving experimental data bases for model validation that are of an hierarchical nature and start with relatively simple problems that encapsulate the most important physics.

In this context, this PhD thesis provides an important contribution to the development of new methodological approaches for modeling complicated and complex reactive flow systems.

This strategy has the notable feature to be realistic and quantifiable in its realism. In particular, a strategy allowing for the analysis of the influence of single subprocesses has been conceived. Moreover, each step has been analyzed in detail in the thesis. It can be thought as divided in various parts, which corresponds to a “Separated Effect Contribution” (SEC). It allows a “Sequential Enlargement Combination” (SEC) of the “separated effects” and the “Side-by-side Experimental/Numerical Checking” (SEC) of the appropriate characterization of the field obtained by the introduction of new “separated effect”.

In particular, an important part of the thesis work has been focused on the first part of this procedure. It is a fluid-dynamic characterization of the patterns of interest when not reacting flows are introduced in fixed control volume, for fixed boundary-initial conditions, for fixed external parameters. The fluid dynamic database, has to be suitable for the characterization of the effects generated by considering the injection of not-diffusing

tracers in the control volume. This part of strategy has been discussed in chapters III, IV and V and a proper test rig has been built in order to characterize the interface which is the building block of this kind of approach.

In particular, concerning the stirring part, the following are the main results that have been obtained:

- An experimental apparatus has been built in order to obtain a fluid-dynamics pattern of gaseous flows;
- The interface between two flows has been generated by means of seeding particles;
- The detection of the material surface has been carried out by means of laser light scattering technique.
- The velocity field in the chamber has been obtained by means of PIV measurements
- Digital image processing algorithms were developed in order to characterize the main quantities related to the stirring process, i.e. interface density and volume fraction;
- Trends of Σ and Φ have been obtained as a function of the main variables, such as the streamwise coordinate, the Reynolds number and the velocity difference.
- Main phenomena affecting the stirring process have been identified and properly discussed;
- The principal limitations of the diagnostic apparatus have been discussed
- Some preliminary results of numerical validation have been obtained by means of a Direct Numerical Simulation with particle lagrangian tracking.

- The efficiency of stirring has been evaluated in relation to the whole combustion process.
- The experimental results that has been obtained lay the foundations for future works in this direction concerning the developments of semi-empirical models of interface evolution.

Moreover, the first part of the thesis works has been focused on the ignition-stage of the presented procedure. Simple diffusive reactive structures in standard and non-conventional combustion conditions have been analyzed in order to show the "critical" points of the ignition-part of MultiSECtioning.

The different types of combustion regimes which may occur in diffusion-controlled conditions have been obtained to show that the chemical/diffusion time scales involved in the process are able to influence the quality of the ignition process which can lead or not to stable combustion conditions.

Specifically, in MILD Combustion processes some behaviours different from those observed in standard combustion conditions have been obtained.

In this case, in fact, has been showed that the classical "flamelet" description of diffusion flames have to be redrawn in order to take into account the reactive structures realized under high dilution and preheating conditions. A "layerlet" assumption seems to be more appropriate in these particular ignition conditions.

In this respect, as emphasized in the second chapter, MultiSECtioning is a strategy able to adapt itself to the different reactive conditions that can occur in a combustion chamber.

In fact, the local combustion conditions affect only the relative values of the quantities that characterize the stirring/mixing processes but the procedures to evaluate them remain the same (as described in Chapter 4).

On the basis of the previous considerations, the most important conclusions from this work are the following:

- MultiSECtioning is a robust, feasible, suitable and flexible approach.
- The proposed strategy has showed two criticities that have been properly addressed:
    a) Identification and Measurability of the main quantities that characterize the stirring process.
    b) Evaluation of chemical/diffusive time scales in relation to the different combustion regimes.

A final remark is devoted to underline an important aspect.

MultiSECtioning procedure is currently a proposal. It is based on steps, which can be followed along the path of previous works. It has been presented with short notations and some references, because it has to be evaluated both for its methodological aspects and for the informations on single pieces.

In this respect the reported methodology has been used both to emphasize the feasibility of such a procedure and to show a reliable path. At the same time it should be clear that the strategy of assembly the different pieces of information or sub-models is a choice itself and it should be pursued with rational clearness of pursuing specific directions.

References

Abtahizadeh E, van Oijen J & de Goey P. (2012). Numerical study of Mild combustion with entrainment of burned gas into oxidizer and/or fuel streams. Combust. Flame, 159(6), 2155-2165.

Adrian RJ and Westerweel J. Particle image velocimetry. Vol. 30. Cambridge University Press, 2010.

Aharonov D. Quantum computing. In annual review of Computational Physics, 1998

Ahmed SF, Mastorakos E. Spark ignition of lifted turbulent jet flames. Combust. Flame 2006;146:215–31.

Amaral LA & Ottino JM. Complex networks. The European Physical Journal B-Condensed Matter and Complex Systems, 38 (2), 147-162, 2004.

Anand RK, Boersma BJ & Agrawal A (2009). Detection of turbulent/non-turbulent interface for an axisymmetric turbulent jet: evaluation of known criteria and proposal of a new criterion. Exp. Fluids 47(6), 995-1007.

Antonia RA & Mi J (1993). Temperature dissipation in a turbulent round jet. J. Fluid Mech., 250(1), 531-551.

Antonia RA, Satyaprakash BR & Hussain AKMF (1980). Measurements of dissipation rate and some other characteristics of turbulent plane and circular jets. Phys. Fluids, 23, 695.

Aref H (1984). Stirring by chaotic advection. J. Fluid Mech., 143(1), 1-21

Aref H & Tryggvason G (1984). Vortex dynamics of passive and active interfaces. Physica D: Nonlinear Phenomena, 12(1), 59-70.

Ashby WR (1962): Principles of the Self-Organizing System, in: Principles of Self-Organization, von Foerster H. & Zopf G.(eds.), (Pergamon, Oxford), p. 255-278.

Barlow RS, Smith NSA, Chen JY & Bilger RW (1999). Nitric oxide formation in dilute hydrogen jet flames: isolation of the effects of radiation and turbulence-chemistry submodels. Combust. Flame, 117(1), 4-31.

Batchelor GK, Howells ID and Townsend AA. Small-scale variation of convected quantities like temperature in turbulent fluid Part 2. The case of large conductivity. J. Fluid Mech. 5.01 (1959): 134-139.

Baydar E and Ozmen Y, An experimental and numerical investigation on a confined impinging air jet at high Reynolds numbers. Appl. Therm. Eng. 25.2: 409-421, 2005.

Beduneau JL, Kim B, Zimmer L, Ikeda Y. Measurements of minimum ignition energy in premixed laminar methane/air flow by using laser induced spark. Combust. Flame 2003;132:653–65.

Bendat JS & Piersol AG (2011). Random data: Analysis and measurement procedures (Vol. 729). Wiley Press.

Berger MJ & Oliger J, Adaptive mesh refinement for hyperbolic partial differential equations. J. Comput. Phys. 53.3: 484-512, 1984.

Bilger RW, Pope SB, Bray KN & Driscoll JF. (2005). Paradigms in turbulent combustion research. Proc. Combust. Inst., 30(1), 21-42.

Birch AD, Brown DR, Dodson MG, Thomas JR. Studies of flammability in turbulent flows using laser Raman spectroscopy. Proc. Combust. Inst. 1978;17:307–14.

Birch AD, Brown DR, Dodson MG. Ignition probabilities in turbulent mixing flows. Proc. Combust. Inst. 1981;18:1775–80.

Blouch JD and Law CK. Effects of turbulence on nonpremixed ignition of hydrogen in heated counterflow. Combust. Flame 132.3 (2003): 512-522.

Bowman CT, Frenklach M, Gardiner WR & Smith G (1999). The GRI 3.0 chemical kinetic mechanism. University of California: Berkeley, CA.

Bradley D, Sheppard CGW, Suardjaja IM, Woolley R. Fundamentals of high-energy spark ignition with lasers. Combust. Flame 2004;138:55–77.

Bray KN. The challenge of turbulent combustion. Symposium (International) on Combustion. Vol. 26. No. 1. Elsevier Science, 1996.

Brethouwer G (2000). Mixing of passive and reactive scalars in turbulent flows. PhD thesis, Delft, the Netherlands.

Buch KA & Dahm WJ (1998). Experimental study of the fine-scale structure of conserved scalar mixing in turbulent shear flows. Part 2. Sc≈ 1. J. Fluid Mech., 364, 1-29.

Campbell CS, Egolfopoulos FN. Kinetics paths to radical-induced ignition of methane/air mixtures. Combust. Sci. Technol. 2005;177: 2275–98.

Candel SM and Poinsot JT. Flame stretch and the balance equation for the flame area. Combust. Sci. Technol. 70.1-3 (1990): 1-15.

Canny J (1986). A computational approach to edge detection. Pattern Analysis and Machine Intelligence, IEEE Transactions on, (6), 679-698.

Catrakis HJ and Dimotakis PE. Mixing in turbulent jets: scalar measures and isosurface geometry. J. Fluid Mech. 317.99 (1996): 369-406.

Cavaliere A and de Joannon M. Mild combustion. Prog. Energy Combust. Sci. 30.4 (2004): 329-366.

Cavaliere A, de Felice G, Denaro FM, Meola C. Eulerian and Lagrangian Simulation of Transport Phenomena in Multiple or Periodical Interacting Planar Jets or Wakes versus Experimental Results. Proceedings of the 6th International Conference on Computational Methods and Experimental Measurements, 1993, pp. 135-150.

Cavaliere A, de Joannon M, Ragucci R, in: D. Dunn-Rankine (Ed.), Lean Combustion: Technology and Control, Academic Press, San Diego, 2008, p. 55.

Cavaliere A, de Joannon M: Mild Combustion. Una lezione nell'atelier di un "nuovo" processo di combustione, European Combustion Meeting 2005, Louvain-la-Neuve, (2005)

Cavaliere A, El-Naggar M and Ragucci R, Experimental analysis of intermaterial surfaces in the study of gaseous mixing characteristics. Int. J. Heat Mass Transfer, 38.2: 317-329 1995.

Cavaliere A, El-Naggar M and Ragucci R. Experimental identification of mixing regimes in the analysis of turbulent diffusion flames. Combust. flame 99.3 (1994): 679-686.

Cavaliere A, Ragucci R, Gaseous diffusion flames: simple structures and their interaction. Prog. Energy Combust. Sci. 27(5): 547-585 2002.

Cerbelli S, Alvarez MM and Muzzio FJ, Prediction and quantification of micromixing intensities in laminar flows, AIChE J. 48, 686 (2002).

Chakraborty N & Cant RS (2007). A priori analysis of the curvature and propagation terms of the flame surface density transport equation for large eddy simulation. Phys. Fluids 19.

Chakraborty N & Cant RS. Direct numerical simulation analysis of the flame surface density transport equation in the context of large eddy simulation. Proc. Combust. Inst. 32.1 (2009): 1445-1453.

Chakraborty N & Cant RS. Unsteady effects of strain rate and curvature on turbulent premixed flames in an inflow–outflow configuration. Combust. Flame 137.1 (2004): 129-147.

Chella, R., & Ottino, J. M. (1984). Conversion and selectivity modifications due to mixing in unpremixed reactors. Chem. Eng. Sci., 39(3), 551-567.

Chen JB and Im HG. Stretch effects on the burning velocity of turbulent premixed hydrogen/air flames. Proc. Combust. Inst. 28.1 (2000): 211-218.

Chen JH, Choudhary A, de Supinski B, DeVries M, Hawkes ER, Klasky S, Liao WK, Ma KL, Mellor-Crummey J, Podhorszki N, Sankaran R, Shende S and Yoo CS. Terascale direct numerical simulations of turbulent combustion using S3D. Computational Science & Discovery 2.1 : 015001, 2009.

Chong MS, Perry AE, & Cantwell BJ. (1990). A general classification of three-

dimensional flow fields. Phys. Fluids, 2, 408-420.

Christo FC and Dally BB. Modeling turbulent reacting jets issuing into a hot and diluted coflow. Combust. Flame 142.1 (2005): 117-129.

Clemens NT. Flow Imaging. Hornak (Ed.), Encyclopedia of Imaging Science and Technology, John Wiley and Sons, New York (2002), pp. 390–419

Clifford MJ, Cox SM and Roberts EP. Lamellar modelling of reaction, diffusion and mixing in a two-dimensional flow. Chem. Eng. J. 71.1 (1998): 49-56.

Coelho PJ & Peters N (2001). Numerical simulation of a mild combustion burner. Combust. Flame, 124(3), 503-518.

Coleman HW Steele WG (2009). Experimentation, validation, and uncertainty analysis for engineers. John Wiley & Sons.

Colucci PJ, Jaberi FA, Givi P and Pope SB. Filtered density function for large eddy simulation of turbulent reacting flows. Phys. Fluids, 1998, 10: 499.

Cote T, Ridley JD, Clements RM, Smy PR. The ignition characteristics of igniters at sub-atmospheric pressures. Combust. Sci. Technol. 1986;48:151–62.

Crowe CT, Chung JN and Troutt TR. Particle mixing in free shear flows. Prog. Energy Combust. Sci. 14.3 (1988): 171-194.

da Silva CB, Dos Reis RJ & Pereira JC (2011). The intense vorticity structures near the turbulent/non-turbulent interface in a jet. J. Fluid Mech., 685, 165-190.

Davis RW, Moore EF, Santoro RJ & Ness JR. (1990). Isolation of buoyancy effects in jet diffusion flame experiments. Combust. Sci. Technol., 73(4-6), 625-635.

De A, Oldenhof E, Sathiah P & Roekaerts D. (2011). Numerical simulation of Delft-jet-in-hot-coflow (DJHC) flames using the eddy dissipation concept model for turbulence–chemistry interaction. Flow Turb. Comb. 87(4), 537-567.

de Joannon M, Cavaliere A, Faravelli T, Ranzi E, Sabia P & Tregrossi A. (2005). Analysis of process parameters for steady operations in methane mild combustion technology. Proc. Combust. Inst., 30(2), 2605-2612.

de Joannon M, Sabia P, Cavaliere A, HDDI MILD combustion, in: Alternative Ignition Systems. Lackner, M. (2009). Verlag ProcessEng Engineering..

de Joannon M, Sabia P, Cozzolino G, Sorrentino G & Cavaliere, A. Pyrolitic and Oxidative Structures in Hot Oxidant Diluted Oxidant (HODO) MILD Combustion. Combust. Sci. Technol. 184.7-8 (2012): 1207-1218.

de Joannon M, Sabia P, Sorrentino G, Cavaliere A. Numerical study of mild combustion in hot diluted diffusion ignition (HDDI) regime. Proc Combust Inst., 32 (2009), pp. 3147–3154).

de Joannon M, Sorrentino G and Cavaliere A. MILD combustion in diffusion-

controlled regimes of Hot Diluted Fuel. Combust. Flame (2012).

Domingo P and Vervisch L. Triple flames and partially premixed combustion in autoignition of non-premixed turbulent mixtures. Symposium (International) on Combustion. Vol. 26. No. 1. Elsevier, 1996.

Dopazo C, Recent developments in PDF methods, in: P.A. Libby, F.A. Williams (Eds.), Turbulent Reacting Flows, Academic Press, London, 1994.

Echekki T and Chen JH. Direct numerical simulation of autoignition in non-homogeneous hydrogen-air mixtures. Combust. Flame 134.3 (2003): 169-191.

Echekki T and Chen JH. Unsteady strain rate and curvature effects in turbulent premixed methane-air flames. Combust. Flame 106.1 (1996): 184-202.

Echekki T. (2009). Multiscale methods in turbulent combustion: strategies and computational challenges. Computational Science & Discovery, 2(1), 013001.

Eckbreth AC. Laser Diagnostics for Combustion Temperature and Species, Abacus Press, Cambridge, 1988

FLUENT 6.3 User Guide.

Fotache CG, Sung CJ, Sun CJ & Law CK. (1998). Mild oxidation regimes and multiple criticality in nonpremixed hydrogen-air counterflow. Combust. Flame, 112 (3), 457-471.

Fung JCH and Vassilicos JC. Fractal dimensions of lines in chaotic advection. Physics of Fluids A: Fluid Dynamics 3 (1991): 2725.

Galaktionov OS, Anderson PD, Kruijt PGM, Peters GWM & Meijer HE. (2001). A mapping approach for three-dimensional distributive mixing analysis. Computers & fluids, 30(3), 271-289.

Galletti C, Parente A and Tognotti L, Numerical and experimental investigation of a mild combustion burner. Combust. Flame 151.4: 649-664, 2007.

Gao F and O'Brien EE, A large eddy simulation scheme for turbulent reacting flows. Phys. Fluids A 5 1282–4, 1993.

Gibson CH (1968). Fine Structure of Scalar Fields Mixed by Turbulence. I. Zero-Gradient Points and Minimal Gradient Surfaces. Physics of Fluids, 11, 2305.

Giona M, Cerbelli S & Adrover A. (2002) Quantitative analysis of mixing structures in chaotic flows generated by infinitely fast reactions in the presence of diffusion. J. Phys. Chem. A 106, 5722–5736

Gonzalez RC & Woods RE (2002). Digital Image Processing. New Jersey: Prentice Hall

Goto S & Kida S (2007). Reynolds-number dependence of line and surface stretching in turbulence: folding effects. J. Fluid Mech., 586, 59.

Gouldin F, Bray K & Chen JY. 1989 Chemical closure model for fractal flamelets. Combust. Flame 77, 241.

Green MA, Rowley CW & Haller G. (2007). Detection of Lagrangian coherent structures in three-dimensional turbulence. J. Fluid Mech., 572(1), 111-120.

Haller G. Distinguished material surfaces and coherent structures in three-dimensional fluid flows. Physica D: Nonlinear Phenomena 149.4 (2001): 248-277.

Hawkes ER and Cant RS. Implications of a flame surface density approach to large eddy simulation of premixed turbulent combustion. Combust. Flame 126.3 (2001): 1617-1629.

Haworth DC and Poinsot TJ. Numerical simulations of Lewis number effects in turbulent premixed flames. J. Fluid Mech., 244.1 (1992): 405-436.

Hesselink L, Post FH & van Wijk JJ (1994). Research issues in vector and tensor field visualization. Computer Graphics and Applications, IEEE, 14(2), 76-79.

Holland TO. Taxonomy for the modeling and simulation of emergent behavior systems. Proceedings of the 2007 spring simulation multiconference-Volume 2. Society for Computer Simulation International, 2007.

Humer S, Seiser R, Seshadri K (2002). Non-premixed and premixed extinction and autoignition of C_2H_4, C_2H_6, C_3H_6, and C_3H_8. Proc Combust Inst., 29(2), 1597-1604.

Hunt J, Wray A, Moin P. Eddies, stream, and convergence zones in turbulent flows, Center For Turbulence Research, Report CTR-S88, 1988

Jenny P and Müller B. Rankine–Hugoniot–Riemann solver considering source terms and multidimensional effects. Journal of Computational Physics 145.2: 575-610, 1998.

Jeong J & Hussain F. (1995). On the identification of a vortex. J. Fluid Mech., 285 (69), 69-94.

Katsuki M and Hasegawa T. The science and technology of combustion in highly preheated air. Symposium (International) on Combustion. Vol. 27. No. 2. Elsevier, 1998.

Keane RD, Adrian RJ and Zhang Y. Super-resolution particle imaging velocimetry. Meas. Sci. Technol. 6.6 (1999): 754.

Keane RD, Adrian RJ. 1990. Optimization of particle image velocimeters. Part I: Double pulsed systems. Meas. Sci. Technol. 1:1202–15

Keane RD, Adrian RJ. 1991. Optimization of particle image velocimeters. Part II: Multiple pulsed systems. Meas. Sci. Technol. 2:963–74

Kee RJ, Rupley FM, Miller JA, Coltrin ME, Grcar JF, Meeks E & Miller SF. (2002). CHEMKIN Collection, Release 3.7. 1, Reaction Design, Inc. San Diego, CA.

Keller JO, Bramlette TT, Westbrook CK, Dec JE. Pulse combustion: The quantification of characteristic times. Combust. Flame 79.2: 151-161 1990.

Kim H and Pitsch H, Scalar gradient and small-scale structure in turbulent premixed combustion, Phys. Fluids 19, 2007

Klinger T. Image processing with LabVIEW and IMAQ Vision. Prentice Hall, 2003.

Knikker R, Veynante D, Meneveau C. A dynamic flame surface density model for large eddy simulation of turbulent premixed combustion. Phys. Fluids 16, L91 (2004).

Kollmann W and Chen JH. Dynamics of the flame surface area in turbulent non-premixed combustion. Symposium (International) on Combustion. Vol. 25. No. 1. Elsevier, 1994.

Kono M, Hatori K, Iinuma K. Investigation on ignition ability of composite sparks in flowing mixtures. Proc Combust Inst. 1984;20:133–40.

Krause E and Jäger W, High Performance Computing in Science and Engineering'01: Transactions of the High Performance Computing Center, Stuttgart (HLRS). Springer Verlag, 2002.

Kravchik T, Sher E, Heywood JB. From spark ignition to flame initiation. Combust. Sci. Technol. 1995;108:1–30.

Kreutz TG and Law CK. Ignition in nonpremixed counterflowing hydrogen versus heated air: Computational study with detailed chemistry. Combust. Flame 104.1 (1996): 157-175.

Kuo, K. K. Principles of Combustion. 2005. John Wiley & Sons, Hoboken, NJ

Law CK. 2006. Combustion Physics, Cambridge University Press, New York

Law CK. Combustion at a crossroads: Status and prospects. Proc Combust Inst. 31.1: 1-29, 2007.

Lefebvre, A. H. 1989 Atomization and Sprays. Hemisphere, New York

Lekien F & Coulliette C. Chaotic stirring in quasi-turbulent flows. Philosophical Transactions of the Royal Society A: Mathematical, Physical and Engineering Sciences, 365 (2007), 3061-3084.

Linan A and Crespo A. An asymptotic analysis of unsteady diffusion flames for large activation energies. Combust. Sci. Technol. 14.1-3 (1976): 95-117.

Linan A and Williams FA. Fundamental aspects of combustion. (1993). Oxford Engineering Science Series.

Linan A. The asymptotic structure of counterflow diffusion flames for large activation energies. Acta Astronautica 1.7 (1974): 1007-1039.

Liu S, Hewson JC, Chen JH & Pitsch H. (2004). Effects of strain rate on high-pressure nonpremixed n-heptane autoignition in counterflow. Combust. Flame, 137(3), 320-339.

Luo K, Yan J, Fan J and Cen K. On coherent structures in a three-dimensional transitional plane jet. Science in China Series E: Technological Sciences, 2008

Lyons KM. Toward an understanding of the stabilization mechanisms of lifted turbulent jet flames: Experiments. Prog. Energy Combust. Sci. 33.2 (2007): 211-231.

Magnussen BF and Hjertager BH. On mathematical modeling of turbulent combustion with special emphasis on soot formation and combustion. Symposium (International) on Combustion. Vol. 16. No. 1. Elsevier, 1977.

Mancini M, Schwöppe P, Weber R & Orsino S. (2007). On mathematical modelling of flameless combustion. Combust. Flame, 150(1), 54-59.

Marble FE, Broadwell JE, The coherent flame model for turbulent chemical reactions, Tech. Rep. Project Squid Report TRW-9-PU, TRW (1977).

Mason SD, Chen JH and Im HG. Effects of unsteady scalar dissipation rate on ignition of non-premixed hydrogen/air mixtures in counterflow. Proc Combust Inst. 29.2 (2002): 1629-1636.

Mastorakos E, Baritaud TA and Poinsot TJ. Numerical simulations of autoignition in turbulent mixing flows. Combust. Flame 109.1 (1997): 198-223.

Mastorakos E. (2009). Ignition of turbulent non-premixed flames. Prog. Energy Combust. Sci. 35(1), 57-97.

McCraw JL, Moore NJ, Lyons KM. Observations on upstream flame propagation in the ignition of hydrocarbon jets. Flow, Turbulence and Combustion 2007;79:83–97.

McIlroy A, McRae G, Basic Research Needs for Clean and Efficient Combustion of 21st Century Transportation Fuels, DOE Office of Basic Energy Sciences, Workshop on Basic Research Needs, 2006

Mellado JD, Sánchez AL, Kim JS, Liñán A. Branched-chain ignition in strained mixing layers. Combustion Theory and Modelling 4.3 (2000): 265-288.

Melling A. Tracer particles and seeding for particle image velocimetry. Measurement Science and Technology 8.12 (1999): 1406.

Meyers RE, O'Brien EE, The Joint Pdf of a Scalar and Its Gradient at a Point in a Turbulent Fluid. Comb. Sci. Technol., 1981, 26, 123-134

Mongia HC, 2008, Recent Progress in Comprehensive Modeling of Gas Turbine Combustion, AIAA Paper No. 2008-1445.

Murase E, Ono S, Hanada K, Oppenheim AK. Initiation of combustion in lean mixtures by flame jets. Comb. Sci. Technol., 1996;113– 114:167–77.

Oberkampf WL & Trucano TG, Verification and validation in computational fluid dynamics. Progress in Aerospace Sciences 38.3: 209-272, 2002.

Ottino JM, 1981, Efficiency of mixing from data on fast reactions in multi-jet reactors and stirred tanks. AIChE Journal 27, 184 192.

Ottino JM, Description of mixing with diffusion and reaction in terms of the concept of material interfaces, J. Fluid Mech., 114, 83-103 (1982).

Ottino JM, Ranz WE & Macosko CW. (1981). A framework for description of mechanical mixing of fluids. AIChE Journal, 27(4), 565-577.

Ottino JM. Mixing, chaotic advection, and turbulence. Annual Review of Fluid Mechanics 22.1 (1990): 207-254.

Ottino JM. The kinematics of mixing: stretching, chaos, and transport. Vol. 3. Cambridge University Press, 1989.

Parente A, Galletti C and Tognotti L. A simplified approach for predicting NO formation in MILD combustion of CH_4–H_2 mixtures. Proc Combust Inst. 33.2: 3343-3350, 2011.

Parente A, Galletti C and Tognotti L. Effect of the combustion model and kinetic mechanism on the MILD combustion in an industrial burner fed with hydrogen enriched fuels. International journal of hydrogen energy 33.24 (2008): 7553-7564.

Pedersen PS and Bjorn Q. A model for the physical part of the ignition delay in a diesel engine. Society of Automotive Engineers, 1974.

Peters N. Local quenching due to flame stretch and non-premixed turbulent combustion. Combustion Science and Technology 30.1-6 : 1-17, 1983.

Peters N. Multiscale combustion and turbulence. Proc Combust Inst. 32.1: 1-25, 2009.

Peters N. Turbulent combustion. Cambridge university press, 2000.

Philip J & Marusic I. (2012). Large-scale eddies and their role in entrainment in turbulent jets and wakes. Physics of Fluids, 24, 055108.

Phuoc X, Chen RH. Use of laser-induced spark for studying ignition stability and unburned hydrogen escaping from laminar diluted hydrogen diffusion jet flames. Optics and Lasers in Engineering 2007;45:834–42.

Pitsch H, Large-eddy simulation of turbulent combustion. Annu .Rev. Fluid. Mech. 2006;

Pitt PL, Ridley JD, Clements RM. An ignition system for ultra lean mixtures. Combustion Science and Technology 1984;35:277–85.

Pope SB (1988). The evolution of surfaces in turbulence. International journal of engineering science, 26(5), 445-469.

Pope SB, Yeung PK and Girimaji SS. (1992) Stretching and bending of material surfaces in turbulence. https://tcg.mae.cornell.edu/pubs/Pope_YG_IBM_92.pdf

Pope SB, Yeung PK and Girimaji SS. The curvature of material surfaces in isotropic turbulence. Physics of Fluids A: Fluid Dynamics 1 (1989): 2010.

Pope SB. Computations of turbulent combustion: progress and challenges. Symposium (International) on Combustion. Vol. 23. No. 1. Elsevier, 1991.

Pope SB. PDF methods for turbulent reactive flows. Prog. Energy Combust. Sci. 11.2: 119-192,1985.

Pope, S. B. (1987). Turbulent premixed flames. Annu .Rev. Fluid. Mech., 19(1), 237-270.

Post FH, Vrolijk B, Hauser H, Laramee RS and Doleisch H. Feature Extraction and Visualization of Flow Fields. In Eurographics 2002 State-of-the-Art Reports, The Eurographics Association, 2002

Prasad RR & Sreenivasan KR. (1989). Scalar interfaces in digital images of turbulent flows. Experiments in fluids, 7(4), 259-264.

Prigogine I, Stengers I & Toffler A, Order out of chaos. Bantam Books, Toronto-New York-London-Sydney. 349 pp. paper 1984.

Qin X, Choi CW, Mukhopadhyay A, Puri IK, Aggarwal SK, Katta VR. Triple flame propagation and stabilization in a laminar axisymmetric jet. Combustion Theory and Modelling 2004;8:293–314.

Rachner M, Becker J, Hassa C & Doerr T. (2002). Modelling of the atomization of a plain liquid fuel jet in crossflow at gas turbine conditions. Aerospace Science and Technology, 6(7), 495-506.

Rashkovsky SA. Spark ignition of ill-mixed gases. In: First Mediterranean Combustion Symposium, Antalya, Turkey; 1999.

Relf CG, Image Acquisition and Processing with LabVIEW CRC, Boca Raton, 2003

Richardson ES, Mastorakos E. Numerical investigation of forced ignition in laminar counterflow non-premixed methane-air flames. Combustion Science and Technology 2007;179:21–37

Roberts E. Determination of the local micromixing structure in laminar flows. Chemical Engineering Journal 160 (2010) 267–276.

Ronney PD. Laser versus conventional ignition of flames. Optical Engineering 1994;33:510–21.

Rosner DE. Transport processes in chemically reacting flow systems. Dover Publications, 2000.

Sadanandan R, Markus D, Schießl R, Maas U, Olofsson J, Seyfried H, Richter M, Aldén M. Detailed investigation of ignition by hot gas jets. Proc Combust Inst. 2007;31:719–26.

Shraiman BI and Siggia ED. (1994) Lagrangian path integrals and fluctuations in random flows. Phys. Rev. E. 49(4), 2912.

Smith MTE, Birch AD, Brown DR, Fairweather M. Studies of ignition and flame propagation in turbulent jets of natural gas, propane and a gas with a high hydrogen content. Proc Combust Inst. 1986 ;21:1403–8.

Smith WJ, Modern Optical Engineering: The Design of Optical Systems, 2nd ed., McGraw-Hill, NY, 1990

Sorrentino G, Ragucci R and Cavaliere A. (2011). Methodological Issues of Interface Characterization in the Framework of MultiSECtioning Strategy. Fifth European Combustion Meeting (ECM2011) 2011.

Sorrentino G, Ragucci R and Cavaliere A. Experimental characterization of interface properties in the framework of multisectioning strategy: preliminary results. In XXXIV Meeting of the Italian Section of the Combustion Institute, 2011.

Sorrentino G, Ragucci R, Cavaliere A, Investigation of the stirring process in a turbulent jet by means of Particle Image Velocimetry. 16th Int Symp on Applications of Laser Techniques to Fluid Mechanics Lisbon, Portugal, 09-12 July, 2012

Sorrentino G, Scarpa D and Cavaliere A. Transient inception of MILD combustion in hot diluted diffusion ignition (HDDI) regime: A numerical study. Proc. Combust. Inst. (2013); 34: 3239-3247.

Sorrentino G, Scarpa D, Cavaliere A. Characteristic times of unsteady autoigniting layerlet. XXXV Meeting of the Italian Section of the Combustion Institute, 2012

Spalding DB (1971). Mixing and chemical reaction in steady confined turbulent flames. 13th Int. Symp. on Combustion, 649-657

Sreedhara S and Lakshmisha KN. Assessment of conditional moment closure models of turbulent autoignition using DNS data. Proc. Combust. Inst. 29.2 (2002): 2069-2077.

Sreedhara S and Lakshmisha KN. Direct numerical simulation of autoignition in a non-premixed, turbulent medium. Proc. Combust. Inst. 28.1 (2000): 25-33.

Sreenivasan KR and Meneveau C. The fractal facets of turbulence. Journal of Fluid Mechanics 173.1 (1986): 357-386.

Sreenivasan KR, Fractals and multifractals in fluid turbulence - Annual Review of Fluid Mechanics, 1991

Strogatz SH. Nonlinear Dynamics and Chaos: With Applications to Physics, Biology, Chemistry and Engineering. Cambridge, MA. 1994. 8

Strogatz SH. Sync: The emerging science of spontaneous order. Hyperion, New York, 2003.

Su LK and Clemens NT. Planar measurements of the full three-dimensional scalar dissipation rate in gas-phase turbulent flows. Exp.Fluids27,507–521(1999).

Swain MR, Filoso PA, Swain MN. An experimental investigation into the ignition of leaking hydrogen. International Journal of Hydrogen Energy 2007;32:287–95.

Takeno T. Transition and structure of jet diffusion flames. Twenty-Fifth Symposium (International) on Combustion. 1994;25:1061-73

Tropea C, Optical Particle Characterization in Flows. Annu. Rev. Fluid Mech., 2011

Trouvé A and Poinsot T. The evolution equation for the flame surface density in turbulent premixed combustion. Journal of Fluid Mechanics 278 (1994): 1-32.

Tsuji H, Gupta AK, Hasegawa T, Katsuki M, Kishimoto K, Morita M. High temperature air combustion: from energy conservation to pollution reduction. Vol. 4. CRC, 2002.

Van Kalmthout E, Veynante D and Candel S. Direct numerical simulation analysis of flame surface density equation in non-premixed turbulent combustion. Symposium (International) on Combustion. Vol. 26. No. 1. Elsevier, 1996.

van Oijen JA (2012). Direct numerical simulation of autoigniting mixing layers in MILD combustion. Proc. Comb. Inst. 34:1163–1171.

van Oijen JA, Flamelet-generated manifolds: development and application to premixed laminar flames. Ph.D. thesis, Eindhoven University of Technology, 2002

Vervisch L and Poinsot T. Direct numerical simulation of non-premixed turbulent flames. Annual review of fluid mechanics 30.1 (1998): 655-691.

Vervisch L, Bidaux E, Bray KNC & Kollmann W. (1995). Surface density function in premixed turbulent combustion modeling, similarities between probability density function and flame surface approaches. Physics of Fluids, 7, 2496.

Veynante D and Vervisch L. Turbulent combustion modeling. Progress in Energy and Combustion Science 28.3 (2002): 193-266.

Veynante D, Lacas F, Maistret E & Candel S. (1991). Coherent Flame Model for Non-Uniformly Premixed Turbulent Flames. In Turbulent Shear Flows 7 (pp. 367-378). Springer Berlin Heidelberg.

Villermaux E & Innocenti C (1999). On the geometry of turbulent mixing. Journal of Fluid Mechanics, 393, 123-147.

Villermaux E, Innocenti C & Duplat J (1998). Scalar fluctuations PDF's in transient turbulent mixing. In Advances in Turbulence VII (pp. 571-572). Springer Netherlands.

Wei GW & Jia YQ. (2002). Synchronization-based image edge detection. EPL (Europhysics Letters), 59(6), 814.

Westbrook CK, Mizobuchi Y, Poinsot TJ, Smith PJ & Warnatz J. (2005). Computational combustion. Proceedings of the Combustion Institute, 30(1), 125-157.

Westerweel J, Elsinga GE & Adrian, RJ. (2013). Particle image velocimetry for complex and turbulent flows. Ann. Rev. Fluid Mech., 45, 409-436.

Westerweel J, Fukushima C, Pedersen JM, Hunt J (2005). Mechanics of the Turbulent-Nonturbulent Interface of a Jet. Phys. Rev. Lett. 95(17), 174501.

Willert CE and Gharib M. Digital particle image velocimetry. Experiments in fluids 10.4 (1991): 181-193.

Williams FA, Combustion Theory 2nd (The Benjamin/Cummings, 1985).

Wünning JA, Wünning JG. Flameless oxidation to reduce thermal NO-formation. Prog. Energy Combust. Sci. 23 (1) (1997) 81–94

Zheng XL, Blouch JD, Zhu DL, Kreutz TG & Law CK. (2002). Ignition of premixed hydrogen/air by heated counterflow. Proceedings of the Combustion Institute, 29 (2), 1637-1643.